Title

Distinguishing Electron-Only Flux Rope Erosion and Electron-Only Onset of Reconnection from Ion-Coupled Reconnection in Earth's Magnetotail

Author

Hubbert, Mark Alexander

Publication Date

2024

Peer reviewed|Thesis/dissertation

UNIVERSITY OF CALIFORNIA
Los Angeles

Distinguishing Electron-Only Flux Rope Erosion and Electron-Only Onset of Reconnection from Ion-Coupled Reconnection in Earth's Magnetotail

A dissertation submitted in partial satisfaction
of the requirements for the degree
Doctor of Philosophy in Geophysics and Space Physics

by

Mark Alexander Hubbert

2024

ABSTRACT OF THE DISSERTATION

Distinguishing Electron-Only Flux Rope Erosion and Electron-Only Onset of Reconnection from Ion-Coupled Reconnection in Earth's Magnetotail

by

Mark Alexander Hubbert
Doctor of Philosophy in Geophysics and Space Physics
University of California, Los Angeles, 2024
Professor Christopher T. Russell, Chair

Magnetic reconnection is a fundamental, ubiquitous process which dictates physical phenomena across Earth's magnetosphere. Reconnection has been well investigated with spacecraft for decades, and the community's understanding of its structure continues to evolve. The recently launched Magnetospheric Multiscale (MMS) Mission has allowed for multi-spacecraft observations of ion-scale and sub-ion scale structures, such as the Ion Diffusion Region (IDR). In 2016, MMS1 and 3 observed oppositely directed electron outflow jets while crossing a thin, electron-scale current sheet in Earth's turbulent magnetosheath. The current sheet lacked the ion outflow jets expected in ion-coupled, turbulent, magnetic reconnection. As a result, this structure was dubbed "electron-only" reconnection. Current sheets labelled as electron-only reconnection have since been reported with simulation work and spacecraft data in Earth's magnetosheath, dayside magnetopause, and magnetotail. However, due to the rarity of electron-only current sheet observations and a lack of consistency/clarity in the underlying physical properties of events, a precise definition and generation mechanism of electron-only reconnection remains unclear.

In this dissertation, we use MMS data to investigate non-reconnecting and reconnecting current sheets in Earth's magnetotail. First, we perform a statistical survey of quiet current sheets, ion-coupled reconnection, and Ion Diffusion Regions in Earth's magnetotail. We compare the properties of these current sheets in tilted vs. equatorial current sheets. We find that all current sheet types occur equally in tilted and equatorial current sheets, and that ion and electron outflow profiles are generally unaffected by the orientation of the current sheet. Next, we define electron-only reconnection as a reconnecting current sheet that is electron-scale in thickness and less than 10 d_e long, such that spacecraft are unable to detect ion acceleration or heating. Using 2D PIC simulations and MMS magnetotail observations of a known Electron Diffusion Region (EDR) and several electron-only reconnection candidates, we develop the following observational criteria for electron-only reconnection in Earth's magnetotail: 1. B_L Reversal, 2. B_{tot} minimum, 3. sub-Alfvénic ion outflow, 4. super-Alfvénic electron outflow, 5. $< 10\%$ change in $T_{i,tot}$, 6. $> 10\%$ increase in $T_{e,tot}$, 7. positive peak in $J \cdot E'$, 8. deviation of $v_{e,\perp}$ from $\frac{E \times B}{B^2}$, 9. meeting the electron tearing criterion, 10. meeting the flux transport velocity criterion, and 11. increase in agyrotropy correlated with an increase in $J \cdot E'$. We report 12 electron-only reconnection candidates in Earth's magnetotail. We utilize preliminary statistics of these candidate events to distinguish electron-only flux rope erosion from electron-only onset of reconnection, where during the onset of magnetotail reconnection, a ≈ 10 second transition phase occurs where only electrons are accelerated. We verify that some event candidates align better with a transition phase than alternative models such as turbulent secondary reconnection and flux rope erosion.

This dissertation confirms that the properties of plasma accelerated by magnetic reconnection are largely unaffected by magnetotail orientation. In addition, our current sheet database will enable future current sheet statistical studies. Establishing universal observational criteria for electron-only reconnection has allowed the community to report electron-only reconnection in new and unexpected places. Our electron-only reconnection candidate pool also provides the first opportunity to explore how electron-only reconnection changes

over time. Lastly, our preliminary electron-only statistics support the hypothesis that electron tearing is the primary driver of reconnection onset, and that electrons couple to the reconnecting fields before the ions.

The dissertation of Mark Alexander Hubbert is approved.

Marco C.M. Velli

Hao Cao

Raymond John Walker

Christopher T. Russell, Committee Chair

University of California, Los Angeles

2024

For my parents, friends, and cohort.

I would not be here without your unwavering support.

Table of Contents

List of Figures

ACKNOWLEDGMENTS

This dissertation is dedicated to my family, friends, committee, and advisor. Without their unyielding support, this would not have been possible. To Prof. Russell, thank you for your time and commitment to my research. Through thick and thin, you always had my back, and I appreciate it more than you know. To my committee, thank you for meeting with me well in advance of the defense and providing several rounds of edits and insightful research feedback. Without your help, the story of this thesis truly would not have been complete. Lastly, to my family and friends, you are the foundation on which this thesis was built. I will cherish your love forever.

I thank the MMS team for the development, cruise, orbit insertion, and operation of the MMS spacecraft. Credit to Springer Nature and Nature Communications for the use of Figure from Lu et al., 2020. All MMS data used in this work are available at the MMS Data Center (https://lasp.colorado.edu/mms/sdc/public/). This research was supported by the NASA Magnetospheric Multiscale Mission, in association with NASA contract NNG04EB99C. The work at UCLA was supported through subcontract 06-001 with the University of New Hampshire.

Thanks to Yi Qi, who collaborated with me to develop the flux transport velocity criterion and investigate the temporal properties of entangled flux ropes. Thanks to San Lu, who collaborated with me to develop the electron-only reconnection simulations found in the Appendices and throughout Chapters 3 and 4.

VITA

2014-2018 B.S. Physics, University of Maryland.
B.S., Astronomy University of Maryland.

2018-Present Ph.D. (Candidate) Geophysics & Space Physics, University of California, Los Angeles.

PUBLICATIONS

Hubbert, M., Russell, C. T., Lu, S., Burch, J. L., Giles, B. L., Moore, T. E. (2024). Distinguishing Electron-Only Onset of Reconnection from Electron-Only Reconnection and Ion Diffusion Regions in Earth's Magnetotail. (in prep)

Qi, Yi, Li, T. C., Russell, C. T., Ergun, R. E., Jia, Y.-D., **Hubbert, M.** (2022). Magnetic Flux Transport Identification of Active Reconnection: MMS Observations in Earth's Magnetosphere. The Astrophysical Journal Letters, 926(2), L34. doi: 10.3847/2041-8213/ac5181.

Lu, S., Lu, Q., Wang, R., Pritchett, P. L., **Hubbert, M.**, Qi, Y., et al. (2022). Electron-Only Reconnection as a Transition From Quiet Current Sheet to Standard Reconnection in Earth's Magnetotail: Particle-In-Cell Simulation and Application to MMS Data. Geophysical Research Letters, 49(11), e2022GL098547. doi: 10.1029/2022GL098547.

Hubbert, M., Russell, C. T., Qi, Y., Lu, S., Burch, J. L., Giles, B. L., Moore, T. E. (2022). Electron-Only Reconnection as a Transition Phase From Quiet Magnetotail Current Sheets

to Traditional Magnetotail Reconnection. Journal of Geophysical Research: Space Physics, 127(3), e2021JA029584. doi: 10.1029/2021JA029584.

Hubbert, M., Qi, Y., Russell, C. T., Burch, J. L., Giles, B. L., Moore, T. E. (2021). Electron-Only Tail Current Sheets and Their Temporal Evolution. Geophysical Research Letters, 48(5), e2020GL091364. doi: 10.1029/2020GL091364.

Qi, Y., Russell, C. T., Jia, Y.-D., **Hubbert, M.** (2020). Temporal Evolution of Flux Tube Entanglement at the Magnetopause as Observed by the MMS Satellites. Geophysical Research Letters, 47(23), e2020GL090314. doi: 10.1029/2020GL090314.

CHAPTER 1

Introduction

1.1 Scientific Background

1.1.1 Solar Wind & Interplanetary Magnetic Field

The Sun's magnetic field and energy generation dictate much of the physics of the Solar System. Outside the solar corona, supersonic solar wind extends to distances well beyond the known planets. Embedded in this solar wind is a magnetic field called the Interplanetary Magnetic Field (IMF). The magnetic field displays a spiral geometry because the Sun rotates as it expels a primarily radial wind. This effect is illustrated in Figure 1.1.

At a distance of 1 Astronomical Unit (AU), the IMF is primarily comprised of comparable radial and transverse components. However, the IMF can also be significant in the normal direction (with respect to the ecliptic plane). Satellite data at 1 AU has shown that the IMF displays comparable amounts of northward and southward components, and is capable of sustaining values above 10 nT (*Liu et al.*, 2014). This variance in the Z component of the IMF can lead to significant interactions with both magnetized and unmagnetized bodies in the Solar System.

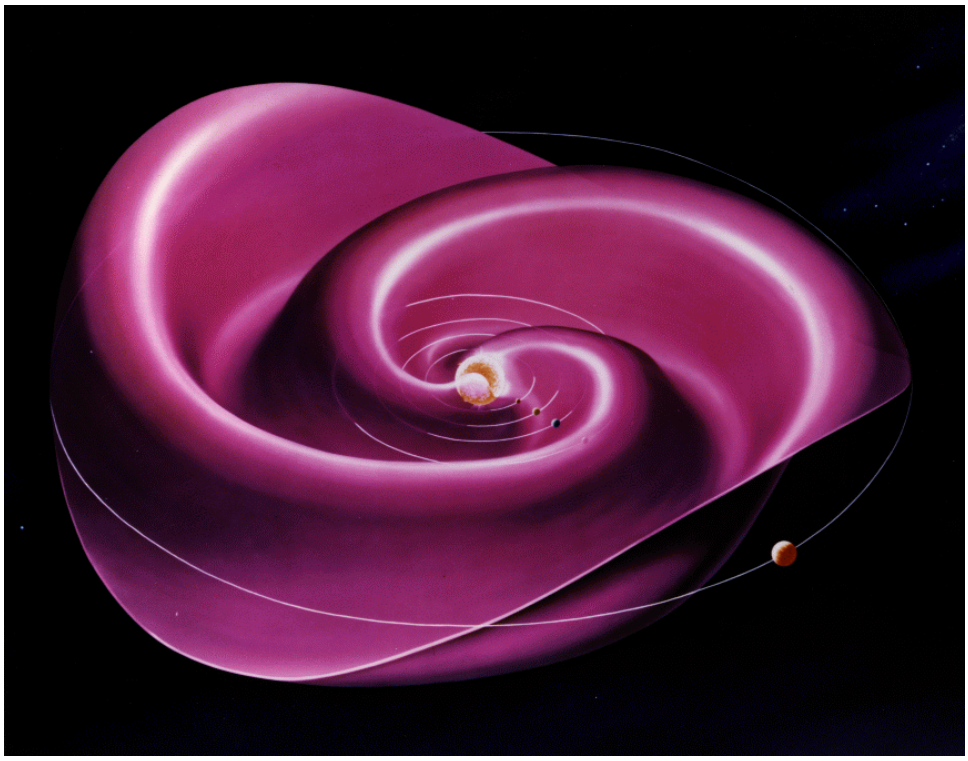

Figure 1.1: Cartoon of the Heliospheric Current Sheet overlaid on the rest of the Solar System. Image from *NOAA*, 2023.

1.1.2 Dungey Cycle & Solar Wind-Magnetosphere Coupling

In 1961, many in the space physics community felt that Earth's magnetosphere was a closed system that rarely accepted energy and particles from the outside solar wind (*Johnson*, 1960). Earth's magnetic field was thought to be a relatively closed, dipole field, guarding Earth from powerful solar wind particles and energy. However, in 1961, Dungey proposed a picture of Earth's magnetosphere that was much more accepting of solar wind energy (*Dungey*, 1961).

Dungey's model of Earth's magnetosphere relies on the presence of Southward IMF BZ for significant time intervals. Dungey proposed that Earth's northward IMF BZ, when in contact with the solar wind's Southward IMF BZ, would break and reconnect with solar wind

field lines. These reconnected fields would have one end connected to Earth and one end connected to the solar wind, making them appear to be "open" field lines. Once reconnected, the persistent solar wind would convect the open field lines over Earth's poles and towards Earth's magnetotail. This convection would continue as oppositely pointed field lines would stretch over the north and south poles. Once in the tail region, these oppositely directed open field lines would get pushed towards the magnetotail equator and undergo a similar type of reconnection that occurred on the dayside. This reconnection would create two new field lines: one closed magnetic field loop with both ends rooted at Earth, and one open field line with both ends rooted in the solar wind.

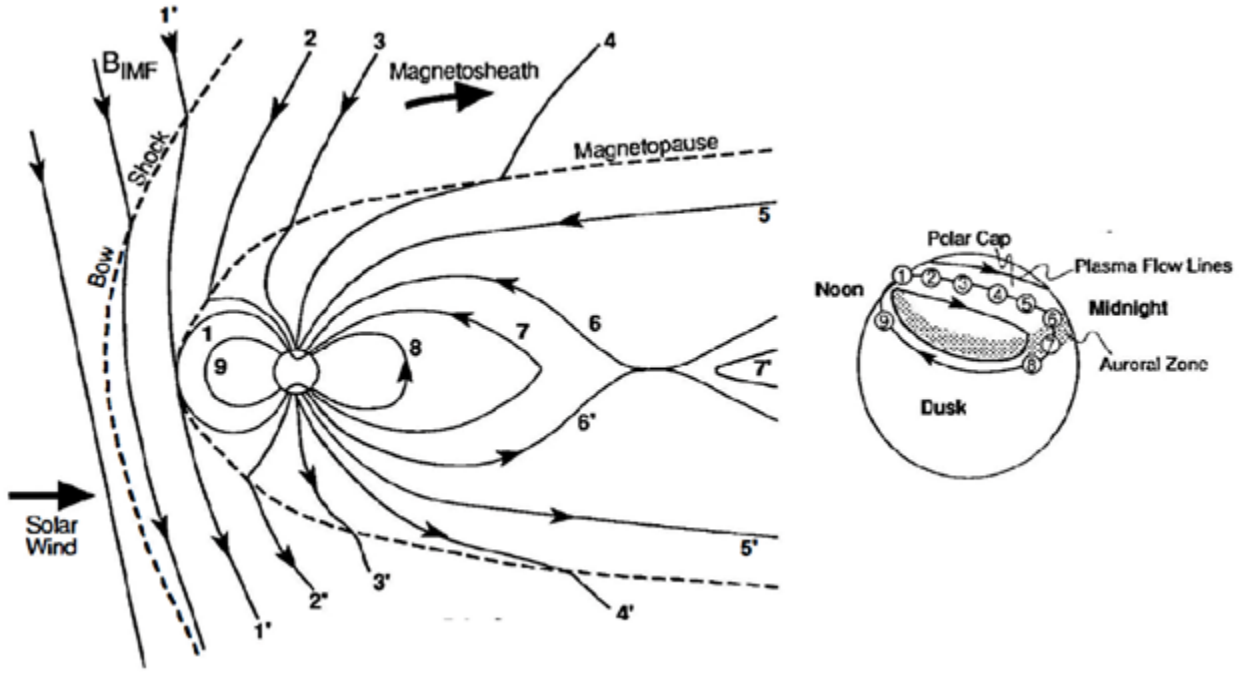

Figure 1.2: Figure adapted from *Dungey*, 1961. Diagram showing the full convection loop of Earth's magnetic field lines as a result of magnetic reconnection.

1.1.3 Earth's Magnetotail

During dayside magnetic reconnection, open magnetic field lines and magnetic flux are carried from the dayside over the magnetic poles to the magnetotail. This creates two "lobe"

regions where magnetic field lines are still open, but have a stronger field strength than the open space plasma environment (*Huang et al.*, 1987). In the southern lobe, the magnetic field is primarily directed in the tailward direction, and in the northern lobe, the magnetic field is primarily directed in the earthward direction. These two lobe regions come together in an interaction region called the plasma sheet. There, the oppositely directed fields cause gyrating particles to change their orbits to meandering orbits in the current sheet. This creates a current in the GSM Y direction called the "cross-tail current" (*Lui*, 1984). This current sheet is present at all times in the plasma sheet.

When discussing the plasma sheet, we utilize a specific coordinate system to consistently describe the physics that occurs within. This is called LMN coordinates, and is calculated using Minimum Variance Analysis (*Sonnerup and Scheible*, 1998). The L component of a current sheet is the component parallel to the antiparallel magnetic field lines creating the current sheet. The N component of a current sheet is the direction where plasma inflows into the reconnection region, and is perpendicular to the L direction in the 2D reconnection plane. Lastly, the M component is directed in the NxL direction. This is the direction in which the cross-tail current flows (*Lui*, 1984).

Within the plasma sheet, there is a smaller region called the neutral sheet (*Russell and McPherron*, 1973). There, the earthward/tailward component of the magnetic field is exactly zero. This environment is ripe for small, electron-scale interactions that produce magnetic reconnection. There, magnetic tension force due to newly closed magnetic field lines drives a straightening of field lines leading to a newly dipolarized field. The newly dipolarized field is slowly transferred back to the dayside, where it eventually becomes the new interaction region between solar wind magnetic field and Earth's dipole field. Reconnection in Earth's magnetotail can trigger processes called substorms (*Newell and Liou*, 2011). During a substorm, field that was reconnected Earthward of the X line creates bursty bulk flows and Earthward moving dipolarization fronts (*Angelopoulos et al.*, 1992; *Zhou et al.*, 2010). These bursty bulk flows and dipolarization fronts send plasma towards Earth that eventually

propagates down to the ionosphere and excites the aurora borealis/australis.

1.1.4 Magnetic Reconnection in Earth's Magnetotail

Before we discuss magnetic reconnection, we outline several fundamental concepts.

First, when charged particles move in an environment with a strong, low-curvature magnetic field, their trajectories follow a helical/gyrating path. One can calculate the frequency at which a gyrating particle completes a full gyration. This value is called the gyrofrequency (ω_c):

$$\omega_c = |q|B/m_p \tag{1.1}$$

where m_p is the mass of the particle, q is the charge of the particle, and B is the strength of the magnetic field. Thus, stronger magnetic fields and less massive particles yield higher gyrofrequencies. Interestingly, a particle's velocity has no influence on its gyrofrequency. The equation dictating the radius of curvature (ρ) of helical path, also called the gyroradius, is as follows:

$$\rho \;=\; \frac{m_p v_\perp \gamma}{|q|B} \;=\; v_\perp \gamma/\omega_c \tag{1.2}$$

where v_{perp} is the field-perpendicular component of the particle's velocity and γ is the Lorentz factor. Particles that are faster or more massive (eg. protons) have larger gyroradii and particles that are slower or less massive (eg. electrons) have smaller gyroradii. In stronger (weaker) magnetic fields, the gyroradius is reduced (increased). Outside of the high-curvature reconnection region, single plasma particles primarily undergo gyrating orbits in the near-Earth magnetotail.

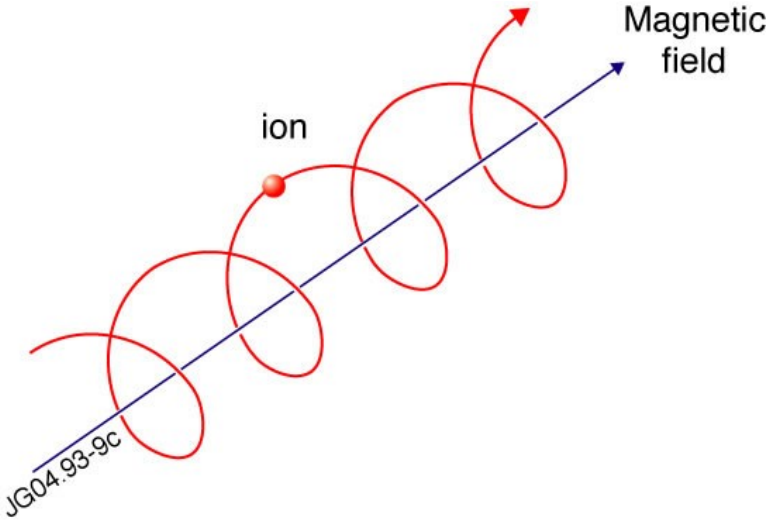

Figure 1.3: Diagram displaying an ion gyrating around a straight magnetic field line. (NOAA)

Also, we need to define the terms "frozen in" and "demagnetize". To do this, we perform a quick derivation. Faraday's Law, Ampere's Law, and Ohm's Law read:

$$\frac{\partial \boldsymbol{B}}{\partial t} = -\nabla \times \boldsymbol{E} \ , \ \nabla \times \boldsymbol{B} = \mu_0(\boldsymbol{J} + \epsilon_0 \frac{\partial \boldsymbol{E}}{\partial t}) \ , \ \boldsymbol{J} = \sigma_0(\boldsymbol{E} + \boldsymbol{U} \times \boldsymbol{B}) \tag{1.3}$$

where σ_0 is the conductivity caused by coulomb collisions, μ_0 is the vacuum permeability, and ϵ_0 is the vacuum permittivity. If we solve Ohm's Law for E and substitute into Faraday's Law, we get:

$$\frac{\partial \boldsymbol{B}}{\partial t} = -\nabla \times (\boldsymbol{U} \times \boldsymbol{B} - \frac{\boldsymbol{J}}{\sigma_0}). \tag{1.4}$$

If we take the curl of Ampere's Law, and neglect $\partial E/\partial t$ because we are not in a relativistic system, we get:

$$-\nabla^2 \boldsymbol{B} = \mu_0(\nabla \times \boldsymbol{J}). \tag{1.5}$$

Substituting this into Equation 1.4, we get:

$$\frac{\partial \boldsymbol{B}}{\partial t} = \nabla \times (\boldsymbol{U} \times \boldsymbol{B}) + \frac{\nabla^2 \boldsymbol{B}}{\sigma_0 \mu_0} \tag{1.6}$$

which is also called the induction equation. $\nabla \times (\boldsymbol{U} \times \boldsymbol{B})$ is often called the convection term, while $\frac{\nabla^2 \boldsymbol{B}}{\sigma_0 \mu_0}$ is often called the diffusion term. In space plasmas, when field lines have low curvature, the diffusion term is negligible. If we apply this to Equation 1.6 and use Faraday's Law to substitute $\partial \boldsymbol{B}/\partial t$ with -$\nabla \times \boldsymbol{E}$, we yield:

$$-\nabla \times \boldsymbol{E} = \nabla \times (\boldsymbol{U} \times \boldsymbol{B}), \tag{1.7}$$

which simplifies to $-\boldsymbol{E} = \boldsymbol{U} \times \boldsymbol{B}$, which is called the "frozen-in" condition. When we call a plasma frozen in, or magnetized, we are saying that it meets this condition. Frozen-in plasma moves at the drift velocity $\boldsymbol{E} \times \boldsymbol{B}/B^2$. Conversely, when a plasma is not frozen-in or demagnetized, that means that -$\boldsymbol{E} \neq \boldsymbol{U} \times \boldsymbol{B}$.

In the previous paragraph, I described the primary method by which charged particles interact with low curvature fields in a space-plasma environment. However, in the small reconnection region, this picture is distorted because the magnetic field is highly curved. A diagram displaying the anatomy of a symmetric reconnection region is shown in Figure 1.4. Inside the ion diffusion region (IDR), the curvature of the magnetic field approaches the gyroradius of ions, causing ion trajectories to deviate from simple gyromotion. Closer to the central reconnection point, in the electron diffusion region (EDR), electrons in tighter gyro-orbits transition to more chaotic orbits (*Fu et al.*, 2006). These two regions allow ions and electrons to be demagnetized, energized, and ejected in jets directed outward in the +/-X direction (*Pritchett*, 2001; *Oka et al.*, 2016).

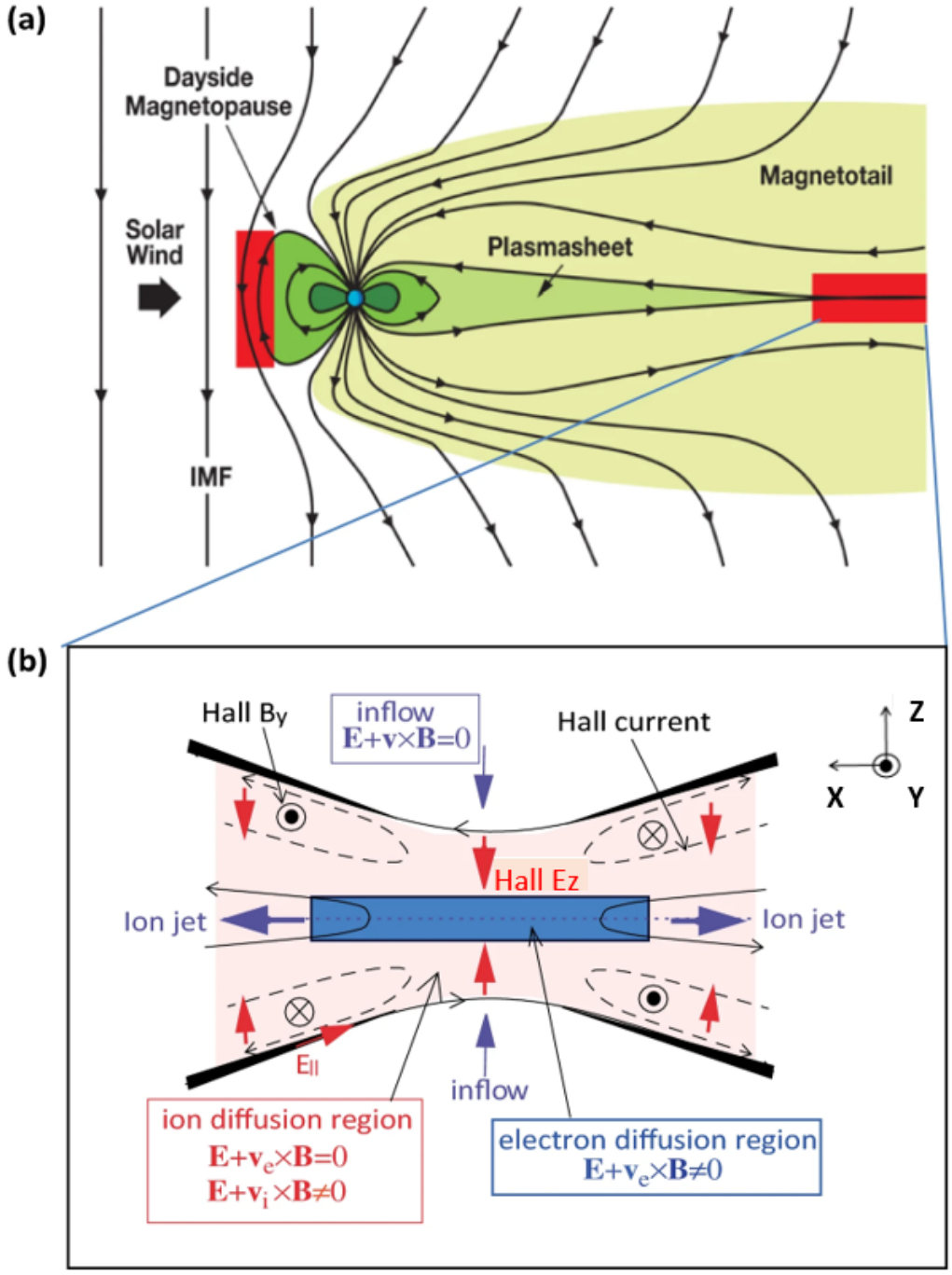

Figure 1.4: Diagram showing the approximate location of magnetotail reconnection and labelling the different sub-regions and plasma and field properties of the reconnection region (*Dai and Wang*, 2022)

.

These two regions may sound similar, but their scale sizes differ significantly. To more precisely define their scale sizes, we first define two parameters: a particle's plasma frequency (ω_p) and inertial length (d_p).

$$\omega_p = \sqrt{q^2 n_0 / \varepsilon_0 m_p} \quad , \quad d_p = c/\omega_p \tag{1.8}$$

where q is the charge of the particle, n_0 is the plasma number density, ε_0 is the permittivity of free space, m_p is the mass of the particle, and c is the speed of light. The plasma frequency is the frequency at which a charge displacement would naturally oscillate an ideal plasma, and a particle's inertial length is the length scale below which the kinetics of that particle become important (*Tóth et al.*, 2017). In this dissertation, something is referred to as sub-ion (electron) scale that indicates a length scale of less than $1d_i(d_e)$. The Hall effect and electron gradient pressure become important on scales approximately less than or equal to the ion inertial length (d_i). These necessary parameters allow us to more easily compare structures in plasmas that have wildly different properties.

Because ions are much more massive than electrons, the IDR ($\approx$ 5-10d_i) is a much larger region than the EDR ($\approx$ 5-10d_e) (*Sonnerup*, 1979; *Yamada et al.*, 2010). This difference is approximately a factor of $\sqrt{m_i/m_e}$, meaning the highlighted regions shown in Figure 1.4 are not to scale.

We define the Ion Diffusion Region (IDR) as the region where ions have demagnetized from the reconnecting fields, but electrons remain frozen-in to the fields. The difference in physics affecting ions and electrons results in phenomena specific to this region. Magnetized electrons continue to move towards the reconnection center until they reach the Electron Diffusion Region and are accelerated away by the reconnection electric field. This creates a looped current structure called the Hall currents, shown in the black dashed lines in Figure 1.4. In the inflow region, currents flow away from the reconnection center, antiparallel to the inward trajectory of the electrons. In the outflow region, currents flow towards from the

reconnection center, antiparallel to the outward trajectory of the electrons. These effective current loops generate quadrupolar magnetic fields in the +/- Y direction and electric fields in the +/- Z direction. Note in Figure 1.4 that the magnetic field in the upper left and lower right quadrants is directed in the +Y direction, whereas the magnetic field in the upper right and lower left quadrants is directed in the -Y direction. Because electrons remain frozen in in the Ion Diffusion Region, the direction of the Hall electric field can be approximated with $-v_{e,out} \times B_{Hall}$ (See Equation 1.7). Thus, the Hall electric field is primarily oriented in the +/-Z direction, towards the current sheet center.

We define the Electron Diffusion Region (EDR) as the region embedded within the Ion Diffusion Region where electrons have demagnetized from the reconnecting fields. This region features a non-gyrotropic electron distribution and electric field supported primarily by the off-diagonal pressure term in generalized Ohm's law. Electrons are accelerated out of the EDR by this electric field, and when they reach the IDR, are directed along the magnetic field away from the reconnection center. A prominent feature of the EDR is an electron jet directed in the -Y direction (*Zhou et al.*, 2019), which manifests as a current in the +Y direction. In addition, we note that electron crescents occur in other current sheet structures in Earth's magnetotail, and thus should not be used alone as a distinguishing indicator of an EDR (*Egedal et al.*, 2012).

The magnetic field lines in the inflow region are not connected to the magnetic fields in the outflow region. As a result, two magnetic separatrices cross through the reconnection region and intersect at the reconnection center, as shown by the green dashed lines in Figure 1.5. These boundaries separate inflow plasma from plasma that has already been accelerated by reconnection (*Jiang et al.*, 2022). The region between the separatrix and the reconnection jet is typically dubbed the separatrix region (SR) (*Retinò et al.*, 2007). The SR is a few d_i wide (perpendicular to the boundary) and spans from the IDR to well into the outflow region. Adjacent to the separatrix, it contains the Hall currents and displays a density cavity, strong Hall electric field, and significant wave turbulence around ω_{pe}.

Observational criteria for identifying IDRs, EDRs, and separatrix flows are laid out in Chapter 2.

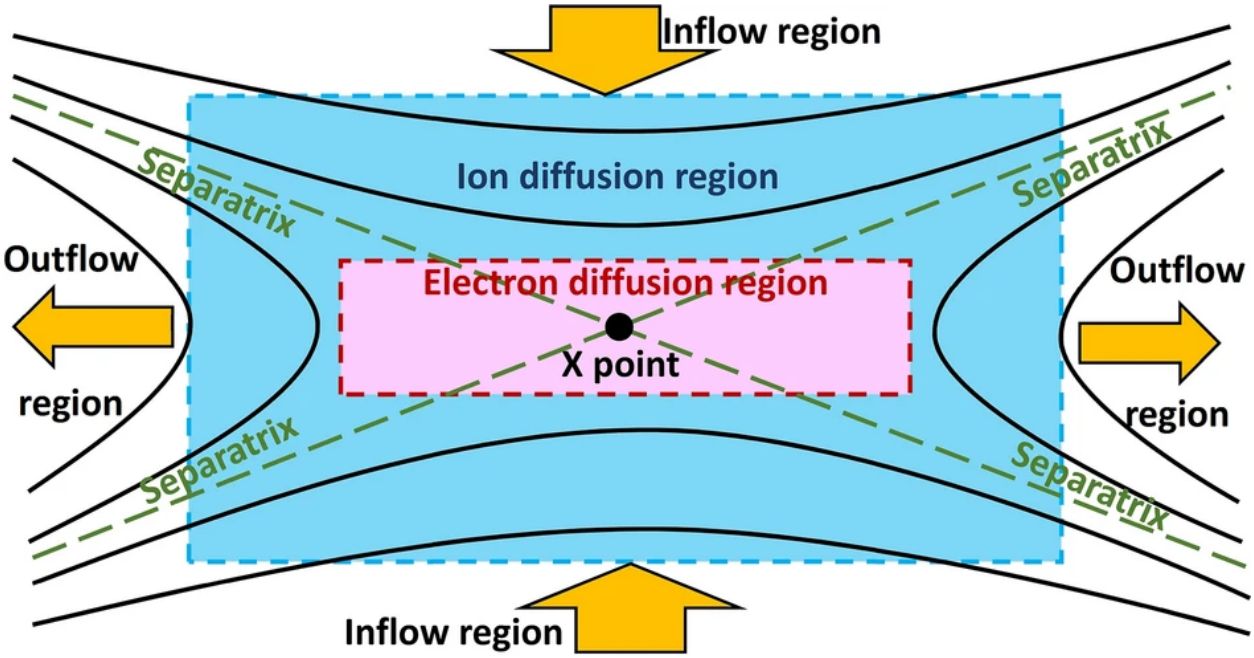

Figure 1.5: Diagram of Separatrices in the context of the Electron Diffusion Region and Ion Diffusion region (*Lee and Lee*, 2020).

1.1.5 Reconnection Onset

In Earth's magnetotail, magnetic reconnection occurs abundantly. A current sheet can only reconnect if it is unstable to a plasma mode that can ultimately generate magnetic dipolarization and changes in the global configuration of Earth's magnetotail. The most plausible mode for this purpose is the tearing mode, which can occur due to a collisionless pinch of oppositely directed lobe fields near the equator. Tearing mode instability relies on a very small normal component of the magnetic field (See Equation 1.9), because a significant normal magnetic field component would magnetize electrons and suppress the Landau damping required to energize the plasma population. (*Coppi et al.*, 1966) in 1966 was the first to apply the tearing instability to the collisionless environment of Earth's magnetotail,

concluding that current filamentation along the tail could break field lines and accelerate the surrounding plasma. However, many pushed (and still push) back against Coppi's interpretation, arguing that the initial current sheet conditions required to achieve tearing instability are nearly impossible to achieve in Earth's magnetotail environment. Specifically, in Earth's magnetotail, the dipolar connection of lobe field lines would inherently contain a large enough normal magnetic field to meet the stabilization condition in Equation 1.9 ((*Lembège and Pellat*, 1982)):

$$\pi \frac{B_z}{B_0} C_d^2 < kL_z < (B_z/B_0)(L_z/\rho_{0e}) \tag{1.9}$$

where k is mode wave number, L_z is the current sheet half-thickness, ρ_{0e} is the thermal electron gyroradius in ambient B_0 field, and $C_d = VB_z/(\pi L_z)$ where $V = \int dl/B$ is the flux tube volume. At electron-scales, B_z can become so small that the right-most side of Equation 1.9 is broken and Landau damping is possible. Later observations have since shown that thin, electron-scale current sheets in Earth's magnetotail are unstable to the tearing mode (*Sitnov et al.*, 2019). This is due to a larger than expected longitudinal gradient of normal magnetic field (*Zelenyi and Artemyev*, 2013). A variant of Equation 1.9 was developed in 2019 by (*Liu et al.*, 2019) which described the onset conditions for electron tearing instability when the normal magnetic field is suppressed by a strong external driver:

$$\frac{B_N}{B_0}\frac{\delta}{d_i} < \frac{f}{2}\sqrt{\frac{m_e T_e}{m_i T_i}} \tag{1.10}$$

where $f = k_L\delta$, k_L is the wave number in L, δ is the current sheet half width, T_e and T_i are electron and ion temperature, respectively, and B_N and B_0 are the normal field and field strength, respectively. This criterion is novel in that each variable can be measured directly by satellite instruments in Earth's magnetotail. As such, Equation 1.10 has been used to determine if magnetotail current sheet observations are electron tearing unstable. We note that this criterion does not argue whether or not reconnection is occurring - only if

the current sheet is electron tearing unstable.

1.1.6 Electron-Only Reconnection

As discussed in Section 1.1.4, the reconnection region in its most common form is understood to be comprised of an electron-scale EDR embedded in an ion-scale IDR. However, reconnection is also suggested to help dissipate energy at kinetic scales in turbulent regions such as Earth's magnetosheath (*Matthaeus and Lamkin*, 1986; *Servidio et al.*, 2009). This turbulent region produces current sheets that are electron-scales in thickness (N) and length (L), which has been shown in simulation work to significantly change the fundamental properties of the reconnection region (*Sharma Pyakurel et al.*, 2019). Before the launch of the MMS mission, while magnetic reconnection had been observed in this turbulent region, the resolution of previous plasma instruments had not been high enough to resolve the plasma response in the reconnection region (*Retinò et al.*, 2007). As a result, direct in-situ observation of plasma jetting had not previously been reported.

Recently, using the high time and spatial resolution of the Magnetosphere Multiscale (MMS) Mission, *Phan et al.*, 2018 reported a fortuitous reconnecting current sheet in Earth's turbulent magnetosheath. Time series data for MMS1 and 3 are shown in Figure 1.6. This figure displays the time series data in minimum variance LMN coordinates, where L is the antiparallel magnetic field direction for MMS3, N is the current sheet normal calculated with four spacecraft timing (see Appendix 1.3), and $M = N \times L$. Also, in Panels A and K, B_M has been shifted by 30 nT for aesthetic purposes. Both spacecraft observed a reversal in B_L (panels a,k), indicating that they crossed a current sheet. They also observed significant electron outflows in the L direction (panels c,m), intense current in the M direction (panels d,n), and positive $j \cdot E'$ (j,t) dominated by $J_{||}E_{||}$ (not shown). This indicates that the two spacecraft observed a reconnecting current sheet in Earth's turbulent magnetosheath.

For more information regarding why the features above were used to identify this event as magnetic reconnection, refer to Chapter 2.

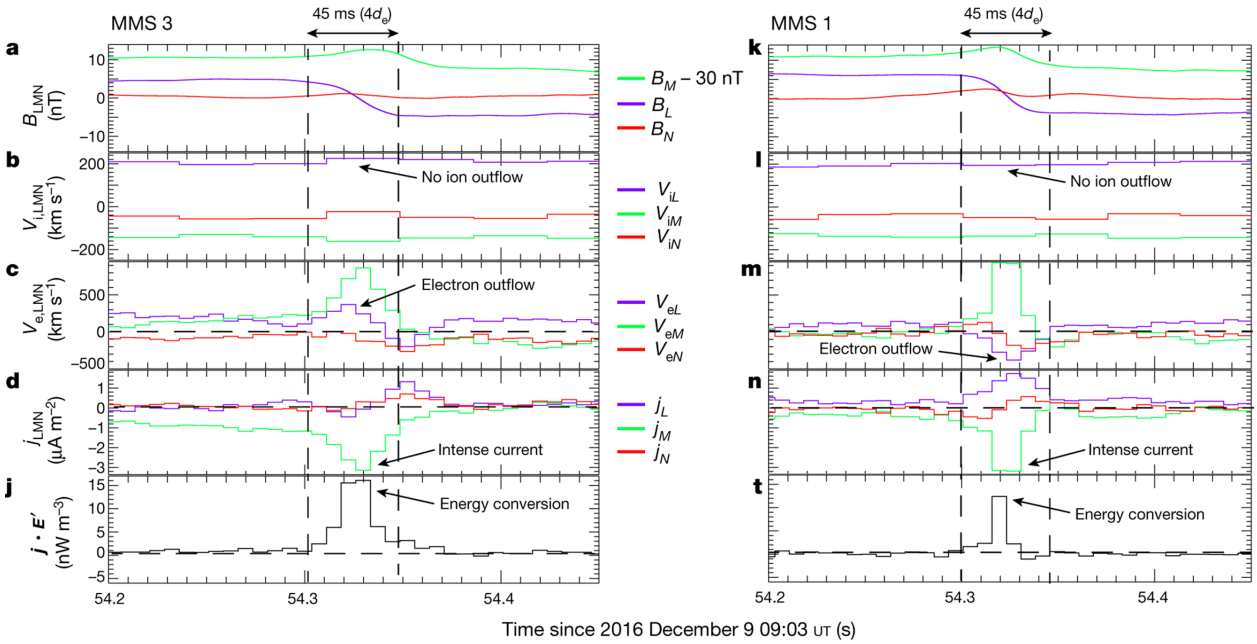

Figure 1.6: MMS time series data of *Phan et al.*, 2018's electron-only reconnection observation. Left column is MMS3 observation, right column is MMS1 observation. L = (-0.09, 0.87, 0.49), M = (-0.25,-0.49, 0.83), and N = (0.96,-0.05, 0.27) in GSE. Note that B_M is shifted by 30 nT for aesthetic purposes. (a,k) Magnetic field (B_L: Purple, B_M: Green, B_N: Red), (b,l) Ion bulk flow velocity, (c,m) Electron bulk flow velocity, (d,n) Current density calculated from plasma measurements (See Appendix 5.2), (j,t) Energy conversion ($j \cdot E' = j \cdot (E + v_e \times B)$)

However, this observation was fortuitous for multiple reasons. First, MMS3 observed electron outflows in the +L direction, while MMS1 observed electron outflows in the -L direction. This means that the two spacecraft straddled the reconnection region (shown in Panel B of Figure 1.7). This is the first reported MMS observation of magnetic reconnection that straddled the reconnection region. Second, neither spacecraft observed the ion outflows expected in a traditional ion-coupled reconnection observation (panels b,l). This was the first reported observation of magnetic reconnection that was missing ion outflows. The lack of ion outflows was especially surprising because ion outflows from magnetic reconnection

span a larger scale and typically extend well past the reconnection region, which should make them easier to observe than electron outflows from reconnection. Due to the apparent lack of ion outflow jets embedded in the reconnecting current sheet, *Phan et al.*, 2018 dubbed the event "electron-only" reconnection.

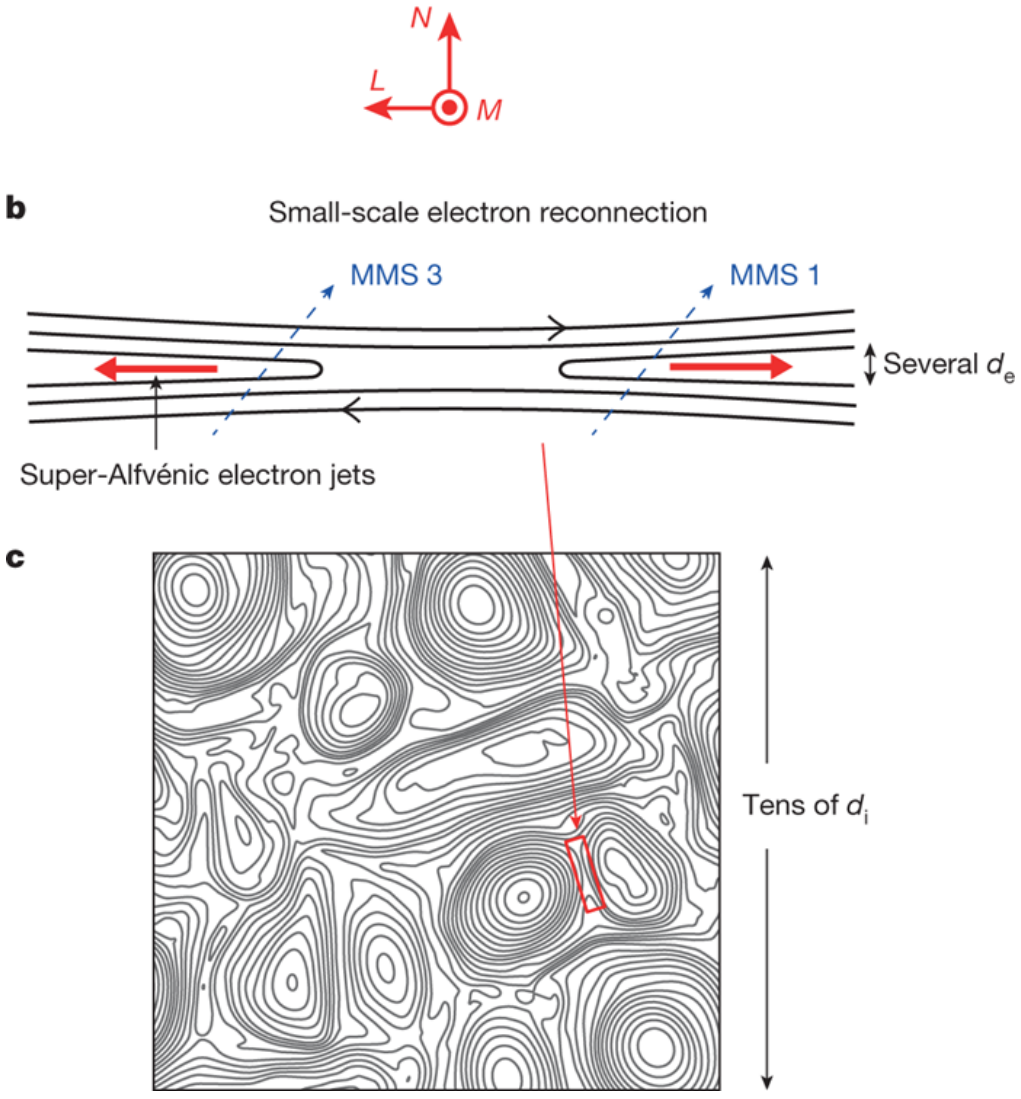

Figure 1.7: Electron-only Reconnection candidate in turbulent magnetosheath (*Phan et al.*, 2018). Diagram displaying MMS's projected orbit through the reconnection region of electron-only reconnection in Earth's turbulent magnetosheath and a sample turbulent environment that could generate such a reconnection region.

Phan et al., 2018 suggested that the lack of ion outflows was due to the current sheet being electron-scale thickness ($\approx 4d_e$) and having a small length (L) to width (N) ratio. This is shown in panel C of Figure 1.7. More specifically, they posed that a reconnecting current sheet in a large guide field would require a minimum length of $10d_i$ in the L direction for ions to couple to the reconnection (*Mandt et al.*, 1994; *Meyer*, 2015). This hypothesis was investigated further with 2.5D PIC simulation work (*Sharma Pyakurel et al.*, 2019; *Zeiler et al.*, 2002). They chose six current sheets with lengths ranging from $2.5d_i$ to $80d_i$ but identical aspect ratios ($Y/X \approx 5$), and initialized reconnection with a small magnetic perturbation. Once the reconnection rate reached steady state, they identified whether or not ions were coupled to the reconnecting current sheet. Results from the smallest scale run ($2.5d_i$, left column) and second-largest scale run ($40d_i$, right column) are shown in Figure 1.8. Panels C and D, featuring v_{ix}, show ions being accelerated by a $40d_i$ current sheet, but not a $2.5d_i$ current sheet. Meanwhile, panels E and F, featuring v_{ex}, show electrons being accelerated by both current sheets. Using the six simulation runs, they found negligible ion outflows due to reconnection for current sheet thicknesses less than $5d_i$, and that ion response gradually increased until the current sheet thickness reached $\approx 40d_i$, where the reconnection rate reached a rate comparable to previous work (*Shay et al.*, 1999).

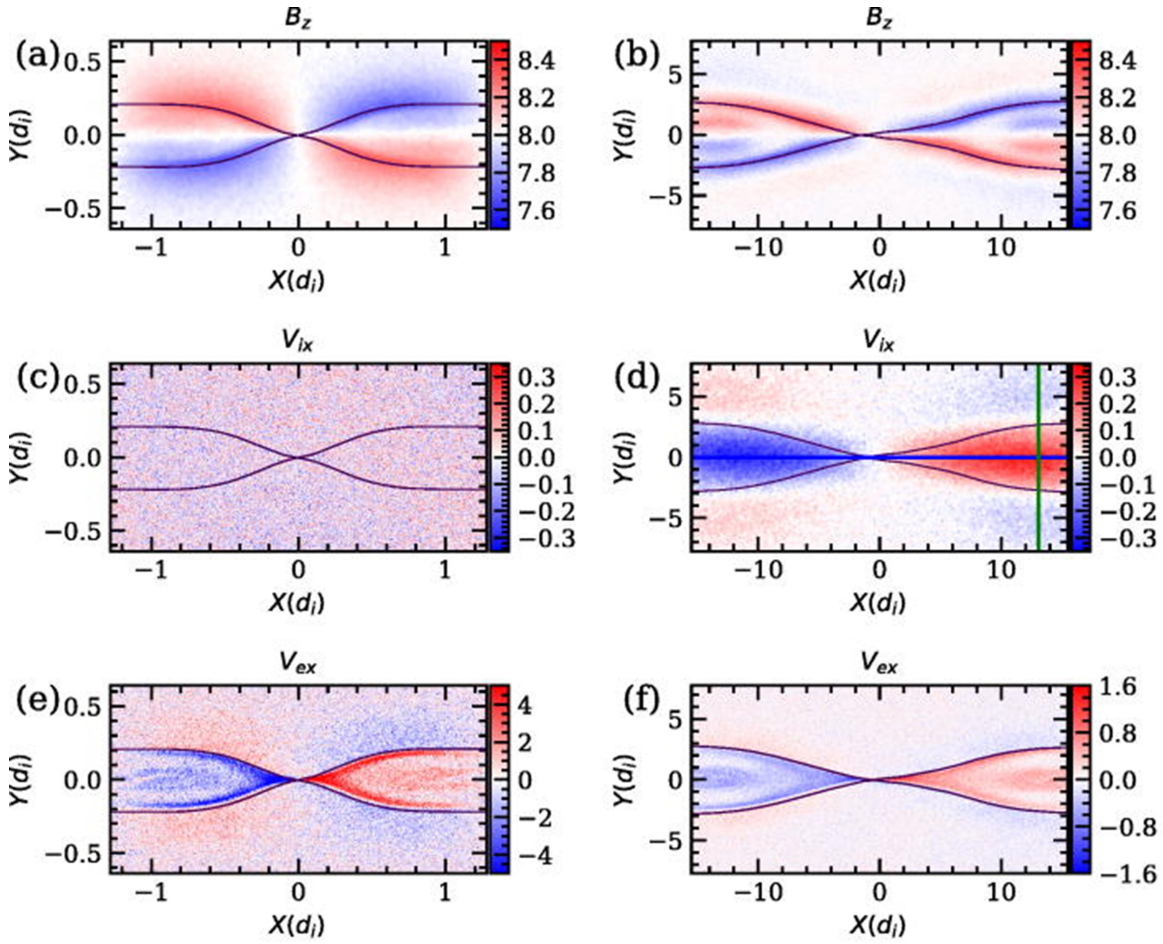

Figure 1.8: Time slices of 2.5D PIC simulations of magnetic reconnection in current sheets of two different lengths (aspect ratio ≈ 5): $2.5d_i$ (left) and $40d_i$ (right) (*Sharma Pyakurel et al.*, 2019). (a,b) B_z out of plane quadrupolar magnetic field, (c,d) v_{ix}, (e,f) $v_{e,x}$

This simulation work along with additional observational and theoretical studies have solidified the hypothesis that reducing the thickness of a current to $> 1d_i$ and the length of a current sheet to below 10 d_i will result in a reconnecting current sheet where the electrons are heated and accelerated, but ions are not. (*Stawarz et al.*, 2019; *Vega et al.*, 2020; *Mallet*, 2020).

Recently, several studies have reported current sheets in other regions of space that display the same features as electron-only reconnection, but are not generated by restricting

the length and width of the current sheet (*Wang et al.*, 2018; *Huang et al.*, 2021; *Man et al.*, 2020a). However, due to few observations and the lack of supporting simulation work, a consensus on their origin or nature has not yet been established.

1.2 Relevant Space Missions and Datasets

1.2.1 Magnetosphere Multiscale Mission

The Magnetospheric Multiscale Mission (MMS) was launched in 2015. It is made up of four, small, identical spacecraft oriented in a tetrahedron. This tetrahedron is unique because the separation is at electron scales. Previous missions like Cluster have similar orientations, but are separated by several R_E. This severely limits the scale size of structures one is able to see. In magnetic reconnection, the electron diffusion region is expected to span $\approx$ 10 km, which is much less than any spacecraft separation from previous missions. MMS aims to maintain a tetrahedron at the separation with which one can resolve the fine electron-scale structures of the electron diffusion region. Separation of the four MMS spacecraft ranges from as few as 10 km to as much as 25 km. MMS is located at a low inclination, allowing them to consistently observe magnetopause reconnection and the magnetotail plasma sheet and neutral sheet.

Each of the four spacecraft carries a suite of instruments. The four MMS spacecraft carry fluxgate magnetometers, search coil magnetometers, triaxial electric field double probes and an electron drift measurement. For plasma measurement, there is a fast plasma investigation (FPI), a hot particle composition analyzer (HPCA), and two energetic particle measurements, i.e. energetic ion spectrometer (EIS) and fly eye energetical particle spectrometer (FEEPS) (*Burch et al.*, 2016a). Measurements from these instruments are used to great effect in this thesis.

The scientific scope of MMS consists of several Orbit Phases. During Phase 1, MMS's

apogee was $\approx 15R_E$. During Phase 2, MMS's apogee was increased to $\approx 25R_E$, where it has remained ever since. Within each phase, MMS undergoes a dayside (subphase A), cusp, and nightside (subphase B) phase. This means that MMS is located in the near-Earth magnetotail during Phase #B. From 2017-2019 (Phase 2B/3B/4B), MMS's apogee was slightly elevated to reflect the slight inclination of the magnetotail neutral sheet. We expect that this allows MMS to consistently observe the magnetotail plasma sheet and neutral sheet. However, from 2020-2022 (Phase 5B/6B/7B), MMS's orbit slowly precessed to lower GSM Z values, well below the expected equatorial plane. This is shown with snapshots in Figure 1.9. As a result, we expect to observe fewer current sheet crossings per tail season after 2020 than before 2020.

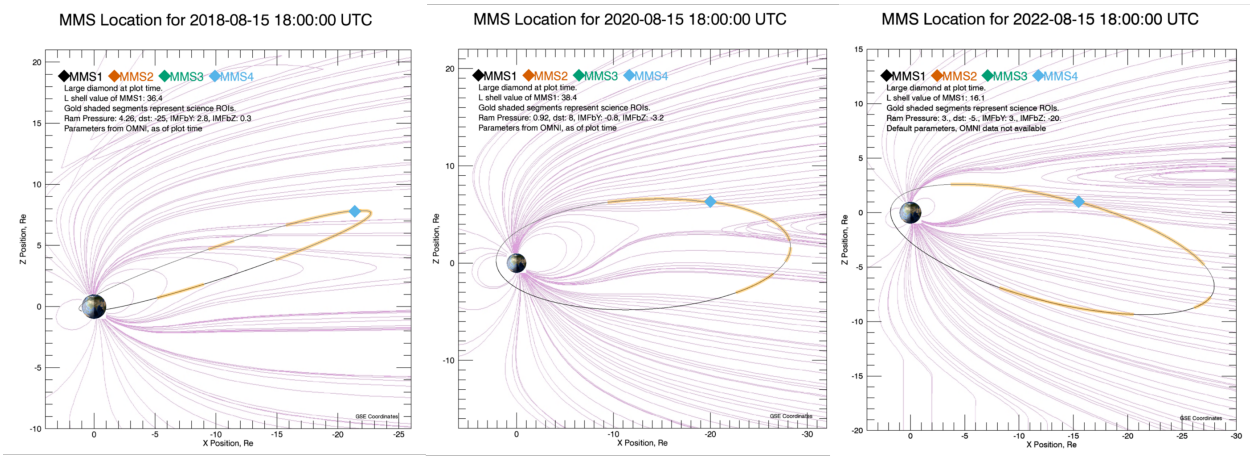

Figure 1.9: 2D XZ GSE projections of the MMS orbit including August 15 for three tail seasons: 2018 (left), 2020 (middle), and 2022 (right). Purple lines indicate the Tsyganenko modelled location of the equatorial magnetotail current sheet. (*Tsyganenko*, 1995)

The magnetic measurements are made with two fluxgate sensors and a search coil on each of the four spacecraft, which enable the usage of the "curlometer" technique. The two fluxgates have different designs and different heritage (*Russell et al.*, 2016). These have been intercalibrated and calibrated against the Earth's field. An electron gun (Electron Drift Instrument, EDI) obtains an independent estimate of the magnetic field that helps

maintain absolute accuracy of the zero levels. The absolute accuracy of the measurements is currently 0.1 nT or better. The relative offset in magnetometer measurements between different spacecraft is also about 0.1 nT. The original data rate for the magnetometer is 128 Hz, but due to the limited bandwidth of the spacecraft download telemetry, it is typically down-sampled before being transmitted down to Earth. The low temporal resolution data is called survey (srvy) mode data and runs at 16 Hz inside Regions of Interest (ROI) and 8 Hz outside of ROI. For the time intervals of special interest, full 128 Hz burst (brst) resolution data are downloaded. The interval of burst mode is selected by a procedure called scientist in the loop (SITL).

The Fast plasma investigation (FPI) onboard MMS spacecraft is capable of measuring the plasma moments and 3-D plasma distribution with an unprecedent temporal resolution (*Pollock et al.*, 2016). In order to achieve this, there are four dual ion spectrometers (DIS) and four dual electron spectrometers (DES) deployed on each of the four MMS spacecraft. Each DIS or DES has two electrostatic analyzers and covers 90 azimuthal degree viewing angle so that the FPI does not depend on the spacecraft rotation to complete one all-sky scan. This configuration of spectrometers enables a data rate of 150 ms per sample for ions and 30 ms for electrons. However, due to telemetry bandwidth limitation, this high temporal resolution can only be downloaded from the spacecraft when the data are in burst mode. In other normal operation periods within ROI, FPI data are only available at 4.5s data rate.

1.2.2 Wind Mission

The WIND satellite was launched on November 1, 1994. From 1994 to 2004, Wind orbited Earth and spent a considerable amount of time in Earth's magnetotail. Starting in 2004, Wind's orbit was expanded and translated to Earth's L1 Lagrange point.

WIND contains several instruments. Starting from 1994, there are 3-second magnetic-field data (*Lepping et al.*, 1995) and (on average) 99-sec plasma data (*Lin et al.*, 1995) available. In our study, we use WIND data from 2017 and 2018.

1.2.3 Auroral Electrojet Index

In June 1957, the World Data Center at Kyoto University in Japan began reporting Geomagnetic Auroral Electrojet data (*Masahito et al.*, 2017). The "Auroral Electrojet" indicates the currents that flow in the D and E regions of the auroral ionosphere. The strength of this current changes with latitude and is strongly influenced by external solar wind and magnetotail conditions. During magnetically quiet periods, the electrojet is confined to the auroral oval. However, during disturbed periods, the electrojet increases and expands in latitude. For example, during a substorm, when energetic plasma propagates down to the auroral ovals, the Region D and E currents increase in strength and generate a stable magnetic field at low altitudes. As a result, the Auroral Electrojet gives a strong indication of the deviation of the ionospheric magnetic field from ambient values in the auroral oval (*Davis and Sugiura*, 1966).

The AE Index is calculated using geomagnetic variations in the horizontal current from 12 ground magnetometers that report data from 61-70 degrees latitude. As a constellation, these stations provide a holistic picture of the auroral electrojet at any point on Earth (*Nakamura et al.*, 2002). However, each of the 12 magnetometers measures a different field value based on its location. To calculate AE, the 12 plots are first superposed as functions of Universal Time (UT). At any given time, the greatest (positive) superposed value is represented by the symbol AU, and the lowest (negative) value is represented by the symbol AL. In other words, AU describes the maximum strength of eastward electrojet currents, while AL describes the maximum strength of westward electrojet currents. The AE Index is calculated by taking the difference between AU and AL (AU-AL). AE is measured in nT and has an ambient value of $\approx$ 25 nT during quiet magnetic conditions. However, when the Auroral Electrojet value exceeds 100 nT, it is considered a small substorm. Larger substorms can display AE peaks of 500, 1000, and even 1500 nT.

The AE Index can help interpret perceived substorm activity found using in situ observa-

tion. For example, it can help determine whether or not magnetic reconnection measured by MMS is part of a substorm. We note that SUPERMAG indices also provide this information, but we do not use SUPERMAG in this dissertation.

1.2.4 OMNI Data Set

The Low Resolution OMNI (LRO) data set is primarily a 1963-to-present compilation of hourly-averaged, near-Earth solar wind magnetic field and plasma parameter data from several spacecraft in geocentric or L1 (Lagrange point) orbits (*King and Papitashvili*, 2005). The data have been extensively cross compared, and, for some spacecraft and parameters, cross-normalized. Time-shifts of higher resolution data to expected magnetosphere-arrival times are done for data from spacecraft in L1 orbits (ISEE 3, Wind, ACE), prior to taking hourly averages.

1.3 Open Questions and Knowledge Gaps

1.3.1 Reconnection Properties in Tilted vs. Equatorial Current Sheets

Magnetotail reconnection occurs in both equatorial and highly tilted current sheets. However, it is currently not well understood whether magnetic reconnection should look the same or different depending on the tilt of the current sheet. Event studies have investigated the properties of individual reconnection events in highly tilted current sheets, but statistics have never been collected to directly compare reconnection in equatorial vs. highly tilted current sheets (*Farrugia et al.*, 2021).

In this dissertation, we identify reconnection events in highly equatorial and highly tilted current sheets. We compare occurrence rates, outflow properties, and local plasma and field conditions of these current sheets to determine if they display fundamentally different properties.

1.3.2 Lack of Ion Diffusion Region Statistics

Ion Diffusion Regions have been reported extensively by previous satellite missions such as Geotail and Cluster (*Nagai et al.*, 1998; *Eastwood et al.*, 2010). These missions helped bring several important properties about this region to light. However, the large separation of spacecraft in previous missions has limited the community's ability to understand spatial changes within the IDR and the transition region between the IDR and EDR.

The recently launched Magnetospheric Multiscale Mission (MMS) utilizes electron-scale spacecraft separation to resolve spatial features in sub-ion scale structures. Previous work has scanned MMS's 2017 tail season to identify and determine the statistical properties within IDRs, but five additional MMS tail seasons (2018-2022) remain unreported (*Rogers et al.*, 2019).

In this dissertation, we identify IDRs during six MMS magnetotail campaigns, from 2017-2023. With this increased dataset, we compare their local plasma and field conditions to those of quiet current sheets and ion-coupled reconnection events.

1.3.3 Reconnection Onset Mechanism

The structure and effects of magnetic reconnection have been well observed in-situ by satellite missions for decades. However, the physical mechanism of reconnection onset is still not well understood. Recently, *Wang et al.*, 2020b and *Lu et al.*, 2020 proposed a mechanism for reconnection onset in Earth's magnetotail where an extremely thin, non-reconnecting current sheet becomes unstable to the electron tearing instability (*Wang et al.*, 2018; *Lu et al.*, 2020). This electron tearing initiates magnetic reconnection, which starts at electron-scales and later expands to ion scales. As a result, ions are not initially coupled to the reconnection process. After 10 seconds, the current sheet width expands, and electrons and ions with larger gyroradii are able to become involved in the reconnection process.

This proposed mechanism was supported by 2D PIC simulations and a satellite observa-

tion shown in Figure 1.10 (*Lu et al.*, 2020). The initial condition is a Lembege-Pellat current sheet, and an external driver is imposed by adding an out-of-plane electric field (*Lembège and Pellat*, 1982). Panel B, in the left column, is a snapshot of a time interval when magnetic reconnection is occurring, but only electrons are being accelerated by the reconnecting fields. This electron-only acceleration is displayed in the third column, which shows a simulated spacecraft cut through the reconnection center at that time. In Panels J and K, it is evident that simulated electrons are accelerated, while ions are not. This simulated spacecraft cut is qualitatively consistent with an in-situ spacecraft observation from June 17, 2017 in the second column (*Wang et al.*, 2018). We note that this event displays the same observational time series features that were used to identify *Phan et al.*, 2018's event as electron-only reconnection, despite manifesting from a different mechanism. Specifically, MMS observes a B_L reversal (Panel i), an electron jet (Panel l), intense current in M (Panel j), positive $J \cdot E'$ (Panel p), and no ion jet (Panel k). The current sheet is also very thin ($\approx 7d_e$), but its length is ambiguous with respect to the 10 d_i limit set in Section 1.1.6.

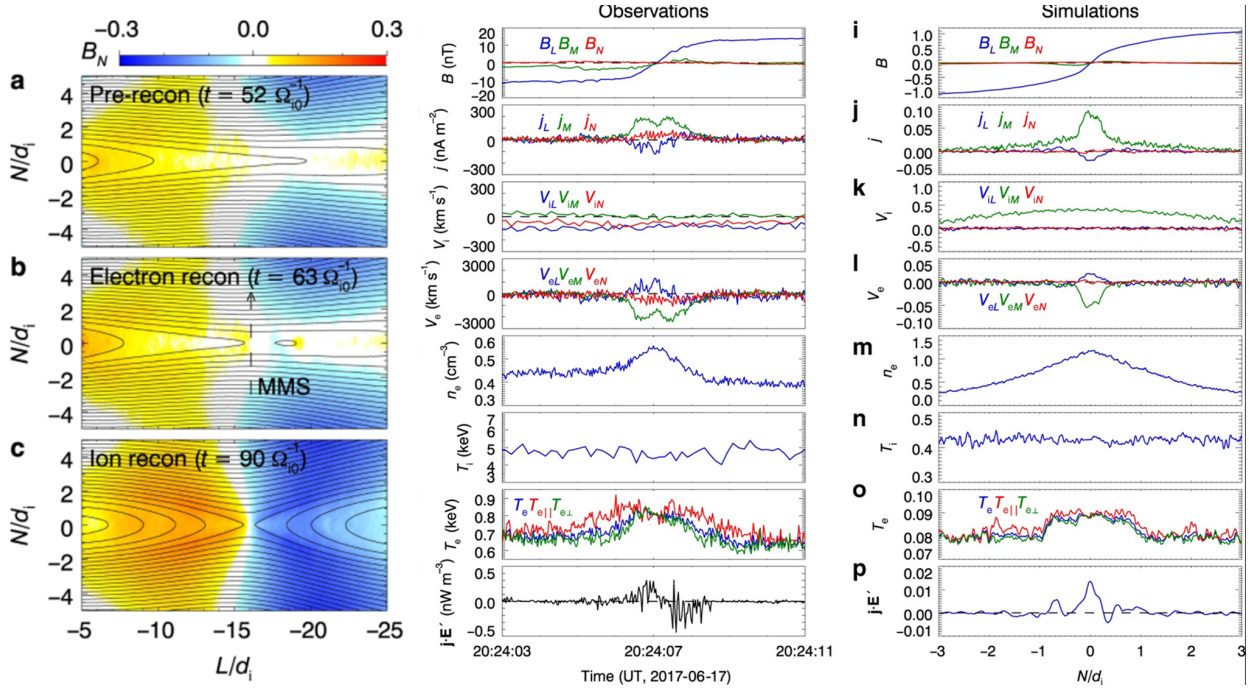

Figure 1.10: Adapted from *Lu et al.*, 2020 2D PIC simulations displaying electron-only onset of reconnection as a transition phase between a quiet, non-reconnecting current sheet and traditional reconnection. Comparison between a simulated spacecraft cut (right) through the reconnection region during this transition phase and a reconnection event observed by MMS (center).

While this simulation and satellite observation provide initial evidence for Lu and Wang's hypothesis, additional electron-only current sheet observations and further simulation work are needed to support or refute this model. In addition, because this hypothesis contains a time interval when reconnection is occurring and electrons are accelerated while ions are not, Lu and Wang call the interval electron-only reconnection. This nomenclature is misleading because, while the current sheet meets the requirements used to deem *Phan et al.*, 2018's event as electron-only reconnection, the mechanism that prevents the ions from coupling to the reconnection is clearly different. As such, for the rest of this thesis, we will label this mechanism as "electron-only onset of reconnection".

In this dissertation, we provide additional data and simulation work that supports this picture of reconnection onset. We also use this data to clarify where this process fits into the larger picture of what electron-only reconnection is and how it affects the surrounding space-plasma environment.

1.3.4 What is Electron-Only Reconnection, and Does it Occur in Earth's Magnetotail?

Several magnetotail observations and simulations of electron-only outflows by MMS have been reported and dubbed electron-only reconnection. However, the core microphysical mechanism that generated these electron-only outflows was highly variable. For example, Earthward-traveling plasmoids generated by multiple reconnecting X-lines were shown to reconnect with dipolarized tail field (*Vogiatzis et al.*, 2011) and form a current sheet whose stunted length generated electron-only outflows (*Man et al.*, 2018, 2020a). Meanwhile, previous work has established that, during the early stages of magnetotail reconnection in the near-Earth plasma sheet, a short time interval of electron-tearing occurs where only electrons are energized (*Wang et al.*, 2018; *Lu et al.*, 2020; *Wang et al.*, 2020a). Finally, traditional magnetotail reconnection during substorm times has been proposed to generate a turbulent outflow region. This turbulence can entangle magnetic field lines and generate sub-ion scale reconnection that violates the frozen-in condition and forms electron-only outflow jets (*Lapenta et al.*, 2018; *Vega et al.*, 2020; *Zhou et al.*, 2021). These three processes have highly variable generating mechanisms and degrees of time dependence, yet all three processes were reported as electron-only reconnection. This lack of clarity in nomenclature raises the philosophical question: What does the name electron-only reconnection mean?

In addition, previous work has established a transition from a quiet, non-reconnecting current sheet to an IDR-embedded EDR by ordering three electron-only observations in time (*Hubbert et al.*, 2021a). However, the rarity of these electron-only transition events has made it difficult for the community to verify whether or not this mechanism should be classified

as electron-only reconnection.

In this dissertation, we clearly define and separate three distinct magnetotail processes that have previously been dubbed electron-only reconnection: 1. electron-only flux rope erosion, 2. electron-only onset of reconnection, and 3. turbulent secondary reconnection. We then survey six magnetotail seasons of MMS data and attempt to identify examples of each process in Earth's magnetotail. We determine their initial statistical properties and use these properties to determine which generating mechanism is most reasonable for each event.

1.4 Outline

This dissertation is organized as follows. In Chapter 2, we identify quiet, non-reconnecting current sheets, ion-coupled reconnecting current sheets, and ion diffusion regions from six seasons (2017-2022) of MMS data in Earth's magnetotail. We first establish the observational criteria required to observe each of the three current sheet types, then survey Earth's magnetotail for the current sheets. With our dataset, we identify the orientation of the magnetotail current sheet for each event and establish that MMS observes all three current sheet types comparably frequently in highly tilted current sheets vs. equatorial current sheets. We then use in-situ observations of ion and electron outflows to pose that ion and electron outflows are unaffected by magnetotail current sheet orientation. Analyses in Section 2.2 and Section 2.3 for the years 2017-2020 are published in *Hubbert et al.*, 2022. Publication of Section 2.4 is currently in preparation. In Chapter 3 and Chapter 4, we perform a statistical survey of electron-only reconnection in Earth's magnetotail and use preliminary statistics to distinguish them from ion-coupled reconnection in Earth's magnetotail. In Chapter 3, we establish a set of required observational criteria for electron-only reconnection in Earth's magnetotail using *Phan et al.*, 2018's electron-only reconnection observation, an MMS magnetotail electron-only onset of reconnection candidate by *Wang et al.*, 2018, and 2.5D Particle

in Cell (PIC) simulation work by *Lu et al.*, 2020. In Chapter 4, using these criteria, we survey six seasons (2017-2022) of MMS data in Earth's magnetotail and identify 11 electron-only reconnection candidates in Earth's magnetotail. With these 12 events, we find that all candidates display additional commonalities that can be used to help identify electron-only reconnection in the future. We compare the plasma and field properties of the electron-only reconnection candidates, ion diffusion regions, and quiet current sheets. We find that the electron-only reconnection candidates are consistent with a transition phase during magnetic reconnection onset where only electrons are accelerated. Observational work in Chapter 3 and Chapter 4 can be found in *Hubbert et al.*, 2021a, *Hubbert et al.*, 2021b, and simulation work can be found in *Lu et al.*, 2022. Section 4.3.4 and Section 4.4.6 are also currently in preparation. We outline the proposed scenarios that could foster electron-only reconnection in Earth's magnetotail and establish that some events are most consistent with a transition phase during traditional reconnection onset (electron-only onset of reconnection), while others are most consistent with *Phan et al.*, 2018's picture of electron-only reconnection. This is an expanded discussion from *Hubbert et al.*, 2022. In Chapter 5, we summarize our findings and propose possible future work.

CHAPTER 2

Comparison of Magnetotail Reconnection Properties in Tilted vs. Equatorial Current Sheets

2.1 The Magnetospheric Multiscale Mission

The major axis of the orbit of the MMS satellites moves relative to the Earth-Sun line as the Earth orbits the Sun, which allows the satellites to probe the dayside, nightside, and cusp regions of Earth's magnetosphere. To survey for quiet, non-reconnecting current sheets in Earth's magnetotail, we studied six magnetotail campaigns, from 2017-2022. During those six years, MMS is primarily located in the magnetotail during the following intervals: June 1, 2017 – August 15, 2017 / June 1, 2018 – August 15, 2018 / June 15, 2019 – September 1, 2019 / June 15, 2020 – September 1, 2020 / July 1, 2021 - September 15, 2021 / July 1, 2022 - September 15, 2022.

We note that, from August 8-19, 2020, MMS's instruments were inactive. Otherwise, MMS's FGM and FPI instruments were active or outside the region of interest during the entire intervals presented in the previous paragraph. With that said, some events only have FPI data at survey mode temporal resolution. When identifying current sheets, it is important to distinguish between survey mode resolution events and burst mode resolution events.

Especially during magnetic reconnection observations, survey and burst mode observations yield significantly different bulk flow velocity magnitudes. This means that, for a given time interval, burst mode data show ion flow being super-Alfvénic while survey mode data show ion flow being sub-Alfvénic. Figure 2.1 shows an ion-coupled EDR in survey (left column) and burst (right column) mode resolutions. In burst mode (panel f), the ion outflows are clearly super-Alfvénic ($>$ 350 km/sec, calculated using Equation 2.1), whereas in survey mode (panel m), it becomes less clear.

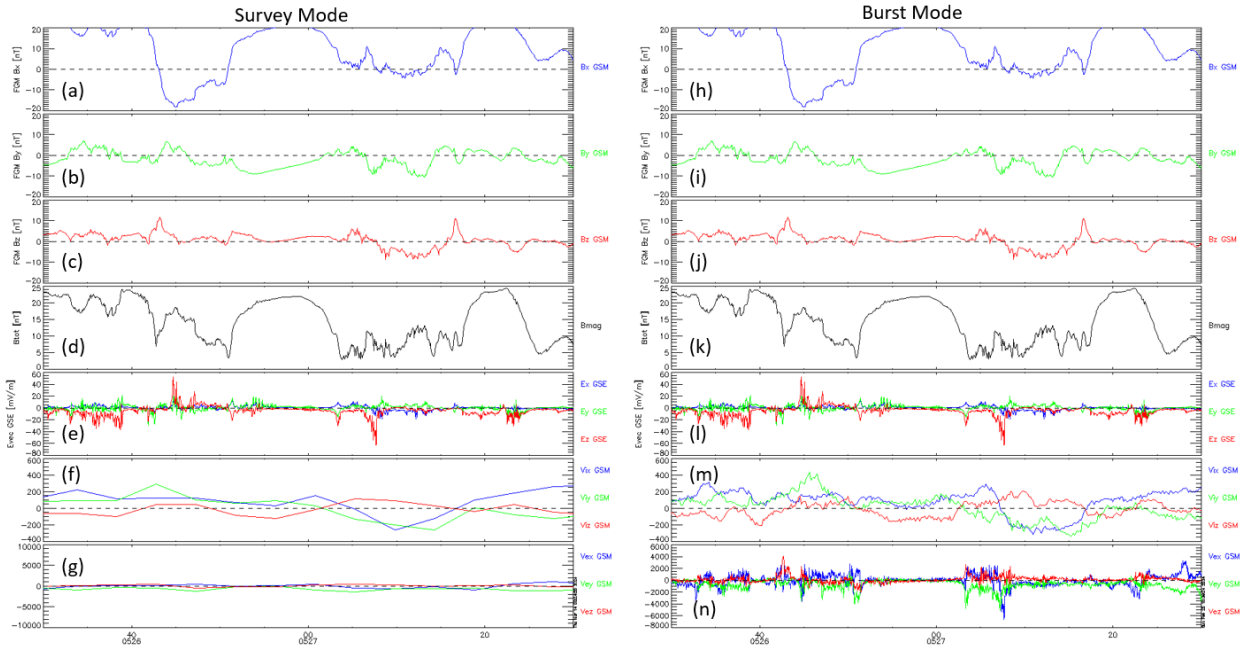

Figure 2.1: Electron Diffusion Region observations by MMS on 7/03/17,05:26:30-27:30 with FPI time series data in survey mode (left) and burst mode (right) resolution. (a-d,h-k) Magnetic field (B_X: Blue, B_Y: Green, B_Z: Red, Magnitude: Black), (e,l) electric field, (f,m) ion bulk flow velocity, (g,n) electron bulk flow velocity.

However, when MMS approaches Earth's magnetosheath, it becomes unclear if these field and plasma signatures are indicative of reconnection or a magnetosheath crossing. These magnetotail intervals allow us to observe many quiet current sheets, while minimizing the number of magnetosheath crossings. Magnetosheath crossings can meet the

same criteria listed earlier for quiet current sheets, but display distinctly different features. Notably, magnetosheath crossings display significant increases in plasma density ($> 10\ \#/cm^3$) and significant increases in the ion and electron omnidirectional energy spectra ($> 10^7 keV/(cm^2\ s\ sr\ keV)$), consistent with higher energy solar wind particles.

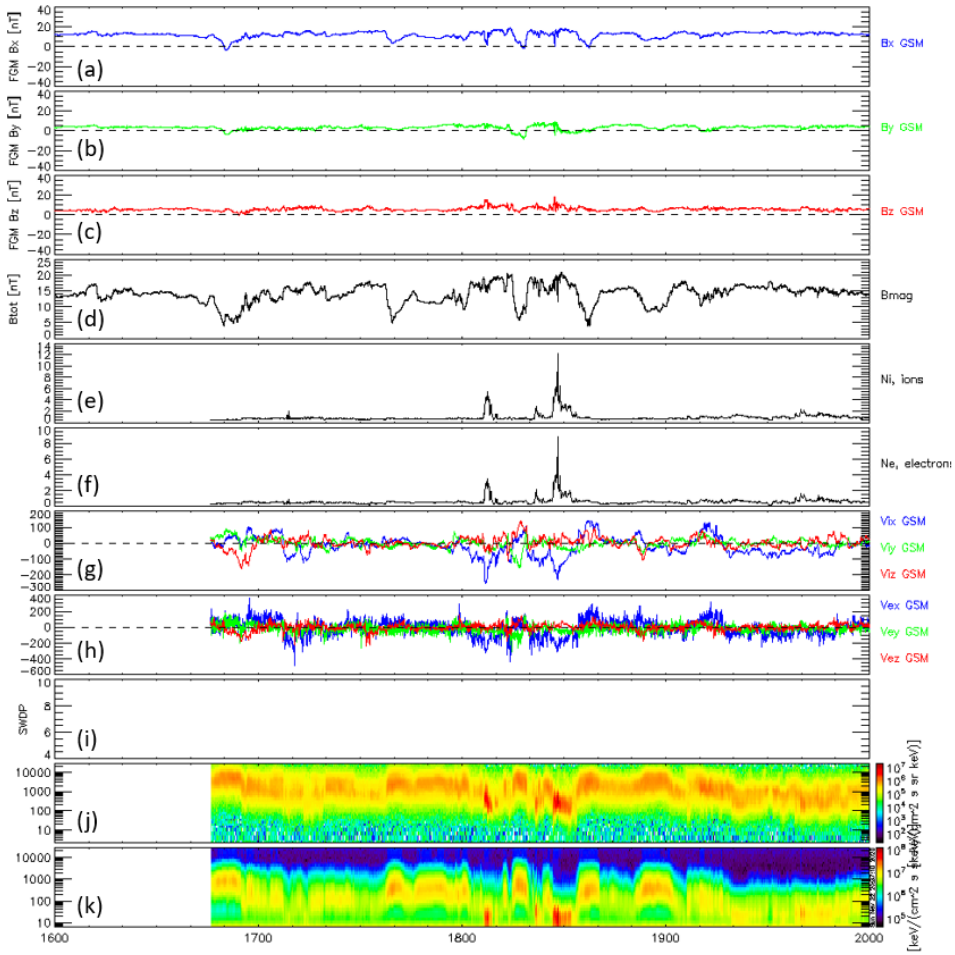

Figure 2.2: Magnetosheath observation by MMS on 7/2/20. (a-d) Magnetic field (B_X: Blue, B_Y: Green, B_Z: Red, Magnitude: Black), (e,f) ion and electron number density, (g,h) ion and electron bulk flow velocity, (i) solar wind dynamic pressure, (j,k) ion and electron energy spectra.

2.2 Statistical Survey of Quiet Current Sheets

2.2.1 Observational Criteria of Quiet Current Sheets

Although MMS consists of a constellation of four satellites, they are separated by only tens of kilometers. As a result, all four spacecraft see approximately the same, ion-scale features. Therefore, in this section, when we use the name MMS, we refer to any arbitrary single spacecraft in the MMS constellation. The MMS satellites are moving at approximately 10-15 km/sec, which is fast on Earth, but slow by magnetospheric dynamics standards. For comparison, substorm processes, current sheet flapping, and flux rope movement occurs at speeds greater than 100 km/sec. Therefore, MMS is approximately stationary in the context of magnetotail plasma processes. Any movement or change in plasma or field properties observed by MMS is attributed to R_E-scale movements in the magnetotail, instead of motions of the spacecraft.

During the crossing of a quiet current sheet, MMS data indicate entrances and/or exits from three different regions. First, MMS must be present in one of Earth's magnetotail lobes. This is comprised of Bx-dominated magnetic fields and smaller magnitude B_y and B_z components in GSM. In addition, the plasma beta of the region should be ≈ 1. Second, MMS needs to enter the plasma sheet region, where the magnetic field strength approaches an absolute minimum and the plasma beta significantly increases. We define an absolute minimum as a field minimum in the ten second range before and after the current sheet crossing. During this interval, the spacecraft cannot detect super-Alfvénic ion or electron exhausts, where the Alfvén speed is calculated in the magnetotail lobe region. This provides a conservative standard for ions and electrons to meet to be considered reconnecting, as Alfvén speed is often calculated using the reconnecting magnetic field at the current sheet center. We define Alfvén speed as:

$$v_A = B_0/\sqrt{\mu_0 \rho_0}. \tag{2.1}$$

where B_0 is the magnetic field strength in the lobe and ρ_0 is the plasma density in the lobe. Magnetic reconnection has been shown to consistently accelerate large populations of ions and electrons to super-Alfvénic speeds and is the dominant process in the magnetotail plasma sheet thought to regularly generate super-Alfvénic ions and electrons (*Angelopoulos et al.*, 1992). As such, sub-Alfvénic electron and ion flow profiles indicate that MMS is not observing magnetic reconnection. Third, MMS must exit the plasma sheet and enter the opposite magnetotail lobe. This region is similar to the first magnetotail lobe in that the plasma beta is lower than that in the plasma sheet and the magnetic field is dominated by Bx. However, the sign of B_X in Region 3 should be opposite to that in Region 1 because the magnetic field is pointed in the opposite direction.

When MMS observes a quiet, non-reconnecting current sheet, it must observe several field and plasma signatures that are consistent from event to event. We require specific features in the time series data. First, MMS must observe an approximately symmetric reversal in B_X (GSM), where B_X starts greater than +10 nT and ends less than -10 nT, or vice versa. This indicates that MMS is observing fields from both lobes and the plasma sheet. Second, MMS must observe an absolute minimum in B_{tot} coincident with B_X approaching zero. This indicates that MMS is crossing the primary magnetotail current sheet instead of a flux rope or dipolarization front. Third, we must observe v_{ix} and v_{ex} values that never exceed v_A, which is calculated using B_0 and ρ_0 values at the point when B_0 equaled -10 nT. A sample event that meets these criteria is shown in Figure 2.3. B_X reverses (Panel A), B_{tot} coincidently approaches absolute minimum (Panel D), and v_{iX} and v_{eX} consistently stay below the local Alfvén speed of 475 km/sec.

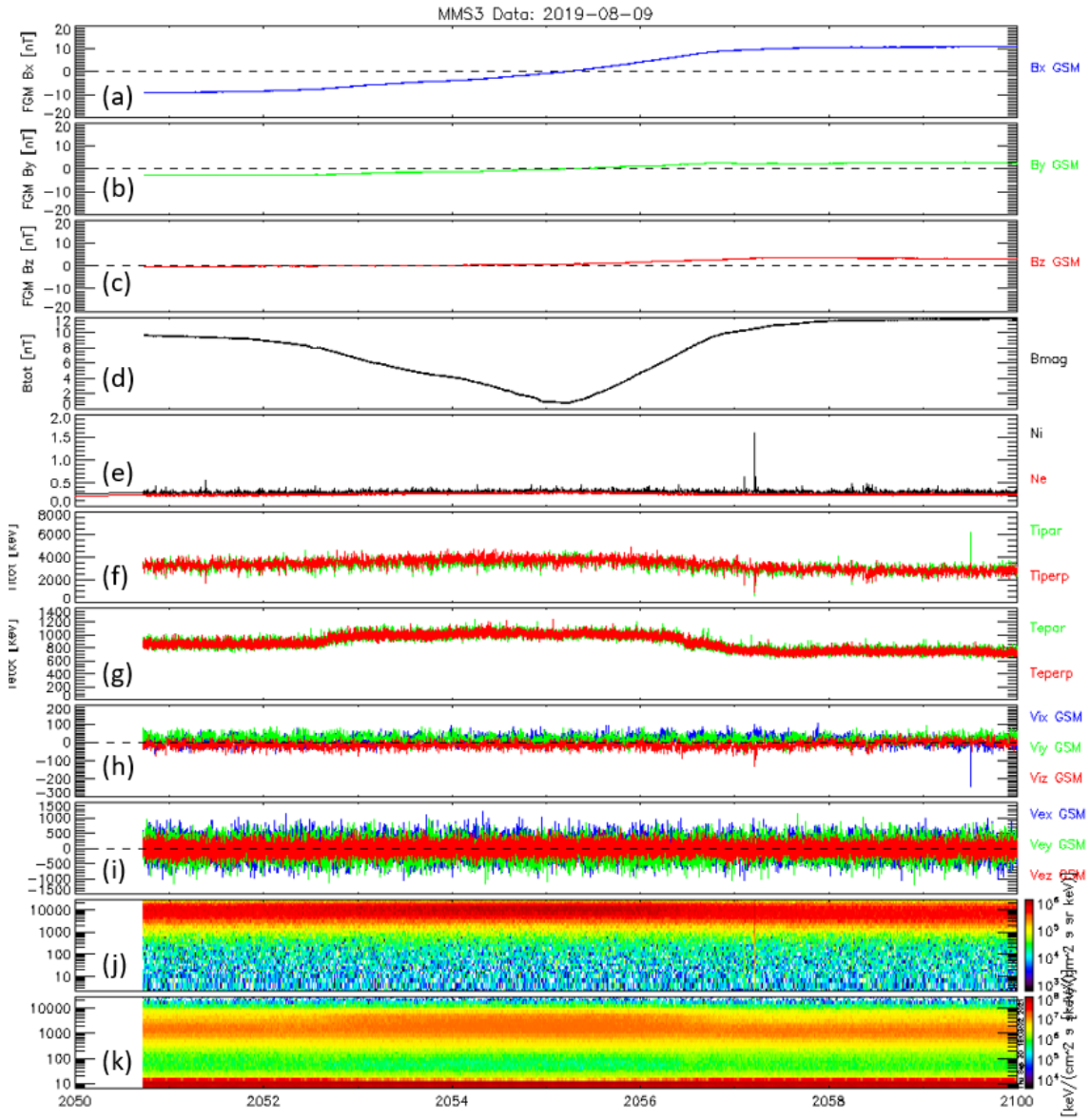

Figure 2.3: Quiet, non-reconnecting current sheet observation by MMS on 6/09/17. (a-d) Magnetic field (B_X: Blue, B_Y: Green, B_Z: Red, Magnitude: Black), (e) ion (black) and electron (red) number density, (f,g) ion and electron temperatures, (h,i) ion and electron bulk flow velocity, (j,k) ion and electron energy spectra.

2.2.2 Data Collection & Dataset Description

We performed a survey over six MMS magnetotail seasons (Phase 2B: June 15 - August 31 2017, Phase 3B: June 15 - August 31 2018, Phase 4B: July 1 - September 15 2019, Phase 5B: July 1 - September 15 2020, Phase 6B: July 15 - September 30 2021, Phase 7B: July 15 - September 30 2022) looking for quiet, non-reconnecting current sheets. Given the criteria listed in Section 2.2.1, we identified 476 quiet, non-reconnecting current sheets. In each of these seasons, MMS was located in the low-latitude magnetotail with an average apogee of $\approx 25\ R_E$ (See Figure 1.9). Dates, time intervals, and locations of quiet current sheets from this manuscript are shown in Section A.2.1.

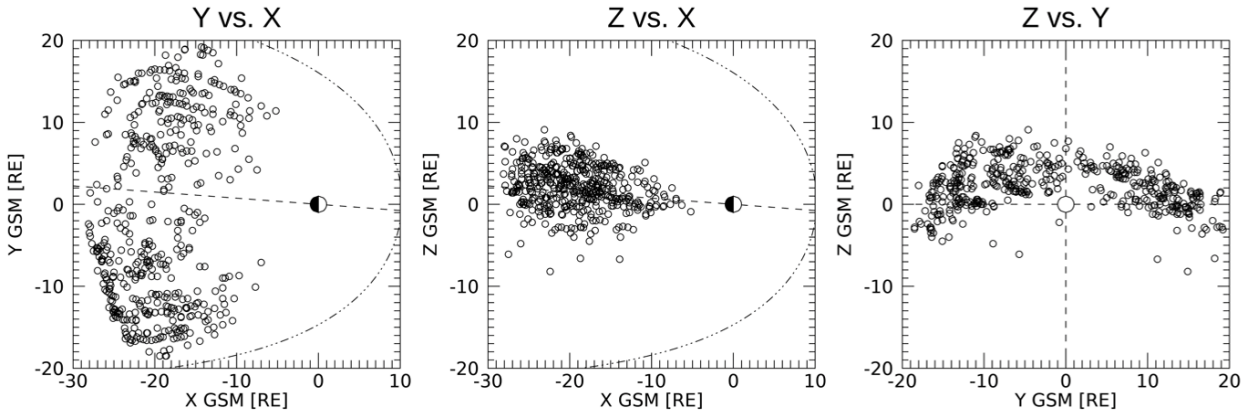

Figure 2.4: 2D cuts of quiet current sheet event locations in the (a) X-Y plane, (b) X-Z, and (c) Y-Z plane in GSM coordinates.

In this study, we identified 476 quiet magnetotail current sheets. Figure 2.4 shows three 2D cuts of event location in the GSM plane. Panels A and B feature a dash-dotted curve and a diagonal, dashed line that crosses through Earth. The dash-dotted curve is a cartoon visualization of the typical location of the magnetopause. The dashed diagonal in Panel A represents the approximate midnight sector given Earth's orbit around the Sun. The slope of the line is due to the orbital speed of Earth (30 km/sec) relative to radial solar wind speed. The dashed diagonal in Panel B represents the typical northward displacement of

the magnetotail current sheet. MMS observes 278 current sheets in the dawn sector and 197 current sheets in the dusk sector. MMS observes 373 current sheets in the North sector ($Z > 0$ GSM) and 103 current sheets in the South sector. MMS also observes 360 events at a distance greater than $20R_E$ and 116 events at a distance less than $20R_E$. We note that in the flanks, where $Y < -10R_E$ or $Y > +10R_E$ GSM, MMS observes quiet current sheets at significantly lower latitudes than in the midnight sector ($-10R_E < Y < 10R_E$ GSM). Also, there is heavy banding in event observations at distances of $\approx 25R_E$ and $22R_E$.

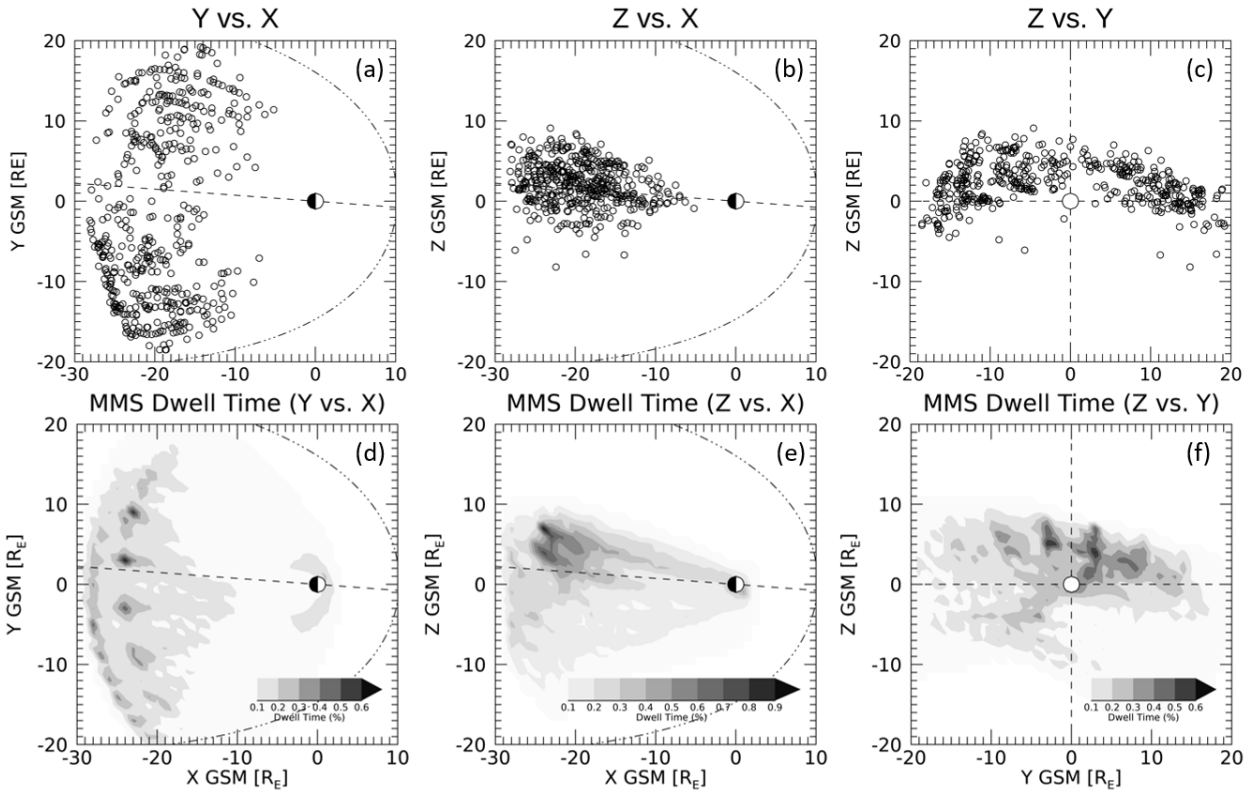

Figure 2.5: 2D cuts of quiet current sheet event locations in the (a) X-Y plane, (b) X-Z, and (c) Y-Z plane. 2D contours of MMS dwell time in the six tail seasons from 2017-2022. All locations are plotted in GSM coordinates.

MMS's dwell time contributes to several of these features (see several 2D cuts of MMS's dwell time in Figure 2.5). In this manuscript, we define MMS's dwell time as the amount of

time MMS spent in a given region of space during the six magnetotail seasons used to identify current sheet events. The 2D contour plots in Figure 2.5 highlight the highest occurrence regions of MMS's orbit. MMS spent 53% of its time in the dawn sector, 47% of its time in the dusk sector, 61% of its time in positive Z GSM, 39% of its time in negative Z GSM, 61% of its time farther than $20R_E$, and 39% of its time closer than $20R_E$. The mission also had an apogee of $\approx 22R_E$ in 2017-2018 and an apogee of $\approx 25R_E$ in 2019-2022, explaining the heavy banding of dwell time and events at those distances. Although MMS's regional dwell time is qualitatively consistent with the regional occurrence rate of quiet current sheets (58% dawn to 42% dusk, 78% positive Z to 22% negative Z, 76% $> 20R_E$ to 24% $< 20R_E$), it does not fully explain the heavy bias towards current sheet events occurring in positive Z and distances farther than $20R_E$. We attribute the heavy bias towards positive Z to the steep inclination of the magnetotail neutral sheet, which we expect to occur at $\approx 3R_E$ in +Z GSM (*Xiao et al.*, 2016). We attribute the higher current sheet occurrence rate at higher distances to MMS's instruments not being operational when MMS was $< 10R_E$ from Earth, resulting in significant non-dwell time. If we remove this dead time, we obtain a more reasonable 70% to 30% dwell time ratio. The quiet current sheet "wings" at the flanks are consistent with MMS's dwell time and the evolution of MMS's orbit from $+Z$ GSM in 2017 to $-Z$ GSM in 2022. However, in the dusk sector close to Earth ($D < 20R_E$), we find that MMS observes significantly more quiet current sheets than expected given MMS's dwell time, and in the dawn sector close to Earth, MMS observes significantly fewer quiet current sheets than expected given MMS's dwell time. We attribute this to the fact that, while MMS was located in the dawn sector close to Earth, it was located in highly negative Z GSM, far away from the magnetotail neutral sheet. Conversely, in the dusk sector, MMS is located in higher Z GSM while close to Earth, providing increased opportunity to observe the near-Earth plasma sheet.

2.2.3 Current Sheet Normal

The "default" orientation of a quiet current sheet is a 2D picture in the GSM X-Z plane. However, under extreme conditions, the current sheet can flap and bend, resulting in a more 3D picture. If the magnetotail neutral sheet is in its typical orientation, as described in Section 1.1.3, and we rotate the data into minimum variance (MVA) current sheet coordinates, we expect L to line up approximately with the GSM X direction, M with GSM Y, and N with GSM Z. The N direction is often dubbed the current sheet normal direction. To calculate the current sheet normal direction for our current sheet events, we use the four-spacecraft timing method popularized by *Russell et al.*, 1983 and explained in further detail in Section A.1.3. This method produces three components of the current sheet normal in GSM coordinates and a current sheet normal speed. Flapping of the magnetotail neutral sheet can change a current sheet's normal direction from the Z direction to the Y or X direction. This flapping, driven by reconnection or the external solar wind, is thought to propagate from the midnight sector to the flanks in the GSM Y directions (*Sergeev et al.*, 2004). As such, MMS frequently observes flapping current sheets that yield a current sheet normal in the Y direction and, less commonly, in the X direction. We classify current sheets with normals in the Z direction to be equatorial current sheets and current sheets with normals in the Y or X directions to be tilted current sheets.

The conventional orientation of the magnetotail neutral sheet primarily features a normal direction in the GSM Z direction. However, it is currently unclear how frequently MMS should expect to observe the neutral sheet in its conventional orientation versus an unconventional orientation. To address this, we calculate the current sheet normal direction for each current sheet. These values can be found in Section A.2.1. In our quiet current sheet dataset, 144 have normals primarily oriented in the Z direction, 203 have normals primarily oriented in the Y direction, 115 have normals primarily oriented in the X direction, and for 14 we were unable to calculate current sheet normal because one or more instruments was turned

off. This indicates that, during the tail seasons of 2017-2022, MMS primarily observed tilted current sheets, particularly in the GSM Y direction. We expect this result given that MMS is stationary. When the magnetotail is calm and in a conventional orientation, the odds of a stationary spacecraft crossing the current sheet should be lower than when the magnetotail is dynamically flapping and increasing the physical area that it reaches. In addition, during flapping, the surface area with a normal in the Y or X direction increases and the surface area with a normal in the Z direction decreases. Increased Y or X surface area and the wave typically propagating in the Y direction results in increased occurrence frequencies of tilted current sheets compared to equatorial current sheets.

We now focus on the Y component of the observed current sheet normal. We investigate whether there is a relationship between event location and the direction of the y component of the current sheet normal. In the dawn sector (Y GSM < 0), 184 current sheets featured a current sheet normal in the -Y direction and 88 featured a current sheet normal in the +Y direction. Conversely, in the dusk sector (Y GSM > 0), 76 current sheets featured a current sheet normal in the -Y direction and 114 featured a current sheet normal in the -Y direction. This indicates that MMS observed the magnetotail neutral sheet preferentially moving away from the midnight sector and toward the flanks. This is shown in Figure 2.6 and consistent with previous spacecraft observations (*Gao et al.*, 2018).

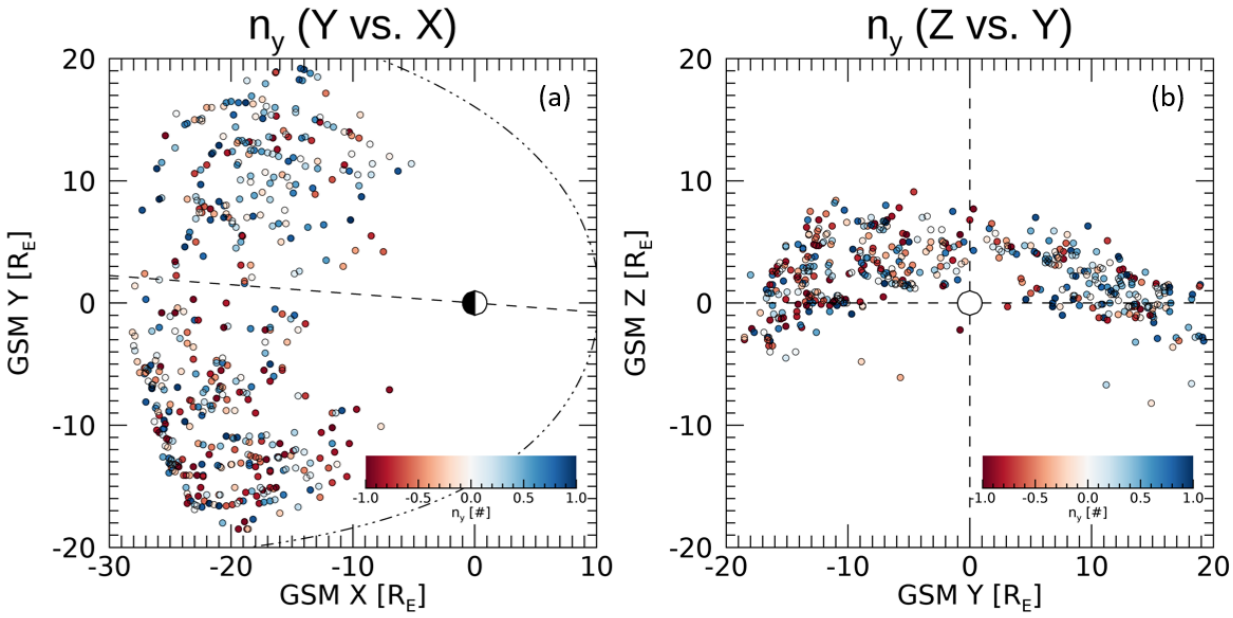

Figure 2.6: 2D cuts of quiet current sheet event locations in the (a) X-Y plane and (b) Y-Z plane. Color bar indicates Y component of current sheet normal, with 1 being in the positive Y direction and -1 being in the negative Y direction. All locations are plotted in GSM coordinates.

To further highlight the significant fraction of events with normals in the Y or X direction, we calculate a parameter which we call "current sheet normal angle":

$$\theta = (\frac{180}{\pi}) \arctan |\frac{\sqrt{n_x^2 + n_y^2}}{n_z}| \tag{2.2}$$

where n_y is the Y component of the current sheet normal and n_z is the Z component of the current sheet normal. This parameter approximately describes how tilted a current sheet is in the 2D [X + Y,Z] plane, where $\theta = 0$ is a fully equatorial current sheet and $\theta = 90$ is a fully tilted current sheet in the X + Y direction. We note that this parameter does not describe the 3D direction of current sheet tilt, as many current sheet orientations can produce a single $\sqrt{X^2 + Y^2}$ magnitude. Despite not providing the complete 3D picture of current sheet tilt, this parameter conveniently distills the current sheet normal direction into

one value and groups together events whose normal directions are 180 degrees apart. Using this parameter, we create histograms of current sheet normal angle and the Y component of current sheet normal direction. For this analysis, we have no need to distinguish current sheet normal directions that are oriented 180 degrees apart (ex. +Y and -Y). We apply this parameter to our events and effectively show how frequently MMS observes a tilted vs. equatorial current sheet (See Figure 2.7).

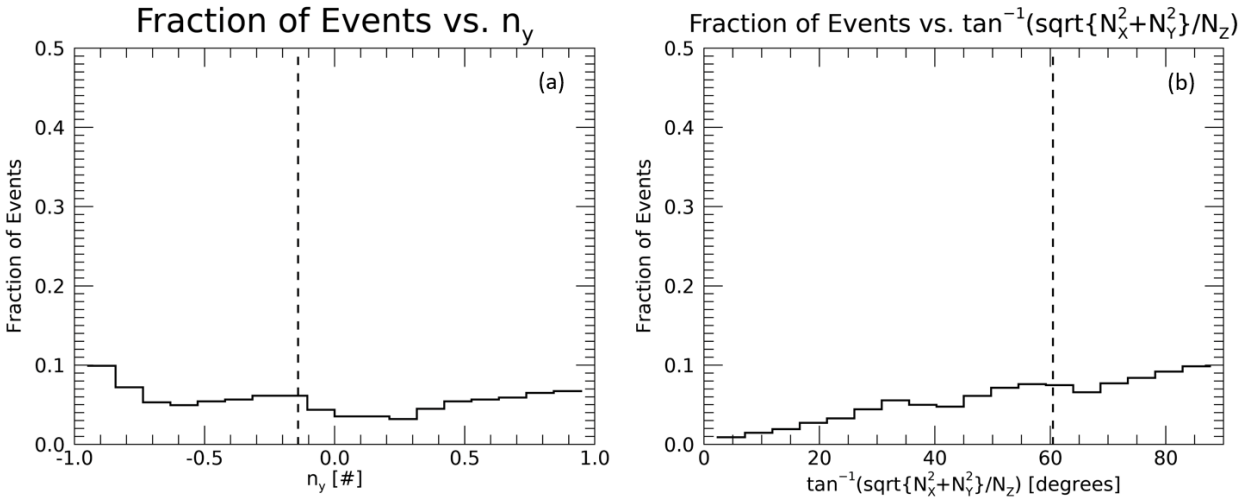

Figure 2.7: Histograms of (a) Y component of current sheet normal and (b) current sheet normal angle as calculated in (2.2). Dashed vertical lines indicate the median value of each parameter.

In panel A, we show that MMS observes current sheets with small (< 0.5) Y normal components approximately as often as large (> 0.5) Y normal components. In Panel B, we show that MMS observes tilted current sheets in either the X or Y direction more frequently than equatorial current sheets. We note that the calculation of $\sqrt{X^2 + Y^2}$ weighs the combination of the X and Y components against the Z component, meaning that a current sheet must dominate both the X and Y components to be deemed truly equatorial. This observation is novel, as it was previously unclear whether a spacecraft should expect to observe equatorial current sheets more or less frequently than tilted current sheets.

2.2.4 Plasma & Field Properties

We now display histograms of several fundamental, local plasma and field features of our quiet current sheet events: $N_i, N_e, T_{e,||}, T_{e,\perp}, T_{i,||}, T_{i,\perp}$, and $E_{L,M,N}$. To extract the parameters of interest, we first quantitatively determine the boundary of each current sheet by calculating $J_\perp$ using the curlometer technique with MMS FGM data. Our definition of current sheet boundary is when $J_\perp$ drops below 50% of its maximum value. After locating the current sheet interval, we extract the maximum and average value of each plasma and field parameter within each current sheet and place them in histograms (See Figure 2.8). We utilize 20 bins because it is less than $\sqrt{476} \approx 21.8$. Then, we overlap the bins by summing up each bin value with the values of surrounding bins. These sums become the new value for each bin and are renormalized. The number of bins corresponding to each current sheet type was found by calculating $\sqrt{n}$, where n is the number of events. We use overlapping bins because we compare these plasma parameters to the parameters of Ion Diffusion Regions and Electron-Only Reconnection candidates, which constitute much smaller data pools. Overlapping bins helps account for the statistical uncertainty of smaller event pools. We note that this may not be necessary for a dataset of this size, we apply this to our Ion Diffusion Region set in Section 2.4. We apply the same methods to each current sheet type for consistency.

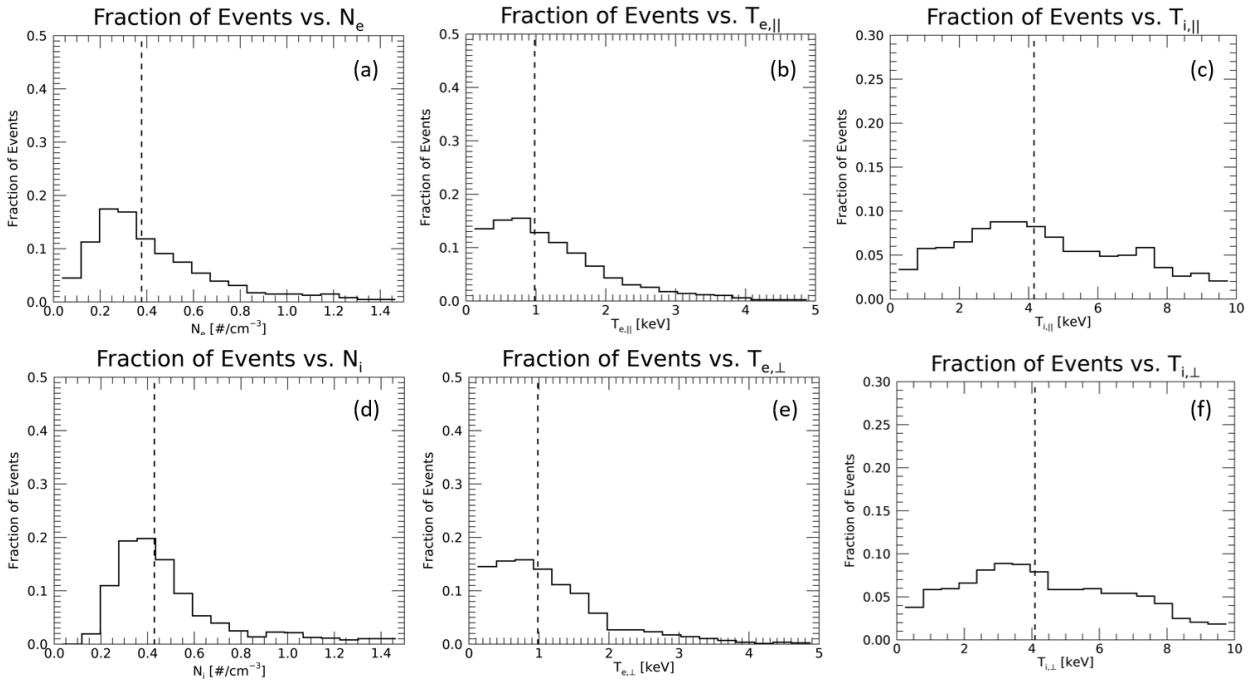

Figure 2.8: Histograms of the maximum value within the current sheet boundary of six plasma parameters extracted from our quiet current sheet events. (a) electron density, (b) ion density, (c) parallel electron temperature, (d) perpendicular electron temperature, (e) parallel ion temperature, and (f) perpendicular ion temperature. Vertical dashed lines indicate the median value.

The parameters shown in Figure 2.8 are the maximum values, not the average values. As shown by the dashed median lines, the typical plasma density, electron temperature, and ion temperature sit at $\approx 0.4\ \#/cm^3$, 1 keV, and 4 keV, respectively. We note that all three distributions have long tails that extend past the plotting region. Meanwhile, as shown in Figure 2.9, electric field sits at ≈ 1 mV/m. We also note that, during reconnection, we expect elevated E_M and E_N, which is not present in these histograms. These ambient background plasma and field values are consistent with previous spacecraft surveys of non-reconnecting magnetotail current sheets (*Lu et al.*, 2019).

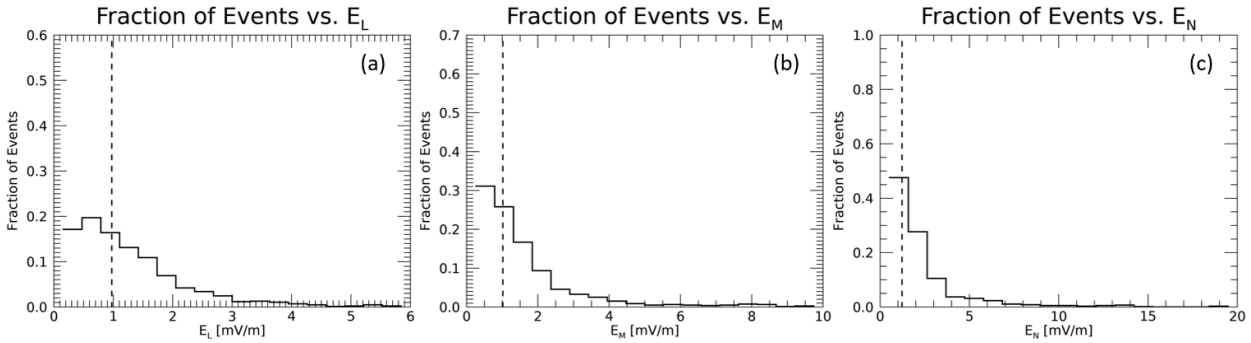

Figure 2.9: Histograms of the maximum electric field components extracted from our quiet current sheet events. (a) E_L, (b) E_M, (c) E_N. Vertical dashed lines indicate the median value.

2.3 Statistical Survey of Ion-Coupled Reconnection

2.3.1 Observational Criteria of Ion-Coupled Reconnection

We now outline the observational criteria required for MMS to classify an event as ion-coupled reconnection. First, MMS needs to observe a current sheet crossing. In Earth's magnetotail, the current sheet is indicated by a reversal of the magnetic field direction from Earthward to tailward, or vice versa. In current sheet minimum variance coordinates, a spacecraft moving from the Northern lobe to the Southern lobe should expect to see strong, positive B_L change to strong, negative B_L. For the rest of the thesis, we call this a B_L reversal.

The second criterion a spacecraft needs to see to identify reconnection is an absolute minimum of the magnetic field strength. In the magnetic lobes, the field strength is stronger than that in the plasma sheet. This should be reflected by the spacecraft observation.

The third criterion a spacecraft needs to see is super-Alfvénic ion exhaust. During magnetotail reconnection, bursty bulk flows and ion exhaust is expected in both Earthward and tailward directions. Specifically, the ion exhaust needs to approach the local Alfvén speed

in the near-Earth magnetotail. This is described by Equation 2.1. If ion bulk flow velocities are not close to the local Alfvén speed, one can argue that the ions are being energized due to other non-reconnection processes like kink-mode instability (*Karimabadi et al.*, 2003a,b) and dipolarization fronts (*Ukhorskiy et al.*, 2017). Past evidence has shown that magnetotail reconnection consistently energizes ions to speeds approaching the ion-Alfvén speed. Thus, I require this ion signature to be present for an interval to classify it as reconnecting. However, the ion signature changes depending on MMS's proximity to the reconnection X-line. For example, MMS can cross the current sheet in the exhaust region, where MMS only sees ion exhaust outflow in one direction. However, MMS can also cross the reconnection region in the L direction, where the spacecraft see ion exhaust outflows in both directions. These signatures were noted and used to separate events in statistical analysis.

The last criterion needed to identify magnetic reconnection is super-Alfvénic electron exhaust coincident with the ion exhaust outflows. This feature combined with ion exhaust outflows creates a smoking gun for full-bodied reconnection in Earth's magnetotail.

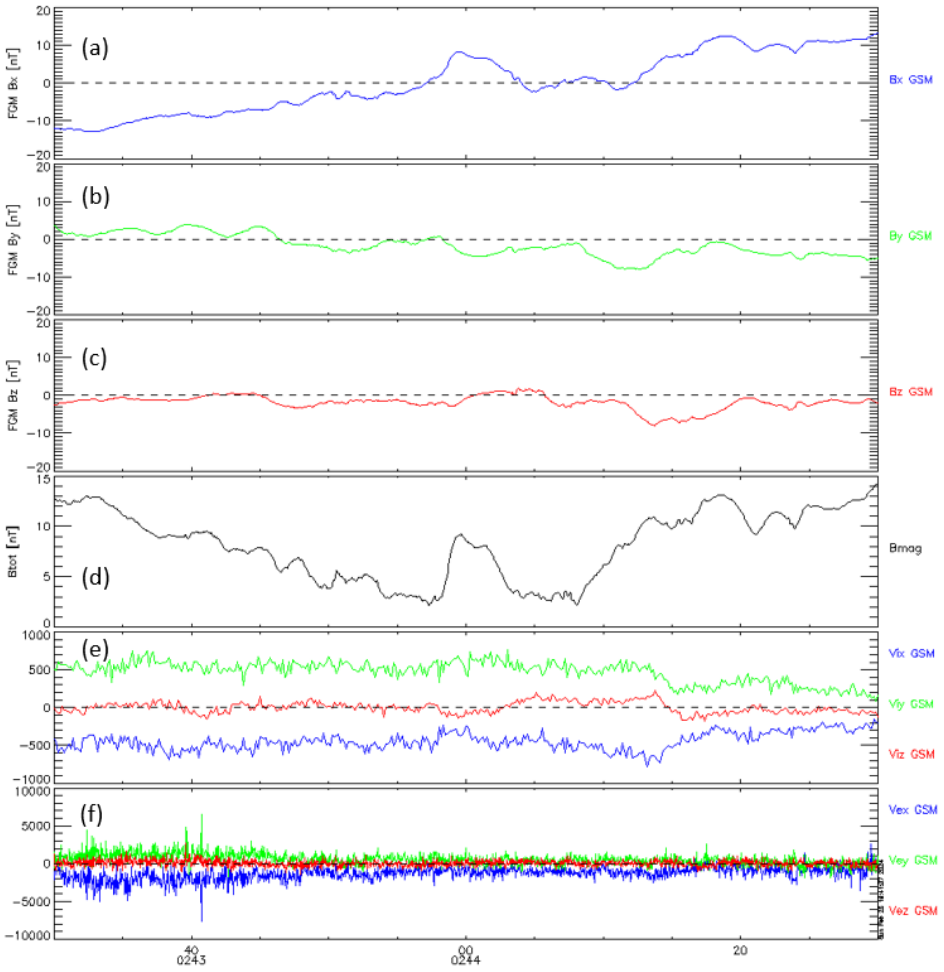

Figure 2.10: Sample traditional reconnection event from 7/26/17, 02:43:30-44:30. (a-d) Magnetic field (B_x: blue, B_y: green, B_z: red, Magnitude: black), (e) ion and (f) electron bulk flow velocity.

In summary, we use the following criteria to identify traditional ion-coupled reconnection in MMS data: 1. B_L reversal (current sheet crossing), 2. B_{tot} minimum, 3. super-Alfvénic v_{iL}, and 4. super-Alfvénic v_{eL}. To highlight these criteria, we show a sample reconnection event in Figure 2.10. This event displays a current sheet crossing with ion and electron bulk flow velocities that exceed the local Alfvén speed of 600 km/sec, calculated using an ambient field strength of 15 nT and plasma density of 0.3 $\#/cm^3$. For ions to be deemed

super-Alfvénic, the bulk velocity must exceed the local Alfvén speed at any point within one minute of the reversal in B_L. This survey does not discriminate against events whose ion velocities peak away from the current sheet center or only show Alfvénicity for a relatively short duration (e.g. 5 seconds vs. 30 seconds).

2.3.2 Data Collection & Dataset Description

Identically to our quiet current sheet survey, we performed a survey over six MMS magnetotail seasons (Phase 2B: June 15 - August 31 2017, Phase 3B: June 15 - August 31 2018, Phase 4B: July 1 - September 15 2019, Phase 5B: July 1 - September 15 2020, Phase 6B: July 15 - September 30 2021, Phase 7B: July 15 - September 30 2022) looking for ion-coupled, reconnecting current sheets. During these intervals, all of MMS's instruments were operating the majority of the time. This is important, as FPI availability is not a given. With that said, some events only have FPI data at srvy mode resolution. For an event to qualify as reconnection, I require both FPI and FGM data to be available. However, I do not distinguish between srvy mode resolution events and brst mode resolution events.

Using the criteria above and searching in the intervals described above, we identified 408 traditional, ion-coupled reconnection events in the MMS dataset (see Figure 2.11). Dates, time intervals, and locations of these events are shown in Section A.2.2.

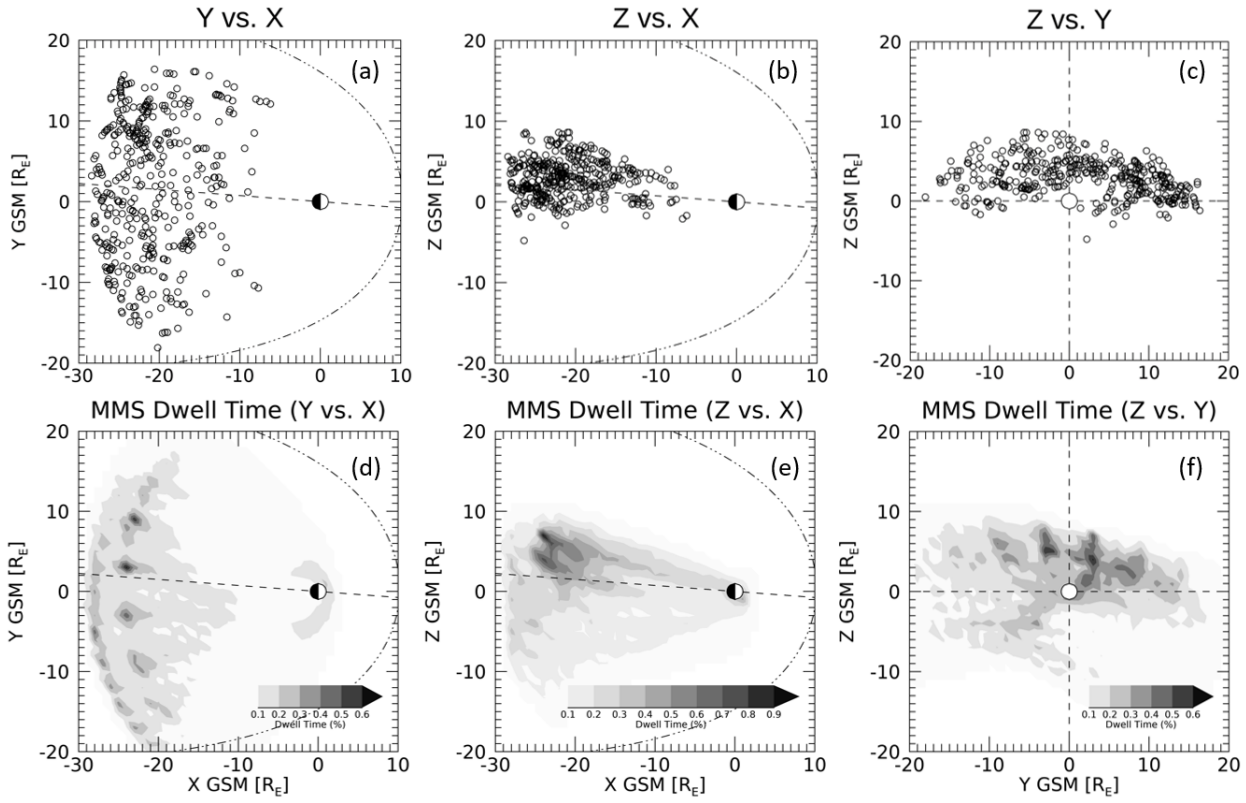

Figure 2.11: 2D cuts of ion-coupled reconnecting current sheet event locations in the (a) X-Y plane, (b) X-Z, and (c) Y-Z plane. MMS dwell time from 2017-2022 in the (a) X-Y plane, (b) X-Z, and (c) Y-Z plane. All locations are plotted in GSM coordinates.

Figure 2.11 shows three 2D cuts of ion-coupled reconnection location in GSM coordinates. MMS observes 172 events in the dawn sector and 236 events in the dusk sector, 360 events in the North sector and 48 events in the South sector, 318 events farther than $20R_E$, and 90 events closer than $20R_E$. We note that, unlike our non-reconnecting current sheets and contrary to MMS's dwell time, more reconnection events appear in the dusk sector than the dawn sector. In addition, there is an increased occurrence of reconnection events in the North sector compared to non-reconnecting current sheets. The increased duskward occurrence of reconnecting current sheets is consistent with the dawn-dusk asymmetry that has been observed in previous missions. The increased Northward occurrence of reconnection

events compared to quiet current sheets, however, is a novel finding. The mechanism driving this disparity is the subject of future research.

Next, we focus on the current sheet normal of our events (see Section A.2.2 for exact values). In our reconnection dataset, 127 have primarily X normals, 132 have primarily Y normals, and 149 have primarily Z normals. Similar to non-reconnecting current sheets, reconnecting current sheets are split in normal orientation. However, unlike quiet current sheets, Z normal is the most common orientation. We isolate the Y component of the current sheet normal as we did for quiet, non-reconnecting current sheets (see Figure 2.12). Unlike quiet current sheets, there is no distinct relationship between event location and Y component of current sheet normal (125 duskward events with positive Y normal, 111 duskward events with negative Y normal, 86 dawnward events with positive Y normal, 86 dawnward events with negative Y normal). Given the significant variance in magnetotail current sheet orientation in both quiet, non-reconnecting current sheets and ion-coupled reconnecting current sheets, we first interpret that reconnection is not more likely to occur in a equatorial current sheet than a highly tilted one. This contradicts previous observation (*Snekvik et al.*, 2012) and simulation (*Lu et al.*, 2019) works, which outline the default orientation of magnetotail reconnection as primarily equatorial (normal in the Z direction). In addition, because the majority of reconnecting and non-reconnecting current sheets were found in current sheets with X and Y dominated normal directions, we conclude that individual reconnection events do not always supply sufficient energy to the magnetotail to disrupt the global configuration of the magnetotail on time scales observable by MMS. We note that reconnection is capable of triggering processes that disrupt the global configuration of the magnetotail, but does not always.

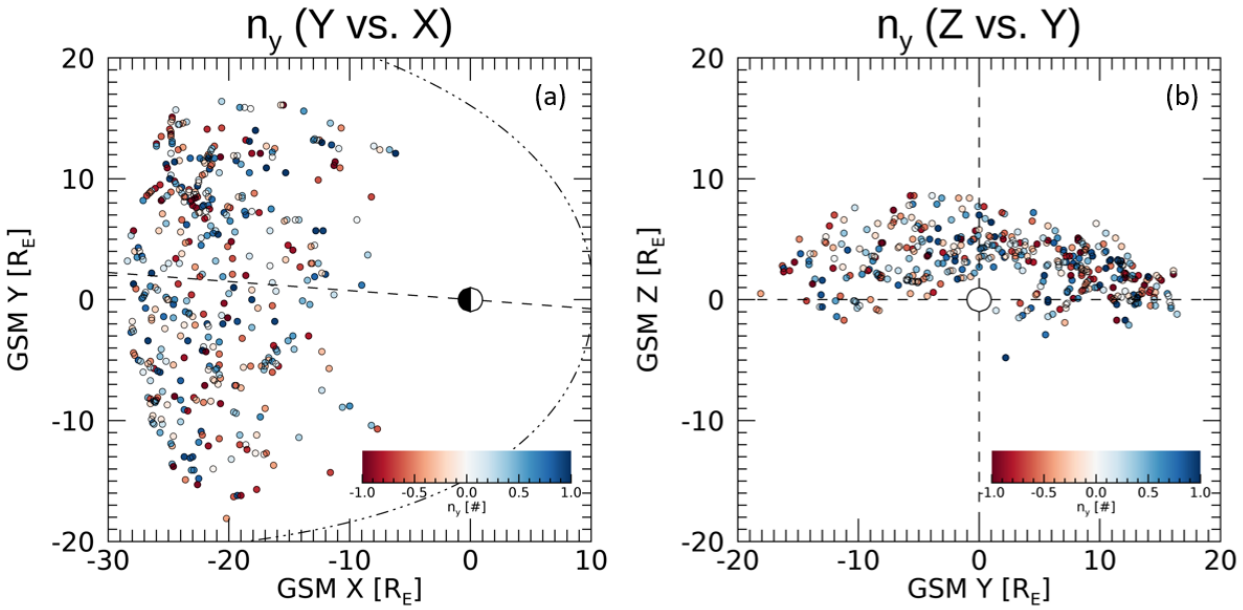

Figure 2.12: 2D cuts of ion-coupled reconnecting current sheet event locations in the (a) X-Y plane, (b) X-Z, and (c) Y-Z plane. Color bar indicates the Y component of the current sheet normal for each event. All locations are plotted in GSM coordinates.

We then compare the Y component of the current sheet normal and current sheet normal angle values of reconnecting current sheets and non-reconnecting current sheets (See Figure 2.13). Both event pools display similar current sheet normal and normal angle features. This is novel because magnetic reconnection is thought to occur predominantly in equatorial current sheets (*Voigt*, 1984). This observation is consistent with the picture that reconnection is an electron-scale process that, while disrupting plasma at much larger scales, is as likely to occur in tilted current sheets as equatorial ones.

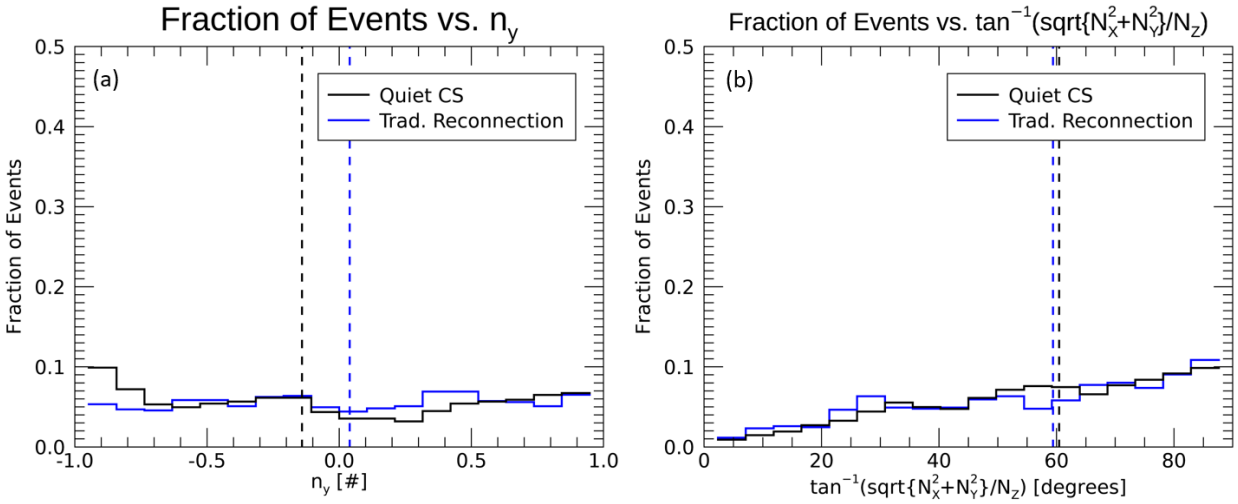

Figure 2.13: Histograms of (a) Y component of current sheet normal and (b) current sheet normal angle as calculated in (2.2), for quiet current sheets (black) and traditional, ion-coupled reconnection (blue). Dashed vertical lines indicate the median value of each parameter.

Next, we compare the plasma and field properties ($N_i, N_e, T_{e,||}, T_{e,\perp}, T_{i,||}, T_{i,\perp}$, and $E_{L,M,N}$) of quiet current sheets and reconnecting current sheets. Like in Section 2.2.4, we plot histograms of the maximum value of each parameter within each current sheet. We use the same bin size of 20 because both event pools are comparable in size.

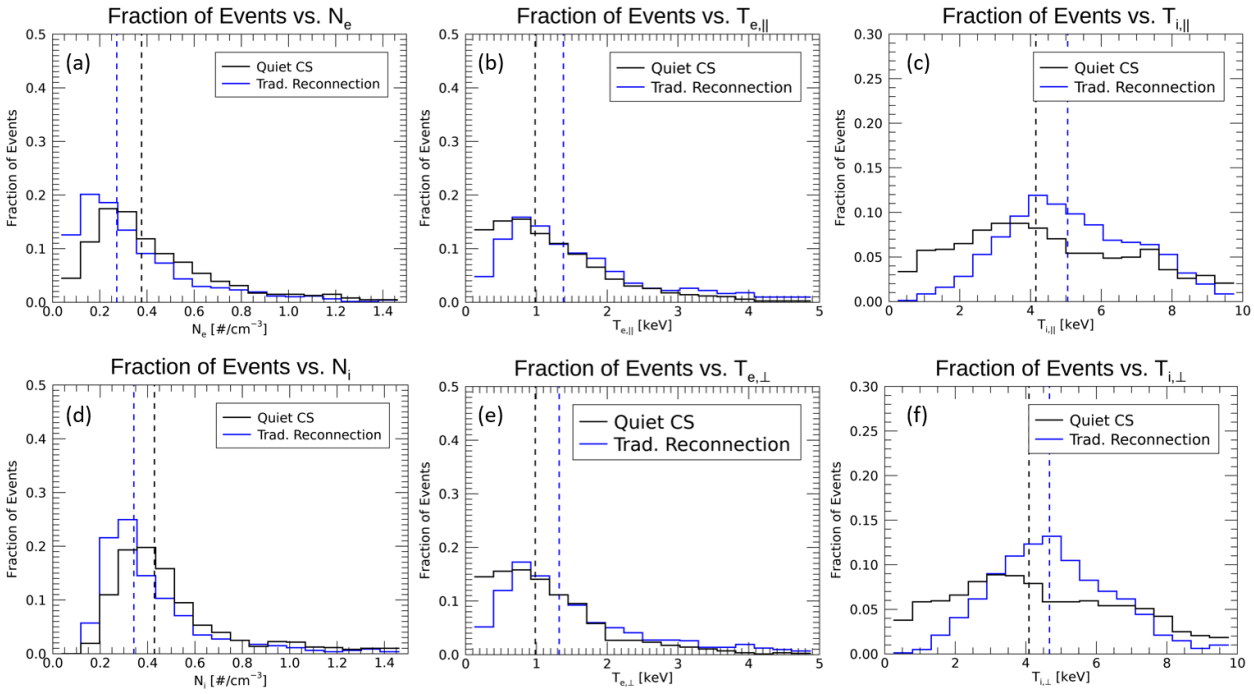

Figure 2.14: Histograms of the maximum value within the current sheet boundary of six plasma parameters extracted from our quiet current sheet events (black) and ion-coupled reconnection events (blue). (a) electron density, (b) ion density, (c) parallel electron temperature, (d) perpendicular electron temperature, (e) parallel ion temperature, and (f) perpendicular ion temperature. Vertical dashed lines indicate the median value.

As shown in Figure 2.14, the typical plasma density, electron temperature, and ion temperature of reconnecting current sheets are ≈ 0.3 $\#/cm^3$, 1.4 keV, and 5 keV, respectively. In Figure 2.15, we find E_L to peak at ≈ 3 mV/m, E_M to peak at ≈ 5 mV/m, and E_N to peak at ≈ 7 mV/m. Reconnecting current sheets feature lower plasma densities, higher plasma temperatures, and stronger electric fields than non-reconnecting current sheets. This is consistent with previous spacecraft observations and *Lu et al.*, 2022's PIC simulations, which will be discussed in further detail in Section 3.2.3. We interpret lower densities as the evacuation of plasma from the reconnection region, higher temperatures as heating of the plasma, and increased electric field as reconnection electric field.

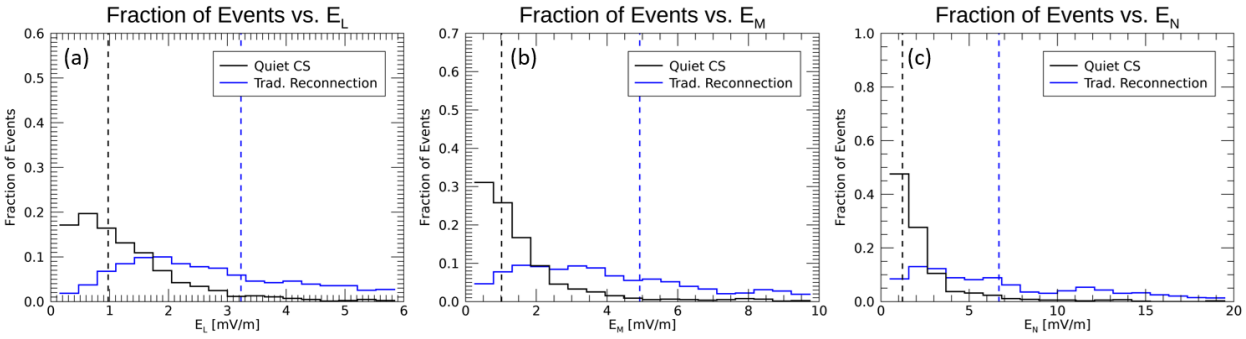

Figure 2.15: Histograms of the maximum electric field components extracted from our quiet current sheet events (black) and ion-coupled reconnection events (blue). (a) E_L, (b) E_M, (c) E_N. Vertical dashed lines indicate the median value.

2.3.3 Ion Outflow Direction vs. Distance Downtail

The near-Earth reconnection region of Earth's magnetotail is thought to be located at $\approx 25R_E$ downtail. We can use observed plasma outflows to determine whether the reconnection center is Earthward or tailward of the MMS spacecraft. Earthward (+X GSM) plasma outflow indicates that the reconnection center is tailward of MMS, and tailward (-X GSM) plasma outflow indicates that the reconnection center is Earthward of MMS. As such, a reveral in plasma outflow indicates that the reconnection center passed by MMS. If the flow reversal is Earthward-tailward, the reconnection center is moving Earthward, and if the reversal is tailward-Earthward, the reconnection center is moving tailward. An interesting question is whether MMS primarily observes reconnection centers that are Earthward or tailward of the spacecraft. In our event pool, we observe 77 tailward flows, 258 Earthward flows, and 73 flow reversals (See Figure 2.16).

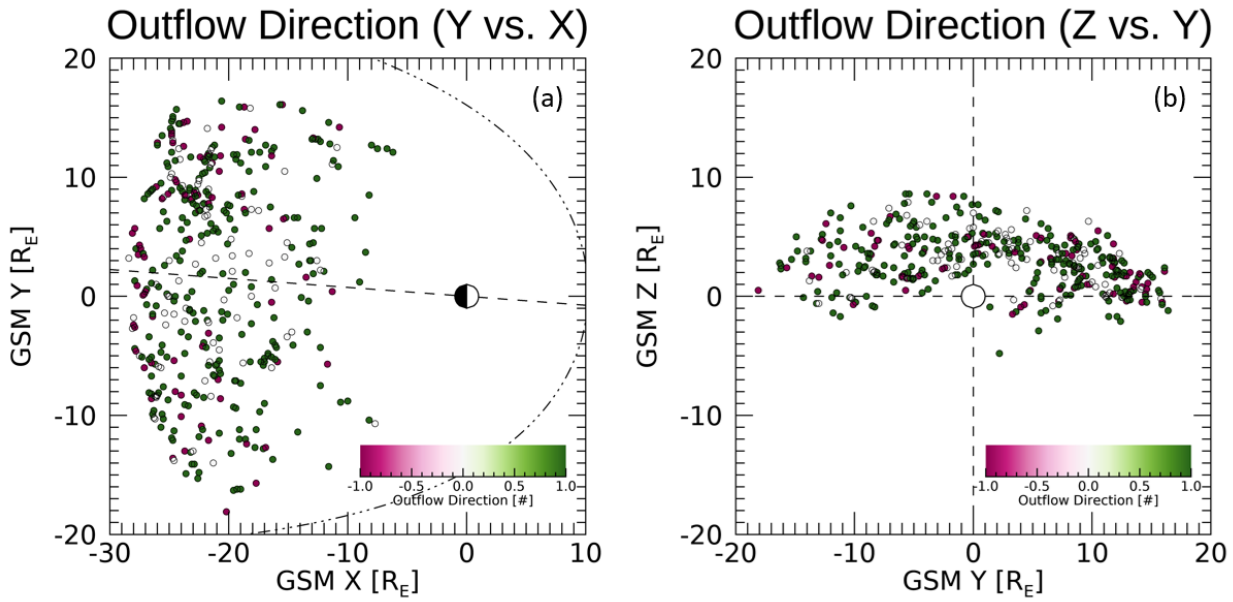

Figure 2.16: 2D cuts of ion-coupled reconnecting current sheet event locations in the (a) X-Y plane and (b) Y-Z plane. Green dots indicate earthward flows, pink dots indicate tailward flows, and white dots indicate flow reversals. All locations are plotted in GSM coordinates.

In Figure 2.16, green dots indicate Earthward flows, pink dots indicate tailward flows, and white dots indicate flow reversals. We find that MMS predominantly observes Earthward flows, indicating that the reconnection center is tailward of the spacecraft. We also find that 68 of 77 tailward flows occur at distances $> 20R_E$ and 42 of 77 tailward flows occur at $> 25R_E$. These findings are consistent with the previously hypothesized $25R_E$ location of the near-Earth magnetotail reconnection region.

2.3.4 Guide Field in Ion-Coupled Reconnection

In Earth's magnetotail, magnetic reconnection is primarily symmetric. In other words, antiparallel field lines (2D picture) are compressed together and reconnect. There is no significant guide field and ion and electron outflows and inflows are symmetric about their respective axes. As a result, it has been understood that traditional magnetotail reconnection

occurs without strong guide field. Hall magnetic field is common, but guide field is not. As a result, when performing a statistical study on traditional reconnection, one would expect little to no guide field reconnection.

To investigate this, we determine the guide field for each traditional reconnection event and find how it depends on location. To calculate guide field, I convert my reconnection events into Minimum Variance LMN coordinates (*Sonnerup and Scheible*, 1998). Once the events are in MVA coordinates, I determine the front and back edge of the plasma sheet by finding when B_L flattens out into a lobe-like field. This interval is then rounded to the nearest second on each end of the interval. Once I've determined the temporal width of each current sheet, I calculated the average B_M value over that interval. This method created guide field values for each "traditional" reconnection event. We visualize these values in two different ways. First, we calculate the raw guide field values on a color shading scale onto two different 2D projections (XY, YZ [GSM]). This is shown in Figure 2.17.

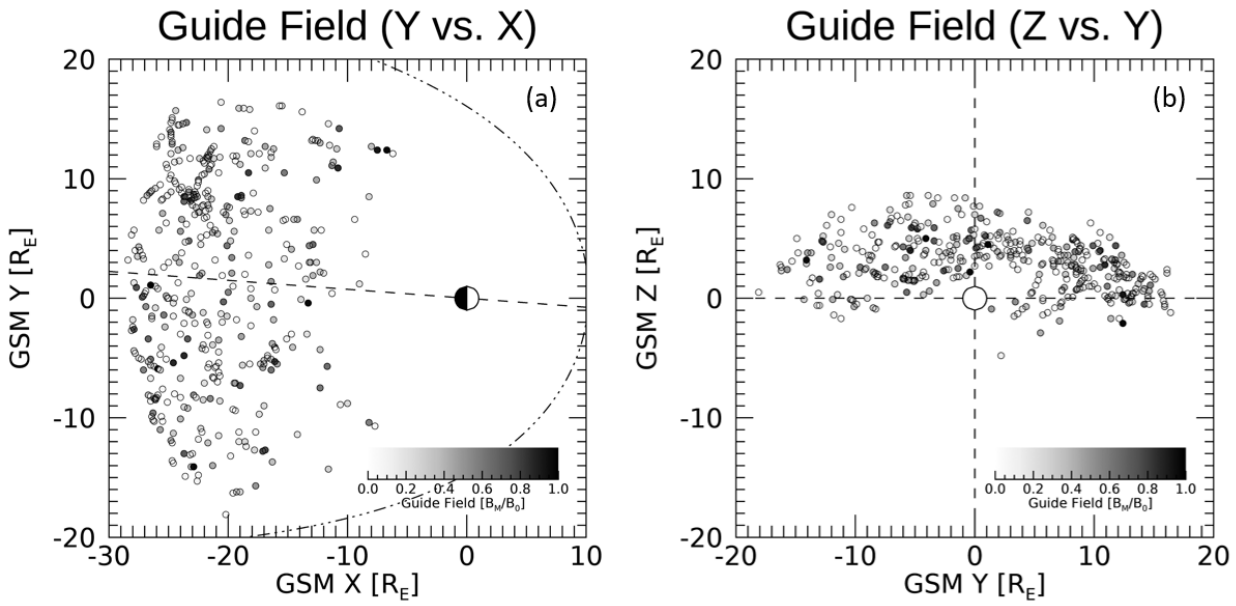

Figure 2.17: 2D cuts of ion-coupled reconnecting current sheet event locations in the (a) X-Y plane and (b) Y-Z plane. Color bar indicates guide field of each event. All locations are plotted in GSM coordinates.

We repeated this calculation for our quiet, non-reconnecting current sheets and compare the guide field features of the two populations. We find that our traditional reconnection events display lower guide fields than our quiet current sheets. This is consistent with the interpretation that reconnection in the magnetotail is primarily symmetric. The presence of guide field requires a more significant external driver (ex. stronger out of plane electric field) to demagnetize electrons and trigger reconnection. We note that there are a non-negligible number of events that feature high guide field, even if ion-coupled reconnection features statistically lower guide field than quiet, non-reconnecting current sheets.

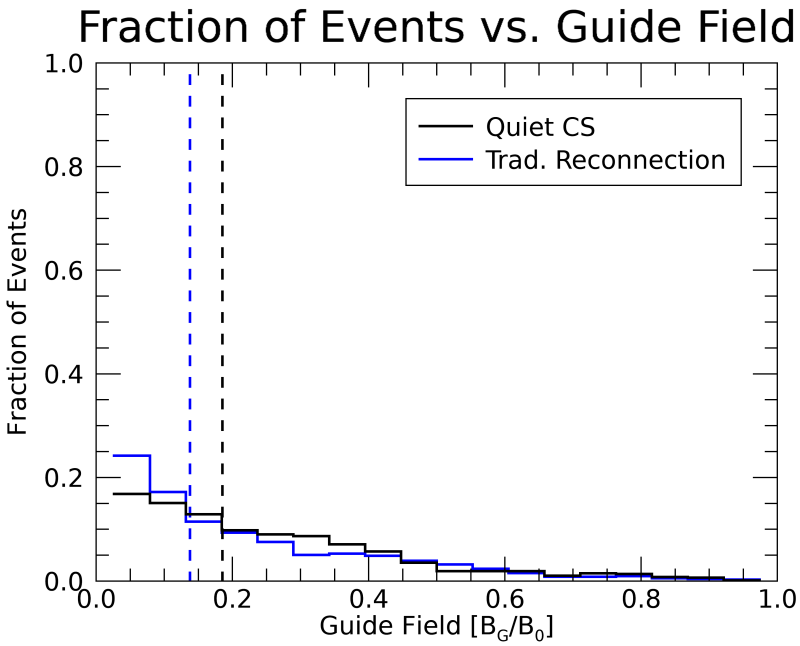

Figure 2.18: Histogram of the guide field for each quiet current sheet (black) and ion-coupled reconnection event (blue). Dashed vertical lines indicate the median value for each event pool.

2.3.5 Plasma Properties vs. Current Sheet Normal

The magnetotail current sheet often changes in orientation from a normal direction primarily in the Z direction to a normal direction primarily in the Y or X direction. This is primarily caused by flapping of the current sheet. Often, due to reconnection or external solar wind driving, current sheet flapping can propagate towards the flanks in the GSM Y directions. As MMS is approximately stationary, if a flapping current sheet passes over the spacecraft, the four-spacecraft timing method would yield a current sheet normal in the Y or X direction. Figure 2.13 shows that magnetic reconnection occurs in tilted current sheets at comparable frequencies as in equatorial current sheets. However, it is currently unclear whether local plasma conditions or plasma outflows during reconnection are affected by the tilt of the current sheet.

We investigate this by extracting background plasma conditions and plasma outflows from ion-coupled reconnection events as described in Section 4.8 and plotting them as a function of current sheet normal angle. In total, we extract the average and maximum values of v_{iL}/v_A, v_{eL}/v_A, T_i, and T_e over the current sheet boundary. When generating our outflow speed plots, we calculate and normalize to the local Alfvén speed. This allows each event to be compared approximately one to one. Our analysis of the maximum value of each plasma parameter vs. current sheet normal angle is shown in Figure 2.19.

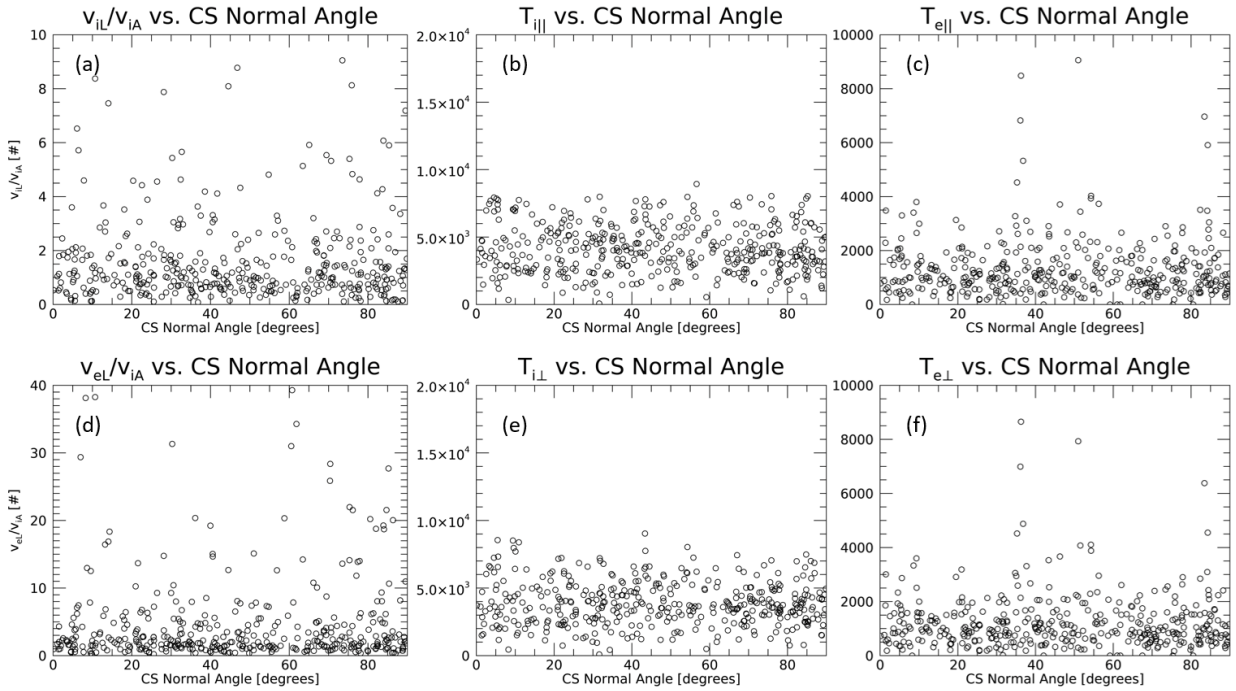

Figure 2.19: Plots of six plasma parameters vs. current sheet normal angle, as calculated by (2.2). (a) ion outflow speed normalized to the local Alfvén speed, (b) electron outflow speed normalized to the local Alfvén speed, (c) parallel ion temperature, (d) perpendicular ion temperature, (e) parallel electron temperature, (f) perpendicular electron temperature.

We do not find a significant relationship between ion or electron outflow speed and current sheet normal angle. We also do not find a significant relationship between electron or ion temperature and current sheet normal angle. We partially attribute this to high variance in outflow speed and temperature, even relative to local Alfvén speed, from event to event. We also attribute this to magnetotail physics. This result is consistent with the interpretation that reconnection outflows are largely unaffected by global scale flapping motions in Earth's magnetotail. We note that our traditional reconnection events do not account for distance from the reconnection region. As such, the change in reconnection outflow speed and ion/electron temperature far from the reconnection center may also contribute to the lack of significant change with current sheet tilt. Also, we note the strong cutoff in ion

temperatures at ≈ 8e3 keV. This differs from electron temperature and outflow speed, which featured more outliers and softer upper boundaries. The reason for this finding will be the subject of future research.

2.4 Statistical Survey of Ion Diffusion Regions

2.4.1 Observational Criteria of Ion Diffusion Regions

The statistics shown earlier in this Chapter do not distinguish between different reconnection regions. They include Ion Diffusion Regions, Electron Diffusion Regions, and bursty bulk flows. However, these reconnection observations display different features. I will outline the features of Ion Diffusion Regions (IDRs) in this section. Classifying a reconnection observation as an Ion Diffusion Region requires different criteria from the ones listed in Section 2.3.1. These criteria are also adopted in *Rogers et al.*, 2019.

First, MMS must observe a correlated reversal in B_z and V_ix, meaning both parameters reverse from negative to positive or vice versa. As shown in Figure 2.20, reversals in B_z and V_{ix} indicate that the reconnection center has passed over the spacecraft. The correlation of reversals is important, as diffusion region outflows in the +X GSM direction will universally occur in positive B_Z and outflows in the -X GSM direction will universally occur in negative B_Z. A reversal in v_{iX} is necessary to constrain the distance of the spacecraft from the diffusion region, as no flow reversal obfuscates the determination of distance of the spacecraft from the reconnection region. In this survey, we require v_{iX} reversals from -100 km/sec to 100 km/sec (or vice versa) and B_Z reversals from -2 nT to 2 nT (or vice versa). We classify B_Z and v_{iX} reversals as correlated if they share sign and if they occur within 30 seconds of each other.

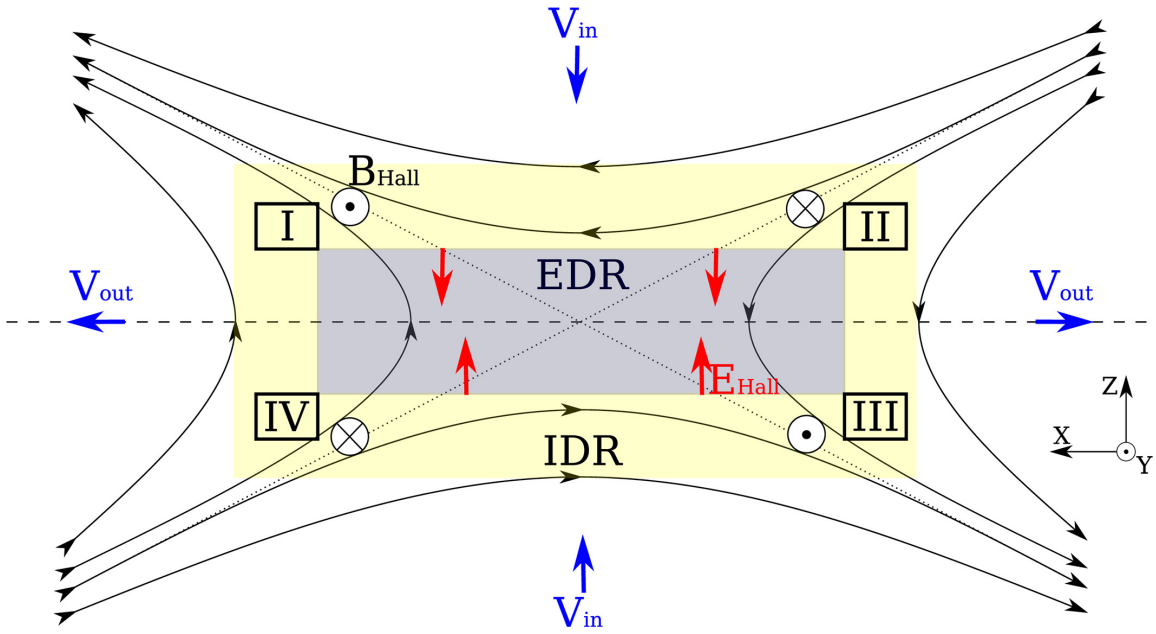

Figure 2.20: Cartoon Diagram of the Ion Diffusion Region including the four quadrants of quadrupolar Hall fields associated with the reconnection region.

Second, MMS must observe significant Hall magnetic and electric field signatures. Again, as shown in Figure 2.20, differentiated motion due to the demagnetization of ions and magnetization of electrons generates an electric field in the Z direction and a magnetic field in Y direction due to the Hall effect. These fields are strong and observable by spacecraft instruments. We classify significant Hall fields as $|E_Z| > 5mV/m$ and $|B_Y| > 2nT$, consistent with previous IDR identification work (*Rogers et al.*, 2019). These values must occur within 15 seconds in either direction of the reconnection observation.

Third, MMS must observe significant electric field signatures at the current sheet center. In *Eastwood et al.*, 2010, IDRs universally displayed elevated electric field strength, consistently exceeding 10 mV/m. To support the presence of Hall electric field, we require electric field strength exceeding 10 mV/m to conform with *Eastwood et al.*, 2010's findings. Like for Hall fields, this value must be observed within 15 seconds in either direction of the reconnection observation.

Lastly, we require that the radius of curvature of the reconnecting magnetic field dips below the ion gyroradius to more directly indicate that the ions are demagnetized. By definition, the IDR features a magnetic field whose radius of curvature drops below the gyroradius of ions, resulting in demagnetization of ions. We calculate the radius of magnetic field curvature as follows:

$$R_C = \frac{1}{|(\hat{b} \cdot \nabla)\hat{b}|} \tag{2.3}$$

where $\hat{b} \equiv \mathbf{B}/|\mathbf{B}|$. We outline our methodology for calculating magnetic field curvature and radius of curvature in Section A.1.4. To meet this criterion, we require that $R_C < \rho_{ci}$ simultaneously with the v_{iX} reversal. There may also be counter-streaming electrons in the L direction.

We note that these criteria does not account for Z-dominant crossings of the IDR and heavily favors MMS moving through the reconnection region in the +/- X GSM direction. Identifying an IDR versus a bursty bulk flow in a Z-dominant crossing is difficult because both crossings display elevated electric fields, B_Z reversals, and radius of curvature below the ion gyroradius. In other words, without seeing a reversal in v_{iX}, it is difficult to precisely determine the distance of the spacecraft from the reconnection center. We also note that we do not require a reversal of B_X to classify an event as an IDR. If an event meets the criteria outlined in this section, but does not reverse in B_X, this indicates a partial crossing, and is still useful for extracting local plasma and field conditions to compare to other current sheet populations.

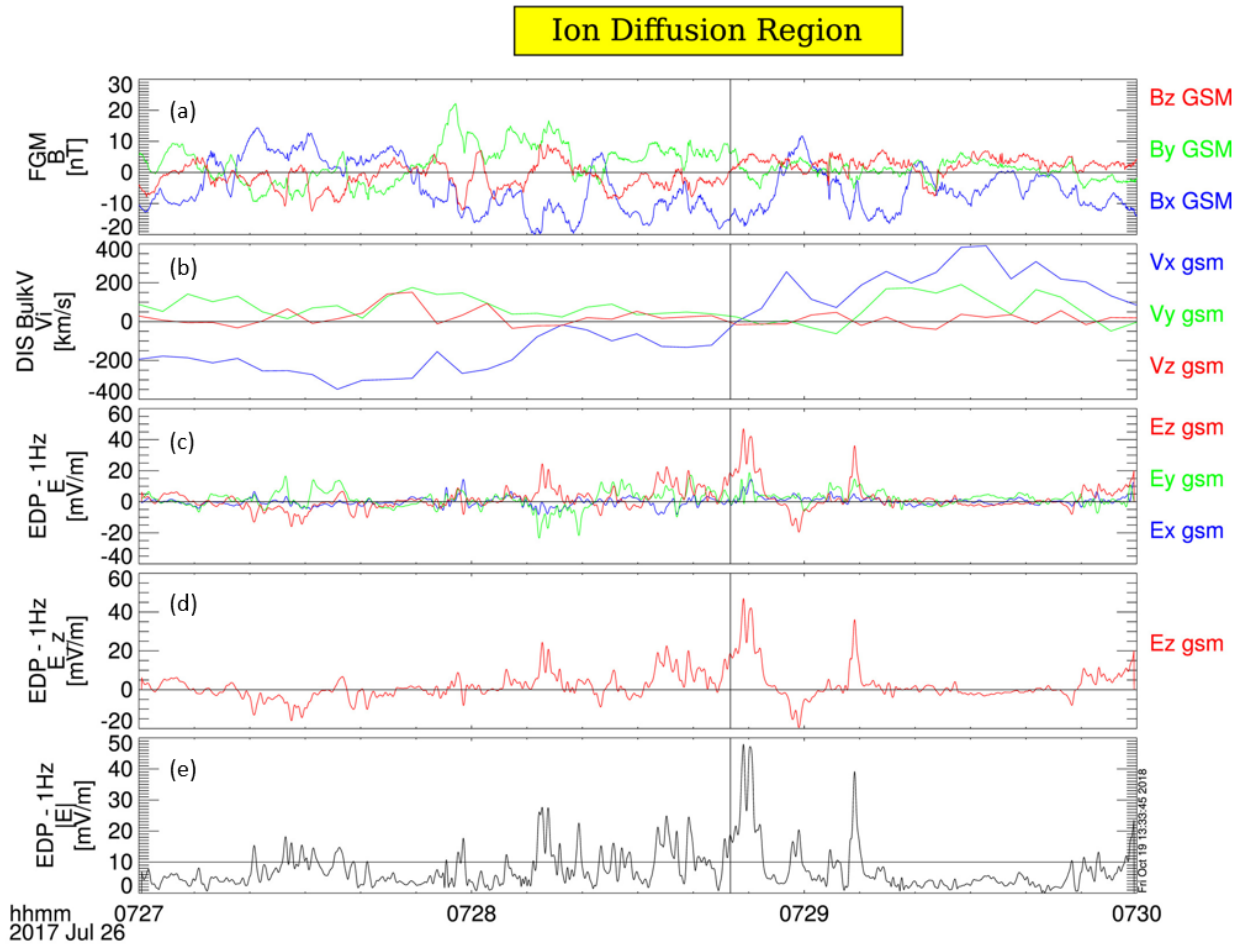

Figure 2.21: One sample Ion Diffusion Region event from 7/26/17, 07:27-30 reported by *Rogers et al.*, 2019. (a) Magnetic field (B_x: blue, B_y: green, B_z: red), (b) ion bulk flow velocity, (c) electric field, (d) E_z, (e) $E_{||}$.

In summary, we use the following criteria to identify IDRs in MMS data: 1. correlated B_Z and v_{iX} reversals, 2. significant Hall electric and magnetic fields, 3. strong electric field magnitude, and 4. magnetic field radius of curvature (R_C) less than the ion gyroradius.

2.4.2 Data Collection & Dataset Description

Identically to our quiet current sheet survey, we performed a survey over six MMS magnetotail seasons (Phase 2B: June 15 - August 31 2017, Phase 3B: June 15 - August 31 2018, Phase 4B: July 1 - September 15 2019, Phase 5B: July 1 - September 15 2020, Phase 6B: July 15 - September 30 2021, Phase 7B: July 15 - September 30 2022) looking for Ion Diffusion Regions. Using the criteria above and in the intervals described above, MMS identified 49 IDRs. Dates, time intervals, and locations of these events are shown in Section A.2.3. These events are not purely a subset of our ion-coupled reconnection dataset. They require different criteria from the prior two current sheet types.

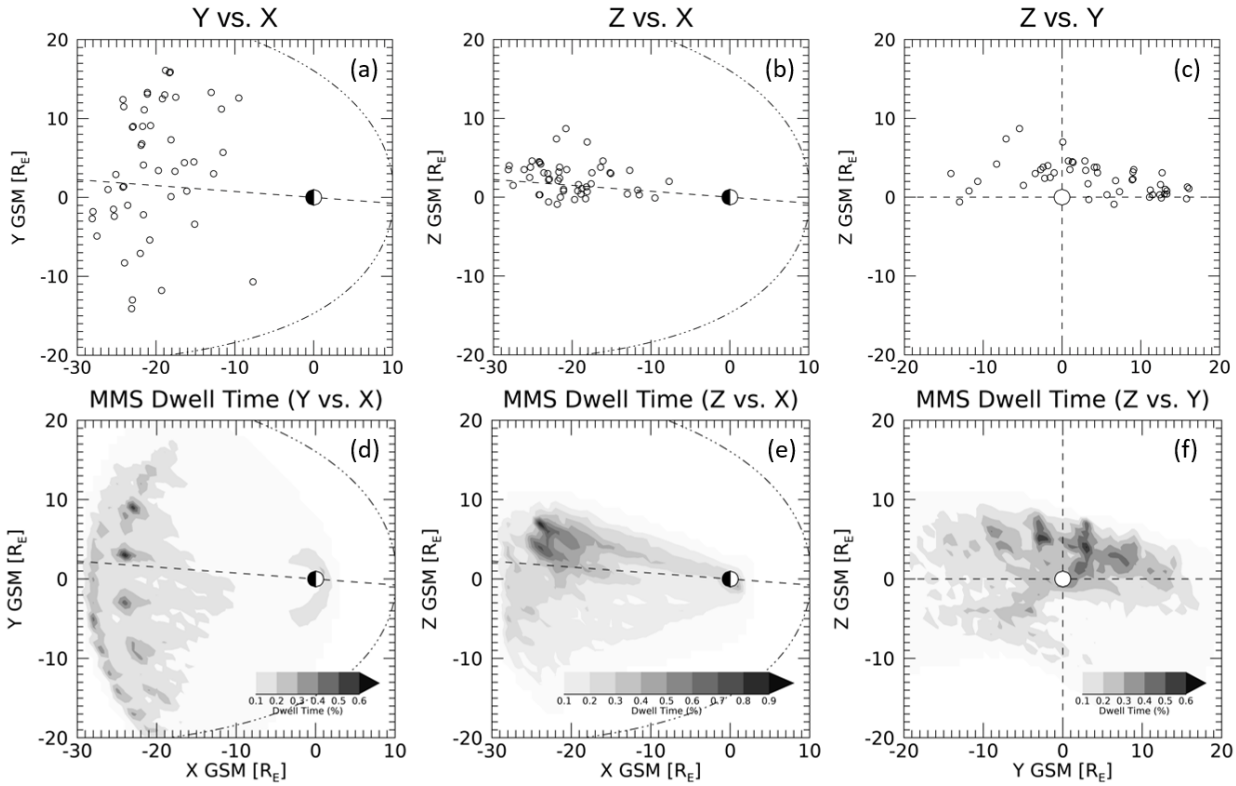

Figure 2.22: 2D cuts of Ion Diffusion Region event locations in the (a) X-Y plane, (b) X-Z, and (c) Y-Z plane. MMS dwell time form 2017-2022 in the (d) X-Y plane, (e) X-Z, and (f) Y-Z plane. All locations are plotted in GSM coordinates.

Figure 2.22 shows 2D cuts of IDR location in GSM. MMS observes 15 events in the dawn sector and 34 events in the dusk sector, 43 events in the North sector and 6 events in the South sector, 35 events farther than $20R_E$, and 14 events closer than $20R_E$. Similar to our ion-coupled reconnection pool, more IDRs appear in the dusk sector than the dawn sector, and IDRs are heavily biased towards the North sector. We note that the observed dawn-dusk asymmetry is more pronounced in IDRs than in the overall ion-coupled reconnection events, while the bias towards the North sector is comparable between the two event pools.

Next, we calculate the current sheet normal from our events (see Section A.2.3 for exact values). Among our IDRs, 18 have primarily X normals, 17 have primarily Y normals, and 13 have primarily Z normals. Similar to our previous event pools, IDRs are split in normal orientation. We isolate the Y component of current sheet normal as we did for previous event pools (see Figure 2.23). Our IDR events exhibit a significant positive bias in current sheet normal (22 duskward events with positive Y normal, 11 duskward events with negative Y normal, 11 dawnward events with positive Y normal, 4 dawnward events with negative Y normal). Particularly in the dusk sector, current sheets typically move away from the midnight sector towards the dusk flank. We interpret that 15 events in the dawn sector is insufficient to determine whether the apparent bias towards positive Y normal is the result of magnetotail physics.

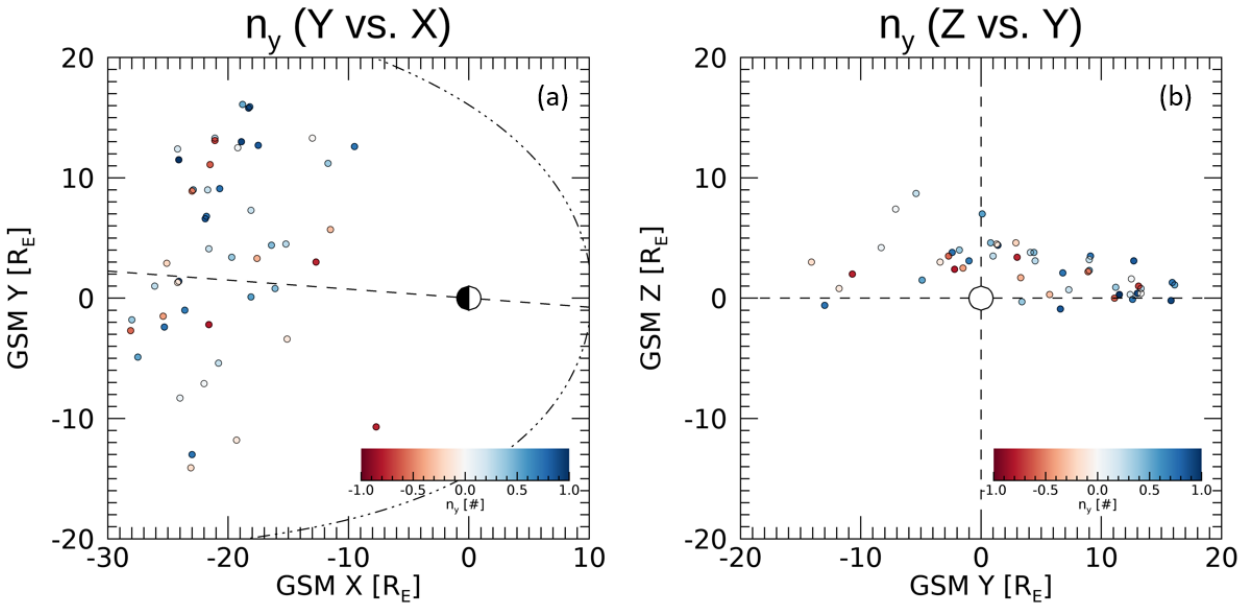

Figure 2.23: 2D cuts of ion-coupled reconnecting current sheet event locations in the (a) X-Y plane and (b) Y-Z plane. Color bar indicates Y component of the current sheet normal. All locations are plotted in GSM coordinates.

We then compare the Y normal and current sheet normal angle of non-reconnecting current sheets, reconnecting current sheets, and IDRs (see Figure 2.24). The significant bias towards positive Y normal in the dusk sector is visible in our IDR event pool, especially when compared to non-reconnecting current sheets and ion-coupled reconnecting current sheet. However, the occurrence of IDRs in tilted versus equatorial current sheets remains comparable to the other event pools. We interpret that IDRs' significant bias towards positive Y normal is a result of a significant bias in event location towards the dusk sector.

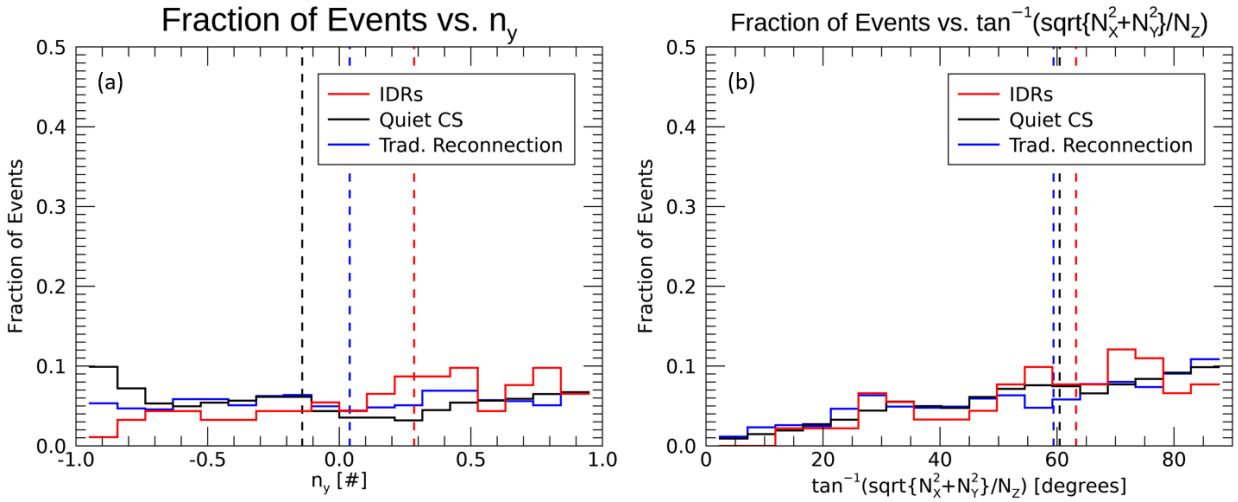

Figure 2.24: Histograms of (a) Y component of current sheet normal and (b) current sheet normal angle as calculated in (2.2), for quiet current sheets (black), traditional, ion-coupled reconnection (blue), and IDRs (red). Dashed vertical lines indicate the median value of each parameter.

Next, we compare the plasma and field properties ($N_i, N_e, T_{e,||}, T_{e,\perp}, T_{i,||}, T_{i,\perp}, and E_{L,M,N}$) of quiet current sheets, reconnecting current sheets, and IDRs. Although our IDR pool is less than 50 events, we plot histograms of the maximum value of each parameter using 20 overlapping bins as described in Section 2.2.4. The overlapping bins remedy the low event number, and the unaffected median line still provides significant insight about the local plasma conditions inside IDRs versus quiert current sheets and ion-coupled reconnection.

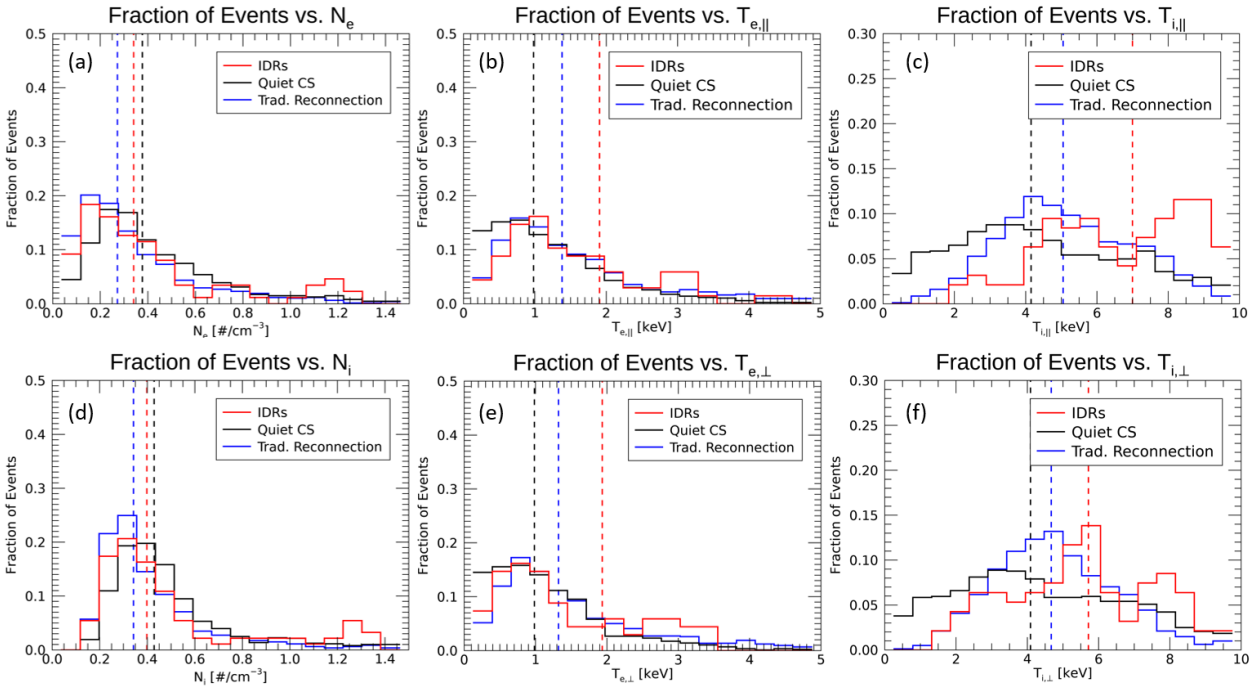

Figure 2.25: Histograms of the maximum value within the current sheet boundary of six plasma parameters extracted from our quiet current sheet events (black), ion-coupled reconnection events (blue), and IDRs (red). (a) electron density, (b) ion density, (c) parallel electron temperature, (d) perpendicular electron temperature, (e) parallel ion temperature, and (f) perpendicular ion temperature. Vertical dashed lines indicate the median value.

As shown in Figure 2.25, MMS observes the following plasma density, electron temperature, and ion temperature of IDRs: ≈ 0.3 $/cm3$, 1.4 keV, and 5 keV, respectively. In Figure 2.26, we find E_L to peak at ≈ 3 mV/m, E_M to peak at ≈ 5 mV/m, and E_N to peak at ≈ 7 mV/m. We find comparable plasma density between each of the three current sheet structures. This is unexpected for IDR observations, as one might expect plasma to evacuate the reconnection region and produce a wake of plasma close to the reconnection center. Next, we find that the electron and ion temperature of IDRs are significantly greater than those of quiet current sheets and traditional reconnection. This indicates that, during MMS's IDR observations, it is primarily observing heated and energized plasma, while when observing

reconnection farther from the current sheet center, it observes both energized plasma and ambient, unaffected plasma. Lastly, we find significantly stronger electric fields in IDRs than in either ion-coupled reconnection or quiet current sheets (we note that the x axes of Figure 2.26 are significantly larger than Figure 2.15 and Figure 2.9). These IDR features are also consistent with *Lu et al.*, 2022's PIC simulations, which reports plasma evacuation from the diffusion region, significant plasma heating close to the reconnection center, and significant Hall electric field inside the diffusion region. We note that the plasma density comparison of IDRs may not be statistically significant, given the smaller event pool of IDRs.

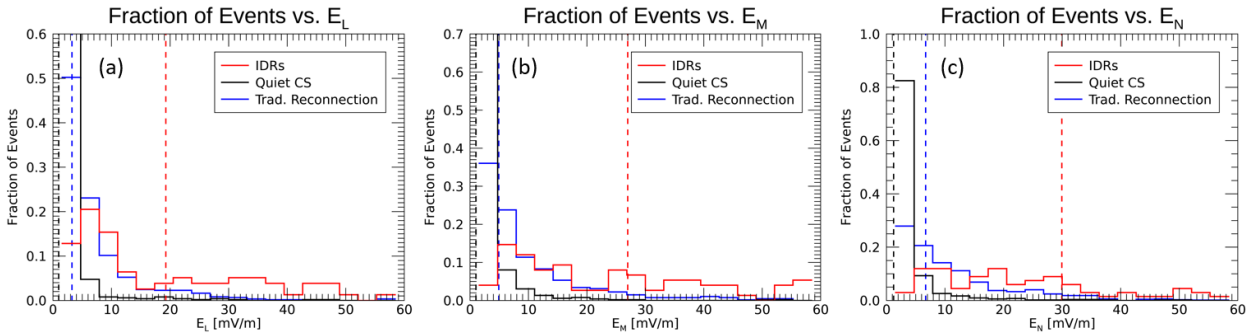

Figure 2.26: Histograms of the maximum electric field components extracted from our quiet current sheet events (black), ion-coupled reconnection events (blue), and IDRs (red). (a) E_L, (b) E_M, (c) E_N. Vertical dashed lines indicate the median value.

2.4.3 Guide Field

Similar to our traditional, ion-coupled reconnection events, we expect little to no guide field in our IDR events. We calculate guide field identically to our ion-coupled reconnecting and quiet current sheets, as described in Section 2.3.4. In Figure 2.27, we compare the guide field of the three current sheet structures. We find that traditional, ion-coupled reconnection presents lower guide field than quiet current sheets, and IDRs display the lowest average guide field of the three current sheet types. This is consistent with the picture that ion-coupled reconnection in Earth's magnetotail is primarily symmetric, without significant shear. We

expect non-reconnecting current sheets to manifest in a wider variety of ways than IDRs, which rely on field antisymmetry to maximize outflow energization.

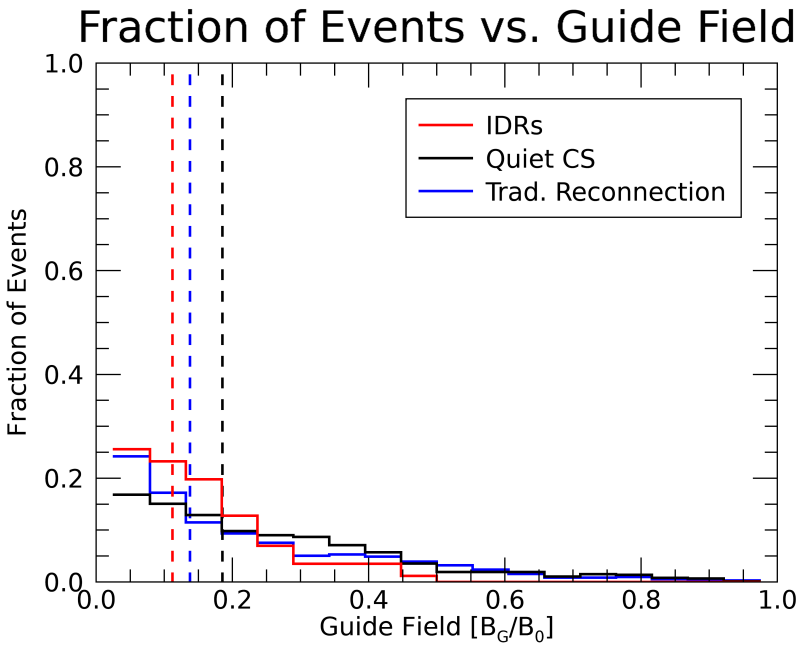

Figure 2.27: Histogram of the guide field associated with our quiet current sheets (black), ion-coupled reconnection (blue), and IDR (red) events. Dashed vertical lines indicate the median value for each event pool.

2.4.4 Plasma Properties vs. Current Sheet Normal

We repeat our analysis from Section 2.3.5 with our IDR dataset. As with our traditional reconnection set, we do not find significant relationships between outflow speed, temperature, and current sheet normal angle. This analysis rules out the interpretation of distance from the reconnection center affecting plasma temperatures and speeds, as MMS passed over the reconnection region for each event shown in Figure 2.28. Also, we note two things: that IDRs feature reversals in v_{iL} which can result in more muted outflow magnitudes, and that IDRs do not necessarily feature reversals in B_L, making the current sheet interval more difficult

to interpret. We posit that these factors contribute to the lack of significant correlations. Although the event number is smaller than the ≈ 400 event pool of traditional reconnection events, we note that the upper boundary of the ion temperature increases from ≈ 8e3 keV to 9e3 or 1e4 keV. The other boundaries are consistent with that of traditional reconnection.

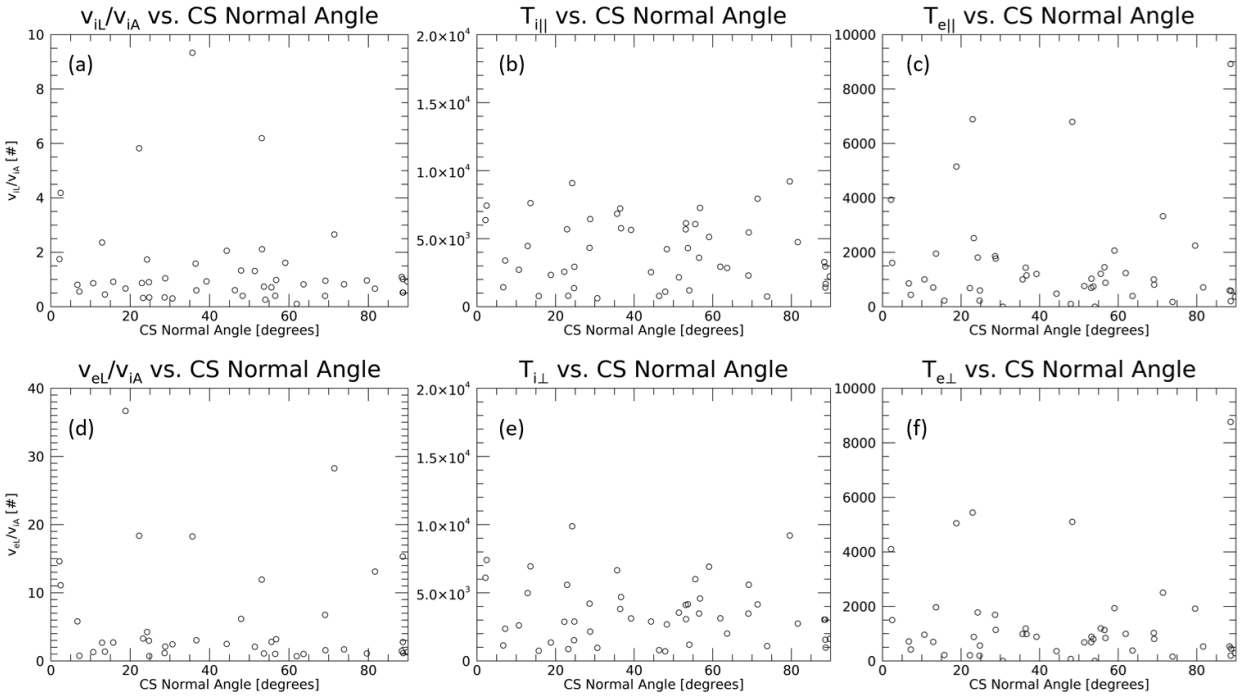

Figure 2.28: Plots of six plasma parameters vs. current sheet normal angle, as calculated by (2.2), for our IDR events. (a) ion outflow speed normalized to the local Alfvén speed, (b) electron outflow speed normalized to the local Alfvén speed, (c) parallel ion temperature, (d) perpendicular ion temperature, (e) parallel electron temperature, (f) perpendicular electron temperature.

2.4.5 Solar Wind Driving & AE Index Response

Lastly, we investigate the solar wind driving properties of IDRs and compare them to those of traditional reconnection and non-reconnecting current sheets. Identically to my precious event pools, I calculated the maximum, minimum, and average values of the follow-

ing parameters: IMF By/Bz, SW Vtot/Vx/Vy/Vz/Ni/DP. Specifically, I found the average/maximum/minimum value of each parameter in the hour preceding the traditional reconnection observation and associated it with its respective event. IDRs display enhanced SWDP, southward IMF B_Z, and solar wind v_x when compared to both non-reconnecting current sheets and traditional reconnection. Conversely, solar wind density, IMF B_Y, solar wind v_y, and solar wind v_z remain unaffected (see Figure 2.29). We attribute the additional preceding solar wind signatures of IDRs to our method of identification. We require an IDR observation to exhibit a v_{ix} flow reversal, which requires the reconnection region to be moving either in the Earthward or tailward direction. This is a prominent feature in substorm onset. Previous work (*Nishida and Cowley*, 1998; *Nagai et al.*, 2005) has found that statistically significant IMF B_Z reversals and elevated solar wind speeds are present less than an hour prior to substorm onset. Our findings are consistent with these previous studies.

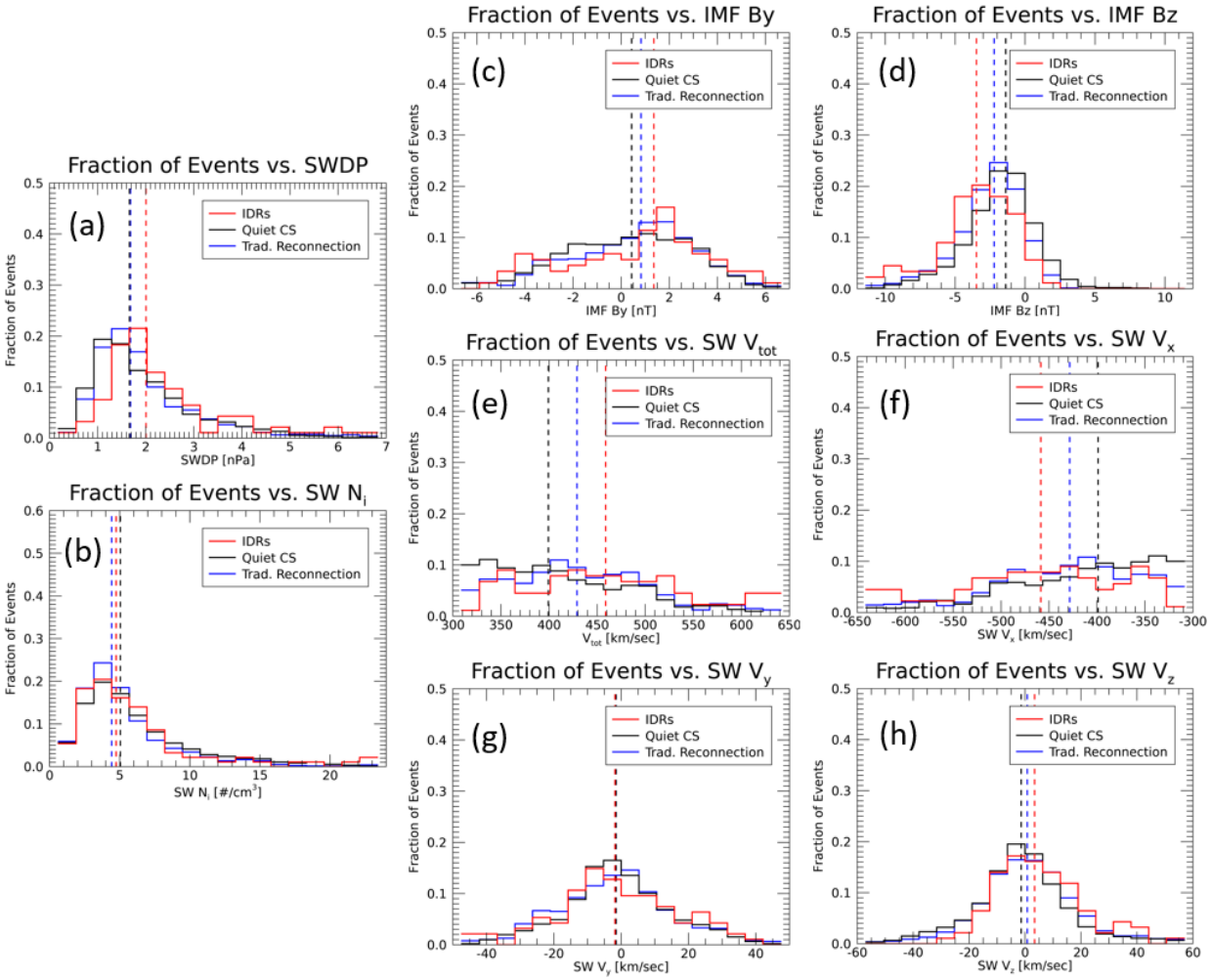

Figure 2.29: Histograms (with overlapping bins) of various solar wind properties in the hour prior to each quiet current sheet (black), IDR (red), and traditional reconnection (blue) observations. Average (a) Solar wind dynamic pressure, (b) solar wind density, (c) IMF By, (d) Solar wind vtot, (e) Solar wind vy, (f) IMF Bz , (g) Solar wind vx, and (h) Solar wind vz for the hour prior to each current sheet observation.

2.5 Conclusions & Interpretations

In this chapter, we reported MMS observations of 476 quiet non-reconnecting current sheets, 408 ion-coupled reconnecting current sheets, and 49 Ion Diffusion Regions (IDRs) in six magnetotail seasons from 2017-2022. Ion-coupled reconnection events and IDRs were significantly biased towards the dusk sector, while quiet current sheets were evenly distributed across the magnetotail. None of the three current sheet types occurred more frequently in equatorial current sheets than tilted current sheets, indicating that reconnection is not more likely to occur in equatorial current sheets than tilted ones. We did not find a significant relationship between ambient plasma properties of reconnection events and current sheet tilt. Most ion-coupled reconnection events featured Earthward flows, indicating that the reconnection center was tailward of the spacecraft, and most ion-coupled reconnection events that did feature tailward flows were located $> 20R_E$ downtail. IDRs displayed significantly lower guide field than quiet current sheets, while the guide field properties of ion-coupled reconnection events were unclear. Ambient plasma density did not exhibit significant change between the three current sheet types. IDRs featured significantly elevated ion and electron temperatures compared to ion-coupled reconnection and quiet current sheet events. Also, IDRs featured significantly greater electric fields than ion-coupled reconnection events, which featured significantly greater electric fields than quiet current sheets. IDRs and ion-coupled reconnection events featured significantly faster solar wind speeds and stronger southward IMF B_z than quiet current sheets.

The occurrence rate of earthward/tailward flows in reconnection events is consistent with the near-Earth reconnection point being located $\approx$ 25-30 R_E downtail (*Ueno et al.*, 1999). Elevated electron/ion temperatures, electric field, solar wind speed, Southward IMF B_Z, and reduced guide field of IDRs are consistent with simulation work from *Lu et al.*, 2022. These are also consistent with Hall fields, dayside solar wind driving, energization/heating of the plasma, and reduced shear (*Vaivads et al.*, 2004) expected in IDR events.

CHAPTER 3

Electron-Only Flux Rope Erosion, Electron-Only Onset of Reconnection, & Electron-Only Reconnection Criteria

In Earth's magnetotail, several mechanisms have been proposed to generate electron-only reconnection. First, Earthward-traveling plasmoids generated by multiple reconnecting X-lines can reconnect with dipolarized tail field (*Vogiatzis et al.*, 2011) and form a current sheet whose aspect ratio is ripe for electron-only reconnection (*Man et al.*, 2018, 2020a). We call this process "electron-only flux rope erosion". Second, during the early stages of traditional reconnection, a short time interval of electron-tearing occurs where only electrons are energized (*Wang et al.*, 2020b; *Lu et al.*, 2020; *Wang et al.*, 2018). We call this process "electron-only onset of reconnection." Lastly, traditional magnetotail reconnection during storm times has been shown to generate a turbulent outflow region. This turbulence can entangle magnetic field lines and generate sub-ion scale reconnection that violates the frozen-in condition and forms electron-only outflow jets (*Lapenta et al.*, 2018; *Vega et al.*, 2020; *Zhou et al.*, 2017). We call this process "turbulent secondary reconnection." Previous work has established a transition from electron-only onset of reconnection to an ion-embedded EDR by ordering three electron-only observations in time (*Hubbert et al.*, 2021a). However, the pre-

vious lack of event statistics has made it difficult for the community to observationally verify its generating mechanisms and properties in Earth's magnetotail. We begin by examining reported examples of both processes observed by MMS in the near-Earth magnetotail.

3.1 Event Study of Electron-Only Flux Rope Erosion in Earth's Magnetotail

In this section, we showcase multiple examples of electron-only outflows during reconnection generated by the collisions of magnetotail flux ropes and Earth's dipolarized field, which we name electron-only flux rope erosion.

3.1.1 Magnetic Flux Ropes

Magnetic Flux Ropes (flux ropes, or MFRs) are self-balanced, force-balanced magnetic structures that occur in various regions where space plasma is prevalent (*Argall et al.*, 2018). These structures are defined by a balance between the outward pressure gradient force and the inward $\mathbf{j} \times \mathbf{b}$ force associated with the curvature of the field. Figure 3.1 shows the structure of a flux rope, along with the balance of the pressure gradient force (green arrows) and magnetic curvature force (blue arrows). We establish a right-handed coordinate system that eases understanding of spacecraft measurements of flux rope crossings with three orthogonal axes: P, Q, and R. R is directed in the axial direction of the flux rope, Q is directed along the transverse crossing of the rope by the spacecraft, and P completes the coordinate system. The Q direction is typically calculated using four-spacecraft timing.

In Earth's magnetotail, flux ropes are typically generated from single or multiple X line reconnection due to the tearing instability (See Section 1.1.5). Earthward propagating flux ropes have been shown to reconnect with Earth's dipole field and dissipate the energy stored by the coiled field (*Huang et al.*, 1987). This dissipation has been speculated to trigger magnetospheric substorms and lead to dipolarization front structures, which are extremely

common in the near-Earth magnetotail (*Runov et al.*, 2009).

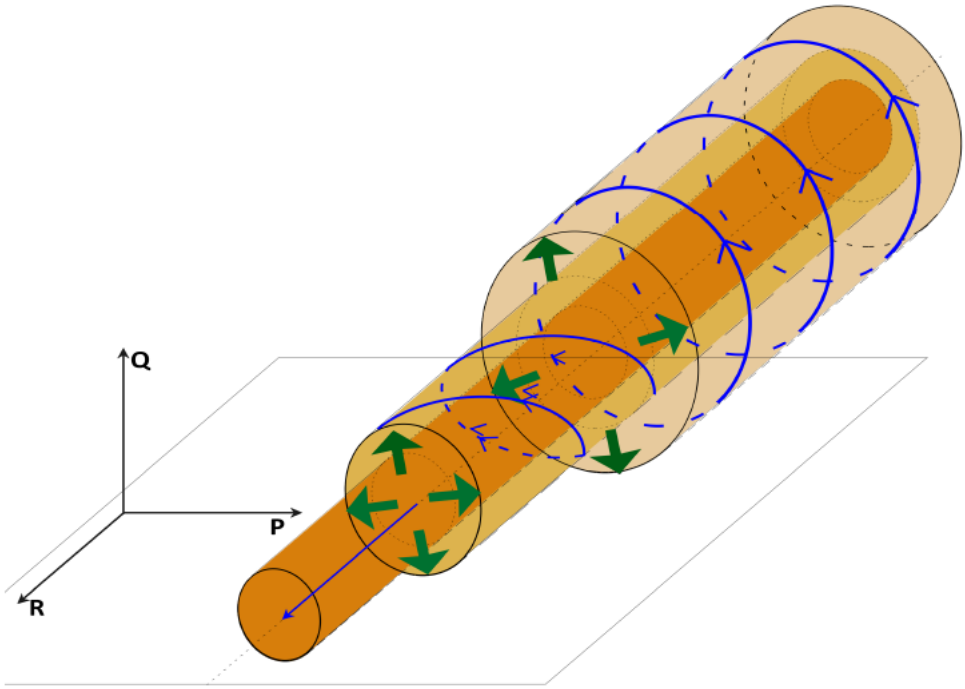

Figure 3.1: 3D diagram of the structure, dictating forces, and coordinate system associated with a flux rope (*Zhao*, 2019). The orange cylinder is the surface of the flux rope, blue lines are magnetic field lines, and green arrows indicate the direction of the pressure gradient force. P, Q, and R are physically intuitive axes used to describe the rope's properties.

3.1.2 8/14/17 Event

This event was first reported in *Man et al.*, 2018. On August 14, 2017, from 18:56:30 - 18:56:45, MMS was located at [X: -18.5, Y: 15.5, Z: 1.3] R_E (GSM) and grazed the near-Earth plasma sheet from the Northern lobe (Figure 3.2). The local coordinate system is: L: [0.2061, -0.2128, 0.9551], M: [0.0715, -0.9702, -0.2316], N: [0.9759, 0.1160, -0.1847] with respect to GSM coordinates. The N direction is the current sheet normal direction calculated using four-spacecraft timing, the L direction is the maximum variance direction (tangential

to the current sheet), and the M-component is $\mathbf{N} \times \mathbf{L}$. We note that the L direction is primarily oriented in the GSM Z direction, while the N direction is primarily oriented in the GSM X direction. This indicates that the current sheet is vertically tilted from an ambient, equatorial current sheet by approximately 90°. The current sheet speed in the normal direction (N) was approximately 240 km/sec, the current sheet was observed for $\approx$ 0.4 sec, meaning that the current sheet thickness was $\approx$ 100 km, or 12 d_e. The upstream plasma density was $\approx 0.4\ \#/cm^3$. Using a heuristic reconnection rate of 0.1 (*Liu et al.*, 2017), the length of of the current sheet is $\approx$ 1000 km, or $\approx$ 120 d_e (2.8 d_i). Energy conversion is calculated using $J \cdot E'$ ($E' = E + v_e \times B$), where J is the current density calculated using the FGM curlometer method ($J = (\nabla \times B)/\mu_0$) and E' uses the four-spacecraft averages of EDP electric field, FPI v_e, and FGM magnetic field.

This event displays many of the signatures used to identify the electron-only nature of *Phan et al.*, 2018's event. Specifically, MMS observed a B_L reversal and B_{tot} minimum consistent with a current sheet crossing (Figure 3.2a,b), super-Alfvénic electron outflows (Figure 3.2d), strong currents (Figure 3.2e), positive $J \cdot E'$ (Figure 3.2g), and a distinct lack of ion Alfvénic ion outflows (Figure 3.2c). Using these signatures, along with the significant tilt in the current sheet, *Man et al.*, 2018 reported a primarily N-directed MMS crossing of an Earthward moving flux rope reconnecting with Earth's dipole field without an ion jet (LEFT, Figure 3.2a,b). They speculate that ion jets were not present for one of two reaons: 1. MMS crossed the current sheet directly through the diffusion region where ion bulk speeds are sub-Alfvénic, or 2. the length of the current sheet was less than the threshold of $\approx$ 10 d_i needed for ion coupling.

However, we note two significant differences between this event (See Figure 3.2) and *Phan et al.*, 2018's event. First, there is little to no guide field (< 0.1) present in this event, which is notable because strong guide field (> 0.3) is thought to further suppress ion outflow in turbulent reconnection (*Horiuchi et al.*, 2014). Second, the four spacecraft MMS constellation did not observe oppositely directed electron jets, meaning they did not

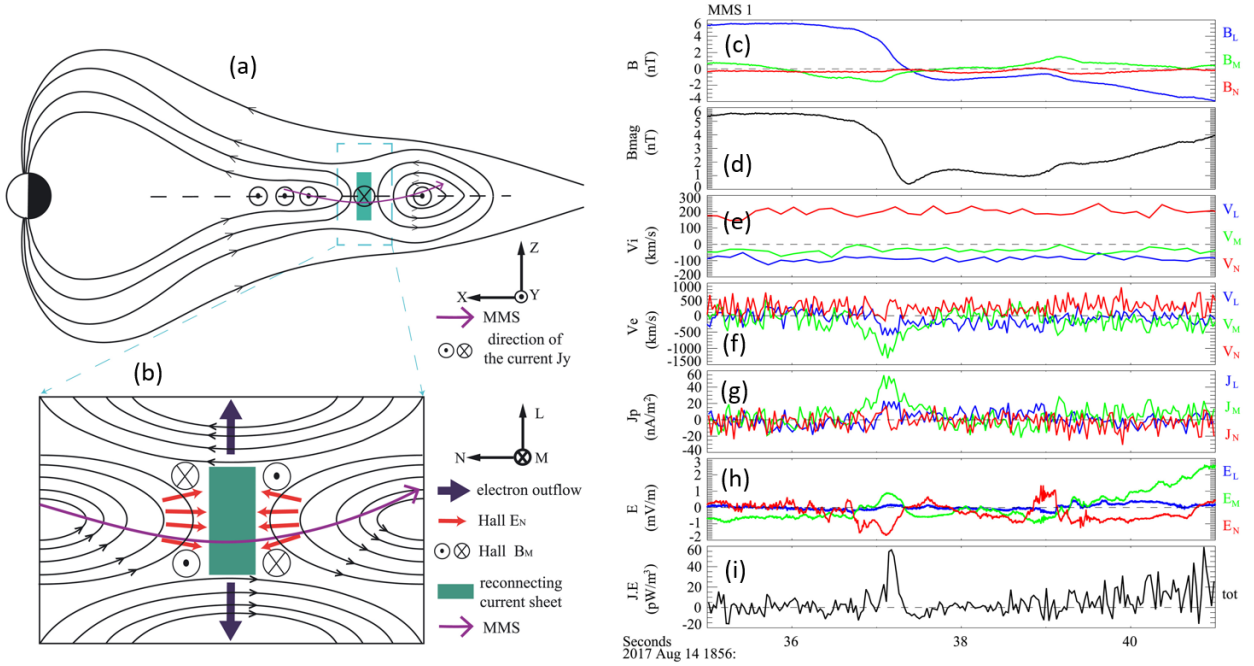

Figure 3.2: LEFT: Schematics of MMS trajectory across the reconnection region between the MFR and the geomagnetic field. (a) large-scale view in the x-z plane in GSM coordinates. (b) Zoomed-in view of the reconnection diffusion region in the L-N plane in LMN coordinate system. The LMN coordinate system is defined in the main text. RIGHT: MMS1 observations of the reconnection diffusion region between 18:56:35 and 18:56:41 UT. (c) Three components of magnetic field; (d) magnetic field strength; (e) ion bulk velocity; (f) electron bulk velocity; (g) electric current density calculated from plasma moments: $J = n_e q(v_i - v_e)$, where ne is the electron number density, q is the unit charge, and V_i and V_e are the ion and electron bulk velocity, respectively; (h) three components of electric field; and (i) energy conversion rate $J \cdot E'$. Vectors are displayed in the LMN coordinate system (*Man et al.*, 2018).

straddle the X-point like in *Phan et al.*, 2018's event. This difference is critical because, in Earth's magnetotail and magnetosheath, instabilities such as the kink instability can generate electron-only currents that display positive $J \cdot E'$. Without seeing oppositely directed electron outflows, interpreting an event as electron-only flux rope erosion becomes more difficult (*Zhu and Winglee*, 1996). In Section 3.1.3, we outline additional features that support the interpretation of this event as electron-only flux rope erosion.

3.1.3 8/23/17 Event

This event was first reported in *Man et al.*, 2020a. On August 23, 2017, from 11:18:30 - 11:19:30, MMS was located at [X: -18.0, Y: 17.1, Z: -3.4] R_E (GSM) and crossed a flux rope in the Southern magnetotail lobe (Figure 3.3). Two rotations are performed to convert the interval to local current sheet coordinates (LMN). First, minimum variance analysis (*Sonnerup and Scheible*, 1998) is performed to convert the interval to flux rope coordinates. This coordinate system is: I: [-0.276, 0.820, 0.501], J: [0.832, 0.465, -0.302], and K: [-0.481, 0.333, -0.811] with respect to GSM coordinates. The Q direction is the axial direction of the flux rope, the R direction is the transverse direction, and P completes the right handed coordinate axes. From PQR flux rope coordinates, an additional rotation is performed into local current sheet coordinates, where the N direction is the current sheet normal direction calculated with four-spacecraft timing (*Russell et al.*, 1983), L is the asymptotic field direction, and M completes the triad. L is calculated with $(\mathbf{B}_1 \times \mathbf{B}_2) \times (\mathbf{B}_1 - \mathbf{B}_2)$, where B_1 and B_2 are the asymptotic magnetic field on opposite sides of the current sheet (blue shading on the right side of Figure 3.3). We note that the angle between J and X_{GSM} is $\approx 30°$, meaning that the flux rope is highly oblique with respect to X_{GSM}. The current sheet normal speed was approximately 210 km/sec, the current sheet observational duration was ≈ 0.5 sec. The current sheet thickness was ≈ 100 km, or 10 d_e. The upstream plasma density was ≈ 0.25 $\#/cm^3$. Using a heuristic reconnection rate of 0.1 (*Liu et al.*, 2017), the length of of the current sheet is ≈ 1000 km, or ≈ 100 d_e (2.3 d_i).

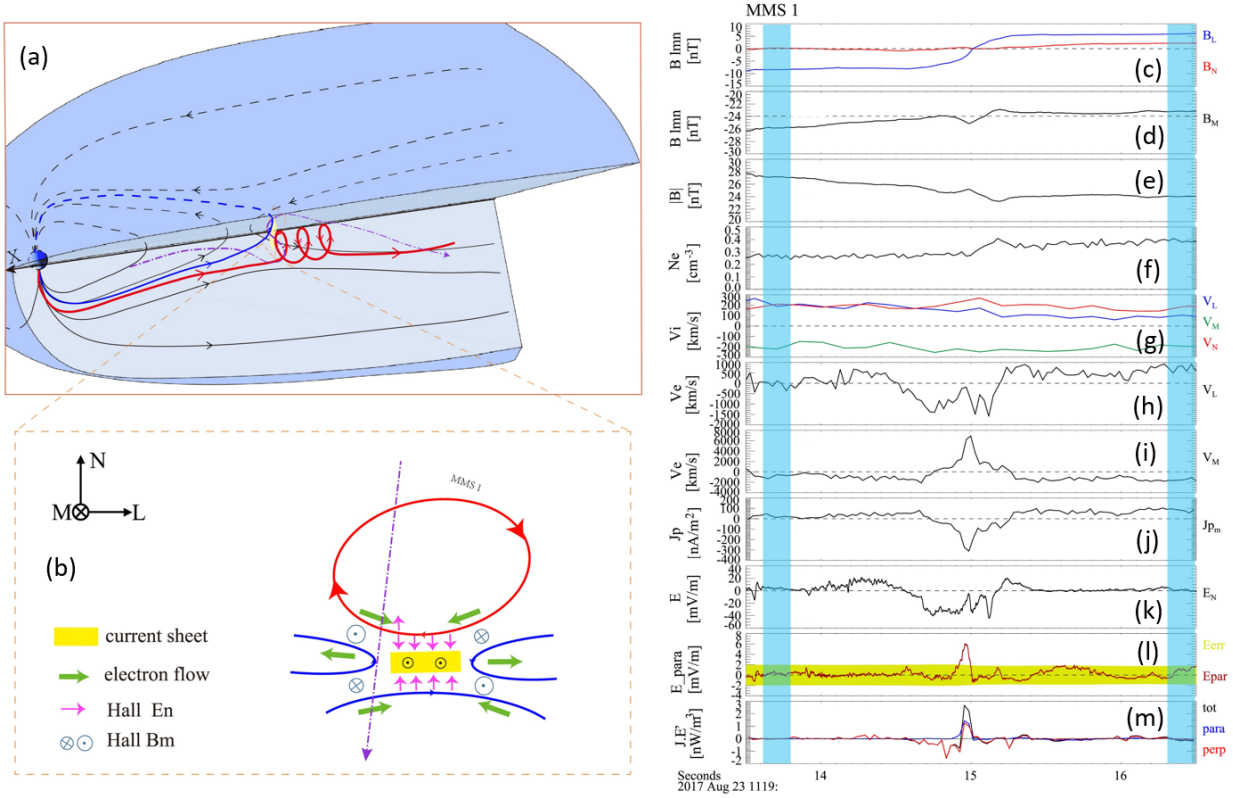

Figure 3.3: LEFT: Schematics of MMS trajectory across an oblique MFR: (a) 3D large-scale view in GSM coordinates and (b) zoomed-in view of the reconnection region in the L-N plane. The purple dotted line represents the trajectory of MMS, and the red curve denotes the MFR. MMS trajectory in panel (b) is inferred from the relationship between the vector k, which is the motion direction of MMS, and N, which is the current sheet normal. RIGHT: MMS1 observations of the reconnection diffusion region between 11:19:13 and 11:19:17 UT. (c) L, N, and (d) M components of the magnetic field; (e) magnetic field strength; (f) electron number density; (g) ion bulk velocity; (h) electron bulk velocity $V_{e,L}$ and (i) $V_{e,M}$; (j) M component of the electric current density calculated from the plasma moments ($J = n_e q(v_i - v_e)$; (k) N component of the electric field; (l) parallel electric field and the measurement errors (yellow shadow); and (m) energy dissipation rate ($J \cdot E'$). (*Man et al.*, 2020a)

Similar to the event found in Section 3.1.2, this event displays many of the signatures used to identify the electron-only nature of *Phan et al.*, 2018's event (See Figure 3.3). Specifically, MMS observed a B_L reversal and B_{tot} minimum consistent with a current sheet crossing (panels a,b,c), significant guide field (panel b), super-Alfvénic electron outflows (panel f,g), strong currents (panel h), positive $J \cdot E'$ (panel k), significant parallel electric field (panel j), and a distinct lack of ion Alfvénic ion outflows (panel e). Using these signatures, along with the significant tilt of the current sheet, *Man et al.*, 2020a interpreted this interval to be a primarily N-directed MMS crossing of an oblique flux rope reconnecting with Earth's dipole field without an ion jet (LEFT, panels a,b). They attribute the lack of ion response to the length of the current sheet being less than the threshold of $\approx 10\ d_i$ needed for ion coupling, not an artifact of directly crossing the diffusion region.

We now replot this event, including the electron pitch angle distribution and energy spectra (Figure 3.4). Panels E-G feature electron pitch angle in three energy ranges: 10-200 eV, 200 eV - 2 keV, amd 2-30 keV, respectively. We highlight several features of this plot. First, we see increased electron flux in the 1-3 keV range from $\approx 10^7$ to $\approx 10^8$ on the side of the current sheet with Northward magnetic field (11:19:15-18), indicating that it should be fully connected to Earth. Second, we note the elevated guide field of the event, consistent with significant magnetic shear from a tilted flux rope. Third, we highlight that on the connected side of the current sheet, trapped parallel and antiparallel electrons are present. Conversely, on the disconnected side of the current sheet, only parallel electrons are present. Lastly, low energy electrons remain parallel across the current sheet (Figure 3.4e). Each of these features indicate that the MMS spacecraft crossed from a disconnected flux rope to field lines that were fully connected to the magnetosphere/ionosphere. They also directly contradict the electron energy spectra and pitch angle features found in electron-only onset of reconnection (outlined in Section 3.2.1).

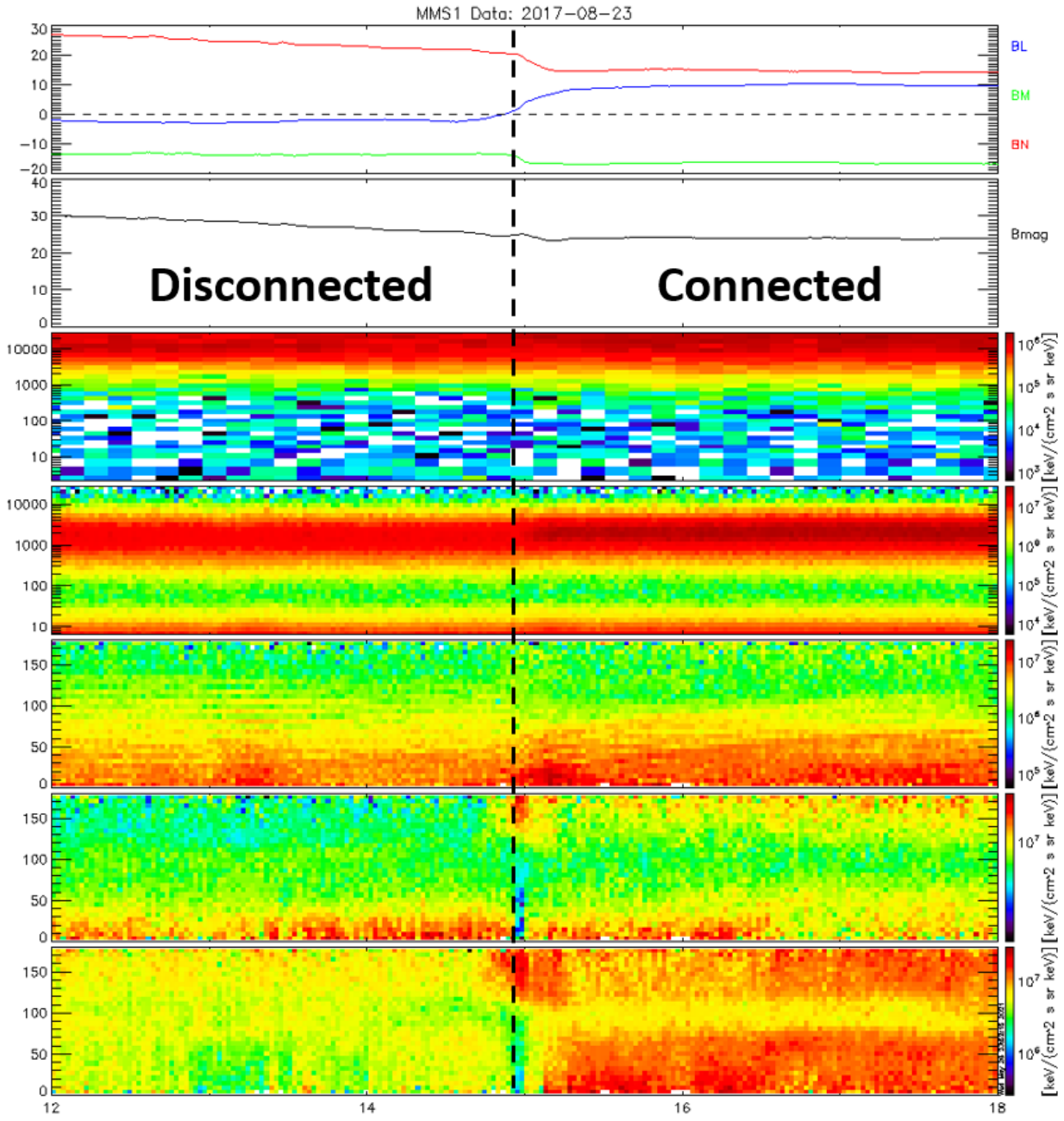

Figure 3.4: 8/23/17 11:19:12-18 MMS1 observation of flux rope erosion. (a) Field-aligned magnetic field components, (b) magnetic field strength, (c) ion and (d) electron energy spectrogram, and (e-g) electron pitch angle distribution for low (10–200 eV), middle (200 eV to 2 keV), and high (2–30 keV) energy range at MMS1.

These electron energy spectra and pitch angle features are consistent with previous observations of flux rope entanglement reported by *Qi et al.*, 2020. There, authors describe three MMS observations featuring the temporal stages of flux rope entanglement. During the third (late) temporal stage, MMS observed trapped energetic magnetospheric electrons on one side of the current sheet and a distinct evacuation of electrons on the other. This was indicative of two flux ropes - one that was fully connected to the magnetosphere and one that was fully disconnected from the magnetosphere. During flux rope erosion, one side of the current sheet (dipolarized field) is fully connected to the magnetosphere. As such, we should expect to see a similar trapped electron population as in the flux rope entanglement picture.

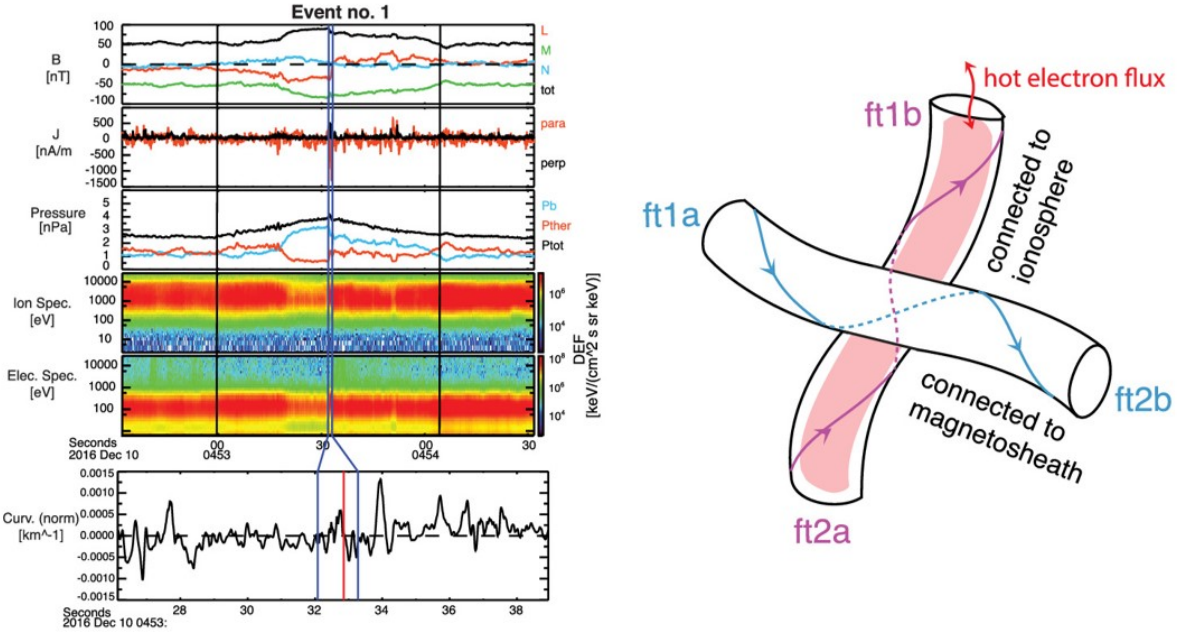

Figure 3.5: Context plot for late stage flux rope entanglement. (a) Four-spacecraft-averaged magnetic field in LMN coordinates and the field strength, (b) current density computed by curlometer technique in field-aligned coordinates, (c) four-spacecraft-averaged pressure (d) ion and (e) electron energy spectrogram at MMS1. The magnetic field curvature projected in the direction of the current sheet normal is plotted in a narrower time interval around the sheet marked by the blue vertical lines. The red vertical line marks the maximum current density location within the current sheet. The LMN directions in GSM for Event No. 1 is L: [0.66, 0.58, 0.48], M: [0.34, 0.34, 0.88], and N: [0.67, 0.74, 0.03]. (*Qi et al.*, 2020)

However, like in Section 3.1.2, we note that the four spacecraft MMS constellation do not observe oppositely directed electron jets, meaning they did not straddle the X-point like in *Phan et al.*, 2018's event. They conclude that the signatures found in the previous paragraph are sufficient to show that the current sheet was reconnecting, but do not discuss other mechanisms that can generate the same features.

3.2 Event Study of Electron-Only Onset of Magnetotail Reconnection

3.2.1 6/17/17 Event

This event was first reported in *Wang et al.*, 2018. On June 17, 2017, from 20:24:00-20:24:30, MMS was located at [X: -19.3, Y: -10.3, Z: 5.5] R_E (GSM) and crossed the near-Earth plasma sheet from the southern lobe to the northern lobe (Figure 3.6). The local coordinate system is: L: [0.948,0.315,-0.049], M: [-0.149,-0.304,0.934], N: [0.180,-0.926,-0.330] with respect to GSM coordinates. We determine the normal direction (N) using the four-spacecraft timing method (*Russell et al.*, 1983). The L direction is the direction of the field in the northern lobe averaged with the negative of the field in the southern lobe. The M-component is $\mathbf{N} \times \mathbf{L}$. Magnetic field (B) and electric field (E) components are averaged to FPI v_e cadence. FPI n_e is averaged to match the time resolution of FPI n_i. We calculate the expected $E \times B$ drift velocity ($v_{E\times B}$) using $E \times B/B^2$, where E and B are the measured electric and magnetic field vectors, respectively. Electric field data are averaged to magnetic field cadence to perform the calculation, then the resulting vector is averaged to FPI v_e cadence. We then compare $v_{E\times B}$ to the perpendicular electron velocity ($v_{e,\perp}$), which is calculated as $-((v_{e\times B}) \times B)/B^2$. Each time series in Figure 3.6 is smoothed using a 3-point running average.

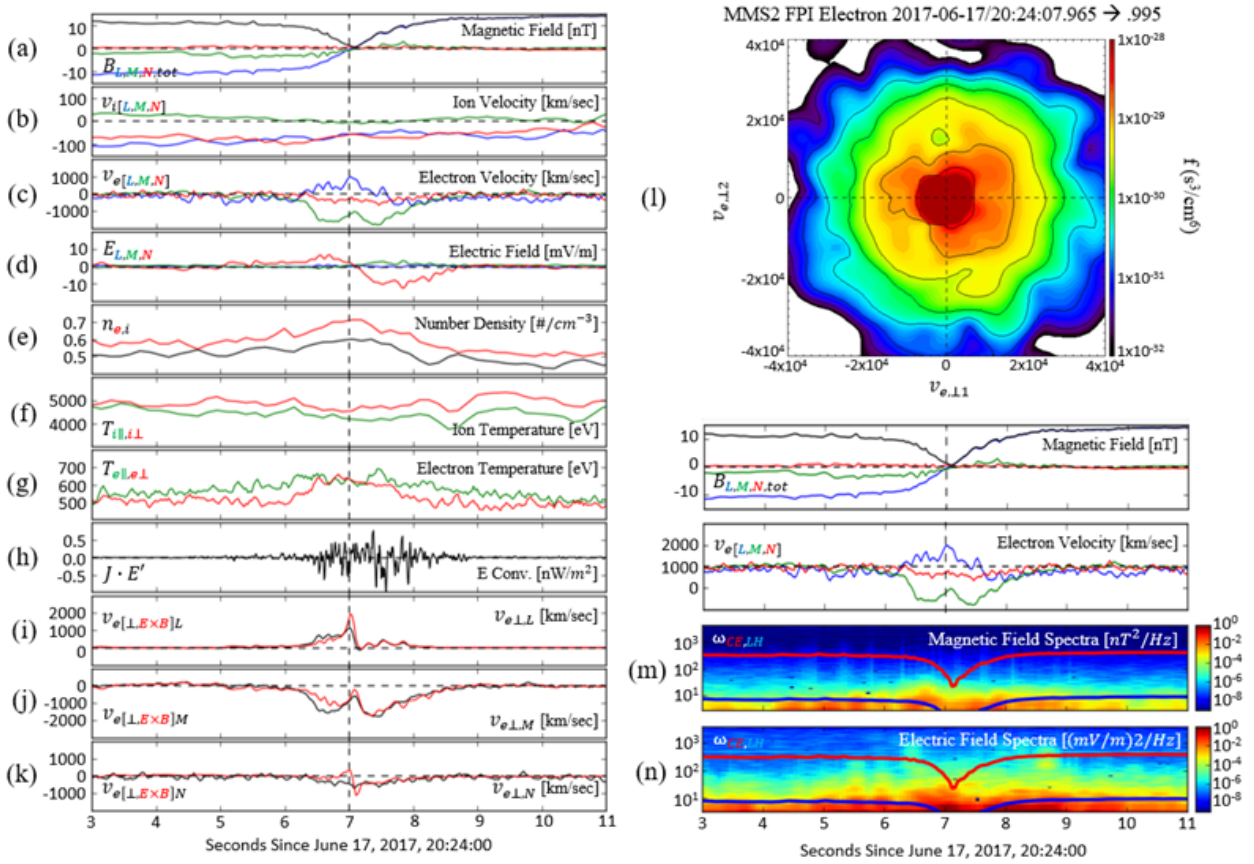

Figure 3.6: June 17, 2017 Event reported by *Wang et al.*, 2018. (a) Magnetic field (B_L: Blue, B_M: Green, B_N: Red, Magnitude (black)), (b) ion bulk flow velocity, (c) electron bulk flow velocity, (d) electric field, (e) electron (red) and ion (black) number densities, (f) perpendicular (red) and parallel (green) ion temperatures, (g) perpendicular (red) and parallel (green) electron temperatures, (h) Energy Conversion, (i,j,k) Perpendicular electron velocity (black) and E×B drift velocity (red) components, (l) perpendicular electron velocity distribution ($v_{e,\perp 1} = ((B \times v_e) \times B)/B^2, v_{e,\perp 2} = (B \times v_e)/B$), (m) magnetic field spectra, and (n) electric field spectra. Within the spectra, the red (blue) line is the electron cyclotron (lower hybrid) frequency $\omega_{ce}(\omega_{LH})$.

The interval in Figure 3.6 shares several features with *Phan et al.*, 2018's electron-only reconnection event. At ≈20:24:07.1, when B_L approaches 0, MMS2 observes an absolute

minimum in B_{tot} (Panel A), a super-Alfvénic v_{eL} jet (Panel C) but no super-Alfvénic v_{iL} (Panel B). The ion Alfven speed (v_{iA}) is calculated as $B_0/\sqrt{\mu_0 m_i n_i}$, where B_0 and n_i are the magnetic field strength and proton density, respectively, in the lobe region surrounding the current sheet crossing. $J \cdot E'$ (Panel H) is significant and positive near the B_L reversal point and significant and negative far from the current sheet center. Positive and negative $J \cdot E'$ is consistent with electrons gaining energy from annihilating electromagnetic fields and transferring energy back to the magnetic fields, respectively (*Torbert et al.*, 2018). This negative-positive-negative $J \cdot E'$ structure is consistent with an N-direction trajectory through the electron demagnetization region of a reconnecting current sheet (*Pucci et al.*, 2018). Using the temporal duration of the current sheet crossing, the thickness of the current sheet was 10 d_e, well below ion-scales ($\approx 0.24 d_i$). However, this event does not feature the strong guide field present in *Phan et al.*, 2018's reconnection event and generates strong Hall-like B_M and E_N fields (Panel A,D), which is expected to be suppressed in electron-only reconnection.

While multiple features of this event deviate from the picture painted by *Phan et al.*, 2018, several other features support that this event can be classified as electron-only onset of reconnection. The ion (n_i) and electron (n_e) densities (Panel E) are equal within FPI uncertainty, indicating that the electrons are primarily carrying the current (*Huang et al.*, 2018). Far from the current sheet, the parallel electron temperature ($T_{e,||}$) exceeds the perpendicular electron temperature ($T_{e,\perp}$) (Panel G), but as MMS2 approaches the current sheet center, both directions are energized, and T_e becomes more isotropic. This is consistent with previously observed ion-coupled EDR crossings during "electron-ion" reconnection in the near-Earth magnetotail (*Chen et al.*, 2019; *Li et al.*, 2019; *Zhou et al.*, 2019). However, the perpendicular ion temperature ($T_{i,\perp}$) only slightly exceeds the parallel ion temperature ($T_{i,||}$) (Panel F) and does not vary during the current sheet crossing. During a typical magnetotail ion-coupled EDR crossing, $T_{i,\perp}$ significantly exceeds $T_{i,||}$ (*Zhou et al.*, 2019). Panels I, J, and K compare each component of $v_{e,\perp}$ and $v_{E\times B}$. Deviation of $v_{e,\perp}$ from $v_{E\times B}$ close to the current sheet center (20:24:06.7 – 20:24:07.3) shows that electrons became demagnetized

in this region (*Torbert et al.*, 2018). Lastly, MMS2 observed a crescent distribution in the $v_{e\perp 1} - v_{e\perp 2}$ plane (Panel L) and strong wave activity near the lower hybrid frequency in both magnetic (Panel M) and electric field (Panel N) power spectra. These features suggest that MMS crossed a current sheet supported mostly by electrons. Within this current sheet, the electrons were demagnetized and energized due to annihilating magnetic field, but ions were mostly unaffected, justifying the terminology electron-only onset of reconnection for this event.

Many features of this event differ from those of a quiet current sheet. For example, the clear v_{eL} exhaust jet, cross-tail v_{eM}, increase in T_e, electron crescent distribution, and positive $J \cdot E'$ indicate that electrons are being heated and accelerated by reconnecting field lines. However, multiple other features of this event are identical to those of a quiet current sheet. Specifically, there is no v_{iL} exhaust jet and no increase in T_i. This is consistent with the conclusion that, while these field lines are reconnecting, only the electrons are involved in the process.

Several features of this event also differ significantly from a traditional reconnection event. For example, strong ion heating and ion outflows are unique to a well-developed, ion-coupled reconnecting current sheet. In addition, non-EDR crossings do not consistently display positive $J \cdot E'$, electron crescent distributions, electron demagnetization, or Hall electric fields. However, multiple features of this event are identical to those of traditional reconnection. Both current sheet types consistently share v_{eL} exhaust and a significant increase in T_e. These shared features indicate that, in both current sheets, field lines are reconnecting and electrons are being demagnetized.

We now will define the criteria to distinguish electron-only onset of reconnection events from electron-only flux rope erosion events in our event pool. First, we require a peak in electron flux in the electron energy spectra at the current sheet center. This peak needs to coexist with symmetric parallel and antiparallel arms in the mid or high energy electrons surrounding the current sheet center. This indicates that the field lines on both sides of the

current sheet are attached to Earth on one end and disconnected on the other end (in other words, they are lobe fields). Second, we require low guide field (< 0.5). Third, we require a reversal in the low energy electron pitch angle from parallel to antiparallel, or vice versa. This reversal indicates that both sides of the current sheet exhibit tailward streaming electrons, which is expected in the lobes. Fourth, we require strong isotropy in higher energy electron pitch angle at the current sheet center. These combined features indicate that electrons are experiencing the greatest heating at the current sheet center. These features are mutually exclusive with the criteria for electron-only flux rope erosion listed in Section 3.1.3, and are displayed in Figure 3.7.

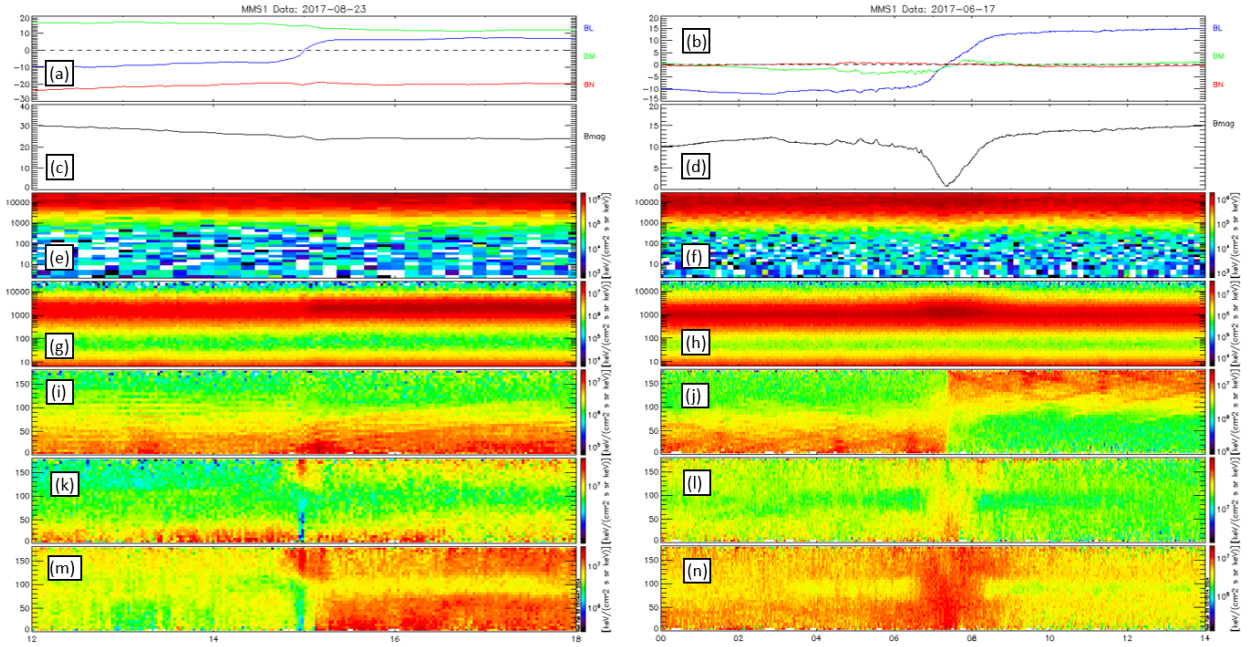

Figure 3.7: (LEFT) 8/23/17 MMS1 observation of electron-only flux rope erosion and (RIGHT) 6/17/17 MMS1 observation of electron-only onset of reconnection. (a,b) Field-aligned magnetic field components, (c,d) magnetic field strength, (e,f) ion and (g,h) electron energy spectrogram, and (i-n) electron pitch angle distribution for low (10–200 eV), middle (200 eV to 2 keV), and high (2–30 keV) energy range at MMS1.

3.2.2 Comparison to 8/10/17 Electron Diffusion Region

We note that previous work by *Wang et al.*, 2020b has compared the June 17th event with an ion-coupled EDR with a similar trajectory, on August 10th, 2017 (See Figure 3.10). To further support the interpretation of the 6/17/17 event (See Figure 3.2.1) as an electron-only onset of reconnection event, we compare it to an ion-coupled EDR observed on 8/10/17. In Figure 3.8, we display the 8/10/17 EDR, first reported in *Zhou et al.*, 2019.

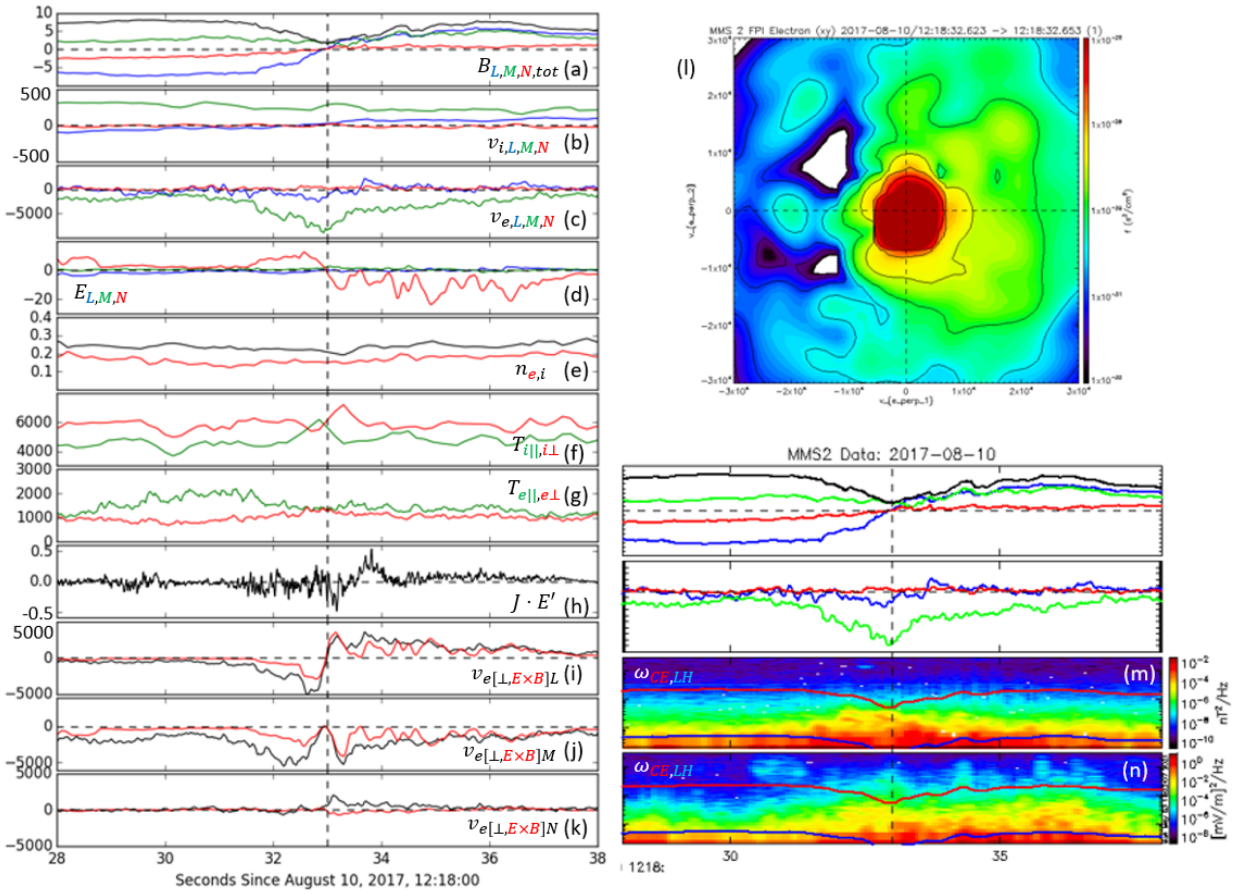

Figure 3.8: 8/10/2017 Event reported by *Zhou et al.*, 2019. (a) Magnetic field (B_L: Blue, B_M: Green, B_N: Red, Magnitude (black)), (b) ion bulk flow velocity, (c) electron bulk flow velocity, (d) electric field, (e) electron (red) and ion (black) number densities, (f) perpendicular (red) and parallel (green) ion temperatures, (g) perpendicular (red) and parallel (green) electron temperatures, (h) Energy Conversion, (i,j,k) Perpendicular electron velocity (black) and E×B drift velocity (red) components, (l) perpendicular electron velocity distribution ($v_{e,\perp 1} = ((B \times v_e) \times B)/B^2, v_{e,\perp 2} = (B \times v_e)/B$), (m) magnetic field spectra, and (n) electric field spectra. Within the spectra, the red (blue) line is the electron cyclotron (lower hybrid) frequency $_{ce}(_{LH})$.

On August 10, 2017, from 12:18:00-12:19:00, MMS crossed a current sheet at [-15.2,4.6,3.0] R_E (XYZ GSM). We use the following LMN coordinate system: L: [0.985,-0.141,0.097], M:

[0.152,0.982,-0.109], N: [-0.080,0.122,0.989] rotated from GSM. At ≈ 12:18:33, MMS2 crossed a traditionally reconnecting current sheet (B_L reversal, minimum in B_{tot}) (panel a) with an L-directed ion exhaust outflow reversal exceeding $0.5v_{iA}$ (panel b) and a super-Alfvénic L-directed electron exhaust outflow reversal (panel c). The current sheet contains strong cross-tail ion and electron currents at the B_L reversal point. We note that MMS crossed this current sheet with a primarily L-directed trajectory, so the magnitude of the ion outflows (v_{iL}) remained below v_{iA} and reversed in direction at the current sheet center. This is consistent with MMS crossing an EDR in the L-direction, where reduced and shifted ion outflows are expected until MMS reaches the exhaust region. MMS observes strong Hall magnetic and electric fields (panel a,d). Electrons are isotropic and heated close to the current sheet center, and parallel temperature dominated far from the current sheet center (panel g). Ions are also isotropic and heated close to the current sheet center, but perpendicular temperature dominates far from the current sheet center (panel f). $J \cdot E'$ (panel h) is significantly positive above the $0.02\ nW/m^2$ noise deviation during the interval at which ions and electrons are isotropic. Throughout the entire interval, $v_{e,\perp}$ consistently deviates from $v_{E\times B}$, indicating that electrons are breaking the frozen-in condition. At ≈ 22:34:03.0, MMS2 observed a strong crescent distribution (panel l), indicating that electrons are being energized and redirected in the region. Lastly, clear enhancements in the magnetic and electric field spectra (panel m,n) are present between the lower hybrid frequency and electron cyclotron frequency. These observations support the picture of an active reconnection site where both ions and electrons were heated and energized.

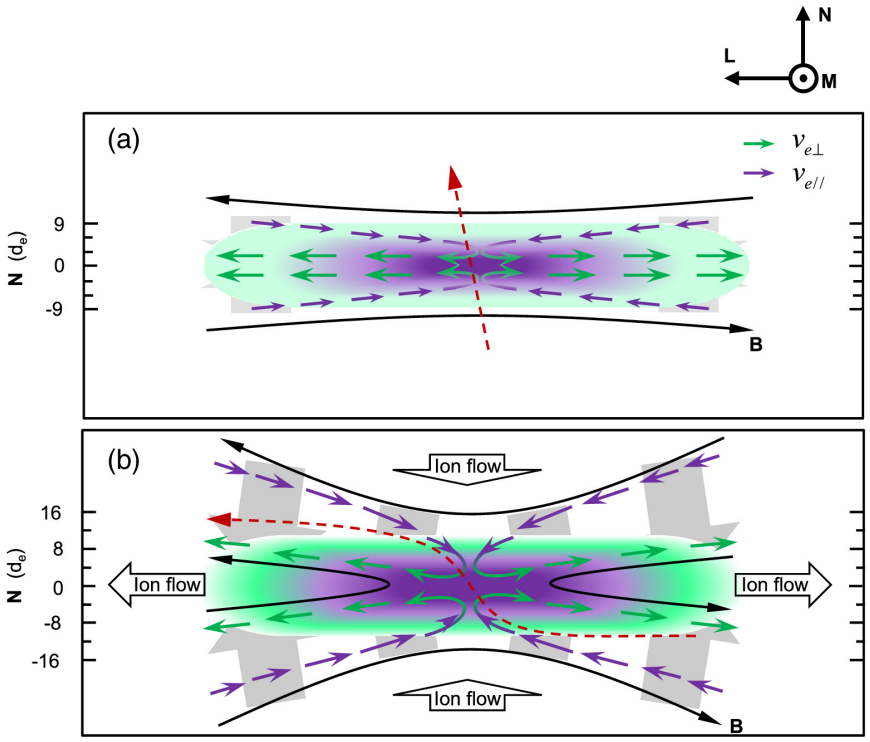

Figure 3.9: Cartoon of MMS trajectories through two reconnection regions. (a) 6/17/17, (b) 8/10/17. The red dashed lines show the spacecraft trajectories.

Several contextual clues also allow us to describe the trajectory of MMS through the EDR. First, the reversals in v_{iL} and v_{eL} at the point of minimum B_{tot} suggests that MMS crossed from one outflow region to the other, indicating a strong L component trajectory. However, the reversals in B_L and v_{iN} suggest that MMS observed both inflow regions, indicating a strong N component trajectory near the current sheet center. B_M being positive on both sides of the current sheet while decreasing to zero at the current sheet center also suggests that MMS approached in the -L/-N quadrant and exited in the diagonal +L/+N quadrant. We compare this to the spacecraft trajectory through the 6/17/17 event. Although Figure 3.6 displays a similar B_L reversal profile as Figure 3.8, it does not display the same B_M, $n_{i,e}$, or v_{eL} profile. At the current sheet center, B_M cleanly reverses, v_{eL} showed a positive enhancement, and $n_{i,e}$. These features indicate that the spacecraft cleanly entered and exited

the reconnection region in the N direction, with very little L component. The contrast between these two trajectories is shown in Figure 3.9.

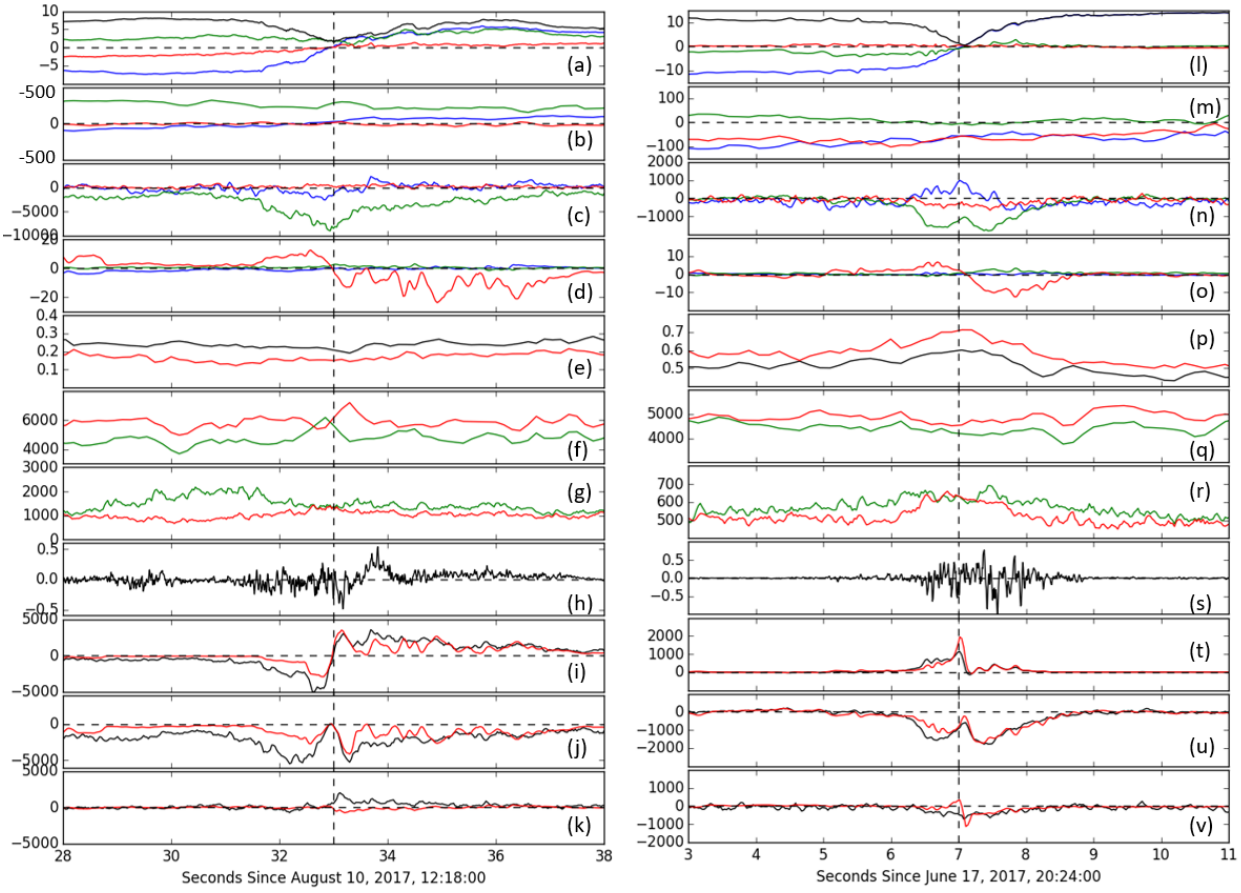

Figure 3.10: LEFT: MMS1 observations of an electron diffusion region on 8/10/17. RIGHT: MMS1 observations of electron-only onset of reconnection on 6/17/17. (a,l) Magnetic field (B_L: blue, B_M: green, B_N: red, Strength: Black), (b,m) ion bulk velocity, (c,n) electron bulk velocity, (d,o) electric field, (e,p) plasma ion (black) and electron (red) density, (f,q) ion parallel (green) and perpendicular (red) temperature, (g,r) electron parallel (green) and perpendicular (red) temperature, (h,s) energy dissipation rate ($J \cdot E'$), (i-k,t-v) Deviation of $v_{e\perp}$ from $v_{eE\times B}$ in L, M, and N directions.

We now discuss the features in 6/17/17 that differ from 8/10/17 and how these differences support an electron-only onset interpretation. In Panel B, we note that ion outflow velocity

(v_{iL}) in 8/10/17 clearly responds to the reconnection by reversing at the current sheet center, while v_{iL} in 6/17/17 does not respond to entering the current sheet, exiting the current sheet, or the reconnection center. This indicates that neither ion inflow nor ion outflow are occurring in the 6/17/17 event. The ion temperature (T_i) in 8/10/17 becomes isotropic at the current sheet center and is primarily $T_{i,\perp}$ dominated far from the current sheet center. In contrast, T_i in 6/17/17 does not display an organized response to the current sheet center or reconnection outflow. This indicates that ions are not being heated or energized by reconnection in this event. Meanwhile, the magnetic field profile, electron velocity ($v_{eL,M}$), electron temperature (T_e), energy conversion ($J \cdot E'$), and electron demagnetization ($v_{[\perp,E\times B]}$) features of the two events are consistent. This comparison supports the interpretation that, during the 6/17/17 event, reconnection is occurring, but ions are not responding to the reconnection process. As such, we preliminarily label this event as electron-only onset.

3.2.3 Comparison to 2D PIC Simulations

Lu et al., 2020, 2022 developed a 2D particle-in-cell (PIC) simulation to describe the temporal transition from a quiet, non-reconnecting current sheet to a traditional, ion-coupled reconnecting current sheet in Earth's magnetotail. To maintain consistency with spacecraft observations, particularly MMS observations, they used an LMN current sheet coordinate system, where L was the horizontal axis, N was the vertical axis, and M was the out of plane direction. The dimensions of the simulation box were $-32d_i \leq L \leq 0$ and $-8d_i \leq N \leq 8d_i$, and the grid size is $\Delta L = \Delta N = d_i/64$. d_i is the ion inertial length calculated with unit density n_0. Their initial configuration utilized a Lembege-Pellat current sheet (*Lembège and Pellat*, 1982). This can be described as a current sheet with magnetic potential and density:

$$A_{0M}(L, N) = B_0 \delta \ln\{\cosh[F(L)(N/\delta)]/F(L)\} \tag{3.1}$$

$$n(L,N) = n_0 F^2(L)\text{sech}^2[F(L)(N/\delta)] + n_b \tag{3.2}$$

$$\text{where } F(L) = \exp[\epsilon(L + 16d_i)/\delta], \qquad \epsilon = (B_N/B_0)_{N=0}. \tag{3.3}$$

Using this description, $F(L)$ describes the spatial distribution of the magnetic potential in the L direction and ϵ describes the constant ratio of normal magnetic field at N = 0. A Lembege-Pellat style current sheet is used because it has been shown to become tearing unstable while externally driven (*Lembège and Pellat*, 1982). This has not been shown with more traditional current sheet configurations such as Harris current sheets. Their current sheet has a half width of $\delta = 2d_i$, a background density of $n_b = 0.2n_0$, $\epsilon = 0.04$, and an ion-electron mass ratio of $m_i/m_e = 400$. This simulation evolves in time at a time step of $\Delta t = 0.00025\Omega_{i0}^{-1}$, where Ω_{i0} is the initial ion gyrofrequency at $t = 0$, calculated using B_0 at $t = 0$. At $t = 0$, they establish uniform initial ion and electron temperatures of $T_{i0} = 0.4167 m_i V_A^2$ and $T_{e0} = 0.0833 m_i V_A^2$, respectively. V_A is the Alfven speed calculated with B_0 and N_0. Lastly, the speed of light is $c = 40V_A$.

On top of these initial conditions, they introduce an external driver in the form of an electric field in the M, out of plane direction:

$$E_M = \hat{E}_M(t)S(L), \tag{3.4}$$

$$\text{where } \hat{E}_M(t) = 2a\omega B_0 \tanh(\omega t)/\cosh^2(\omega t) \tag{3.5}$$

$$\text{and } S(L) = \text{sech}^2[(L + 16d_i)/D_L] \tag{3.6}$$

In these forms, $\hat{E}_M(t)$ describes the external driver's temporal evolution, and $S(L)$ describes the spatial distribution of the driver in the L direction. a sets the size of the region where field

lines are deformed from the upper and lower N boundaries, ω sets the timescale of the external driver, and D_L is the half-width of the driver. This simulation utilizes $a = 2d_i$, $\omega = 0.05\Omega_i$, and $D_L = 5d_i$. They impose open boundary conditions at the L boundaries, $1.5E9$ particles are utilized across the simulation domain, and unit density n_0 is the equivalent of 376 particles per cell. Given this simulation setup, they advance the simulation to $\Omega_i t = 100$, which is sufficient for a thick, non-reconnecting current sheet to compress, begin reconnecting, and develop into an ion-coupled reconnecting current sheet (see Figure 3.11). We note that out of plane current, j_m, is represented by the color bar. Panel b, corresponding to $\Omega_i t = 63$, displays significant thinning of the current sheet due to the externally driven electric field, but no initiation of magnetic reconnection. Panel c, at $\Omega_i t = 68$, displays the first occurrence of magnetic reconnection, and Panel d, at $\Omega_i t = 100$ displays the completed evolution to traditional, ion-coupled reconnection.

Notably, starting at $\Omega_i t = 63$, the current sheet decreases in thickness to $< 1d_i$, and B_N decreases and to approximately $0.001B_0$, which is sufficient to consider the current sheet unstable to the electron tearing mode instability. In addition to j_m, they were able to map many other plasma and field conditions during each of these timesteps. They successfully reproduced several magnetic field components (B_M, B_N), electric field components (E_L, E_M, E_N), ion outflows (v_{iL}, v_{iM}, v_{iN}), electron outflow (v_{eL}, v_{eM}, v_{eN}), plasma density, ion and electron temperature (T_i, T_e), and energy conversion ($J \cdot E'$). Several of these components are displayed in Figure 3.12, and the rest can be found in Section A.3. These component maps help us gain insight of where different plasma populations change over time and by how much. In Figure 3.12 , we note that several color bars in columns 1 and 2 have different limits compared to the color bars in column 3.

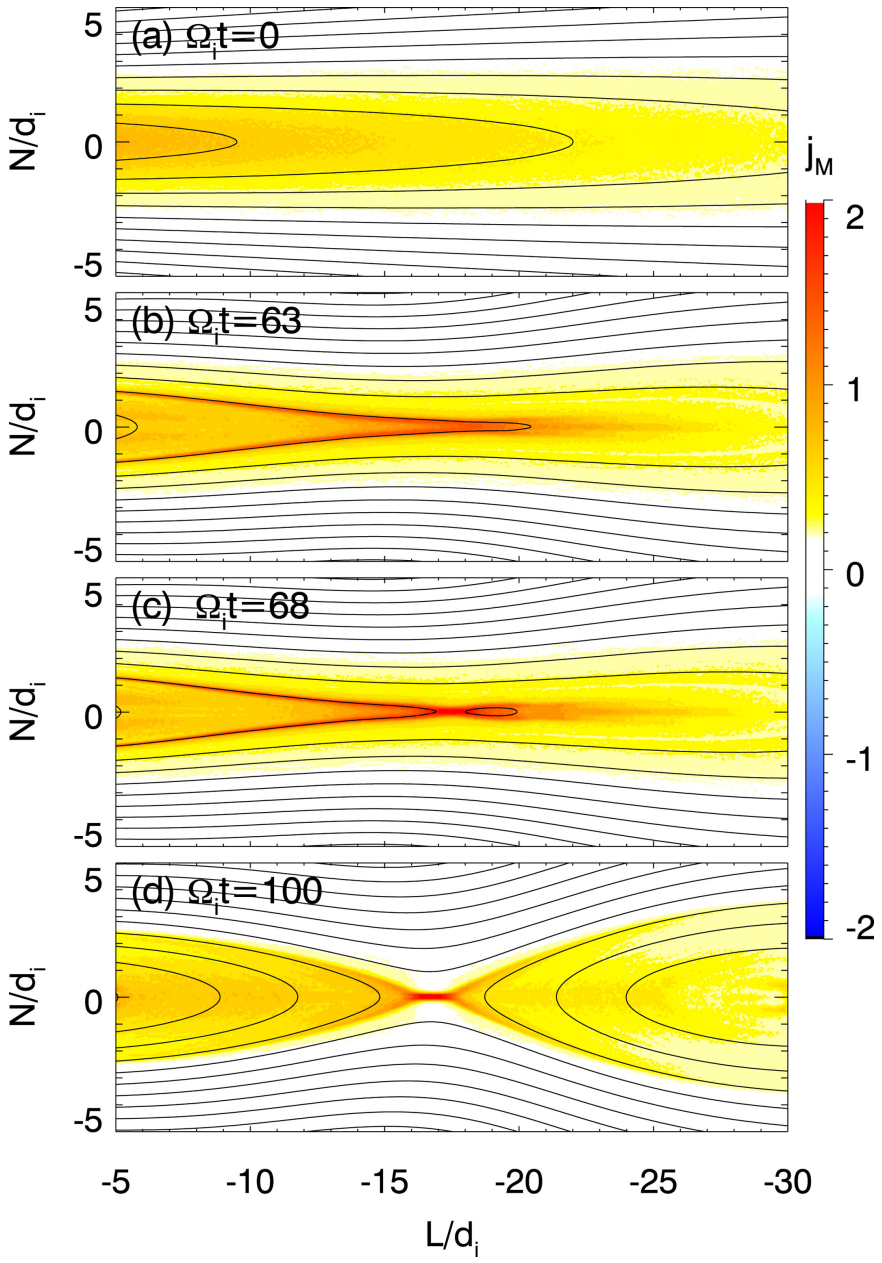

Figure 3.11: Four stages of current sheet and reconnection evolution in *Lu et al.*, 2022 simulation. (a) $\Omega_i t = 0$, (b) $\Omega_i t = 63$, (c) $\Omega_i t = 68$, (d) $\Omega_i t = 100$.

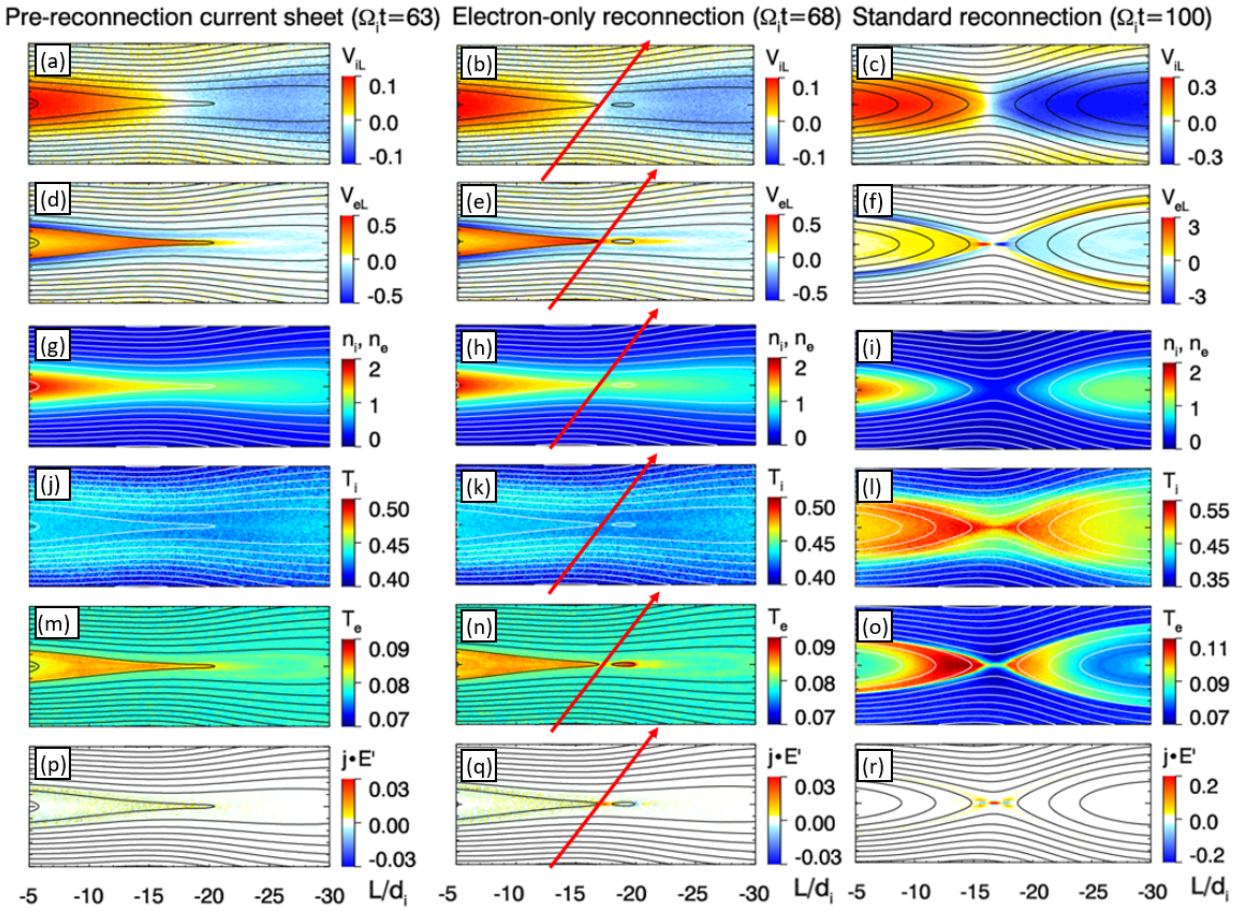

Figure 3.12: Three time snapshots of colored 2D contours of (f) ion outflow velocity, (i) electron outflow velocity, (l) plasma density, (m) ion temperature, (n) electron temperature, and (o) energy conversion. Red arrows represent typical MMS trajectory through the reconnection region. Black curves represent the magnetic field lines in the L-N plane.

Several features of these 2D contours change significantly over time. In Row 1, ion outflow velocity remains approximately at ambient levels when reconnection begins at $\Omega_i t = 68$, but increases to elevated levels once reconnection is fully developed at $\Omega_i t = 100$. In Row 2, electron outflow is increased at $\Omega_i t = 68$ and continues to increase through $\Omega_i t = 100$. Importantly, at $\Omega_i t = 68$, the electron outflow velocity significantly increases, while the ion outflow velocity does not. As a result, *Lu et al.*, 2022 labels this column as electron-

only onset of reconnection. In Row 3, the plasma density at the reconnection region is slightly reduced at $\Omega_i t = 68$ compared to $\Omega_i t = 63$, but evacuates much more significantly at $\Omega_i t = 100$. In Row 4, ion temperature remains approximately at ambient levels when reconnection begins at $\Omega_i t = 68$, but increases significantly at $\Omega_i t = 100$. Importantly, ion temperature increases significantly in both the outflow region and the very center of the reconnection region, indicating that IDR-coupled EDRs should display a significant amount of ion heating. In Row 5, electron temperature increases minorly at $\Omega_i t = 68$, but increases more significantly at $\Omega_i t = 100$. This heating is much stronger in the outflow region than at the reconnection center. Lastly, in Row 6, significant energy conversion in positive $J \cdot E'$ is present at $\Omega_i t = 68$ and continues to increase through $\Omega_i t = 100$. We note that each parameter displayed in Figure 3.12 either changes significantly from Column 1 to Column 2 (v_{eL}, T_e, $J \cdot E'$) or changes significantly from Column 2 to Column 3 (v_{iL}, T_i, n_p). This indicates that these parameters can be used to distinguish electron-only onset of reconnection events from quiet, non-reconnecting current sheets (v_{eL}, T_e, $J \cdot E'$) and from traditional, ion-coupled reconnection (v_{iL}, T_i, n_p).

In addition to their color contours, we add red arrows through each panel of the center column to indicate a sample MMS orbit through the region. This orbit is very similar to MMS's trajectory through the current sheet during the 6/17/17 reconnection event described in Section 3.2.1. If the trajectory of a spacecraft through a reconnecting current sheet is well understood, this trajectory can be mapped directly onto these simulation regions to approximate what features the spacecraft should expect to see. Given MMS's highly N-direction dominated trajectory on 6/17/17, *Lu et al.*, 2020 extracted simulated time series data from a fully N-directed path through the reconnection region at $\Omega_i t = 68$ (See Figure 3.13). Directly comparing the simulated time series data to MMS's 6/17/17 observation, they yielded a strong, qualititative agreement between the MMS observation and the simulated plasma and field cuts.

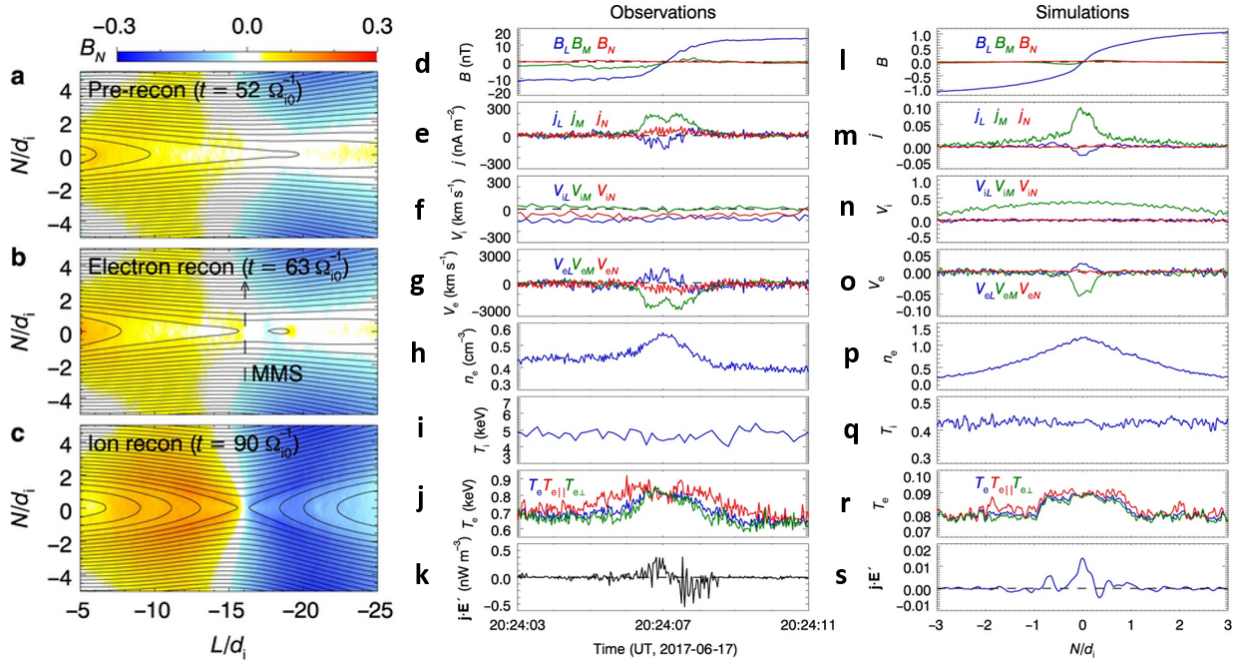

Figure 3.13: LEFT: 2D contour of B_N at three (a-c) time steps ($\Omega_i t = 52, 63, 90$). Black dashed arrow indicates 6/17/17-like spacecraft trajectory. MIDDLE: MMS observations at 6/17/17. RIGHT: PIC simulation results along the virtual MMS spacecraft trajectory. (d,l) Magnetic field, (e,m) current density, (f,n) ion bulk velocity, (g,o) electron bulk velocity (h,p) electron density, (i,q) ion temperature (j,r) electron temperature, (k,s) energy conversion ($j \cdot E$). In the PIC simulations, magnetic field is in units of B_0, current density is in units of en_0V_{eA}, ion bulk velocity is in units of V_A, electron bulk velocity is in units of V_{eA}, electron density is in units of n_0, electron and ion temperatures are in units of $m_iV_A^2$, and $j \cdot E'$ is in units of $en_0V_A^2B_0$.

Interpreting 6/17/17 as electron-only onset of reconnection is complicated for multiple reasons. First, we note that MMS's trajectory was directed primarily in the N direction (*Wang et al.*, 2018), which may obscure ion response in v_iL (*Farrugia et al.*, 2021). Second, even if MMS is truly observing the electron-only onset of magnetic reconnection, should this process share the name electron-only reconnection with a different physical process in

Earth's magnetosheath? Electron-only reconnection in Earth's magnetosheath is a steady-state, turbulent process that occurs because the length of the current sheet is stunted, which is not happening in *Lu et al.*, 2022's simulations (*Phan et al.*, 2018).

We discuss both complications in more detail using statistics in Section 4.4.7. In the context of the individual 6/17/17 event, we address the first complication by showing that MMS observes a significant enhancement in $J \cdot E'$, but no enhancement in T_i. As shown in Figure 3.12, an N-directed reconnection observation can only be classified as ion-coupled reconnection if it displays an enhancement in both T_i and $J \cdot E'$, even at the extreme reconnection center, where ion outflow may be sub-Alfvénic. Because MMS's 6/17/17 observation displays a $J \cdot E'$ enhancement, but no T_i enhancement, we classify it as the initial stage of reconnection. We address the second complication by agreeing that this process should not be named electron-only reconnection and should instead be named electron-only onset of reconnection.

3.2.4 Response to *Farrugia et al.*, 2021

As described in Section 3.2.3, recent PIC simulations have shown that, during the onset of traditional, ion-coupled reconnection, there is a short ($\approx$ 10 sec) transition phase where field lines are reconnecting, but only the electrons are accelerated by the reconnection. Delayed coupling of ions to the reconnection process has been proposed in other simulation work (*Walker et al.*, 1999), but did not comment on the state of electrons during the pre-ion phase. These simulations were supported by an observation from 6/17/17, which qualitatively agreed with a simulated spacecraft trajectory through this electron-only onset of reconnection.

Wang et al., 2020b's 6/17/17 observation was previously the only magnetotail observation to support this interpretation, which was hotly debated. In a counter-paper by *Farrugia et al.*, 2021, it was argued using 2D PIC simulations that MMS crossing an ion-coupled EDR in exclusively the N-direction when a current sheet was extremely tilted would reproduce the

signatures of the 6/17/17 event. Specifically, they noted that the lack of ion velocity could be attributed to MMS crossing directly through the EDR, where ion outflow is muted relative to the outflow region. We agree that ion outflow should be muted in the EDR, but in a response paper by *Lu et al.*, 2022, we state that even when deep in an EDR, MMS should still expect to observe significant ion heating, which is not present in the 6/17/17 event. *Farrugia et al.*, 2021 discusses this briefly in the appendix, attributing the lack of ion heating to uncertainty of the FPI instrument and citing that the TWINS spacecraft, which was located in the near-Earth magnetotail, saw enhanced ion temperatures in the global magnetotail for the 10 minutes following the 6/17/17 observation. We note that the TWINS spacecraft has a 2 minute resolution, which is not sufficient to resolve the highly time-dependent temperature properties during the 6/17/17 interval, and when it does observe ion heating, it observes it in on the opposite side of the magnetotail from the 6/17/17 event. While we conclude that the 6/17/17 event is an electron-only onset of reconnection event, we note that this discussion prompts the need for additional events to further distinguish ion-coupled EDRs from electron-only onset of reconnection.

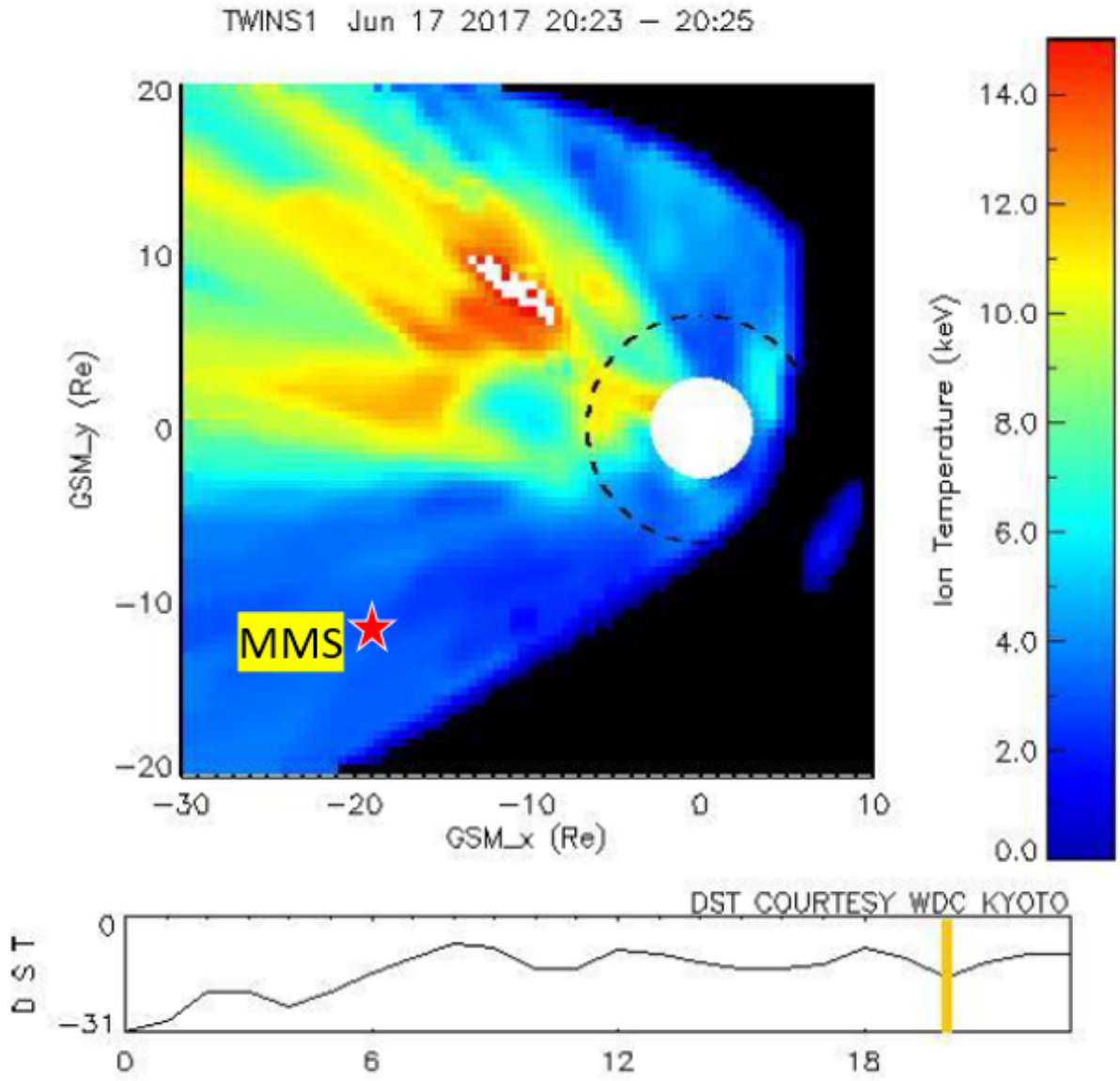

Figure 3.14: Heat map of ion temperature observed by the TWINS spacecraft on 6/17/17 from 20:23-20:25. Red star indicates MMS location during electron-only onset event in question. (bottom) DST from 00:00-23:59 on 6/17/17.

3.3 Defining Observational Features of Magnetotail Electron-Only Reconnection

While individual electron-only flux rope erosion and electron-only onset of reconnection candidates have been reported and discussed, nobody has attempted to collect statistics of either population. In this thesis, we perform a survey of six MMS magnetotail seasons searching for electron-only reconnection candidates. To perform the survey, using the events described in Section 3.1.2, Section 3.1.3, and Section 3.2.1, we establish a set of generalized criteria that can be used to identify "electron-only reconnection" in Earth's magnetotail. The criteria in black are not intended to distinguish between electron-only flux rope erosion and electron-only onset of reconnection, and the criteria in red are intended to distinguish between the two processes. While performing our initial survey, we utilize only the black criteria and, as such, we will indiscriminately label our events electron-only reconnection. The full criteria list is shown below:

Table 3.1: Table higlighting the total criteria for electron-only flux rope erosion vs. electron-only onset. Red criteria are unique to electron-only flux rope erosion and green criteria are unique to electron-only onset.

EO Flux Rope Erosion	**EO Onset**
B_L Reversal	B_L Reversal
B_{tot} Minimum	B_{tot} Minimum
$v_{iL} < 0.5 v_{iA}$	$v_{iL} < 0.5 v_{iA}$
$v_{eL} > v_{iA}$	$v_{eL} > v_{iA}$
No T_i response ($< 10\%$)	No T_i response ($< 10\%$)
T_e increase ($> 10\%$)	T_e increase ($> 10\%$)
Positive $J \cdot E'$	Positive $J \cdot E'$
$v_{e,\perp} \neq v_{E\times B}$	$v_{e,\perp} \neq v_{E\times B}$
Electron Tearing ((1.10))	Electron Tearing ((1.10))
Alfvénic U_ψ, $\nabla \cdot U_\psi > 0.1 f_{ce}$	Alfvénic U_ψ, $\nabla \cdot U_\psi > 0.1 f_{ce}$
Increased electron flux on side connected to Earth	Peak electron flux at CS center
High Guide Field (> 0.5)	Low Guide Field (< 0.5)
Parallel & Antiparallel electrons on side connected to Earth	Electron Pitch angle reversal
Parallel or Antiparallel electrons on side disconnected from Earth	Electron Pitch Angle Isotropy at CS center

I will now explain the black criteria that can be used to identify both electron-only flux rope erosion and electron-only onset below.

3.3.1 B_L Reversal

In Earth's magnetotail, two lobes of oppositely directed magnetic field are compressed and merged due to magnetic reconnection. These lobe fields have an average field strength of $\approx$ 25-30 nT, and are primarily oriented in the GSM +/- X direction. In other words, the magnetic field conditions surrounding the equatorial magnetotail current sheet are comprised of strong, oppositely directed Bx. Given the approximate orbital speed of the MMS spacecraft, MMS can be regarded as approximately stationary relative to the motion of the equatorial magnetotail current sheet. Therefore, spacecraft observations are dictated almost entirely by the motion of the current sheet. Earth's magnetotail is thought to kink and flap significantly in the GSM Y and Z direction, typically propagating from the midnight sector towards the flanks. As a result, a stationary spacecraft should expect to observe the current sheet moving in primarily the Y and Z directions. MMS crossing the equatorial current sheet from the Northern lobe to the Southern lobe should see a continuous change from lobe-like, positive B_x to lobe-like, negative B_x. When observing magnetic reconnection, we often use LMN (minimum variance) coordinates. With this picture in mind, a B_L reversal is very similar to a B_x (GSM) reversal in an equatorial magnetotail current sheet.

3.3.2 B_{tot} minimum

As described in the previous paragraph, the magnetotail lobes are compressed and merge due to reconnection. By default, the nature of the magnetic field strength when crossing a current sheet is regime and reconnection-dependent. For example, at Earth's magnetopause, due to the asymmetric field strength on each side of the current sheet, the magnetic field strength transitions relatively smoothly from the field strength of one region to the other. Similarly, in Earth's magnetotail, during a current sheet crossing, the magnetic field strength is not significantly affected, often staying flat or dropping only slightly.

Conversely, when a current sheet is reconnecting, the magnetic field strength at the cur-

rent sheet center is directly affected. For example, in Earth's magnetopause, we observe a field strength decrease to a value that is below even the ambient value in the magnetosheath. Similarly, in Earth's magnetotail, spacecraft should expect to observe a significant decrease in the magnetic field strength, often an absolute minimum. When a magnetic field is reconnecting, field lines are literally merging. As a result, one should expect a point at the exact current sheet center where the magnetic field strength is literally zero. In this region, the primarily L-oriented fields are annihilated. This will manifest in a decrease in the total field strength in the region surrounding the reconnection region as the field transitions from 0 nT to ambient levels in a non-reconnecting tail region.

3.3.3 No Alfvénic Ion Exhaust Outflows

One of the universal, landmark features of magnetic reconnection is the acceleration, heating, and evacuation of ions from the reconnection region. This has been shown in event studies and statistically in large sample studies of magnetic reconnection in all regions of space. However, in event studies of electron-only reconnection in Earth's magnetosheath and magnetotail, ions are shown to not respond to the current sheet in the bulk flow velocity. The ions remain at ambient velocities and directions. However, this description is entirely qualitative. When determining if a spacecraft is observing ions that have been accelerated due to reconnection, one calculates if the ion outflow speed exceeds the ambient ion Alfvén speed. The ion Alfvén speed and how to calculate it using spacecraft data was explained in Section 2.2.1.

One note is that some community members argue that reconnection-driven ion jets will not always reach the local ion Alfvén speed – instead exceeding 50% of the ion Alfvén speed. Therefore, when deciding if ions are not being accelerated, we apply a conservative threshold that ion speed does not change from its ambient value by greater than 50%. This excludes any borderline events that have been described in previous works. With this quantitative threshold, we are describing a reconnection event where ions are distinctively not being

accelerated.

3.3.4 Super-Alfvénic Electron Exhaust

During traditional, ion-coupled magnetic reconnection, both ions and electrons are accelerated and heated. Although electrons are heated and accelerated in a much smaller region (EDR) than ions (IDR), the effects of this acceleration and heating manifest on similar scales to the ions. For example, identically to ions, electrons are also accelerated to speeds exceeding the local ion-Alfvén speed in the outflow regions of a reconnecting current sheet. Some community members argue that electrons should exceed the electron Alfvén speed (defined and calculated in Section 2.2.1), but Electron Diffusion Region observations in Earth's magnetotail and magnetopause have displayed that reconnection rarely accelerates electrons to the electron-Alfvén speed, even in the strongest reconnection event observations (July 11, December 10). As a result, much of the community has agreed that electrons exceeding the ion Alfvén speed are accelerated enough to point to reconnection, when paired with the above current sheet criteria and super-Alfvénic ions.

One note is that super-Alfvénic ions and super-ion Alfvénic electrons appear to be coupled in reconnection observations in Earth's magnetotail. There are no examples of super-Alfvénic ions without super-ion Alfvénic electrons. Super-ion Alfvénic electrons without super-Alfvénic ions are more common, but quiet current sheets driven primarily by electrons can readily display this feature. The rest of the criteria later on this list serve to distinguish electron-only quiet current sheets from electron-only reconnection events.

3.3.5 No Ion Temperature Response

Similarly to criterion 3, another, albeit less universal and less distinct, feature associated with a spacecraft observation of magnetic reconnection is the heating of ions. When an ion enters the reconnection region, energy from the magnetic field is transferred to the ions,

resulting in an increase in kinetic energy (acceleration) and thermal energy (heating). In MMS observations, this heating is manifested in the pressure tensor of the ions/electrons, and by proxy, the integrated ion and electron temperatures. A recent study comparing statistical properties of reconnecting current sheets to quiet, non-reconnecting current sheets in Earth's magnetotail showed that ions in a reconnecting current displayed significantly higher temperatures than ions in a quiet current sheet (*Hubbert et al.*, 2022). In addition, from the edge of the current sheet to the current sheet center, ions displayed a statistically significant temperature increase of 10%. This is supported by the August 10th EDR event (See Figure 3.8), which displays a temperature increase of 10%.

During electron-only reconnection, if the ions are not responding to magnetic reconnection, they should not gain thermal energy from the reconnecting fields and remain at ambient temperatures throughout the current sheet. This is supported by the June 17th electron-only event (See Figure 3.6), which does not display a temperature increase, and the August 10th, 2017 EDR event, which does displays a significant change in the ion temperature at the current sheet center.

One note is that this criterion only applies to Earth's magnetotail. For example, in Earth's magnetosheath, where the original electron-only event was found, ion temperatures were very different on either side of the current sheet. As a result, it is much more difficult to detect a local change in ion temperature due to reconnection heating. Similarly, at Earth's magnetopause, which separates two entirely different plasma regimes, the ion temperature profile changes enough due to the regime change that it is also difficult for MMS to resolve reconnection heating using ion temperature. With these other regimes in mind, we conclude that using increase in ion temperature as a reconnection criterion is valid only in Earth's magnetotail and other plasma regimes where plasma conditions are symmetric on each side of the current sheet. One other regime where this criterion is viable is when observing magnetic reconnection in the tail flanks due to Kelvin-Helmholtz instability. One event reported by *Blasl et al.*, 2023 showed electron-only reconnection due to KH in oppositely symmetric

plasma conditions. Other regimes where this criterion is applicable is the subject of future work.

3.3.6 Electron Temperature Response

As described earlier, both electrons and ions are heated during magnetic reconnection, although the heating occurs in different regions. Both are thought to be heated in their respective outflow regions. This manifests in a noted statistical increase in electron temperature of traditionally reconnecting current sheets vs. quiet, non-reconnecting current sheets. Looking at individual events, this heating also manifests in a local increase in temperature at the current sheet center with respect to the current sheet boundary. Quantitatively, we require a temperature increase of 10% to qualify as "significant" heating. This is supported by Figure 3.10.

3.3.7 Positive Peak in $J \cdot E'$

Although magnetic reconnection displays all of the features described above, heating and super-Alfvénic flows are not enough to distinguish reconnection from other flows in Earth's magnetotail such as bursty bulk flows. Fortunately, there are additional features that can be used to distinguish the reconnecting nature of a current sheet.

For example, when looking at a reconnecting current sheet, $J \cdot E'$ can be calculated using MMS time series data. The exact methodology we use to calculate $J \cdot E'$ is described in Section 3.3.7. Physically, $J \cdot E'$ is a local parameter that can describe how the fields and plasma are interacting. In a current sheet, the plasma can transfer energy to the surrounding fields, during which a spacecraft will observe a positive $J \cdot E'$ value. Conversely, surrounding fields can transfer energy to the plasma, during which a spacecraft will observe a negative $J \cdot E'$ value. Whether one expects to see a positive or negative $J \cdot E'$ value depends on which region of a reconnecting current sheet the spacecraft passes through. For example,

the inflow regions and separatrix regions of a reconnecting current are coupled with negative $J \cdot E'$. On the other hand, in the center of each diffusion region, a spacecraft would expect to observe a positive $J \cdot E'$ value. As a result, if a spacecraft primarily passes through a diffusion region in the normal direction, a time series profile of $J \cdot E'$ should change from negative to positive to negative as it passes through one inflow region, the diffusion region, and the opposite inflow region.

Importantly, significantly positive $J \cdot E'$ is not something that a spacecraft will typically observe if it passes through a quiet, non-reconnecting current sheet. By coupling this parameter with the above parameters, we can determine without a doubt whether the current sheet is reconnecting. When we say statistically significant, we calculate the noise in the $J \cdot E'$ profile surrounding the diffusion region. If the $J \cdot E'$ value in the diffusion region is positive and $> 3\times$ the magnitude of the noise, it is considered to be significantly positive.

One note is that $J \cdot E'$ as a parameter is inconsistent when a spacecraft passes through the outflow region. This means that a spacecraft observing reconnection from afar may not observe a significantly positive $J \cdot E'$ at the current sheet center. This restricts our ability to observe electron-only reconnection because only events close to the diffusion region will meet this criterion. Any statistics that come out of this study are thought to be a lower limit because of the difficulty of identifying electron-only reconnection without significantly positive $J \cdot E'$.

3.3.8 Electron Demagnetization

Physically, when ions enter the ion diffusion region, the radius of curvature of the magnetic field approaches the gyroradius of an ion. As a result, the ions transition from a magnetized orbit to a more chaotic orbit. As electrons approach the much smaller electron diffusion region, electrons also transition from a magnetized orbit to a more chaotic orbit. Therefore, a parameter describing whether electrons and ions are magnetized would help glean if a spacecraft is observing reconnection. The frozen-in condition, defined as $E = -v \times B$, is

commonly used to describe whether ions and electrons are magnetized in their orbits. By calculating E and comparing it to the in-situ v and B values, we can see if the local electrons are demagnetized (if E does not equal $-v \times B$) (*Chen et al.*, 2019).

In practice, just calculating E and $-v \times B$ is not what we display in our figures. Instead, we calculate a more physically relevant parameter of the plasma velocity when driven by the $E \times B$ drift. We calculate the expected $E \times B$ drift velocity ($v_{E\times B}$) using $E \times B/B^2$, where E and B are the measured electric and magnetic field vectors, respectively. We then compare $v_{E\times B}$ to the perpendicular electron velocity ($v_{e,\perp}$), which is calculated as $-((v_{e\times B}) \times B)/B^2$. This is an equivalent comparison to comparing $E = -v \times B$, but now we can separate the three components of velocity and determine which components of velocity are most affected by the demagnetization. Plus, as a sanity check, we can compare the plasma-calculated velocity profiles with the bulk flow velocity profiles.

When determining if electrons are demagnetized, we need to determine the quantitative definition of significantly demagnetized. If, in the time series data, the calculated $-v \times B$ value differs from the local E value by greater than 50%, the plasma population is thought to be significantly demagnetized.

3.3.9 Electron Tearing Criterion

As described in Section 1.1.5, the electron tearing instability is the most plausible mechanism by which reconnection is initiated in Earth's magnetotail. In addition, the electron tearing criterion written in Equation 1.10 and repeated below describes if a current sheet is electron tearing unstable, i.e. ripe for reconnection. We expect this condition to hold while observing electron-only reconnection because we expect it to be an electron-scale, transient process that does not significantly disturb the ion-scale or larger magnetotail neutral sheet while in its electron-only phase.

$$\frac{B_N}{B_0}\frac{\delta}{d_i} < \frac{f}{2}\sqrt{\frac{m_e T_e}{m_i T_i}} \tag{3.7}$$

We require our electron-only reconnection candidates to meet this criterion to confirm that the current sheets in question are electron tearing unstable.

3.3.10 Magnetic Flux Transport Criterion

In our set of criteria for identifying electron-only reconnection, we include a reliable criterion for identifying reconnection. This is called the magnetic flux transport (MFT) criterion and utilizes a parameter U_ψ. Defining and deriving U_ψ requires manipulating magnetic field and electric field into the form of the 2D magnetic flux advection equation:

$$\frac{\partial \psi}{\partial t} + (\mathbf{U}_\psi \cdot \nabla_\perp)\psi = 0. \tag{3.8}$$

where $\mathbf{U}_\psi$ has units of velocity and ψ has units of magnetic flux. We determine $\frac{\partial \psi}{\partial t}$ by first establishing a 2D description of magnetic field - an in-plane component (X and Y) and an out-of-plane component (Z, guide field):

$$\mathbf{B} = \hat{\mathbf{z}} \times \nabla\psi + B_0\hat{\mathbf{z}}. \tag{3.9}$$

If we cross Faraday's law with unit z:

$$\hat{\mathbf{z}} \times [\frac{\partial \mathbf{B}}{\partial t} + c(\nabla \times \mathbf{E}) = 0] \tag{3.10}$$

then substitute our form of $\mathbf{B}$, we obtain:

$$\frac{\partial \psi}{\partial t} = cE_z. \tag{3.11}$$

However, this electric field is not in the frame of the electrons. To remedy this, we substitute the z component of the electron momentum equation:

$$\hat{\mathbf{z}} \cdot [\mathbf{E} + \mathbf{v_e} \times \mathbf{B}/c = \mathbf{E'_e}] \tag{3.12}$$

where $\mathbf{E'_e}$ describes the nonideal electric field in the electron frame. This substitution and solving for $\mathbf{U}_\psi$ yields:

$$\mathbf{U}_\psi = \frac{cE_z}{B_p}(\hat{\mathbf{z}} \times \hat{\mathbf{b}}_\mathbf{p}) \tag{3.13}$$

where $\hat{\mathbf{b}}_\mathbf{p} \equiv \mathbf{B_p}/B_p$ is the unit vector of the in-plane magnetic field $\mathbf{B_p}$. U_ψ, with units of velocity, represents the velocity at which flux is being transported into or out of the reconnection region. Its divergence, $\nabla \cdot U_\psi$, with units of $time^{-1}$, describes if magnetic flux is inflowing or outflowing and the timescale at which flux is diverging from the reconnection center. Both U_ψ and $\nabla \cdot U_\psi$ are necessary to define the MFT criterion. Two criteria must be met for an event to be actively reconnecting. First, U_ψ must be Alfvénic ($\geq 0.5 v_A$) in both the X and Y directions. Second, $\nabla \cdot U_\psi$ must be at least on the order of 0.1 electron cyclotron frequency ($\geq 0.1 f_{ce}$).

U_ψ and $\nabla \cdot U_\psi$ can be directly measured or approximated in four-spacecraft missions such as MMS. To calculate U_ψ, we first perform minimum variance analysis to rotate a given current sheet into current sheet LMN coordinates. We then directly measure $E_Z = E_M$, calculate B_p as $\sqrt{B_L^2 + B_N^2}$, and establish $\hat{\mathbf{b}}_\mathbf{p} = \mathbf{B_{L,N}}/B_p$. To approximate $\nabla \cdot U_\psi$, we apply the linear gradient technique (*Chanteur and Harvey*, 1998). An example of the MFT criteria in the context of a dayside EDR observation is shown in Figure 3.15. In Panel F, the L and N components of U_ψ are clearly Alfvénic (the dashed line is the local Alfven speed). In Panel G, $\nabla \cdot U_\psi$ clearly exceeds $0.1 f_{ce}$. As a result, this event represents a positive result for the MFT criteria.

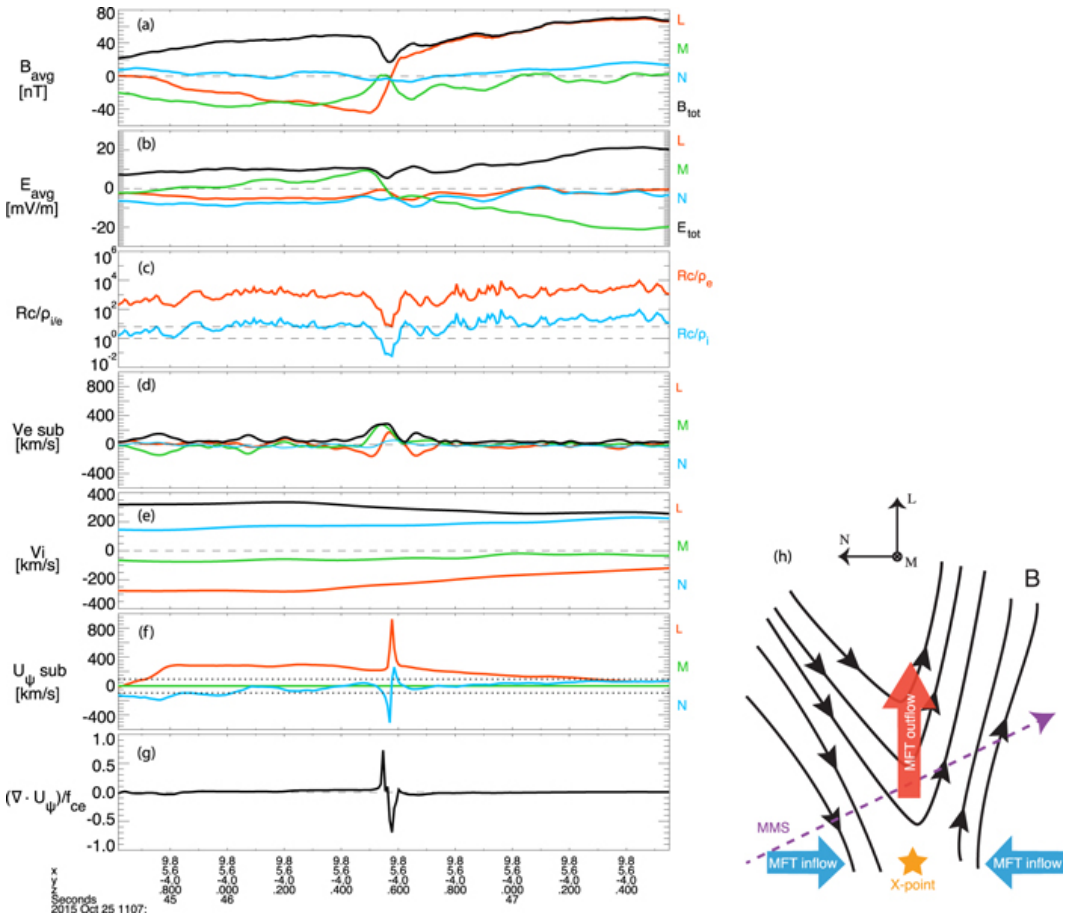

Figure 3.15: MMS observations of an example event on 2015 October 25. Vectors are transformed in LMN coordinates (L = [0.31, −0.91, 0.28], M = [0.31, 0.37, 0.87], N = [−0.90, −0.19, 0.40] in GSE). Four-spacecraft-averaged (a) magnetic field and (b) electric field. (c) Radius of curvature R_c normalized to the electron (red) and ion (blue) gyroradius. (d), (e) Electron bulk flow velocity (with ion velocity subtracted) and ion bulk flow velocity. (f) MFT velocity U_ψ (with ion velocity subtracted). (g) $\nabla \cdot U_\psi$ normalized to the local electron cyclotron frequency f_{ce} (h) Sketch of the MMS trajectory and expected MFT flows, adapted from (*Eriksson et al.*, 2018).

With these methods, *Qi et al.*, 2022 tested the effectiveness of the MFT criteria on 37 community established EDRs and electron-only reconnection events in Earth's magnetosheath,

magnetopause, and magnetotail, including *Phan et al.*, 2018's magnetosheath electron-only flux-rope erosion event and *Wang et al.*, 2018's magnetotail electron-only onset event. As shown in Figure 3.16, all 37 events met both MFT criteria. Although not shown, the MFT criteria also successfully eliminated 50 quiet, non-reconnecting current sheets. This indicates that MFT can and should be used to identify magnetic reconnection in Earth's magnetotail.

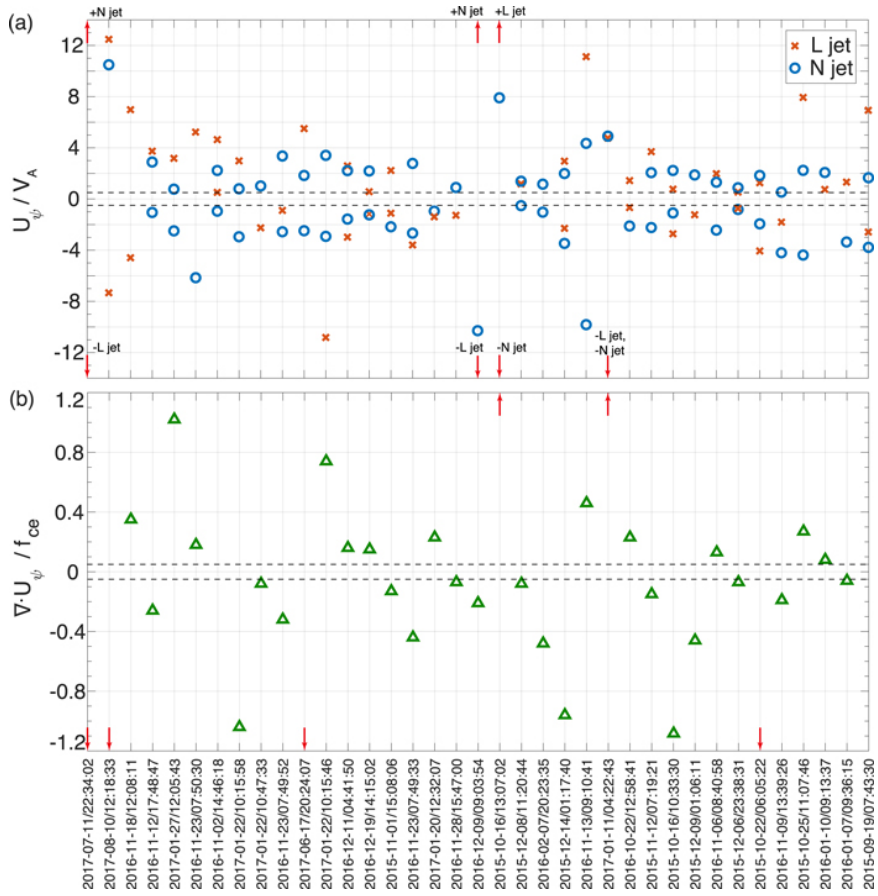

Figure 3.16: MFT signatures in 37 events. The peak values of (a) U_ψ in the L and N directions normalized to v_A and (b) $\nabla \cdot U_\psi$ normalized to f_{ce}. The red arrows indicate L/N jets and $\nabla \cdot U_\psi$ out of the plotted range. The dashed lines represent (a) $\pm$ 0.5 v_A and (b) $\pm$ 0.05 f_{ce}.

3.4 Conclusions & Interpretations

In this chapter, we have displayed three magnetotail reconnection events. Two events, on 8/14/17 and 8/23/17, display features of electron-only flux rope erosion. One event, on 6/17/17, displays features of electron-only onset of reconnection. We distinguish between these two processes using the electron energy spectra and pitch angle distribution. Lastly, we establish universal criteria for identifying electron-only flux rope erosion and electron-only onset of reconnection in Earth's magnetotail using MMS. Establishing these universal criteria presents a nomenclature problem inherent in the name electron-only reconnection. Previous reports of electron-only flux rope erosion, electron-only onset of reconnection, and other processes in Earth's magnetotail have been dubbed electron-only reconnection, presumably inspired by the name used in *Phan et al.*, 2018's landmark observation. However, when investigating Earth's magnetotail, this nomenclature is inappropriate. Electron-only flux rope erosion is a steady-state process that excludes ions because the current sheet is not wide or long enough to couple with ions, and electron-only onset of reconnection is a time-dependent transition phase that excludes ions because ions have not had time to respond to the reconnection.

CHAPTER 4

Statistical Survey of Electron-Only Reconnection

In this chapter, we have surveyed MMS data during six magnetotail seasons and report on sets of quiet current sheets, electron-only reconnection, and traditional reconnection observed in the tail current sheet.

4.1 Observational Criteria of Electron-Only Reconnection

In this chapter, we do not distinguish between electron-only flux rope erosion events from electron-only onset of reconnection events until Section 4.5. Using the criteria described in Section 3.3, we have identified twelve MMS observations of electron-only reconnection in the near-Earth magnetotail. We used the following criteria: 1. Current Sheet Crossing (B_L reversal), 2. Absolute B_{tot} minimum, 3. Lack of ion exhaust jets ($v_{iL} < 0.5 v_{iA}$, no v_{iL} reversal), 4. Super-Alfvénic electron exhaust jets ($v_{eL} > v_{iA}$), 5. Lack of total T_i response ($< 10\%$), 6. Significant T_e energization ($> 10\%$), 7. Positive $J \cdot E'$, 8. Deviation of $v_{e,\perp}$ from $v_{E\times B}$, 9. Electron Tearing Criterion (See Equation 1.10), and 10. Magnetic Flux Transport Criteria (Alfvénic U_ψ, $\nabla \cdot U_\psi > 0.1 f_{ce}$).

4.2 Data Collection & Dataset Description

Given the criteria listed above, we found 12 electron-only reconnection events over six MMS tail seasons (June 15 - August 31 2017, June 15 - August 31 2018, July 1 - September 15 2019, July 1 - September 15 2020, July 15 - September 30 2021, July 15 - September 30 2022). Red events are electron-only reconnection events, and black events are electron-only onset of reconnection events. Events in this paper were found during MMS Phase 2B (June-August 2017), 3B (June-August 2018), 4B (June-August 2019), and 5B (June-August 2020), when MMS was in the low-latitude magnetotail with an apogee of 25 R_E (See Figure 1.9). Times and locations of electron-only reconnection candidates from this manuscript are shown in Table 4.1. We note that no events were found during the 2021 or 2022 seasons. We attribute this to MMS's prolonged duration in negative GSM Z, far from the magnetotail neutral sheet. This prolonged period in negative Z GSM affected the observation rate of all current sheet types in this thesis (See Table 4.2).

Table 4.2: Occurrence of Quiet current sheets (Column 1), traditional reconnection (Column 2), IDRs (Column 3), and electron-only reconnection (Column 4) by year.

	Quiet CS	**Trad Reconnection**	**IDRs**	**EO Reconnection**
2017	47	72	15	5
2018	100	83	9	1
2019	86	117	11	2
2020	136	88	10	4
2021	73	35	1	0
2022	34	15	3	0

Table 4.1: Electron-only Reconnection (Column 1) Event Number, (Column 2) Event Time Interval, (Column 3-5) Current Sheet Normal Orientation (GSM), (Column 6) Current Sheet Thickness in electron inertial lengths ($d_e = c(4\pi n_e e^2/m_e)^{-1/2}$) where n_e is the surrounding lobe electron number density, (Column 7) Current Sheet Thickness in kilometers normalized to the electron thermal gyroradius ($\rho_{th} = v_{T_e}/\omega_{ce}$) using B_0, the value of B_L and the observed current sheet boundary, and T_e, (Column 8) Current Sheet Normal Speed, (Column 9-11) MMS Spacecraft Location (GSM), and (Column 12) the ratio of the maximum observed L-directed ion bulk flow speed to the local ion Alfvén speed. Each event's largest current sheet normal component is bolded. Red events are electron-only reconnection events and black events are electron-only onset of reconnection events. Events 1-3 are used in Section 6 to analyze electron-only reconnection's evolution in time. Cells labelled N/A could not be calculated because MMS4 did not provide data for the given interval.

		CS Normal Direction			**CS Thickness**		**Norm. Speed**	**MMS Location**				
#	**Time Interval**	**X**	**Y**	**Z**	[$\mathbf{d_e}$]	[$\mathbf{km/\rho_{th}}$]	**[km/sec]**	**X[$\mathbf{R_E}$]**	**Y[$\mathbf{R_E}$]**	**Z[$\mathbf{R_E}$]**	$\mathbf{v_{iL,max}/v_{iA}}$	$\mathbf{B_M/B_0}$
1	7-20-17/09:59-10	0.36	0.88	-0.29	9.3	16.8	77	-21.6	7.9	1.3	0.21	0.33
2	6-17-17/20:24-25	0.18	-0.93	-0.33	10	27.2	69	-19.3	-11.1	3.5	0.32	0
3	7-26-17/17:39-40	0.65	0.75	0.03	72	113.2	284	-23.5	6.4	4.6	0.42	0.29
4	8-14-17/18:56-57	0.98	0.12	-0.18	12	61.2	240	-18.5	15.5	1.3	0.45	0.16
5	8-23-17/11:19-20	-0.48	0.33	-0.81	11	55.9	210	-18.1	17.1	-3.4	0.17	0.9
6	7-26-18/13:05-06	-0.58	0.73	-0.36	60	86.5	120	-18.7	7.0	4.2	0.49	0.14
7	7-05-19/01:55-56	0	0.51	0.86	N/A	N/A	N/A	-17.4	-15.6	2.6	0.14	0.9
8	8-31-19/11:30-31	0.3	0.9	-0.32	10.4	9.2	66	-12.5	13.2	0.4	0.27	0.98
9	8-03-20/00:35-36	0.14	0.25	0.97	N/A	N/A	N/A	-28	-5	1	0.23	0.7
10	8-05-20/19:42-43	-0.92	0.24	-0.32	2.5	1.5	30	-27	0	4	0.16	0.78
11	9-09-20/20:06-07	-0.89	-0.43	0.11	6.3	12.9	13.4	-23	15	4	0.19	0.5
12	9-13-20/02:43-44	0.26	-0.07	0.96	7.7	10.2	98	-20	15	5	0.49	0.3

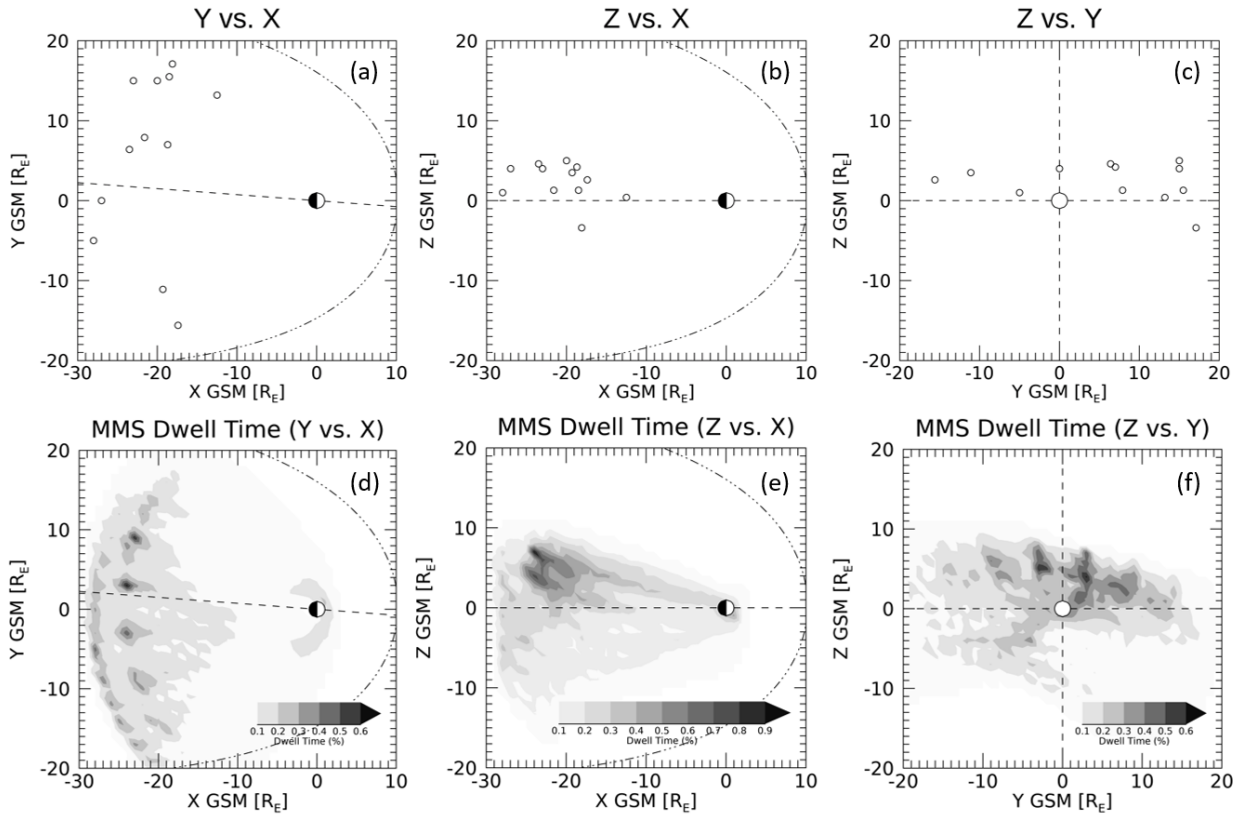

Figure 4.1: 2D slices of locations of electron-only reconnection candidates (top) and MMS dwell time (bottom) ranging from 2017-2022. (a,d) GSM Y vs. GSM X, (b,e) GSM Z vs. GSM X, (c,f) GSM Z vs. GSM Y. Dashed lines indicate (a,d) Midnight shifted due to solar wind aberration, (b,e) $Z = 0$, and (c,f) $Y = 0, Z = 0$.

Although the sample size is small, we can make a few notes about of our events. All but one event are located in positive Z GSM, 7 of 12 events are located in the dusk sector, and our events do not appear to favor the midnight sector vs. the flanks. Positive Z GSM is consistent with MMS's typical mangetotail orbit (See Figure 1.9) and the positive deflection of the magnetotail neutral sheet, favoring the dusk side is consistent with dawn-dusk reconnection asymmetry in the magnetotail, and the wide spread in Y of event locations is consistent with the broad region at which reconnection occurs. We note that the one event located in negative Z GSM was observed in 2017. This is unusual because, while MMS spends a

minority of its dwell time in negative Z GSM, the 2021 and 2022 were the years that MMS spent the most of its time in negative Z GSM.

4.3 Notable Features In Electron-Only Reconnection

4.3.1 Current Sheet Thickness & Normal

Using the four-spacecraft timing method (*Russell et al.*, 1983) on the B_x measurement, we calculated the current sheet normal orientation, speed (See Table 4.1, and Figure 4.2). These values are consistent throughout each crossing. We calculate current sheet thickness by multiplying the temporal width of each perpendicular current (in sec) enhancement with each current sheet normal speed in km/sec. This thickness is converted to electron inertial lengths (d_e) using the upstream electron number density ($d_e = c * (4n_e e^2/m_e)^{-1/2}$).

2D projections of each event's location, current sheet normal velocity, and current sheet thickness (See Table 4.1) are plotted in Figure 4.2. In the XY plane, the current sheet center is rotated to account for solar wind aberration due to Earth's orbit. 2D projections of current sheet normal velocity are presented as arrows whose midpoints are fixed at the event location. An arrow's length and direction indicate a 2D projection of the current sheet normal speed and orientation, respectively. Meanwhile, current sheet thickness during each event is presented as shaded points. The shade of each point indicates its current sheet thickness in d_e. These events appear in both the dawn and dusk sectors, and are all located in positive GSM Z. We attribute this to MMS surveying mostly positive GSM Z during Phases 2B and 3B. These events are typically composed of slow (200 km/sec) current sheets split evenly in orientation between GSM Y and Z. No current sheets are moving primarily in the GSM X direction. Events range in thickness from sub-ion scale ($\approx 8d_e$) to ion scale ($\approx 2.1d_i$), indicating that these thin current sheets need not be sub-d_i to occur.

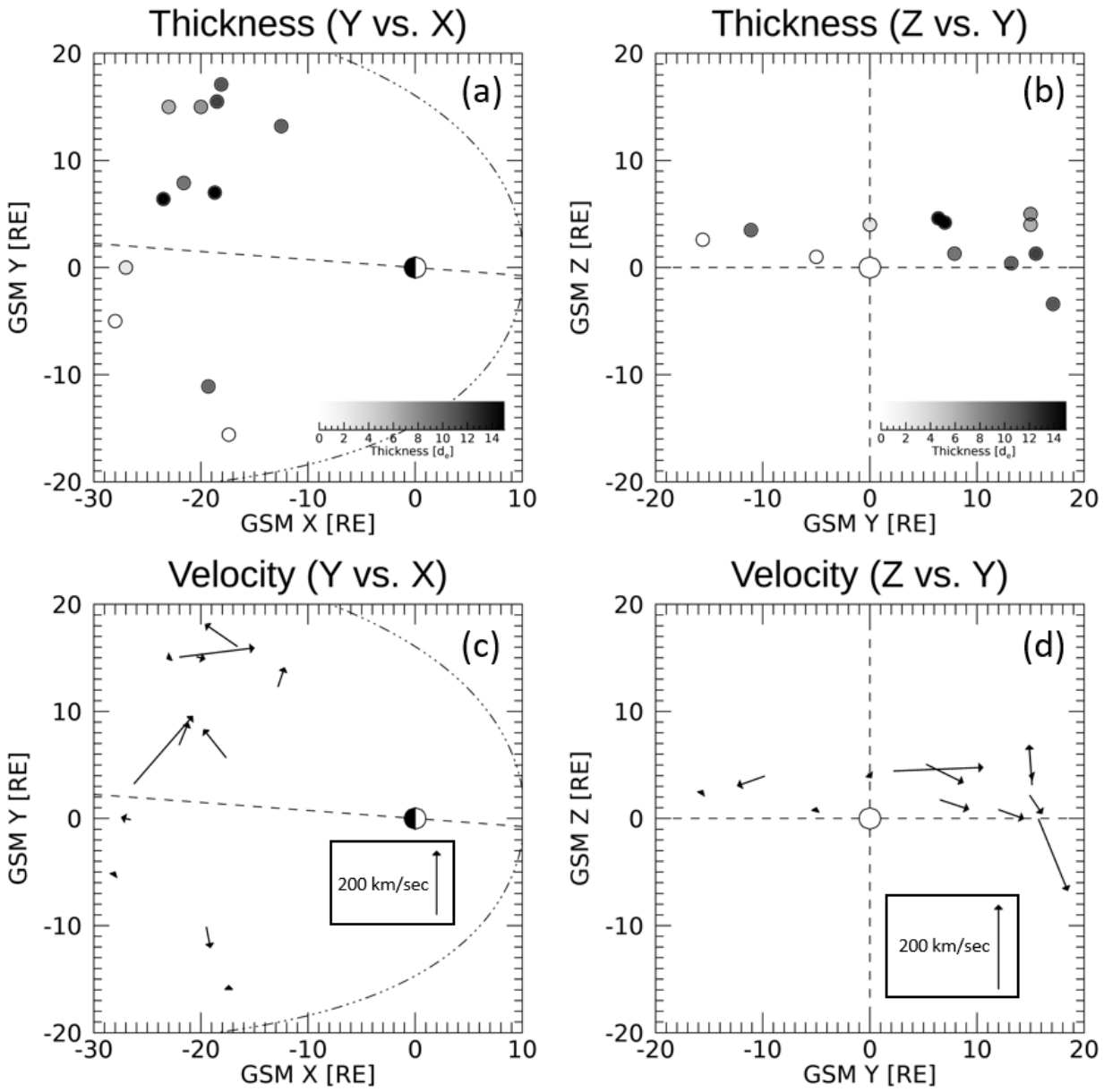

Figure 4.2: Projection of event locations, current sheet normal orientation (arrow direction), and current sheet normal speed (arrow length) onto the (a) XY GSM and (b) YZ GSM plane. Projection of event location (point) and current sheet thickness in d_e (shading) onto the (c) XY GSM and (d) YZ GSM plane. Boxed arrows in panels (a,c) indicate the arrow length of a speed projection of 200 km/sec. Dashed lines in panels (a,c) are tilted by the aberration of solar wind due to Earth's orbital motion. Events labeled in panels (a,b) are used to postulate the time evolution of electron-only reconnection in Section 4.5.3.

Although the magnetotail current is thought to have a traditional orientation with its normal direction in the Z direction, the sheet often flaps and changes in orientation (ex. the Y direction). As found in Section 2.3, MMS consistently observes magnetotail reconnection in current sheets oriented primarily in the GSM Y direction, which differs from our previous understanding of magnetic reconnection.

4.3.2 Guide Field

Similar to "traditional" magnetotail reconnection, the role of guide field in electron-only reconnection is very important in determining its driving mechanisms and influence on the surrounding plasma. I determine the guide field of my electron-only events identically to the method used to calculate guide field in my traditional reconnection events. In Figure 4.3, I present the guide field as a color shader in several 2D projections (XY, XZ, YZ [GSM]) of my event pool.

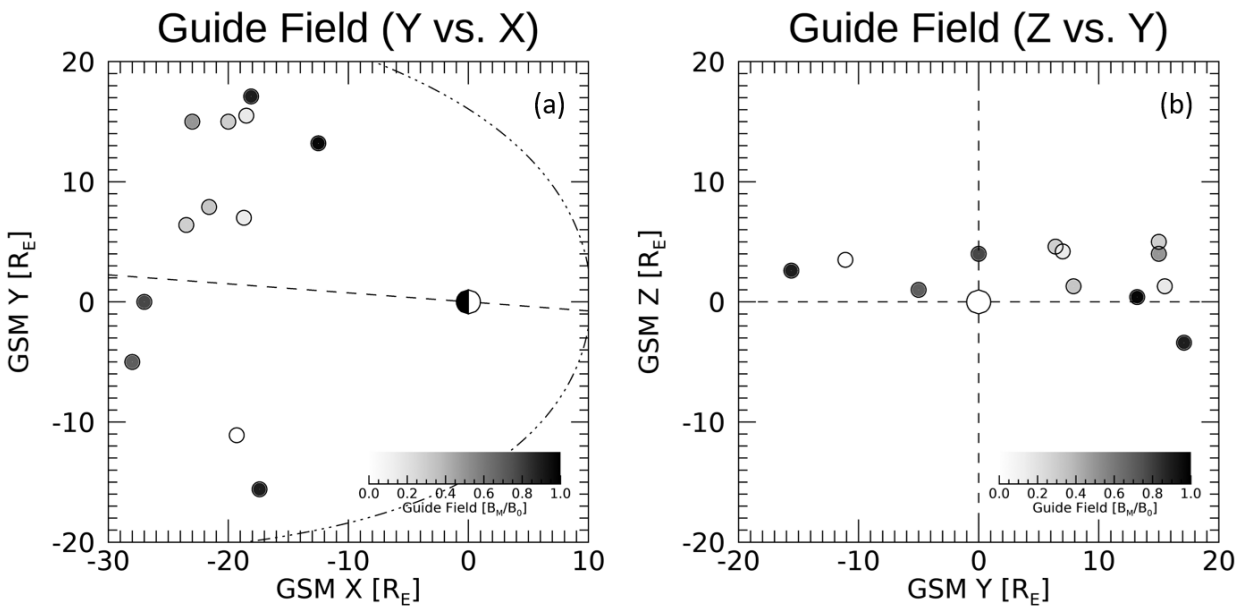

Figure 4.3: Projection of event locations, guide field onto the (a) XY GSM and (b) YZ GSM plane. Dashed lines in panel (a) is the aberration of solar wind due to Earth's orbital motion.

As shown above, the majority of electron-only events occur in a plasma environment with at least moderate guide field ($B_G/B_0 > 0.2$). In addition, 5 of 12 events occur in high guide field ($B_G/B_0 > 0.5$). This distribution appears to be independent of event location and solar wind conditions. This guide field presence is not typical in traditional reconnection but is consistent with *Phan et al.*, 2018's electron-only reconnection event and the electron-only events found in Section 3.1.2. This indicates that, even in Earth's magnetotail, the base conditions at which electron-only reconnection occurs differ strongly from those during traditional reconnection (See Figure 4.3). Turbulent regions with strong guide field are present in Earth's magnetosheath, but occur much less frequently in Earth's magnetotail. As such, it is notable that high guide field still manifests in Earth's magnetotail, despite not selecting for it with our electron-only reconnection criteria.

4.3.3 $\tilde{\Delta}$ Parameter

A qualitative survey of our 12 electron-only reconnection candidates indicates that all our events displayed an increase in the plasma number density at the current sheet center with respect to the current sheet boundary. For example, in panel E of Figure 3.6 displaying the 6/17/17 event, the electron number density increases by greater than 10% from the asymptotic value of 0.55 $\#/cm^3$ to a central value of 0.7 $\#/cm^3$.

To quantify this increase, we developed a parameter called $\tilde{\Delta}$ which describes the extent to which the number density at the current sheet center changes with respect to the current sheet boundary. We define $\tilde{\Delta}$ below:

$$\tilde{\Delta} n_e = (n_{e,center} - n_{e,PSB})/n_{e,PSB} \tag{4.1}$$

Using this parameter, we can determine whether the given variable increases or decreases at the current sheet center ($n_{e,center}$) with respect to the current sheet boundary ($n_{e,PSB}$), and by how much normalized by the asymptotic value of the variable. Given the noise level of

plasma density data, we assume that a $\tilde{\Delta}$ value from $-0.1 < \tilde{\Delta} < 0.1$ indicates no significant change, while $\tilde{\Delta} > +0.1$ indicates a significant increase and $\tilde{\Delta} < -0.1$ indicates a significant decrease. In the 6/17/17 example, $\tilde{\Delta}n_e = +0.31$, indicating a significant increase in the plasma density at the current sheet density and supporting our initial interpretation made with visual inspection. Values of $\tilde{\Delta}n_e$ and $\tilde{\Delta}n_i$ can be found in Table 4.3, which quantifies and supports our visual inspected interpretation that all 12 events display significantly increased plasma density at the current sheet center.

Table 4.3: $\tilde{\Delta}n_e$ and $\tilde{\Delta}n_i$ for our 12 electron-only reconnection candidates. Green cells indicate $\tilde{\Delta}$ values above 0.1, white cells indicate $\tilde{\Delta}$ values between -0.1 and 0.1.

EO Reconnection

Time	$\tilde{\Delta}n_e$	$\tilde{\Delta}n_i$
2017-06-17/20:24:00-20:24:10	0.31	0.16
2017-07-20/09:59:30-09:59:35	0.13	0.09
2017-07-26/17:39:36-17:39:39	0.21	0.37
2017-08-14/18:56:35-18:56:41	0.07	0.12
2017-08-23/11:19:14-11:19:16	0.15	0.04
2018-07-26/13:05:00-13:05:15	0.10	0.03
2019-07-05/01:55:40-01:55:50	0.41	0.33
2019-08-31/11:30:25-11:30:35	0.05	0.12
2020-08-03/00:35:50-00:36:00	0.11	-0.03
2020-08-05/19:42:31-19:42:36	0.12	-0.03
2020-09-09/20:06:10-20:06:20	0.25	0.12
2020-09-13/02:43:45-02:44:00	0.52	0.40

4.3.4 Agyrotropy Parameter $\sqrt{Q_{P_e}}$

Swisdak, 2016 derived a scalar parameter, popularly known as the agyrotropy parameter ($\sqrt{Q}$), whose purpose was to measure the gyrotropy of an arbitrary pressure tensor in the form of a time series. A pressure tensor by definition can be written as a symmetric positive semi-definite matrix, meaning that the determinants of all submatrices created by deleting the same number row and column (i.e. row 1 and column 1, row 2 and column 2, row 3 and column 3) are nonnegative. To visualize this, we first establish an arbitrary pressure tensor below:

$$P = \begin{bmatrix} P_{\parallel} & P_{12} & P_{13} \\ P_{12} & P_{\perp} & P_{23} \\ P_{13} & P_{23} & P_{\perp} \end{bmatrix}. \tag{4.2}$$

Then, because this tensor is symmetric positive semidefinite, we obtain the following inequalities:

$$P_{12}^2 \leq P_{\parallel} P_{\perp} \qquad P_{13}^2 \leq P_{\parallel} P_{\perp} \qquad P_{23}^2 \leq P_{\perp}^2. \tag{4.3}$$

When we add these inequalities, we obtain a scalar value:

$$Q = \frac{P_{12}^2 + P_{13}^2 + P_{23}^2}{P_{\perp}^2 + 2P_{\parallel} P_{\perp}}. \tag{4.4}$$

Q was designed to be a natural measure of gyrotropy, where $Q = 0$ indicated a fully gyrotropic tensor, and $Q = 1$ indicated a maximally agyrotropic tensor. While raw, instrument-produced pressure tensors may not be in the form given by Equation 4.2, they can be easily rotated into a frame where it is in the form of Equation 4.2.

Magnetic reconnection of all forms is known to produce significant electron agyrotropy (*Burch et al.*, 2016b). As a result, elevated Q_{P_e} ($\sqrt{Q_{P_e}} > 0.1$) has been frequently used

to identify regions of electron agyrotropy in both simulations and spacecraft observations (*Walker et al.*, 2018; *Genestreti et al.*, 2017). Specifically, the simulation shown in the left column of Figure 4.4 highlights regions of $\sqrt{Q_{P_e}} > 0.2$ in black, and the MMS observation in the right column of Figure 4.4 uses a spike of $\sqrt{Q_{P_e}} > 0.1$ in Panel F to support the interpretation that they are observing magnetic reconnection.

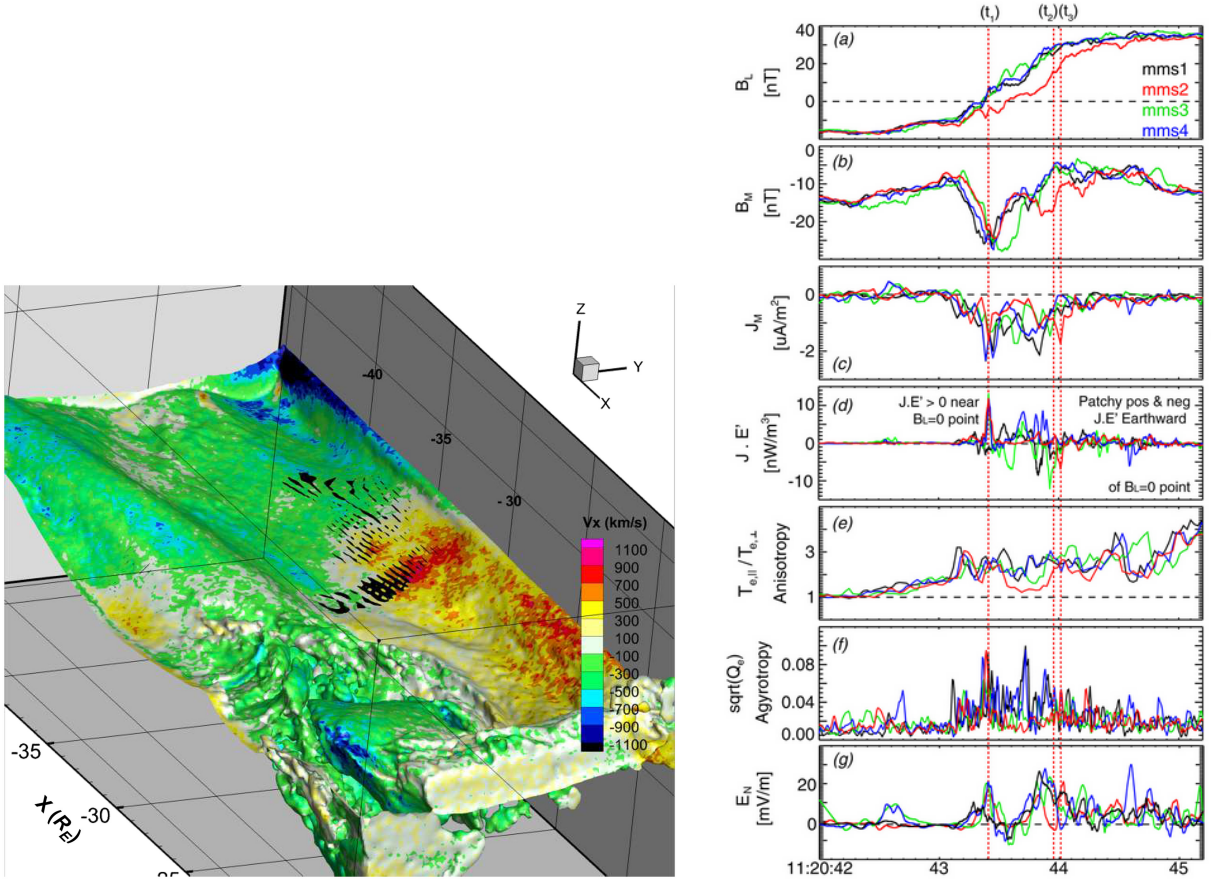

(a) (b)

Figure 4.4: LEFT: 3D simulation of equatorial magnetotail current sheet defined by $B_x = 0$. Adapted from (*Walker et al.*, 2018). RIGHT: Four spacecraft reconnection observation from 12/8/15. Adapted from (*Genestreti et al.*, 2017). MMS1 (black), MMS2 (red), MMS3 (green), and MMS4 (blue). (a) B_L, (b) B_M, (c) J_M, (d) Energy conversion $J \cdot E'$, (e) electron anisotropy ($T_\parallel / T_\perp$), (f) the electron agyrotropy ($\sqrt{Q_{P_e}}$), and (g) E_N.

Despite $\sqrt{Q_{P_e}}$'s intended purpose of identifying reconnection in simulations and time series data, the effectiveness of this parameter in identifying reconnection in Earth's magnetotail has not been rigorously tested. To address this, we calculated $\sqrt{Q}$ across the current sheet crossings of our 12 electron-only reconnection candidates and 15 community established magnetotail IDRs and EDRs to investigate its effectiveness. We find that only 3 of our 12 electron-only reconnection events meet the $\sqrt{Q_{P_e}} > 0.1$ standard used in previous spacecraft event studies, and only one meets the $\sqrt{Q_{P_e}} > 0.2$ standard used in *Walker et al.*, 2018. In addition, we find that only 7 of the 15 IDRs and EDRs meet the $\sqrt{Q_{P_e}} > 0.1$ standard. This indicates that $\sqrt{Q_{P_e}} > 0.1$ is not a consistent identifier of reconnection in Earth's magnetotail, electron-only or traditional.

We conclude that $\sqrt{Q_{P_e}}$ is not a reliable parameter in Earth's magnetotail for two reasons. First, Earth's magnetotail has a lower plasma density than other regions of Earth's magnetosphere. This lower density results in greater noise in $\sqrt{Q_{P_e}}$, making it more difficult to identify spikes in $\sqrt{Q_{P_e}}$. Multiple events displayed $\sqrt{Q_{P_e}} > 0.1$ throughout the entire interval, making it impossible to discern if $\sqrt{Q_{P_e}} > 0.1$ at the current sheet center has any physical significance. Second, the pressure tensor used to calculate Q_{P_e} is integrated over all electron energy levels. This means that agyrotropy present at solely lower energies may be obscured by the global integration (*Argall et al.*, 2018). Previous work has found that lower energy ($\approx 66eV$) agyrotropic crescent populations can be masked if they mix with a denser, gyrotropic background population. We posit that calculating a "filtered" energy tensor only at low energies or only at high energies would display more significant enhancements in regions of interest. We note that in other regions of space, such as Earth's magnetopause, the plasma density is greater and, as a result, is more likely to yield reliable results from $\sqrt{Q_{P_e}}$.

Lastly, we find a strong correlation between $\sqrt{Q_{P_e}}$ and guide field in our electron-only reconnection candidates ($p = 0.82$), as shown in Figure 4.5. We note that the event featuring the highest $\sqrt{Q_{P_e}}$ deviates from this trend, displaying greater guide field than predicted by the trend line. We hypothesize that this is due to the method we use to calculate guide field

and $\sqrt{Q_{Pe}}$. In our methodology, the maximum possible guide field and $\sqrt{Q_{Pe}}$ are both 1.0. Unless the highest possible observable $\sqrt{Q_{Pe}}$ is 0.2, then a wide range of $\sqrt{Q_{Pe}}$ values is not accounted for in this plot. This increases the uncertainty of the fit line, especially at high guide fields. We leave the physical explanation for this as a subject for other future studies.

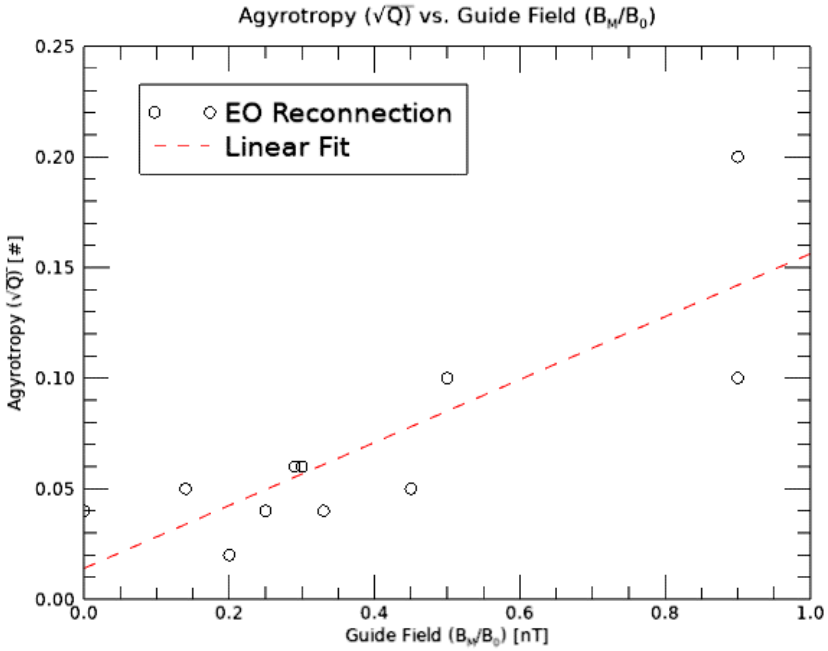

Figure 4.5: Agyrotropy ($\sqrt{Q_{Pe}}$) vs. Guide Field (B_M/B_0) for 12 electron-only reconnection candidates, and linear fit (red). Correlation value of p = 0.82.

4.3.5 X-Line Location

We can use the direction of reconnection outflow to interpret whether MMS crossed the reconnection region Earthward or tailward of the X-line. If MMS observes negative v_{eX} GSM outflow, then the spacecraft is tailward of the X-line, and if MMS observes positive v_{eX} GSM outflow, then the spacecraft is Earthward of the X-line. Of the 12 events, 7 were observed Earthward of the X-line and 5 were observed tailward of the X-line. On average, our events are $\approx 25\ R_E$ away from Earth, which is consistent with the expected location of

the near-Earth X-line.

4.4 Distinguishing Electron-Only Reconnection from Ion-Coupled Reconnection

4.4.1 Observational Criteria of Quiet Current Sheets, Ion-Coupled Reconnection, & IDRs

As described in **Chapter 2**, when identifying quiet current sheets, we require: 1. A B_L reversal, 2. An Absolute B_{tot} minimum, 3. No L-directed ion exhaust outflow ($|v_{iL}| < 0.5v_{iA}$) near the B_L reversal point, 4. No L-directed electron exhaust outflow ($|v_{eL}| < v_{iA}$) near the B_L reversal point, and 5. No significantly positive $J \cdot E'$.

Also as described in **Chapter 2**, when identifying traditional, ion-coupled reconnecting current sheets, we require: 1. B_L reversal, 2. Absolute minimum in B_{tot}, 3. L-directed ion exhaust outflow ($|v_{iL}| > 0.5v_{iA}$) within 60 seconds of the B_L reversal point and 4. Super-Alfvénic L-directed electron exhaust outflow ($|v_{eL}| > v_{iA}$) within 60 seconds of the B_L reversal point. We do not distinguish between bursty bulk flows (BBFs) (*Angelopoulos et al.*, 1992), IDRs, and EDRs in our survey. Thus, any tail current sheet crossing containing strong ion and electron exhaust outflows is attributed to reconnection.

Lastly, as described in **Chapter 2**, when identifying ion-coupled IDRs, we require: 1. B_L reversal, 2. Absolute minimum in B_{tot}, 3. L-directed ion exhaust outflow ($|v_{iL}| > 0.5v_{iA}$) near the B_L reversal point, 4. Super-Alfvénic L-directed electron exhaust outflow ($|v_{eL}| > v_{iA}$) near the B_L reversal point, 5. Reversals in B_N and V_{iL}, 6. Significant electric field signatures, 7. Significant Hall magnetic field signatures, and 8. Radius of curvature of the reconnecting magnetic field dipping below d_i.

4.4.2 Dataset of Quiet Current Sheets, Ion-Coupled Reconnection, IDRs, & Electron-Only Reconnection

Given the criteria listed above, we found 476 quiet current sheets, 407 ion-coupled reconnection events, and 49 IDRs over six MMS tail seasons (June 15 - August 31 2017, June 15 - August 31 2018, July 1 - September 15 2019, July 1 - September 15 2020, July 15 - September 30 2021, July 15 - September 30 2022). Events in this thesis were found during MMS Phase 2B (June-August 2017), 3B (June-August 2018), 4B (June-August 2019), and 5B (June-August 2020), when MMS was in the low-latitude magnetotail with an apogee of 25 RE (See Figure 1.9). Times and locations of the quiet, non-reconnecting current sheets, ion-coupled reconnection events, and IDRs can be found in Section A.2.

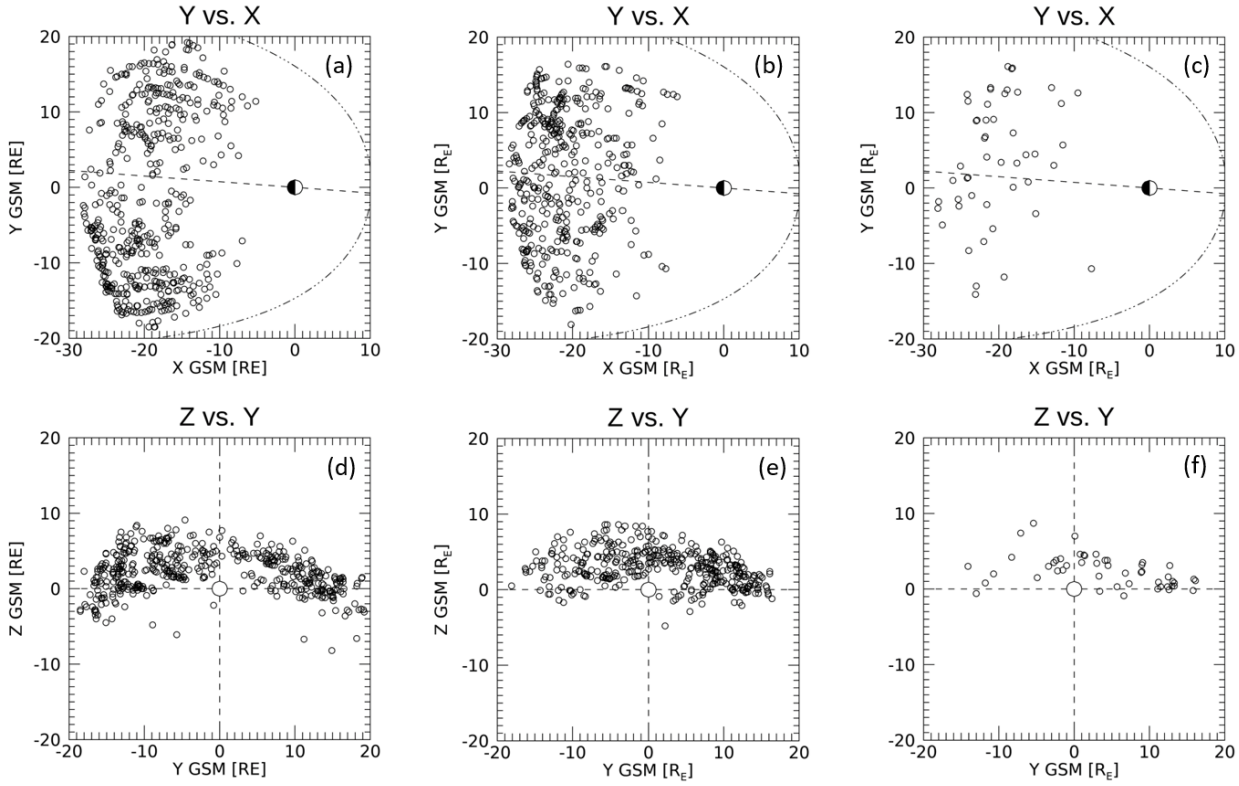

Figure 4.6: 2D cuts of quiet current sheet event locations in the (a) X-Y plane and (b) Y-Z plane. 2D cuts of traditional reconnection event locations in the (c) X-Y plane and (d) Y-Z plane. 2D cuts of IDR event locations in the (e) X-Y plane and (f) Y-Z plane. All locations are plotted in GSM coordinates.

In this study, we have identified many quiet magnetotail current sheets and traditional reconnection events. Figure 4.6 shows 2D cuts of event location for each current sheet type. Quiet current sheets and ion-coupled reconnection have approximately identical location distributions. MMS spent the vast majority of each tail season in positive GSM Z (See Figure 2.5), which explains the Northward bias in event location. We note the importance of electron-only reconnection occurring everywhere that traditional reconnection occurs. This supports the picture of the two processes being coupled or occurring in identical current sheet conditions.

4.4.3 Solar Wind Driving & AE Index Response

To understand how traditional reconnection differs from electron-only reconnection, we need to analyze the differences in the features of the solar wind, which are the primary drivers of most reconnection events found in the tail. Specifically, Solar Wind Dynamic Pressure (SWDP), solar wind speed, and IMF B_z are thought to be the most direct drivers of the reconnection rate and location in Earth's magnetotail. We note that 12 electron-only reconnection events are being split into 20 bins, so the electron-only reconnection bins are highly unreliable given the significant uncertainty due to statistics of small numbers. However, when determining if a median electron-only reconnection value is statistically significantly different from the median values of other parameters, we calculate the uncertainty of the median and assess if the differences are within the uncertainty.

To paint a more complete picture of the differences between traditional and electron-only reconnection, we compare the following solar wind characteristics: IMF B_y/B_z, SW $n_i/V_{tot}/V_x/V_y/V_z$, and SWDP. Despite the disparity in event number between the two phenomena, there appears to be no significant difference between these process's solar wind driving conditions. This finding is consistent with the interpretation that electron-only reconnection is a time dependent phase coupled with traditional reconnection, as one would expect the same process to be driven by the same solar wind conditions (see Figure 4.7). Specifically, we expect biases towards Southward IMF B_z turning prior to tail reconnection observation, and we expect tail reconnection to occur in the region of the magnetotail corresponding to the IMF B_y direction. Both features are present in both EO and traditional reconnection. In Section 4.4.6, we will repeat this analysis and replace the blue traditional reconnection events with red IDR events.

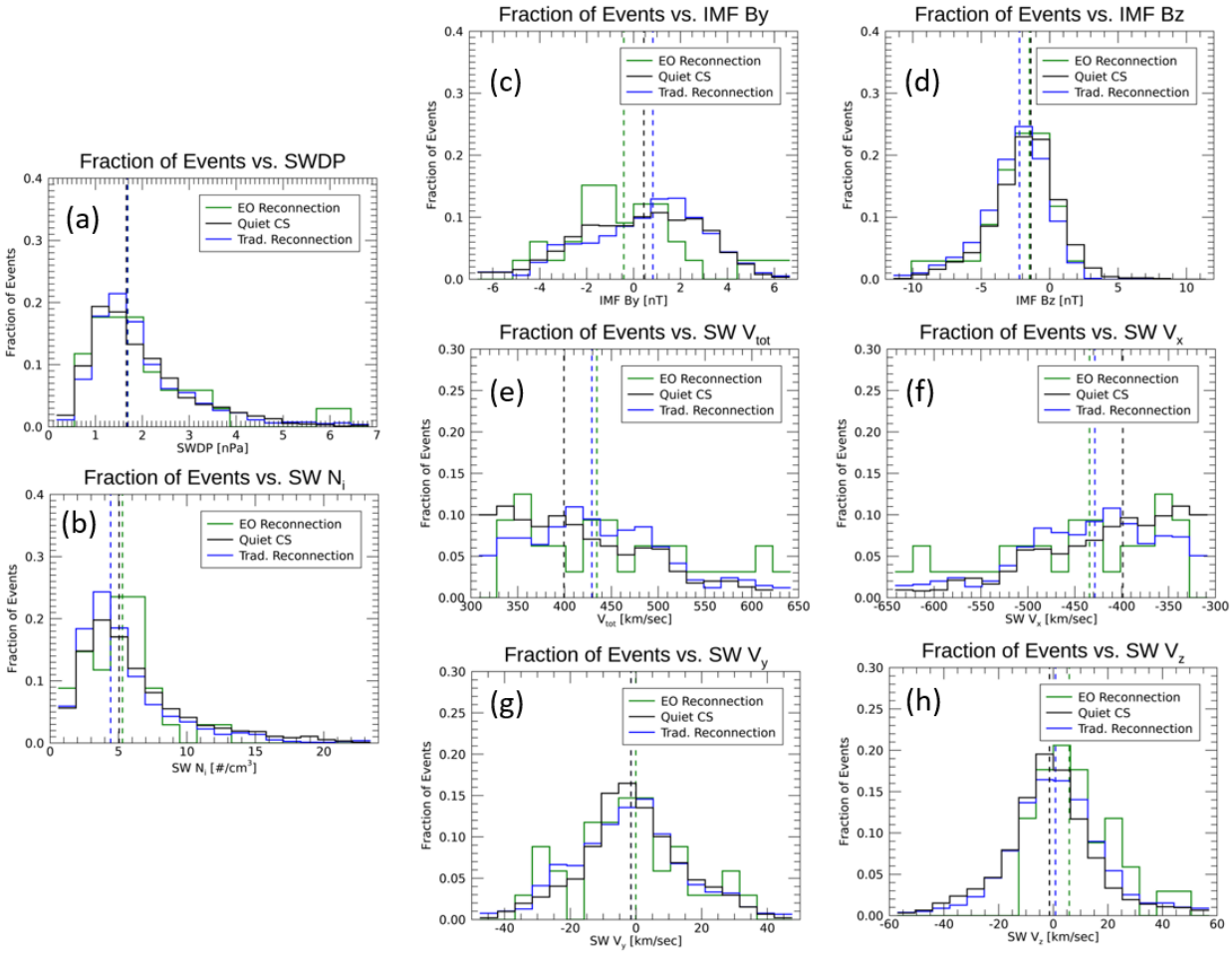

Figure 4.7: Histograms (with overlapping bins) of various solar wind properties in the hour prior to each quiet current sheet (black), electron-only reconnection (green), and traditional reconnection (blue) observations. Average (a) Solar wind dynamic pressure, (b) solar wind density, (c) IMF B_y, (d) Solar wind v_tot, (e) Solar wind v_y, (f) IMF B_z, (g) Solar wind v_x, and (h) Solar wind v_z prior to each current sheet observation.

Figure 4.7 displays several histograms of various solar wind driving conditions corresponding to each process. Solar wind conditions are found using 1 minute resolution OMNI data located at Earth's magnetopause. All solar wind field and plasma values (except IMF B_z) represent the average value of each parameter found by OMNI over the hour prior to

each current sheet observation. We extracted the minimum IMF B_z value for the hour prior to each current sheet observation for multiple reasons. First, averaging the IMF B_Z will drown out finer structures that occur during the hour. To highlight this, we compare two hypothetical intervals. In one interval, IMF B_Z is south for 30 minutes and north for 30 minutes, and in another interval, IMF B_Z is steady and zero for the entire hour. In both events, the average IMF B_Z would equal zero. However, the event that featured 30 minutes of negative IMF B_Z is much more likely to generate reconnection than the event with steady, zero IMF B_Z. Second, Southward IMF B_z turning has a higher correlation with triggering reconnection and substorms than sustained southward IMF B_z (**?**). We note that our method is limited in that extracting the minimum IMF B_Z value equally weights events with sustained negative IMF B_Z and events with a relatively short IMF B_Z southward turning. We value resolving IMF B_Z turning over the duration of Southward IMF B_Z.

These mean/minimum solar wind parameter values are placed in histograms corresponding to each current sheet type. Then, we overlap the bins by summing up each bin value with the values of surrounding bins. These sums become the new value for each bin and are renormalized. The number of bins corresponding to each current sheet type was found by calculating $\sqrt{n}$, where n is the number of events. This helps account for the statistical uncertainty of smaller event pools.

Solar wind driving conditions corresponding to electron-only reconnection and traditional ion reconnection are mostly identical. IMF B_Y prior to electron-only reconnection events is tightly centered around zero, while IMF B_Y prior to traditional reconnection events has a much broader distribution. In addition, the minimum IMF B_z distribution is biased in the Southward direction for quiet current sheets, electron-only reconnection, and traditional reconnection. There are two reasons for this. First, our selection method of extracting the minimum IMF B_Z value in each interval will bias every event in the negative direction. Second, this feature is consistent with the idea that IMF B_z was favorably oriented for dayside reconnection, which is expected to eventually lead to nightside reconnection. Solar wind

plasma density and dynamic pressure for all three current sheets appear identical, which we believe is indicative of quiet solar wind conditions during solar minimum rather than local physical drivers. Solar wind v_y and v_z for electron-only reconnection and traditional reconnection are identical and centered around zero. v_x and v_{tot} for quiet current sheets is significantly lower than for electron-only reconnection and traditional reconnection, indicating that our electron-only reconnection and traditional reconnection events occur during intervals of faster solar wind. However, the lack of significant dynamic pressure/IMF B_z variation between the three current sheet types indicates that there is no simple causal link between solar wind parameters and occurrence of electron-only reconnection.

We note that MMS not observing reconnection does not mean that reconnection is not happening anywhere in the magnetotail. Although bursty bulk flows can propagate in the GSM X direction for tens of R_E from the reconnection region, an MMS observation in the dawn sector does not give insight on reconnection conditions in the dusk sector. As such, we must proceed with caution when examining the statistical properties of solar wind properties connected to quiet current sheet observations.

4.4.4 Plasma Sheet Characteristics

We then compare tail plasma features between the three current sheet types. As with solar wind driving parameters, when determining if a median electron-only reconnection value is statistically significantly different from the median values of other parameters, we calculate the uncertainty of the median and assess if the differences are within the uncertainty. To create each histogram, we quantitatively determine the boundary of each current sheet by calculating $J_\perp$ using the curlometer technique with MMS FGM data. We then examine the $J_\perp$ enhancement to determine the entrance and exit from each current sheet. After locating the current sheet interval, we extract the maximum of each plasma parameter within each current sheet. These values are placed in histograms, and their bins are overlapped using the same methodology described in the solar wind condition histograms.

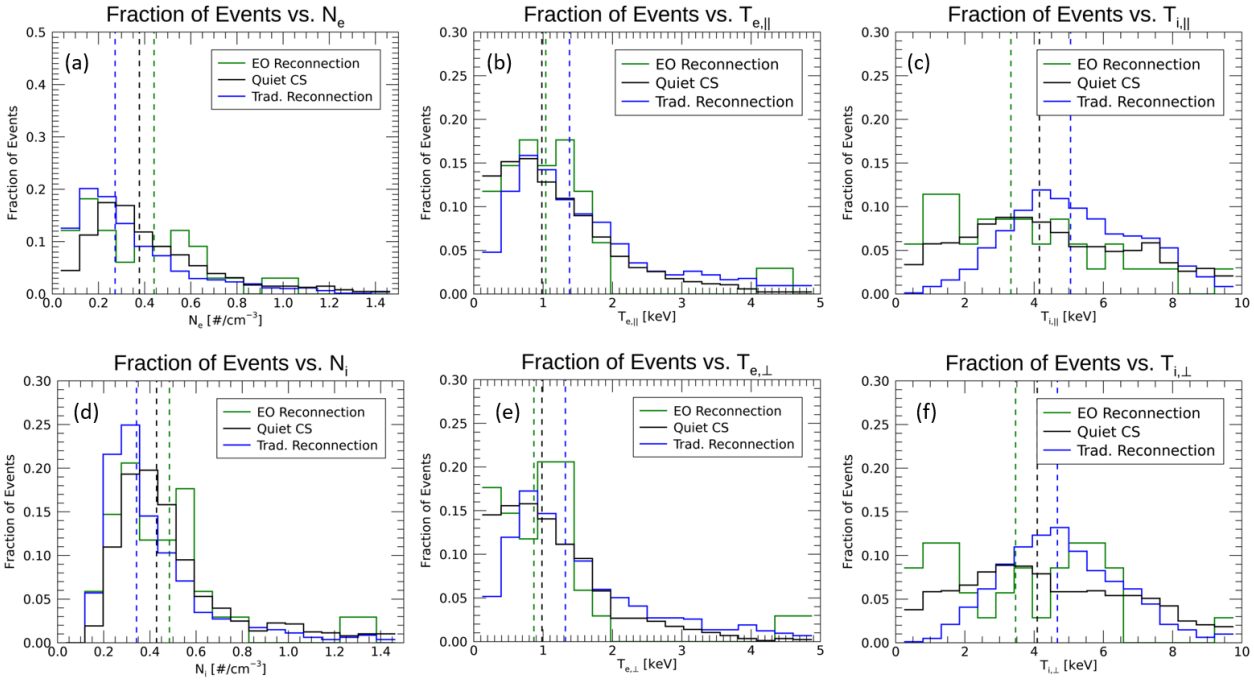

Figure 4.8: Histograms (with overlapping bins) of various magnetotail plasma properties inside quiet current sheet (black), electron-only reconnection (green), and traditional reconnection (blue) observations. Maximum (a) electron density, (b) ion density, (c) parallel electron temperature, (d) perpendicular electron temperature, (e) parallel ion temperature, and (f) perpendicular ion temperature inside each current sheet.

We find several magnetotail plasma features in electron-only reconnection that are consistent with an evolution of the current sheet from a quiet current sheet to traditional reconnection. First, the electron density (Figure 4.8a) in quiet current sheets is significantly greater than in electron-only and traditional reconnection. This indicates that, in electron-only reconnection and traditional reconnection, plasma is being evacuated from each reconnection region. This is less clear in the ion density histogram (Figure 4.8b), because ion density measurements become unreliable at less than 0.2 particles/cm^3. Thus, any difference in ion and electron density could be of instrument origin. Second, the electron temperature (Figure 4.8c,d) in quiet current sheets is less than in electron-only reconnection and traditional

reconnection. This indicates that electrons are heated in both electron-only and traditional reconnection. Meanwhile, the ion temperature (Figure 4.8e,f) in quiet current sheets and electron-only reconnection peaks at a lower temperature than in traditional reconnection. In addition, the perpendicular ion temperature distribution of quiet current sheets and electron-only reconnection display two peaks, while for traditional reconnection, the distribution is more Gaussian. This indicates that ions are not heated in electron-only reconnection.

4.4.5 Local Field Conditions

Lastly, we compare tail electric and magnetic field features between the three current sheet types. As with solar wind and plasma parameters, when determining if a median electron-only reconnection value is statistically significantly different from the median values of other parameters, we calculate the uncertainty of the median and assess if the differences are within the uncertainty. To create each electric field histogram, we use $J_\perp$ to determine MMS's entrance and exit from each current sheet identically to the tail plasma histograms. Within these intervals, we calculate the absolute value of each electric field component and extract the maximum value from each interval. Guide field is calculated by placing the magnetic field in minimum variance LMN coordinates, then calculating B_M/B_0, where B_0 is the value of B_L at the current sheet boundary. Bins are overlapped identically to previous histograms.

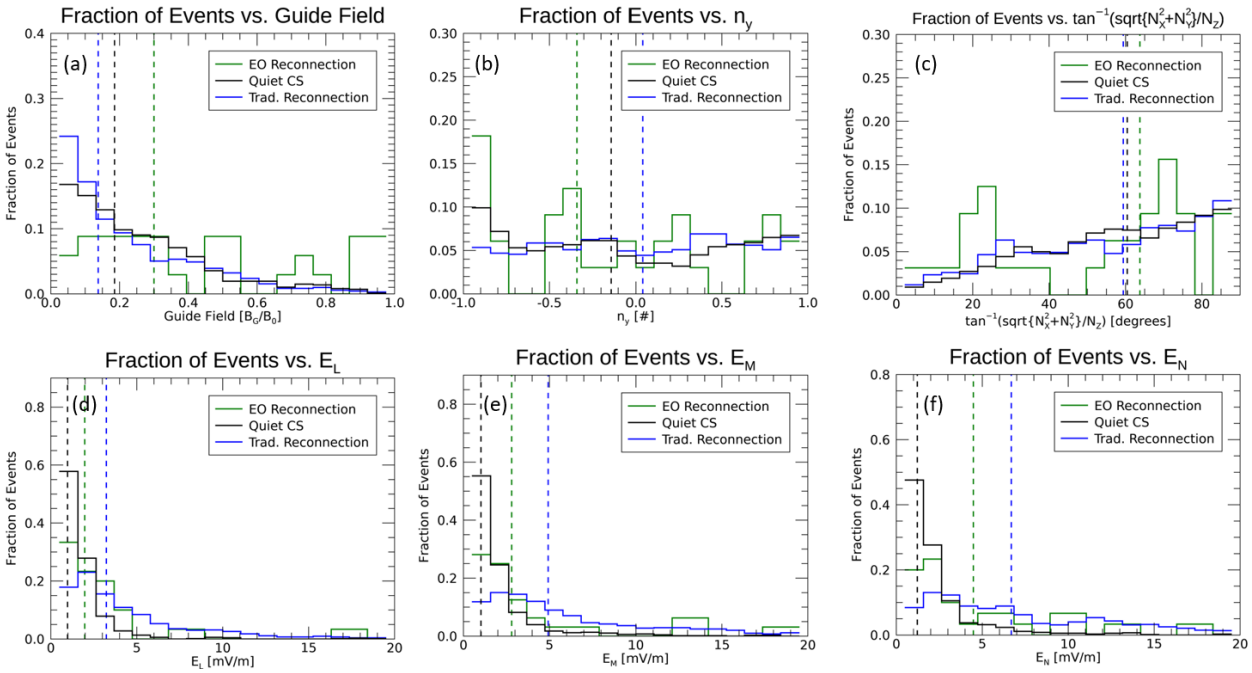

Figure 4.9: Histograms (with overlapping bins) of various magnetotail electric and magnetic field properties inside quiet current sheet (black), electron-only reconnection (green), and traditional reconnection (blue) observations. Maximum (a) guide field (B_G/B_0), (b) E_L, (d) E_M, and (f) E_N inside each current sheet. (c) GSM Y component of the Current Sheet Normal NY and (e) $tan^{-1}(\sqrt{N_Y^2 + N_X^2}/N_Z)$.

We find several magnetotail field features in electron-only reconnection that are consistent with current sheet evolution. From quiet current sheets to electron-only reconnection to traditional reconnection, all three electric field component histograms (Figure 4.9b,c,d) broaden and become centered at higher values. Because the electric field present in traditional reconnection is not typically present in quiet current sheets, electron-only reconnection as a transition phase between the two current sheets should straddle the two distributions. Although the median $tan^{-1}(\sqrt{N_Y^2 + N_X^2}/N_Z)$ value (Figure 4.9) for electron-only reconnection indicates significant bias toward Y-oriented current sheet normals compared to quiet current sheets and traditional reconnection, it remains unclear from the histograms if the cur-

rent sheet types exhibit different current sheet normal orientations (Figure 4.9c,e). However, electron-only reconnection events occur in higher guide fields (Figure 4.9a) than quiet current sheets and traditional reconnection events. This indicates that electron-only reconnection can occur in other contexts other than as a transition phase into traditional reconnection. For example, the turbulent outflow region could produce thin, high shear current sheets that can reconnect.

The CS Normal orientation required for electron-only reconnection vs. traditional reconnection are currently unclear. This lack of clarity is present in both electron-only reconnection and traditional reconnection. Specifically, the community's consensus of the orientation of the current sheet has been with a normal direction in the Z direction. However, we show that both traditional and electron-only reconnection can occur in current sheets with normals oriented in both the Y and Z directions. There does not appear to be a preference in whether the current sheet normal is Y or Z oriented.

As shown earlier, guide field is uncommon in traditional tail reconnection. This is due to the difficulty for magnetotail geometry to generate an environment with a strong guide field. Consistent with this interpretation, traditional reconnection is shown to have guide field below 0.25 B_0. Critically, electron-only reconnection differs from traditional reconnection in this feature. Of our 12 events, 8 occur in higher guide field environments ($B_G > 0.3B_0$). This indicates that electron-only reconnection occurs in non-standard tail configurations along with more traditional tail configurations.

4.4.6 Comparison to Ion Diffusion Regions

In previous sections, we compared plasma and field properties of quiet current sheets, traditional ion-coupled reconnection, and electron-only reconnection. However, our "traditional" reconnection pool does not distinguish between IDRs, bursty bulk flows, and close vs. far encounters of reconnection. In Chapter 2, we identified 49 IDR events, and in this section, we repeat these comparisons between quiet current sheets, IDRs, and our electron-only re-

connection candidates. This comparison will better align with *Lu et al.*, 2022's simulations, as they primarily simulate the diffusion region, not the outflow region. These comparisons are shown in Figure 4.10 and Figure 4.12.

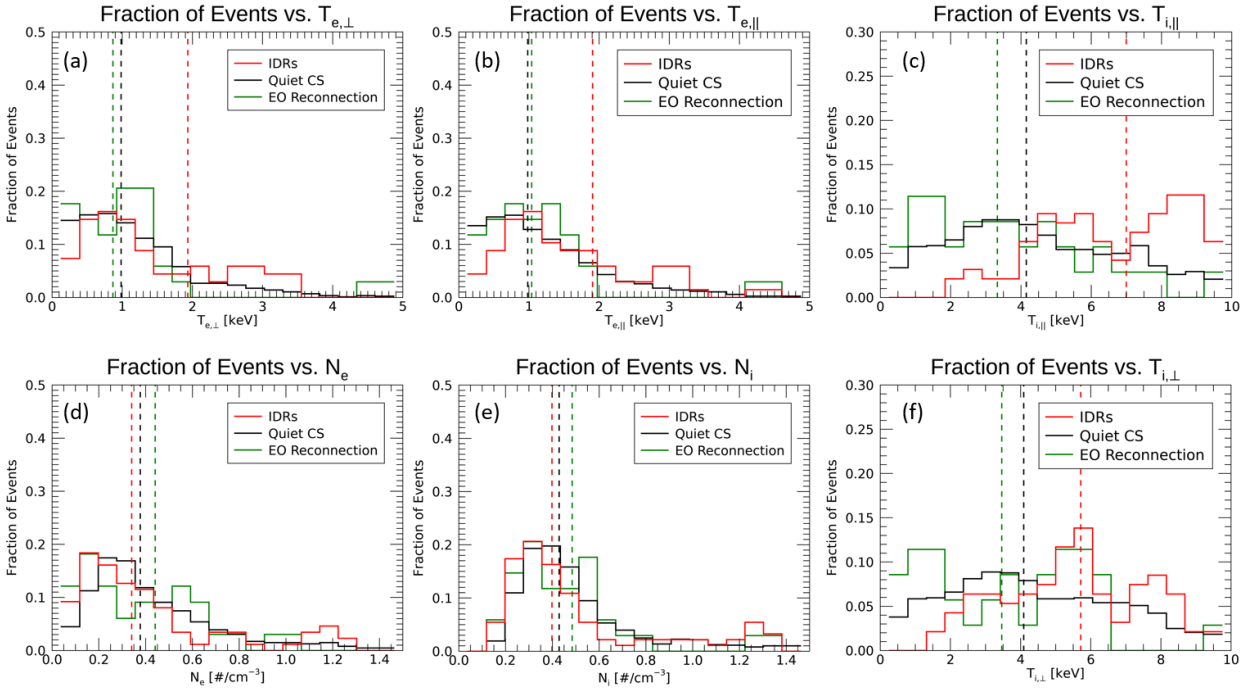

Figure 4.10: Histograms (with overlapping bins) of various magnetotail plasma properties inside quiet current sheet (blue), electron-only reconnection (green), and IDR (red) observations. Maximum (a) electron density, (b) ion density, (c) parallel electron temperature, (d) perpendicular electron temperature, (e) parallel ion temperature, and (f) perpendicular ion temperature inside each current sheet.

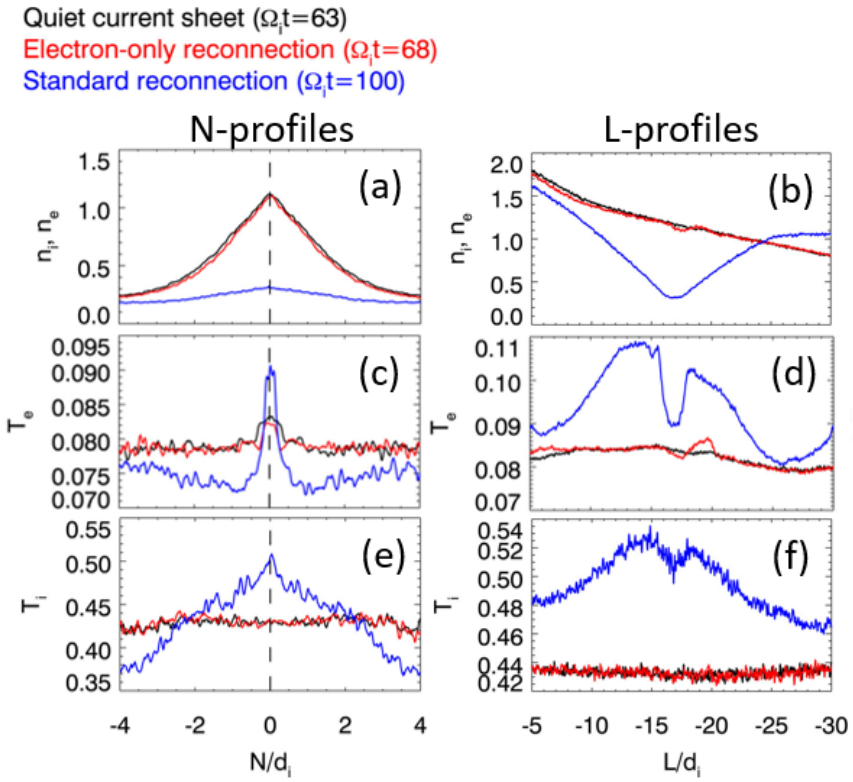

Figure 4.11: Simulated N (left) and L (right) profiles of (a,b) plasma density, (c,d) electron temperature, and (e,f) ion temperature. Black lines represent non-reconnecting current sheet, red lines represent electron-only reconnection, and blue lines represent ion-coupled reconnection. Adapted from (*Lu et al.*, 2022).

We find several notable plasma features that distinguish our electron-only reconnection candidates from IDRs. IDRs occur in significantly higher electron and ion temperatures and lower plasma densities than our electron-only reconnection candidates. These features are consistent with simulation work discussed in Section 3.2.3. As shown in Figure 4.11, we expect electron-only onset of reconnection to feature very similar background densities and temperatures as quiet current sheets, despite featuring local enhancements in the electron temperature at the current sheet center. Our statistics are consistent with these simulation results. We note that the plasma density of our electron-only events is significantly greater

than the plasma densities of either quiet current sheets or IDRs. We investigate this further in Section 4.4.7.

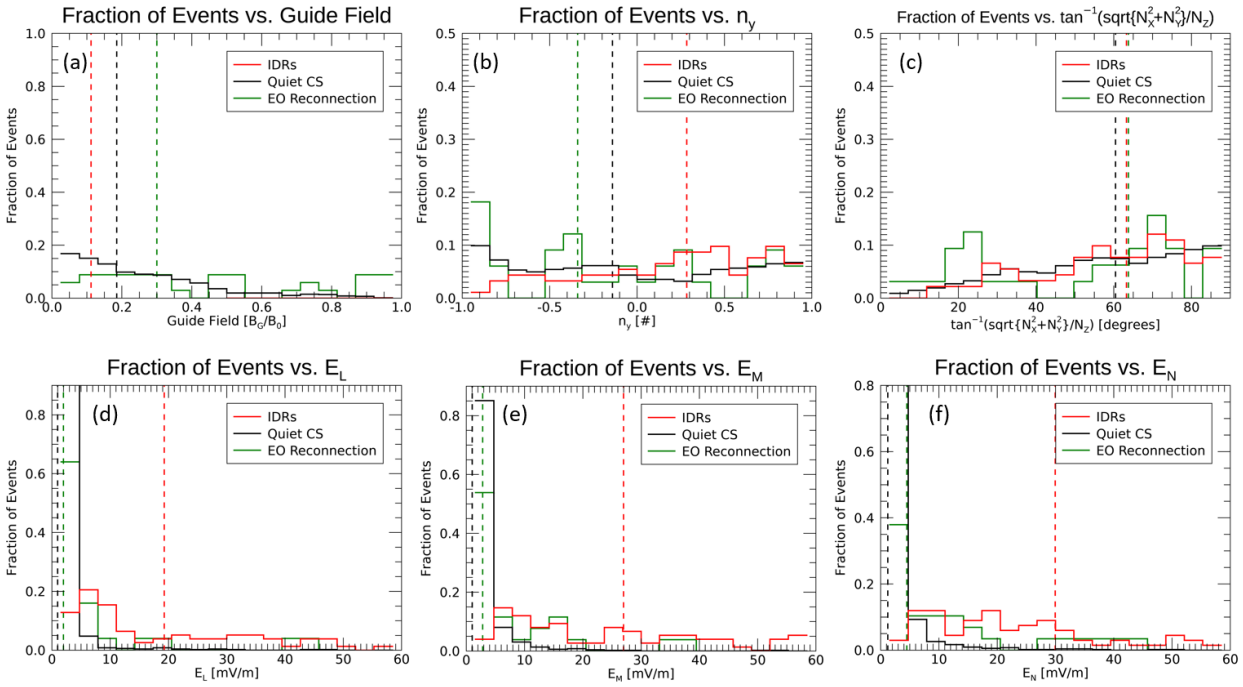

Figure 4.12: Histograms (with overlapping bins) of various magnetotail electric and magnetic field properties inside quiet current sheet (black), electron-only reconnection (red), and traditional reconnection (blue) observations. Maximum (a) guide field (B_G/B_0), (b) E_L, (d) E_M, and (f) E_N inside each current sheet. (c) GSM Y component of the Current Sheet Normal NY and (e) $tan^{-1}(N_Y/N_Z)$..

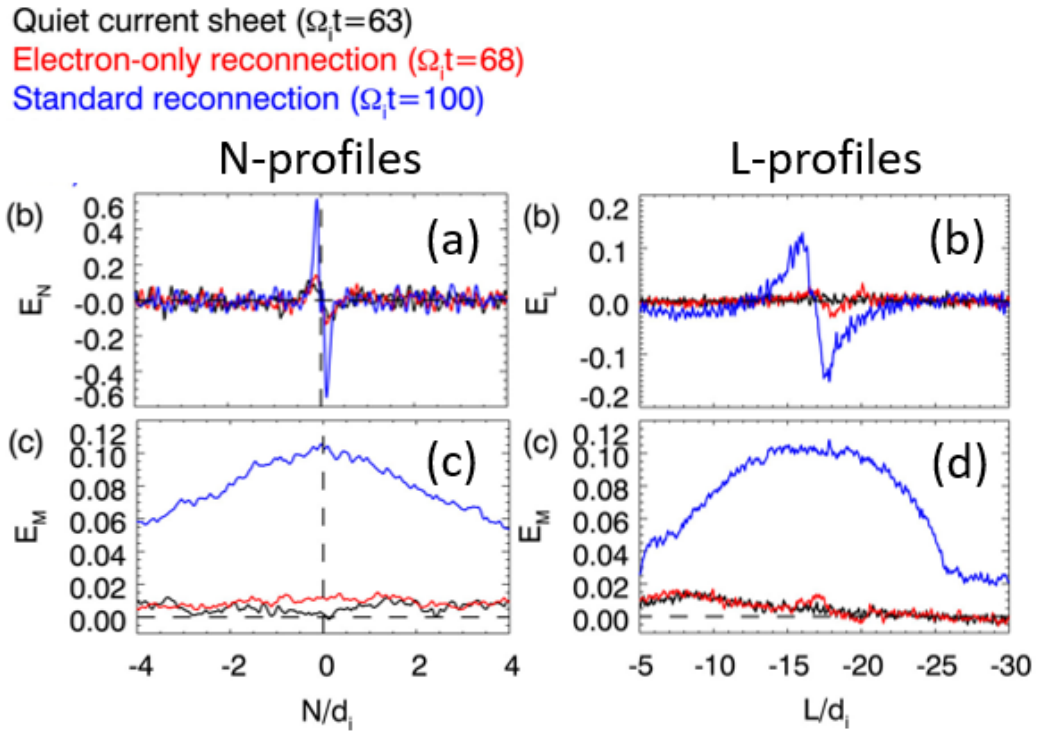

Figure 4.13: Simulated N (left) and L (right) profiles of (a,b) E_L or E_N, (c,d) E_M. Black lines represent non-reconnecting current sheet, red lines represent electron-only reconnection, and blue lines represent ion-coupled reconnection. Adapted from (*Lu et al.*, 2022).

We also find several notable magnetic and electric field features that distinguish our electron-only candidates from IDRs. Our electron-only events display significantly elevated guide field compared to both quiet current sheets and IDRs and elevated E_N that is still significantly lower than in IDRs. However, we note that all three current sheet structures occur in comparable current sheet normal angle. These features are also consistent with simulation work from Section 3.2.3. As shown in Figure 4.13, we expect minor elevations in all three components of the electric field during electron-only reconnection relative to non-reconnecting current sheets, but weaker electric fields than ion-coupled reconnection. Our statistics are consistent with these simulation results.

This difference in conditions suggests two different interpretations of what is occurring in

electron-only reconnection. One interpretation, electron-only onset of reconnection, is a time-evolving transition phase during the onset of traditional reconnection. This requires little to no guide field, and should look identical to traditional reconnection, minus the ion flows and heating required for "traditional" reconnection to be deemed "traditional" reconnection. Another interpretation, electron-only flux rope erosion, is a steady-state reconnection process can occur between flux ropes and dipolarized field in Earth's magnetotail. This has been observed and was recently reported by *Man et al.*, 2020b. This process would artificially produce a higher guide field while not changing the temperature and density profiles of the tail environment that MMS crosses. These two different processes could meet all ten of our observational survey criteria through different means while differing significantly in guide field.

4.4.7 $\tilde{\Delta}$ Parameter

Earlier, in Section 4.4.7, we established the definition for the parameter $\tilde{\Delta}$ and established that our 12 electron-only reconnection candidates displayed a significant, positive $\tilde{\Delta}n_e$. In this section, we compare these results to the $\tilde{\Delta}n_e$ of ion-coupled IDRs and EDRs.

As shown in Table 4.4, conversely from our electron-only reconnection candidates, ion-coupled IDRs and EDRs display a distinctly zero or negative $\tilde{\Delta}n_e$. This indicates that, in these events, plasma has evacuated from the current sheet center. This contrast is consistent with simulated spacecraft cuts through electron-only reconnection and ion-coupled reconnection from (*Lu et al.*, 2022).

Table 4.4: $\tilde{\Delta}n_e$ and $\tilde{\Delta}n_i$ for our 12 electron-only reconnection candidates (left) and community established IDRs/EDRs (right). Green cells indicate $\tilde{\Delta}$ values above 0.1, white cells indicate $\tilde{\Delta}$ values between -0.1 and 0.1, and pink cells indicate $\tilde{\Delta}$ values below -0.1. Bolded events in the IDR/EDR table represent community established EDR events.

EO Reconnection

Time	$\tilde{\Delta}\mathbf{n_e}$	$\tilde{\Delta}\mathbf{n_i}$
2017-06-17/20:24:00-20:24:10	0.31	0.16
2017-07-20/09:59:30-09:59:35	0.13	0.09
2017-07-26/17:39:36-17:39:39	0.21	0.37
2017-08-14/18:56:35-18:56:41	0.07	0.12
2017-08-23/11:19:14-11:19:16	0.15	0.04
2018-07-26/13:05:00-13:05:15	0.10	0.03
2019-07-05/01:55:40-01:55:50	0.41	0.33
2019-08-31/11:30:25-11:30:35	0.05	0.12
2020-08-03/00:35:50-00:36:00	0.11	-0.03
2020-08-05/19:42:31-19:42:36	0.12	-0.03
2020-09-09/20:06:10-20:06:20	0.25	0.12
2020-09-13/02:43:45-02:44:00	0.52	0.40

IDR/EDR

Time	$\tilde{\Delta}\mathbf{n_e}$	$\tilde{\Delta}\mathbf{n_i}$
2017-05-28/03:58:30-03:58:33	0.07	-0.16
2017-07-06/15:35:17-15:35:23	0.23	0.09
2017-07-06/15:46:38-15:46:43	-0.16	-0.30
2017-07-26/00:03:50-00:04:00	-0.23	-0.36
2017-07-11/22:33:45-22:34:15	-0.61	-0.55
2017-08-10/12:18:27-12:18:39	0.05	-0.07
2017-07-03/05:27:00-05:27:10	-0.04	-0.11

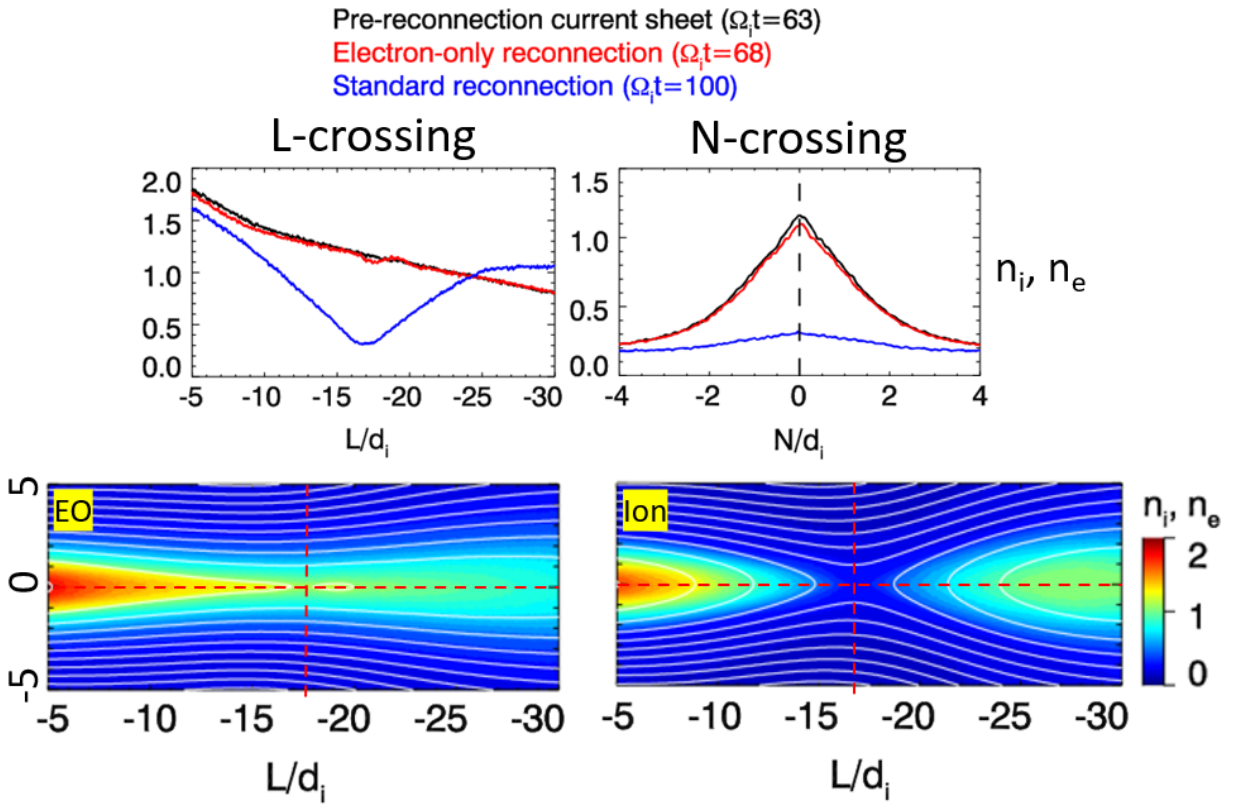

Figure 4.14: Simulated spacecraft trajectories through a non-reconnecting current sheet (black), electron-only reconnecting current sheet (red), and ion-coupled reconnecting current sheet (blue). TOP LEFT: trajectory in the L direction. TOP RIGHT: trajectory in the N direction. BOTTOM LEFT: Simulated plasma density map during electron-only reconnection. BOTTOM RIGHT: Simulated plasma density map during ion-coupled reconnection. Dashed lines indicate simulated trajectories plotted in top left and right. (*Lu et al.*, 2022)

The distinct contrast in $\tilde{\Delta}n_e$ between our electron-only reconnection candidates and ion-coupled reconnection events indicates that $\tilde{\Delta}n_e$ should be strongly considered as a criterion to distinguish the two processes.

4.5 Distinguishing Electron-Only Flux Rope Erosion from Electron-Only Onset

4.5.1 Electron-Only Flux Rope Erosion

As described in Table 3.1, four features are required to distinguish electron-only flux rope erosion from electron-only onset of reconnection. First, we require increased electron flux on the side of the current sheet connected to Earth. Second, we require elevated guide field, consistent with significant magnetic shear from a tilted flux rope. Third, we require trapped parallel and antiparallel electrons on the connected side of the current sheet. Lastly, we require that low energy electrons do not reverse in pitch angle across the current sheet. Each of these features indicate that the MMS spacecraft crossed from a disconnected flux rope to field lines that were fully connected to the magnetosphere/ionosphere, or vice versa.

We apply these four criteria to our 12 electron-only events and find that four events (4, 5, 7, 11) meet these three criteria in addition to the electron-only criteria outlined in Section 4.1. We note several notable commonalities between these events. First, electron-only flux rope erosion events occur exclusively in the flanks, where $GSM|Y| > 15R_E$ (See Figure 4.15). This is notable, considering that flux ropes are statistically seen evenly throughout the midnight and dawn/dusk sectors (**?**). Second, these 4 events exhibit elevated X components of current sheet normal (2 of 4 feature X normals that exceed Y and Z normal) compared to the other 8 events (1 of 8 is X-normal dominated). This is consistent with the classical mid-plane plasmoid erosion picture (*Moldwin and Hughes*, 1994; *Man et al.*, 2018), which argued that the normal orientation of the current sheet would be biased in the GSM X direction. We also note a significant variance in the guide field of these events (0.28 - 0.9), indicating that strong guide field is not required for electron-only flux rope erosion to occur. Previous observations of flux rope erosion (*Vogiatzis et al.*, 2011) support the interpretation that electron-only flux rope erosion could occur in an extremely variable guide field, because

an eroding flux rope should collide with Earth's dipolarized field at highly variable angles, resulting in variable current sheet normal direction. We do not see that electron-only flux rope erosion events occur closer to Earth than electron-only onset events or ion-coupled reconnection events, which may have been expected if a flux rope or plasmoid was interfacing with Earth's dipolarized field.

We note that previous MHD simulation work by *Richard et al.*, 1989 also reported flux rope erosion, but coined the process as "coalescence". In *Richard et al.*, 1989, it was hypothesized that reconnection outflows would occur both parallel and perpendicular to the neutral sheet, but that the process would be difficult to observe because of the speed of the structure in space and efficiency of the reconnection. While the current sheet normals of our electron-only flux rope erosion events are primarily in the X direction, their normal speeds are highly variable (15 km/sec - 250 km/sec), indicating that the speed of plasmoids generated through this process are highly variable. With only 4 events, it is difficult to make any conclusions about the speeds of these structures.

4.5.2 Electron-Only Onset

As described in Table 3.1, four features are required to distinguish electron-only onset from electron-only flux rope erosion. First, we require a peak in electron flux at the current sheet center coincident with symmetric parallel and antiparallel arms in the mid or high energy electrons surrounding the current sheet center. Second, we require low guide field (< 0.5). Third, we require a reversal in the low energy electron pitch angle from parallel to antiparallel, or vice versa. Fourth, we require strong isotropy in higher energy electron pitch angle at the current sheet center. These features are mutually exclusive with the criteria for electron-only flux rope erosion listed in Section 4.5.1.

We apply these criteria to our 12 electron-only candidates and find that seven events (1,2,3,6,8,10,12) meet these three criteria in addition to the electron-only criteria outlined in Section 4.1. We note several notable commonalities between these events. First, unlike

electron-only flux rope erosion, electron-only onset occurs closer to midnight (See Figure 4.15). Second, six of the seven events have current sheet normals primarily oriented in the Y direction. This indicates that electron-only onset of reconnection is more likely to be observed in highly tilted current sheets than equatorial current sheets. While the mean guide field of these seven events is less than the mean guide field of the electron-only flux rope erosion events, it is difficult to reach a definitive conclusion about the nature of guide field in electron-only onset of reconnection without more events. As reported by *Zhang et al.*, 2020, all events display a strong, ambient tailward flow of electrons in the pitch angle distribution.

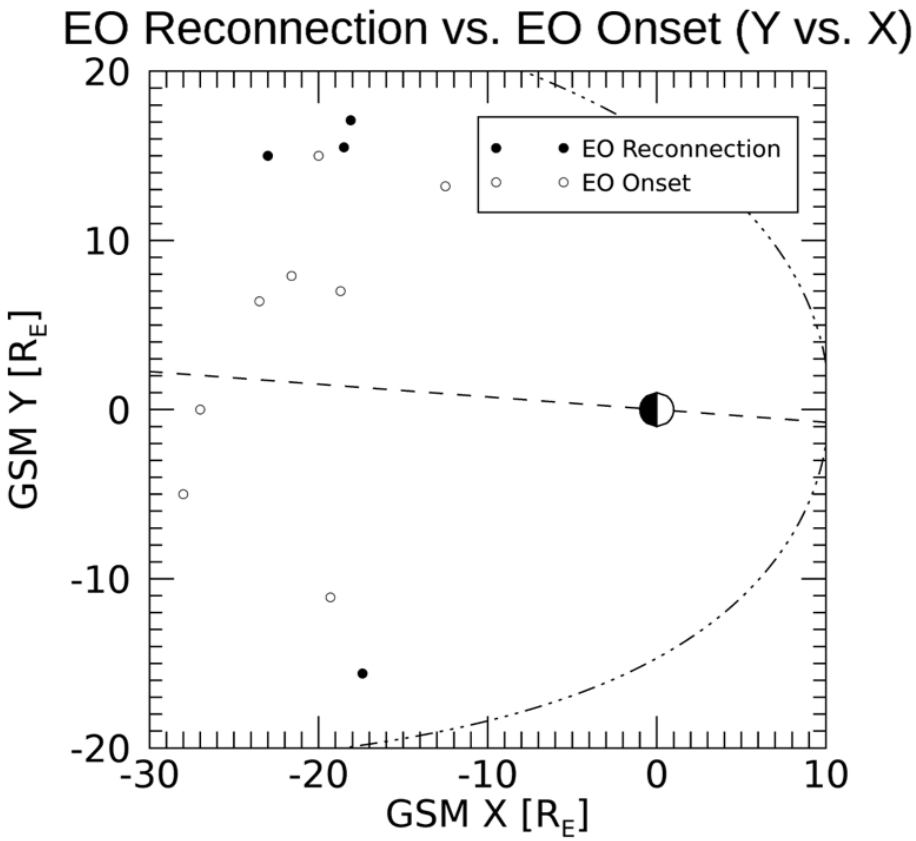

Figure 4.15: XY Location of Electron-Only Flux Rope Erosion (black) and Electron-Only Onset (white) events.

4.5.3 Temporal Evolution of Electron-Only Onset

We now use three electron-only onset of reconnection events (Event 1 (t_1), Event 2 (t_2), and Event 3 (t_3) (*Yu et al.*, 2019), italicized in Table 1) and one magnetotail ion-coupled EDR crossing by MMS during traditional ion-coupled reconnection to describe the time evolution of a thin current sheet from the electron-only onset phase to traditional "electron-ion" reconnection. Specifically, we pose that these three "pre-ion reconnection" events act as snapshots (Events 1, 2, and 3 corresponding to t_1, t_2, and t_3, respectively) displaying a transition from a relatively undisturbed, thin current sheet to a well-developed, traditionally reconnecting current sheet. MMS's EDR observations were taken from the interval 08-10-2017/12:18-19 (*Li et al.*, 2019; *Zhou et al.*, 2019) (See Table 1, row labelled "EDR"). We argue that these "pre-ion reconnection" events are approximately steady-state because, during Events 2 (2 seconds) and 3 (6 seconds), we observe a static current sheet normal speed and symmetric electron velocity profile. We classify these electron-only events as "pre-ion reconnection" events because all three electron-only events are followed fewer than ten minutes later by traditional reconnection. Specifically, MMS observes traditional "electron-ion" reconnection signatures fewer than 10 minutes following Event 1 (t_1) and Event 3 (t_3) (See Figure 4.16 below), and the AE Index grows significantly ($> 100\%$) fewer than 10 minutes after Event 2 (t_2). We note the limitations of our interpretation that these events are snapshots in the same time-dependent process, as these observations were made days apart and have no direct causal link. We also note that, in Event 3, there is a change in both parallel and perpendicular components of ion temperature, but the total ion temperature does not change significantly.

The electron-only events are thin ($\leq 21\ d_e$), slow (≥ 100 km/sec) current sheets (*Forbes et al.*, 1981) with varied current sheet normal orientations (two in Y, one in Z). However, to compare the features of these events one-to-one, we convert time to distance from the current sheet center. We calculate the current sheet thickness in d_e by multiplying the perpendicular

current's temporal width by the current sheet normal speed and converting to electron inertial lengths (d_e) using the upstream electron number density ($d_e = c * (4\pi n_e e^2/m_e)^{-1/2}$). We first indicated the temporal current sheet center of each event using the time at which B_{tot} reached its minimum value. We then converted time separation into d_e the same way we calculated current sheet thickness. The "distance" resolution of each line was then averaged to match the distance resolution of the lowest resolution array. Presenting the data in this format allows current sheet properties to be compared one-to-one, regardless of ambient tail conditions or coordinate system.

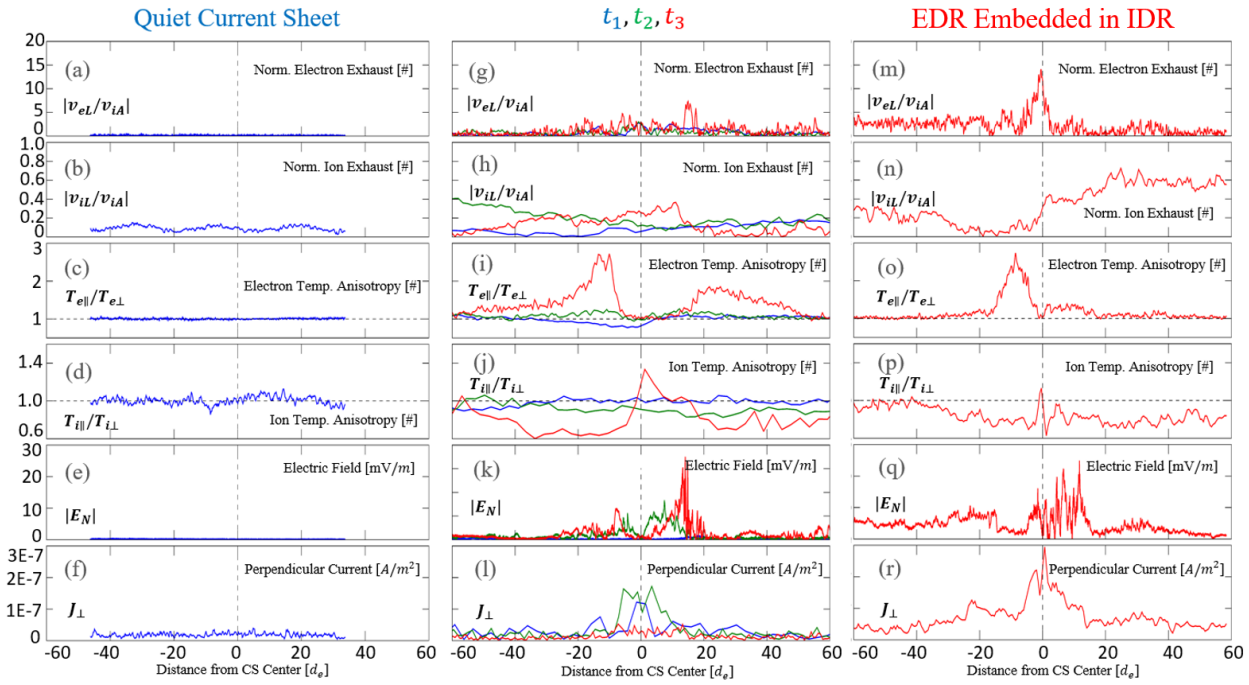

Figure 4.16: Comparison of various features of a quiet current sheet (06-05-2017/12:35-40), Electron-Only Onset of Reconnection (Events 1-3, Table 3), and ion-coupled reconnection (08-10-2017/12:18-19) over distance from the current sheet center. (a,g,m) $|v_{eL}/v_{iA}|$, (b,h,m) $|v_{iL}/v_{iA}|$, (c,i,o) $T_{e,\|}/T_{e,\perp}$, (d,j,p) $T_{i,\|}/T_{i,\perp}$, (e,k,q) $|E_N|$, and (f,l,r) $J_\perp$ of each current sheet type. Column 1 displays a quiet current sheet, Column 2 displays three electron-only onset of reconnection events (t_1 in Blue is Event 1, t_2 in Green is Event 2, and t_3 in Red is Event 3), and Column 3 displays an ion-coupled EDR.

Event 1 (labeled t_1 in Figure 4.16) displays weak perpendicular electron heating (Figure 4.16a), displays no ion heating (Figure 4.16c), and occurs in the thinnest current sheet (Figure 4.16e). However, as the process develops (Event 2), $T_{e,||}/T_{e,\perp}$ and $T_{i,\perp}/T_{i,||}$ increase far from the current sheet center. $J_\perp$ width (Figure 4.16e) and E_N also increase. Eventually (Event 3, labeled t_3 in Figure 4.16), the temperature anisotropy and current sheet thickness of "electron-only" reconnection become consistent with the thickness and anisotropy of well-developed reconnection in the near-Earth magnetotail (Figure 4.16b,d,f). Importantly, in the furthest developed example of "electron-only" reconnection (Event 3, t_3), $T_{i,||}$ appears to strongly exceed $T_{i,\perp}$ close to the current sheet center (Figure 4.16c). This feature is also seen in well-developed reconnection (Figure 4.16d). We note that Events 2 and 3 contain a thick ($\approx 20d_e$) region close to the current sheet center in which the electrons are isotropic, and Event 3 contains a thin ($< 10d_e$) region where parallel ion heating surpasses perpendicular ion heating. While the ion-coupled EDR observation also displays these features, they occur in a notably thinner ($< 5d_e$) region. The process that would reduce the size of this region is a subject for future study.

To further explore this hypothesis, we select one quiet current sheet (06-02-2017/12:18-19, included in Table 1), three electron-only onset events (Event 1 (t_1), Event 2 (t_2), and Event 3 (t_3) (*Yu et al.*, 2019), bolded in Table 3) and one ion-coupled magnetotail EDR (08-10-2017/12:18-19 *Li et al.* (2019); *Zhou et al.* (2021), included in Table 2) to showcase the transition from a quiet, pre-reconnection current sheet to electron-only onset to traditional reconnection. We note that this interpretation is limited, because these events occurred weeks apart and are not directly causally linked. Electron-only events used in this section occurred fewer than ten minutes before traditional reconnection observations, showed primarily steady-state electron outflows and heating (*Hubbert et al.*, 2021a). In addition, all five events (including the quiet current sheet and EDR) occurred in low guide field environments ($B_M/B_0 < 0.2$), and the three electron-only events and EDR occur in similar plasma beta environments (≈ 500). In this context, we interpret these events as approximate snapshots

that, when placed in the correct order, describe the transition from a quiet, pre-reconnection current sheet to a traditionally reconnecting current sheet.

Our previous work (*Hubbert et al.*, 2021a) did not compare these electron-only events to the current sheet conditions of quiet current sheets to show that electron-only onset conditions could arise from a quiet current sheet. We compare a quiet current sheet to the three electron-only event snapshots and show that electron-only onset can rise out of quiet current sheet conditions and transition into ion-coupled EDR conditions. First, for each event, we set the zero-distance from the current sheet center to the time containing the minimum B_{tot} value. We then converted time to distance from the current sheet center in d_e. Because the plasma density varies from event to event, the time to distance ratio of each event also varies. Therefore, despite each event having the same temporal resolution, each event will have varying "distance" resolution. For plots containing multiple events, we resample the "distance" resolution of each array to that of the event with the lowest resolution. This allows the time series of our events to be compared one to one.

In Figure 4.16, t_1 shows current sheet features that are very similar to the conditions of a quiet current sheet. Specifically, the electron and ion temperature isotropy, lack of ion exhaust outflow velocity, and lack of E_N are similar between t_1 and the quiet current sheet. However, t_1 differs from the quiet current sheet in that it displays super-Alfvénic electron exhaust flows. t_2 separates itself from t_1 and the pre-reconnection current sheet because the electron temperature anisotropy increases to ≈ 1.3, which is greater than the anisotropy found in 98% of quiet current sheets. This indicates that there is most likely a new mechanism of energization that is not typically present in a quiet current sheet. In addition, EN, ion temperature anisotropy, and ion exhaust velocity increase to values rarely seen in quiet current sheets. Electron outflow bursts continue to be present at the current sheet center. Lastly, at t_3, the electron temperature anisotropy is greater than 100% of 572 quiet current sheets observed by MMS (*Artemyev et al.*, 2020) and is comparable to anisotropy found in an ion-coupled EDR in Earth's magnetotail (*Chen et al.*, 2019). Electron

exhaust outflows in t_3 have stronger bursts than in t_1 and t_2. Similarly, the ion temperature anisotropy, EN, and ion outflow exhaust of t_3 approach values comparable to numerous tail EDRs. However, t_3 still differs from the ion-coupled EDR crossing because it displays a lack of ion outflow and energization. The width of $J_\perp$ in d_e also increases from t_1 to t_2 to the IDR-embedded EDR, indicating that the current sheet is expanding during this current sheet evolution. We note that the width of $J_\perp$ in t_3 is unclear due to the small amplitude of the current. This is consistent with the interpretation that, as the current sheet thickens, ions can better couple with the reconnecting field geometry (*Sharma Pyakurel et al.*, 2019). In addition to clarifying features posed in previous work, the inclusion of a quiet current sheet provides additional context to help showcase that electron-only onset of reconnection is a capable transition phase from a quiet current sheet to traditional reconnection.

Several additional features drawn out of these comparisons are consistent with electron-only onset of reconnection evolving into ion-coupled reconnection. First, an increase in current sheet thickness would meet criteria established by previous simulation work for the inclusion of ions in the reconnection process (*Sharma Pyakurel et al.*, 2019). Second, a transition into traditional reconnection should be coupled with an increase in the temperature anisotropy of both ions and electrons. Third, in a quiet current sheet, electron agyrotropy should be relatively low because the particles are merely drifting across the tail. As a result, seeing an increase in agyrotropy from electron-only onset of reconnection to traditional reconnection is consistent with physical intuition. Fourth, T_i being statistically cooler in electron-only onset of reconnection than in traditional reconnection is consistent with the picture that field lines are reconnecting, but in a thin enough current sheet that ions are not yet interacting with the system. Lastly, if these two processes are truly coupled, statistically similar current sheet normal orientations by location makes sense. In addition, regardless of location, electron-only onset of reconnection does not occur in tilted current sheets any more frequently than quiet current sheets or traditional reconnection, which further supports that the processes are coupled. We note that, even when we exclude electron-only flux rope

erosion events, electron-only onset of reconnection still occurs in higher guide field than quiet current sheets. This is not consistent with the picture of traditional reconnection.

4.6 Turbulent Secondary Reconnection

4.6.1 Simulation Work

Kinetic reconnection has been shown in both simulation and observation work to successfully energize plasma in localized regions of Earth's magnetosphere. From this work, others have simulated reconnection such that the initiation of reconnection was followed by a cascade of secondary reconnection sites. Several mechanisms have been proposed to generate these secondary reconnection sites within ion-scale outflows: 1. KH instability driven by velocity shears, 2. drift instabilities driven by density and temperature gradients, 3. interchange instabilities driven by field line curvature in the separatrices, 4. kink instability driven by flux rope generation, and 5. streaming instabilities driven by whistler waves. These instabilities are thought to convert energy on global scales.

For example, simulation work by *Lapenta et al.*, 2015, 2018 generated secondary reconnection sites within reconnection exhaust. Starting with a Harris-like current sheet, their reconnection generated a flux rope that was interchange unstable and generated reconnection within the exhaust region. As shown in Figure 4.17, several reconnection field line topologies were not compatible with central X-line reconnection (magenta lines), indicating that secondary reconnection was triggered. The color bar in Panel C indicates the strength of electron outflow and shows that electron outflow is super-Alfvénic. Further work calculating the electron contribution vs. ion contribution to current during these secondary reconnection events yielded that reconnection currents were electron-dominated, supporting that the secondary reconnection was electron-only.

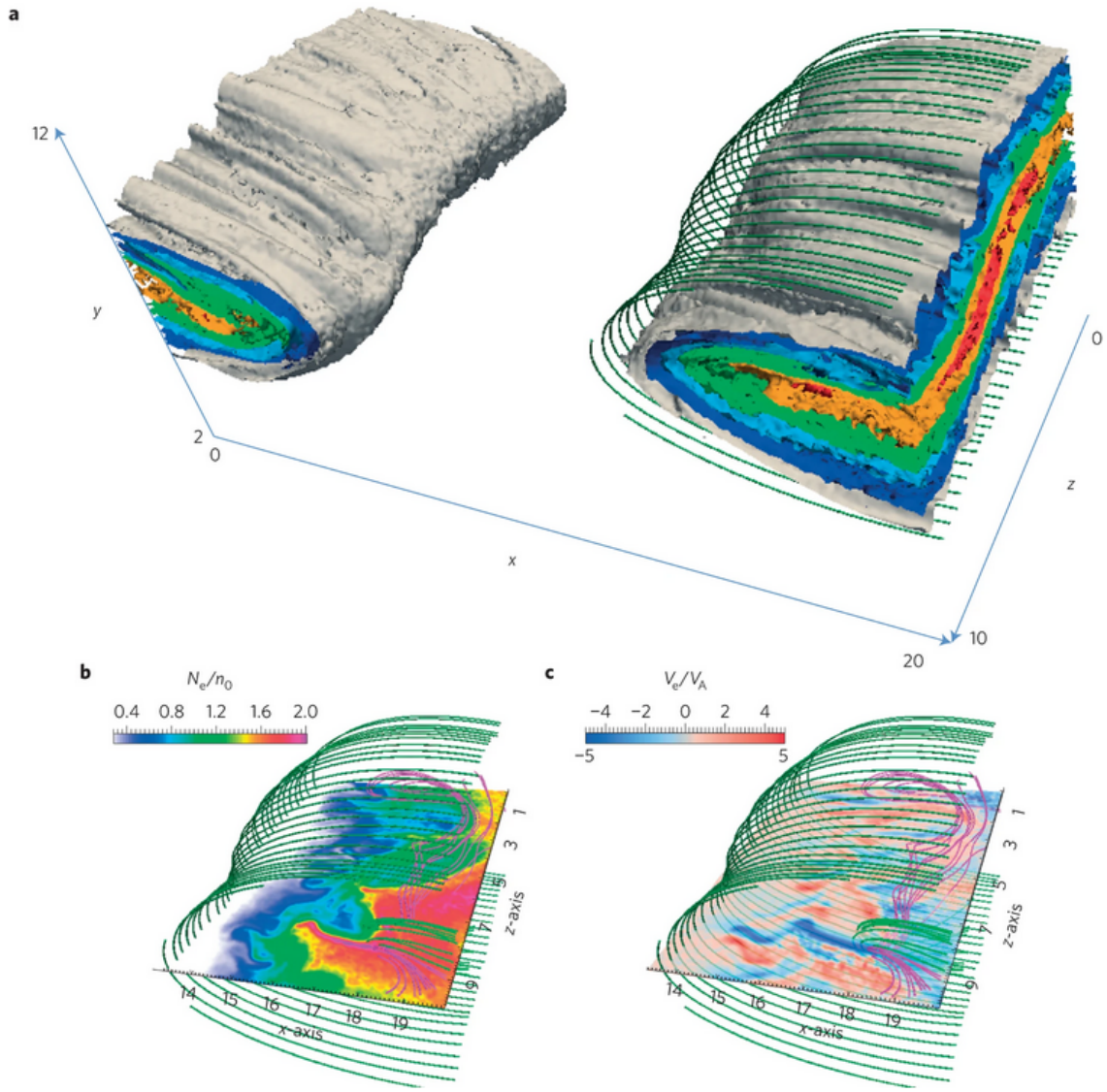

Figure 4.17: MHD simulations of symmetric reconnection by *Lapenta et al.*, 2015. In the bottom row, green lines indicate field lines that reconnected with the primary X-line, pink lines indicate field lines that could not have reconnected with the primary X-line and must have undergone secondary reconnection.

Simulations of these secondary reconnection sites have several important features that can be compared to observations. First, these sites are embedded in ion-scale reconnection exhaust, meaning that a spacecraft should observe super-Alfvénic ion exhaust from

the primary reconnection site. Similarly, if ions are energized, ion temperatures should be consistent with that of traditional, ion-coupled reconnection. Significant energy conversion ($J \cdot E'$), parallel electric fields, and agyrotropy were found in virtual spacecraft cuts through this region and used to support the demagnetization and meandering of electrons in this region. Like in Section 3.1, we note that the turbulent secondary reconnection interpretation is built on *Phan et al.*, 2018; *Sharma Pyakurel et al.*, 2019's model: a steady-state process driven in a turbulent environment because the width and length of the current sheet was too short to couple with ions.

4.6.2 Observation Work

Two spacecraft observations, one in Earth's magnetotail (*Zhou et al.*, 2021) and one at Earth's magnetopause (*Pyakurel et al.*, 2023), have supported this interpretation (see Figure 4.18). Both observations were embedded in long duration ($>$ 30 minutes) ion exhaust regions and feature super-Alfvénic ion exhaust and electron outflow. In addition, both events feature strong parallel electric fields, positive $J \cdot E'$, electron-scale thickness, electron-dominated currents, high current sheet tilt, and elevated guide field.

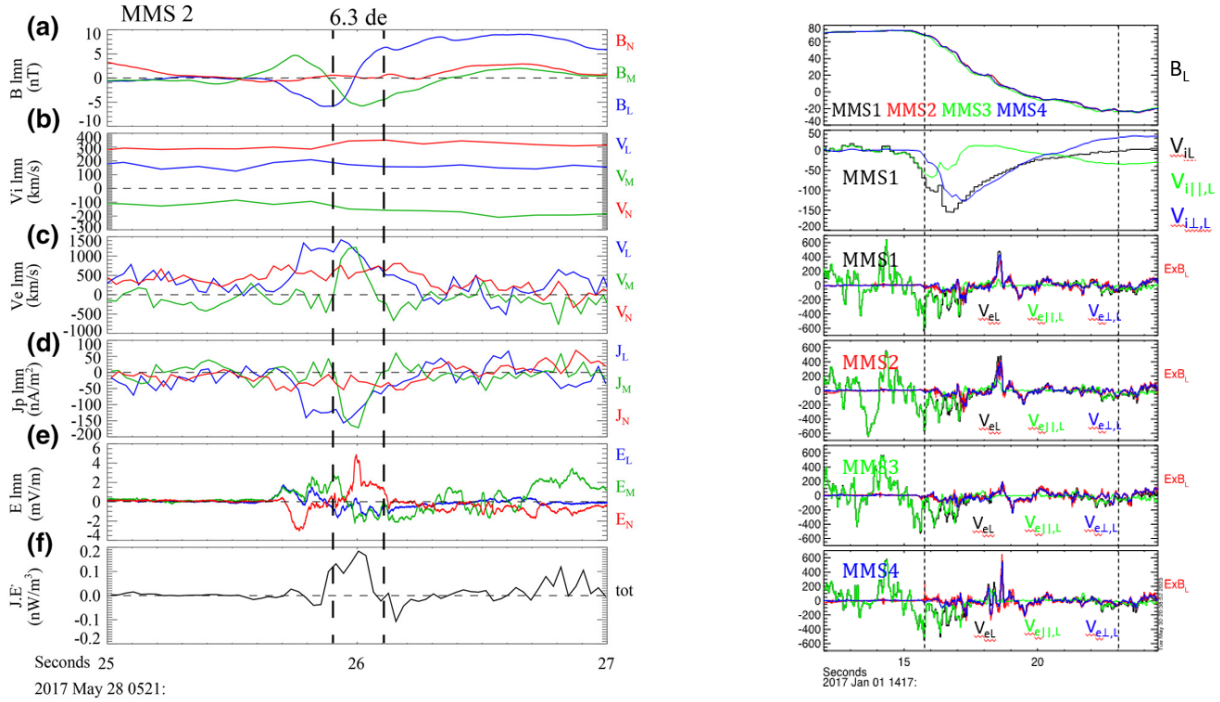

Figure 4.18: (left) 5/28/17 magnetotail observation of an electron-dominated current by *Zhou et al.*, 2021 during an extended stay in the outflow region by MMS. (right) 1/1/17 magnetopause observation by *Pyakurel et al.*, 2023 of electron-only reconnection within turbulent ion outflow by MMS.

We note that in the *Zhou et al.*, 2021 event, it is unclear how the authors distinguished secondary reconnection from electron exhaust due to the primary reconnection event. MMS remained in the outflow region for over an hour, and crossed several current sheets during that interval. While many of them were significantly tilted, consistent with the interpretation of secondary reconnection, we cannot rule out that MMS was observing electron exhaust flows from the primary reconnection region in a tilted magnetotail neutral sheet. Ideally, an electron flow reversal would have been present to indisputably show that MMS was observing a secondary X-line. This problem is highly relevant to our events as well, because none of our events display electron flow reversals or oppositely directed electron outflows by different MMS spacecraft. Confirming that the event meets the flux transport criterion or observing

some sort of electron agyrotropy in the form of elevated electron temperature or electron crescent distributions would improve the credibility of this interpretation.

4.6.3 Consistency with Dataset

Based on previous simulation and observation work, we expect several observational features that differ from the electron-only reconnection criteria listed in Section 3.3 when observing turbulent secondary reconnection. First, the turbulent ion exhaust region would be ripe for high guide field reconnection because antiparallel magnetic fields often interact at significant angles. Second, because this reconnection would occur in a turbulent exhaust region, we expect ion outflows and temperatures to match the ion outflows and temperatures found in traditional reconnection. This is supported by the sole observation of this phenomenon in the tail (*Zhou et al.*, 2021). Third, because the ion exhaust region is extremely turbulent, we expect current sheets with extremely variable normal orientations, regardless of where the traditional reconnection is occurring.

The majority of our electron-only reconnection events occur in guide field > 0.5, which is consistent with the turbulent secondary reconnection picture. However, our event criteria exclude events with strong ion outflows and ion heating by definition, so none of our events display these features. Also, statistically, our 12 electron-only reconnection events occur no more frequently in tilted current sheets than the other current sheet types. In fact, our electron-only flux rope erosion candidates primarily have normals in the GSM X direction, while our electron-only onset candidates primarily have normals in the GSM Y direction. This apparent order disagrees with the condition that secondary turbulent reconnection should occur in approximately random normal orientations. As such, we conclude that none of our events fall under this interpretation. We leave a statistical survey utilizing these observational criteria as a subject for other future study.

4.7 Electron-Only Reconnection in Kelvin-Helmholtz Instability

Recent simulation work in Earth's magnetotail and flank magnetopause have reported that turbulence due to the Kelvin-Helmholtz instability in Earth's flank magnetopause can generate electron-scale length and width current sheets capable of reconnecting. For example, recent 2.5D PIC simulation work successfully generated reconnection within turbulence generated by the Kelvin-Helmholtz instability and found that the reconnection lacked ion coupling (*Blasl et al.*, 2023). This simulation was supported by an MMS observation from 9/23/17 (Figure 4.19). Similarly to the 6/17/17 event described in Section 3.2.1, a simulated spacecraft trajectory through the reconnection region within KH instability was able to successfully reproduce the qualitative features of the MMS observation (Figure 4.20). This MMS observation met all ten electron-only reconnection criteria described in Section 3.3, indicating that our criteria are applicable to other regions of Earth's magnetosphere.

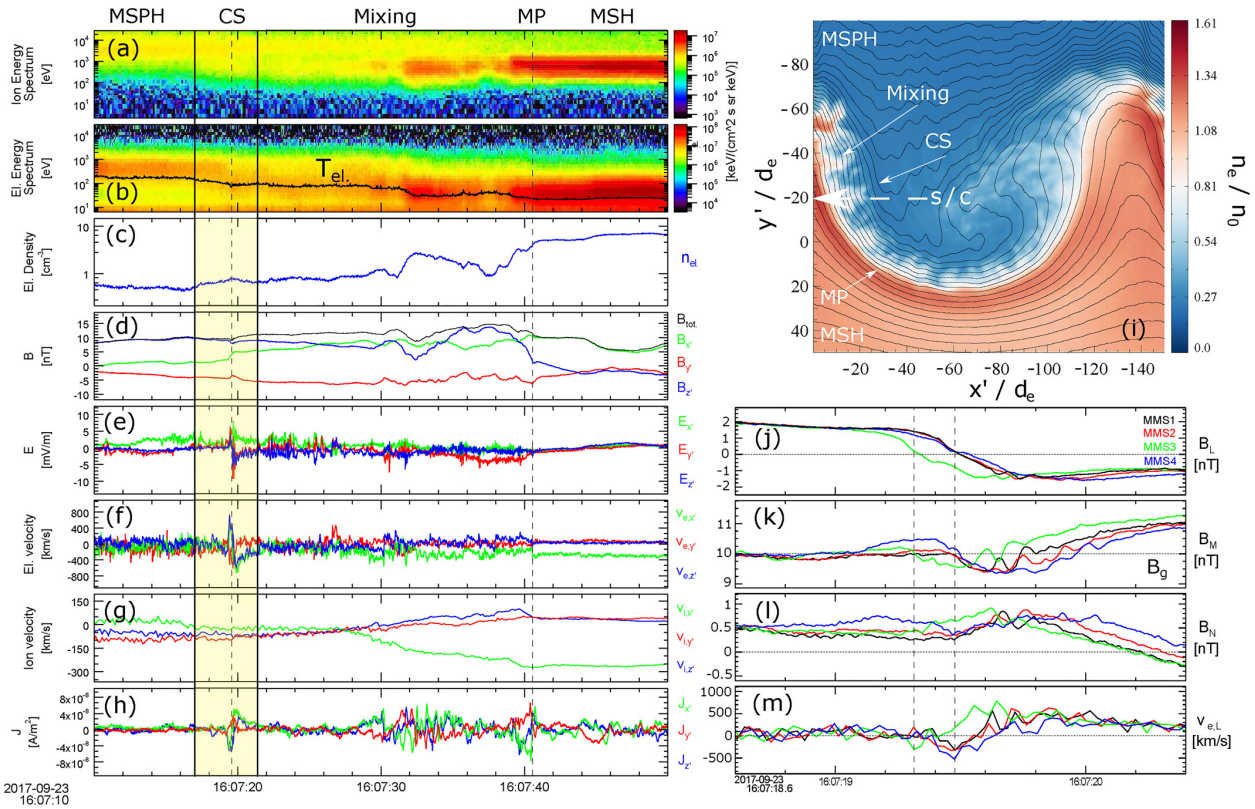

Figure 4.19: 9/23/17 MMS observation and PIC simulation displaying electron-only reconnection within Kelvin Helmholtz instability at Earth's flank magnetopause. (*Blasl et al.*, 2023)

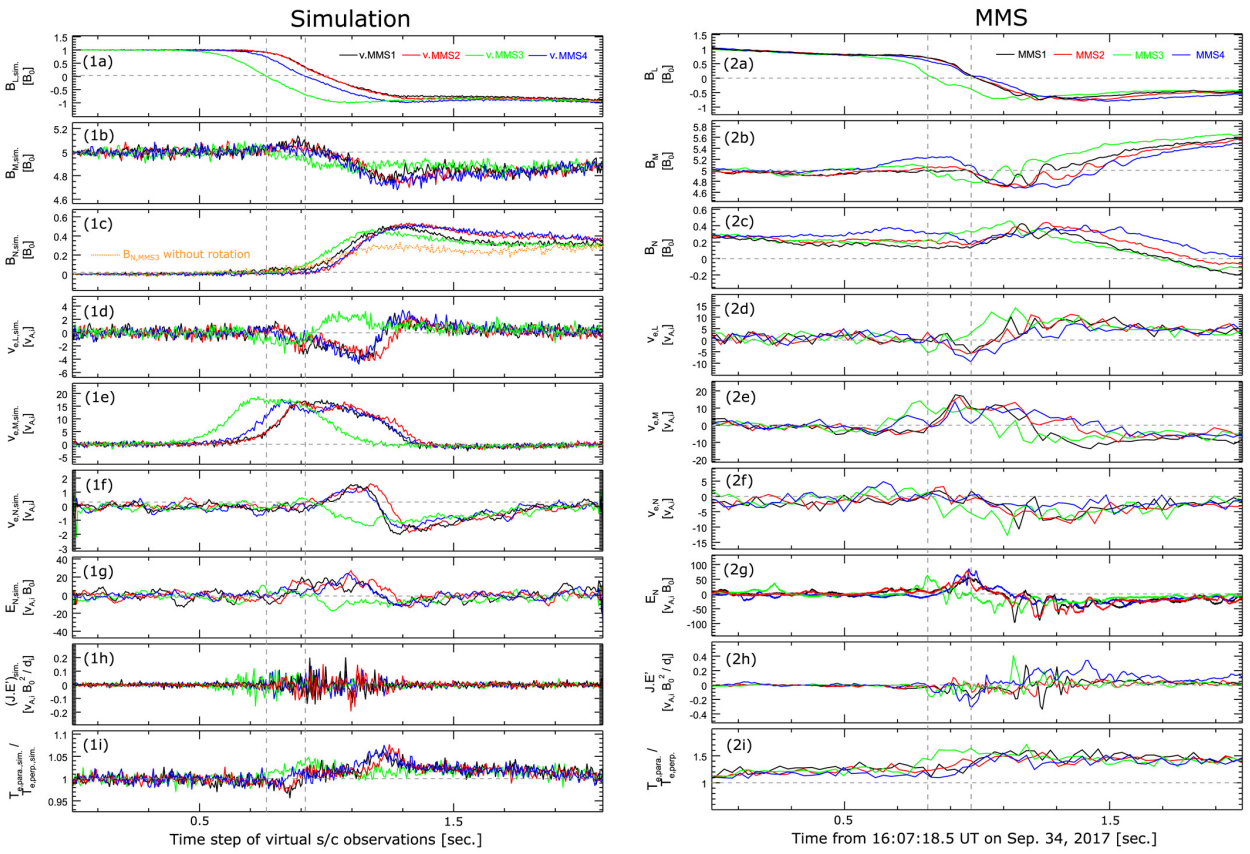

Figure 4.20: Simulated spacecraft cut through reconnection due to Kelvin Helmholtz instability (left) and MMS cut of 9/23/17 observation of electron-only reconnection at Earth's flank magnetopause (right).

We note that the microphysical mechanism driving electron-only reconnection in this event is consistent with *Phan et al.*, 2018; *Sharma Pyakurel et al.*, 2019's picture of electron-only reconnection: a steady-state process driven in a turbulent environment because the width and length of the current sheet was too short to couple with ions.

4.8 Conclusions & Interpretations

In Chapter 4, using the observational criteria for electron-only reconnection in Section 3.3, we reported MMS observations of 12 electron-only reconnection candidates in six magnetotail seasons from 2017-2022. These events were electron-scale in thickness, primarily occurred in tilted current sheets, displayed elevated guide field relative to the other three current sheet types discussed in this thesis, and featured increases (or "bumps") in plasma density at the current sheet center as the spacecraft crossed the current sheet. This plasma density bump contrasts strongly with the plasma density profile of ion-coupled IDRs and EDRs, which is exclusively flat or decreasing at the current sheet center. We found that agyrotropy ($\sqrt{Q_{Pe}}$) is not a reliable parameter to identify ion-coupled or electron-only reconnection in Earth's magnetotail. Electron-only reconnection shares ambient field and plasma conditions with quiet current sheets, which is consistent with simulations from *Lu et al.*, 2022. We then classified 4 events as electron-only flux rope erosion events and 7 events as electron-only onset of reconnection events. We place three electron-only onset events in time order to show that they are compatible with the interpretation of electron-only onset of reconnection. Lastly, we report an electron-only reconnection candidate in Earth's flank magnetopause driven by turbulence in Kelvin-Helmholtz instability that meets all ten observational electron-only reconnection criteria.

CHAPTER 5

Summary of Research and Future Work

While magnetic reconnection has been investigated for decades, there still remain many open questions and issues about the ubiquitous process in Earth's magnetosphere. One such question is whether the local plasma and field properties of magnetic reconnection in tilted current sheets should be the same as those in equatorial current sheets. A second problem is that there is a lack of high-spatial resolution statistics of Ion Diffusion Regions in Earth's magnetotail, despite being reported extensively in previous missions such as Cluster and Geotail. This has resulted in a limited understanding of the transition region from the IDR to the EDR. A third question is that while we have successfully observed magnetic reconnection for decades, we do not have observational evidence of the mechanism of reconnection onset. While several theories have been developed and electron tearing has been promoted by many in the community, there remains no observational evidence supporting any theory of reconnection onset. A fourth question is whether or not electron-only reconnection occurs in Earth's magnetotail. In 2018, *Phan et al.*, 2018 reported the first MMS observation of electron-only reconnection in Earth's magnetosheath, but a universal set of observational criteria for electron-only reconnection has not yet been established and other regions of Earth's magnetosphere have not yet been scoured for this process. In this dissertation, we use the Magnetospheric Multiscale (MMS) Mission to present statistical surveys of quiet cur-

rent sheets, ion-coupled reconnection, Ion Diffusion Regions, and electron-only reconnection candidates in Earth's magnetotail in efforts to address each of these four questions.

In Chapter 2, we performed statistical surveys of quiet, non-reconnecting current sheets, ion-coupled reconnecting current sheets, and Ion Diffusion Regions (IDRs) from six magnetotail seasons ranging from 2017-2022 in order to compare their local plasma and field properties in both equatorial and tilted current sheets. Our event pool of 49 IDRs is the largest pool of MMS-observed IDRs that has been reported. We found that Ion Diffusion Regions display significantly greater electron/ion temperatures and electric field signatures than ion-coupled reconnection, which display significantly greater electron/ion temperatures and electric field signatures than quiet, non-reconnecting current sheets. All of these current sheet structures occur in low guide field (< 0.2) and elevated solar wind speed compared to the other current sheet types. We also find that all three current sheet populations occur in tilted current sheets as frequently as in equatorial current sheets. This is a novel finding, as prior understanding was that reconnecting current sheets were most likely to occur in equatorial current sheets (*Voigt*, 1984). However, when we compare plasma properties of tilted current sheets compared to equatorial current sheets, we do not find significant changes in outflow velocity, plasma density, temperature, electric field, or guide field. This indicates that reconnection is a local process that, while sending disrupted plasma far from the reconnection region, does not significantly disrupt the global configuration of the magnetotail.

In the future, we can use our reconnection dataset to identify Electron Diffusion Regions (EDRs) in Earth's magnetotail. Currently, only four community accepted ion-coupled EDRs have been reported using MMS, and our current sheet database would ease the search for such an electron-scale process. In addition, we can use our four spacecraft capabilities to investigate if the properties of our IDRs change significantly within the distance of the spacecraft separation. *Øieroset et al.*, 2021 reported a high guide field EDR/IDR crossing in Earth's turbulent magnetosheath and investigated how plasma density and temperature changed closer and farther from the EDR. With a fortuitous magnetotail IDR observation,

this process could be repeated in a lower guide field environment. Lastly, as MMS moves to a more palatable orbit for observing the near-Earth magnetotail (positive Z GSM) in 2023 and beyond, we can continue to add statistics to each of our event pools, especially our IDR pool. 49 events require special care when performing statistics, and obtaining 100 or more events will allow for a wider parameter range when performing statistical analyses.

In Chapter 3, we present observations of electron-only reconnection generated by flux rope erosion called "electron-only flux rope erosion", introduce a new process titled "electron-only onset of reconnection" supported by an electron-only magnetotail current sheet and supporting PIC simulations, and establish a set of universal observational criteria by which spacecraft can identify electron-only reconnection in various regions of Earth's magnetosphere. "Electron-only reconnection" as defined by *Phan et al.*, 2018 refers to steady-state magnetic reconnection in a turbulent environment where current sheets are extremely thin (electron-scale), and the length of the current sheet in the L direction was short enough the ions are unable to couple to the reconnection process. Our observations of electron-only flux rope erosion are consistent with this picture, as the observed current sheets were extremely tilted and stunted because they were attached to flux ropes. However, we argue that, during the onset of ion-coupled reconnection in Earth's magnetotail, a short ($\approx$ 10 sec) interval occurs where the thinned current sheet is reconnecting but does not present any ion flows. We dub this structure "electron-only onset of reconnection" to distinguish it from electron-only flux rope erosion. We distinguish this process because, unlike electron-only flux rope erosion, it changes quickly in time and can occur in longer, ion-scale current sheets. Using these events, we develop ten criteria that can be used to identify either electron-only flux rope erosion or electron-only onset of reconnection in Earth's magnetotail: 1. B_L reversal, 2. Absolute minimum in B_{tot}, 3. No L-directed ion exhaust outflow ($|v_{iL}| < 0.5v_{iA}$, no v_{iL} reversal), 4. Super-Alfvénic L-directed electron exhaust outflow ($|v_{eL}| > v_{iA}$), 5. No total T_i response, 6. Significant T_e response, 7. Positive $J \cdot E'$, 8. Deviation of $v_{e\perp}$ from $v_{E\times B}$, 9. Electron Tearing Criterion, and 10. Magnetic Flux Transport Criterion.

At Earth's magnetopause, a recent report claimed to have observed electron-only reconnection in the form of secondary reconnection within a turbulent ion outflow, which we dub "turbulent secondary reconnection". In the future, we can develop a second set of criteria to identify turbulent secondary reconnection within turbulent outflows in the magnetotail. Because this secondary reconnection occurred within a strong ion outflow, our third criterion would be violated. This means that our criteria are either over exclusive or are only appropriate for electron-only flux rope erosion and electron-only onset of reconnection. Also, we can investigate a method to determine the distance of a four-spacecraft tetrahedron from the reconnection center. Previous work (*Retinò et al.*, 2006) utilized magnetic field orientation changes over the spacecraft separation and a linear extrapolation to estimate reconnection center distance, but it is thought that this typically underestimates distance from the reconnection center. Gaining a better understanding of distance from the reconnection center without observing a flow reversal could allow us to approximate the length of the current sheet during our electron-only reconnection candidates. Lastly, we can introduce guide field to the PIC simulations that were used to generate electron-only onset of reconnection and investigate if electron-only onset of reconnection can develop when there is notable guide field in the system.

In Chapter 4, we perform a statistical survey for electron-only reconnection from six magnetotail seasons ranging from 2017-2022, and identify 12 electron-only reconnection candidates. We further identify 4 of these events as electron-only flux rope erosion and 7 of these events as electron-only onset of reconnection. We find that these current sheets are extremely thin (electron-scale), exhibit high guide field (> 0.3), predominantly occur in highly tilted current sheets, and display an increase in plasma density at the center of the current sheet. Each of these features, which were not accounted for in our criteria, are consistent with *Lu et al.*, 2022's PIC simulations and the definition of electron-only reconnection established by *Phan et al.*, 2018. We find that electron-only reconnection displays quiet current sheet-like plasma density, ion temperature, electric field, while featuring reconnection-like

electron temperatures and $J \cdot E'$, consistent with 2D PIC simulations described in previous chapters. We find that four electron-only flux rope erosion events display elevated electron flux on the Earthward side of the current sheet, elevated guide field (> 0.5), and parallel and antiparallel electrons on the connected side of the current sheet. Conversely, we find that seven electron-only onset of reconnection events display a reversal in the low energy electron pitch angle distribution, strong isotropy in higher energy electron pitch angle at the current sheet center, and peak electron energy in the current sheet center. We place 3 low guide field, electron-only onset of reconnection candidates in time order to display the evolution from a quiet, non-reconnecting current sheet to a traditional, ion-coupled reconnecting current sheet.

In the future, we can utilize our electron-only reconnection criteria to search for electron-only reconnection in other regions of the magnetosphere such as the dayside magnetopause, flank magnetopause, or even the solar corona. For example, *Blasl et al.*, 2023 successfully used our criteria to identify electron-only reconnection within Kelvin-Helmholtz instability at the flank magnetopause. This indicates that our criteria have potential for use in other locations. Including magnetosheath events could even provide additional insights when comparing electron-only onset of reconnection to traditional, ion-coupled reconnection. Also, we can investigate if our electron-only reconnection candidates change with current sheet tilt, similar to the analysis we performed on our set of quiet current sheets, ion-coupled reconnection, and IDRs. This analysis could also help provide insight into distinguishing electron-only flux rope erosion from electron-only onset of reconnection.

APPENDIX A

Appendix

A.1 Methodologies/Techniques

A.1.1 Curlometer Technique

The curlometer technique is a calculation that uses four spacecraft measurements to approximate the current density vector of various magnetospheric current structures, including magnetopause currents, the magnetotail current sheet, ring current, and field aligned currents (FAC) at the poles. This method is derived from Ampere's Law:

$$\mu_0 \mathbf{J} = \nabla \times \mathbf{B} - \mu_0 \epsilon_0 \frac{\partial \mathbf{E}}{\partial t} \tag{A.1}$$

where $\mathbf{J}$ is the current density and $\mathbf{B}$ is the magnetic field. In space plasmas, the displacement current is typically negligible, allowing us to express $\mathbf{J}$ in the following notation:

$$\mathbf{J} = \frac{1}{\mu_0} \nabla \times \mathbf{B} \tag{A.2}$$

In this form, because using the integral form of $\nabla \times \mathbf{B}$:

$$\int\int \mathbf{J} \cdot ds = \frac{1}{\mu_0} \oint \mathbf{B} \cdot dl \tag{A.3}$$

Dunlop et al., 2021 derived the approximate average current sheet density:

$$\mathbf{J}_{av} \cdot (\Delta\mathbf{r}_i \times \Delta\mathbf{r}_j) = \frac{1}{\mu_0} \Delta\mathbf{B}_i \cdot \Delta\mathbf{r}_j - \Delta\mathbf{B}_j \cdot \Delta\mathbf{r}_i \tag{A.4}$$

where $\mathbf{J}_{av}$ is the mean current density, $\Delta\mathbf{r}_i \equiv \mathbf{r}_i - \mathbf{r}_{ref}$, and $\Delta\mathbf{B}_j \equiv \mathbf{B}_j - \mathbf{B}_{ref}$. In this nomenclature, ref indicates one spacecraft reference, for example, MMS1. i and j represent two of the other three spacecraft, for example, MMS2 and 3. This calculation can be performed three times with the three combinations of non-reference spacecraft (MMS2/3, MMS2/4, MMS3/4) to yield the components of average current in the normal directions of the three spacecraft planes connected to the reference spacecraft (MMS1). This technique is performed by the mmscurl procedure in the SPEDAS library, which also calculates $\nabla \cdot \mathbf{B}$ and $\nabla \times \mathbf{B}$.

This technique requires several prerequisites. First, it requires the four spacecraft to be in a regular tetrahedron formation. Second, it requires all measurements to be made within the same current sheet. If one or more spacecraft are observing different current sheets, the approximation will become unreliable. Third, it requires a linear magnetic field gradient between the spacecraft. By default, we expect a linear gradient at distances greater than 15 RE downtail and a non-linear field in the inner magnetosphere. As such, if the measurement is being taken within 15 RE, the contributing geomagnetic field must be subtracted from the measured field value before making the calculation. With that said, the advantage of this method over calculating the electric current from the motions of the electrons and the ions is that the derived current may have a much faster temporal resolution since the magnetic field measurement is much faster. It can be as fast as 128Hz for burst mode of fluxgate magnetometer (FGM) onboard MMS spacecraft, which is about four times faster than the plasma measurement.

A.1.2 Plasma Moment Current Calculation

The curlometer method, while useful to approximate the current density at the magnetotail current sheet under the right circumstances, is not always an appropriate method. For example, in regions of extremely low magnetic field strength, the required condition of $\nabla \cdot B = 0$ is often broken, compromising the accuracy of the curlometer technique. As such, we can also calculate current density using direct plasma measurements from the four spacecraft using current's definition as the rate of flow of electric charge:

$$\mathbf{J} = qn_p(\mathbf{v_i} - \mathbf{v_e}) \tag{A.5}$$

where q is the Coulomb charge of a proton/electron, n_p is the plasma number density, $\mathbf{v_i}$ is the bulk ion velocity vector, and $\mathbf{v_e}$ is the bulk electron velocity vector. We note that, in some events, there are small populations of heavier elements such as He+ and O+, resulting in a negligible contribution to the bulk plasma velocity. This allows us to utilize solely proton moments when calculating current density.

One advantage of this method is that the fast plasma Investigation (FPI) onboard the MMS spacecraft can directly measure plasma moments with a very fast cadence (150ms for protons and 30ms for electrons), allowing for meaning time series of directly calculated current. Another advantage of current derived from plasma measured by MMS spacecraft fleet is that we can get four current measurement at slightly separated locations for a single event. One disadvantage of plasma moment calculation is that the highest temporal resolution for current calculated from plasma should be 150ms/sample, restricted by the time resolution of the ion measurement. When observing events that change quickly on the order of 1 second, this yields only six measurements in a 1 second span. We can mitigate this by assuming that ions do not have high frequency perturbations within 150ms, allowing us to interpolate the ion moments to the 30 ms resolution of electrons and generate a 30 ms resolution measurement of the current density.

A.1.3 Four-Spacecraft Timing

Measuring the normal orientation and velocity of space plasma structures is essential to understanding their evolution. One key challenge in determining these values is that, using a single spacecraft, it is difficult to distinguish spatial variation from temporal variation of the structure in question. However, with four spacecraft, the spatial variation can be determined definitely, allowing us to calculate the velocity of the structure. This multi-spacecraft timing method is highlighted in *Russell et al.*, 1984. Qualitatively, we can use one spacecraft as a reference, then use the spacecraft locations (distance) and time difference at which the spacecraft cross a boundary (time) to calculate a velocity that includes a normal vector and magnitude. In order to utilize this method, we assume that the structure is planar at the scale of the spacecraft separation. This is reasonable for analyzing the magnetotail current sheet, as MMS's tetrahedron separation (10km) is typically much smaller than the curvature radius of the magnetotail current sheet (¿100km). We also assume that the discontinuity in question can be unambiguously identified by each of the four spacecraft. This method requires that the temporal variation is small compare to the duration of the structure recorded by the spacecraft, which allows us to attribute any temporal boundary variation to the spatial velocity profile.

In order to determine the normal direction $\hat{\mathbf{n}}$ and velocity V of a structure, we establish MMS4 as the arbitrary reference spacecraft and introduce the vector:

$$\mathbf{m} = \frac{\hat{\mathbf{n}}}{V} \ , \ \ D\mathbf{m} = \mathbf{T} \tag{A.6}$$

where D is the following 3×3 matrix:

$$D = (\mathbf{r}_1 - \mathbf{r}_4, \mathbf{r}_2 - \mathbf{r}_4, \mathbf{r}_3 - \mathbf{r}_4) \tag{A.7}$$

and $\mathbf{T}$ is the array:

$$\mathbf{T} = \begin{pmatrix} t_1 - t_4 \\ t_2 - t_4 \\ t_3 - t_4 \end{pmatrix}. \tag{A.8}$$

T represents the time difference when the four spacecraft observe the same signature of the same structure, and D represents the vector spatial separation between MMS4 and the other three spacecraft We can then solve for $\mathbf{m}$ and, consequently, $\hat{\mathbf{n}}$ and V by finding the inverse of D and calculating:

$$\mathbf{m} = D^{-1}\mathbf{T}. \tag{A.9}$$

To highlight the feasibility of this method, we show four spacecraft measurements of a magnetotail current sheet crossing by MMS in Figure A.1. In this event, and other events in this manuscript, we extract the time at which the B_X measured by each MMS spacecraft crosses 0 to calculate T:

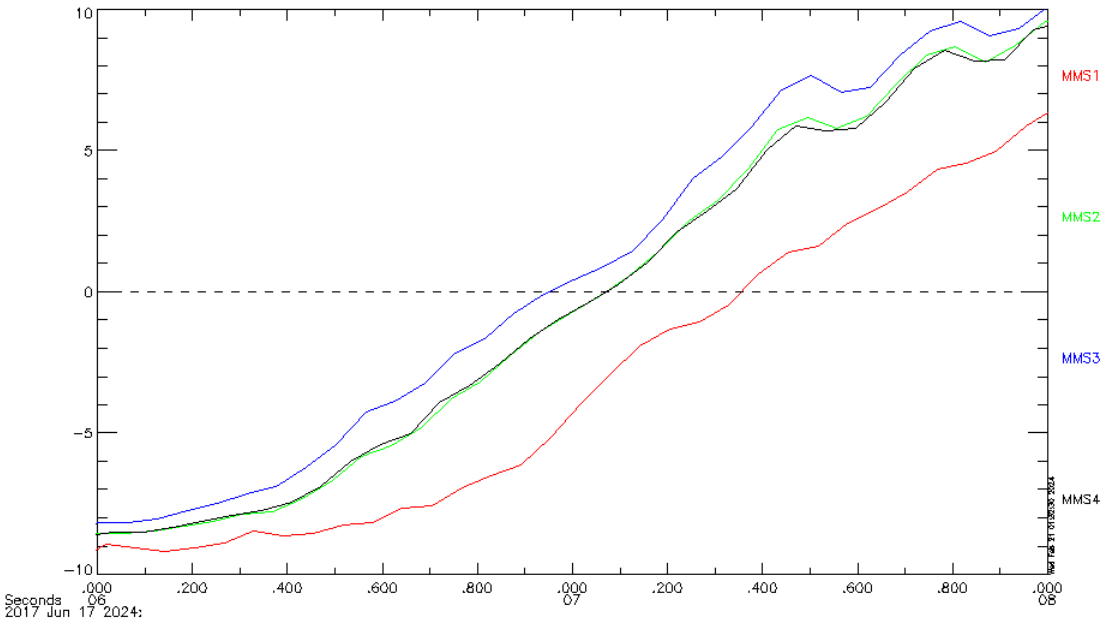

Figure A.1: Times series of B_x GSM measured by four MMS spacecraft on June 17, 2017, 20:24:06-08

Solving this set of equations will result in the normal direction of this structure nd the velocity of the structure along the normal. The local planar structure is a limitation to this method. For structures with radius of curvature on the order of the spacecraft separation, such as shocks and the electron diffusion region, the timing method becomes unreliable. To address this, we compare the radius of curvature and the spacecraft separation to validate this timing method.

A.1.4 Curvature Vector & Radius of Curvature

The curvature of magnetic field is another important physical parameter for space plasma physics. The measurement of curvature helps to understand the topology of the magnetic field lines and enables the estimation of magnetic curvature force imposed onto the plasma.

The curvature vector and radius of curvature of the magnetic field can be described as:

$$\kappa = \mathbf{b} \cdot \nabla \mathbf{b} \tag{A.10}$$

where $\mathbf{b}$ is the unit vector of the magnetic field.

The gradients of the directly measured physics quantities, such as pressure and magnetic field, are also of great importance. Using MMS's four spacecraft tetrahedron, we can calculate the gradient of both scalar quantities and vector quantities. We utilize a linear numerical method developed by *Shen and Dunlop*, 2023 to calculate the gradient of a vector or scalar field. ∇b is calculated using this method.

We note that the left hand side of the dot product can be used as the average of the magnetic field directions measured by four MMS spacecraft. Using κ, the radius of curvature can be described as:

$$R_C = \frac{1}{|\kappa|} \tag{A.11}$$

A.2 Event Lists

A.2.1 Quiet Current Sheets

Table A.1: List of Quiet, non-reconnecting current sheet events observed by MMS in Earth's magnetotail from 2017-2022.

Event #	**Date/Time**	**X (GSM)**	**Y (GSM)**	**Z (GSM)**
1	6-05-17/12:18-19	-20.3	-7.9	3.6
2	6-02-17/12:35-40	-18.3	-6.9	2.5
3	6-02-17/22:24-26	-20.9	-11.7	0.3
4	6-03-17/04:46-48	-20.9	-13.4	2.9
5	6-03-17/05:45-47	-20.8	-13.5	3.6

6	6-06-17/03:13-14	-21.1	-13.3	2.6
7	6-06-17/08:08-09	-20	-13.2	5.6
8	6-06-17/08:16-17	-20	-13.2	5.6
9	6-08-17/05:30-31	-20	-6.5	2.4
10	6-08-17/07:07-08	-20.6	-7	3.1
11	6-08-17/12:17-20	-21.8	-8.6	4.6
12	6-08-17/20:34-35	-21.9	-12.1	1.9
13	6-09-17/00:45-47	-21.3	-12.9	2.1
14	6-09-17/01:21-23	-21.1	-13	2.3
15	6-09-17/03:15-16	-20.6	-13.1	3.3
16	6-13-17/20:54-55	-20.8	-5.5	1.9
17	6-13-17/22:15-17	-21.3	-6.1	1.9
18	6-14-17/00:58-59	-22.1	-7	2.3
19	6-14-17/02:00-02	-22.3	-7.3	2.6
20	6-17-17/04:05-06	-23.3	-8	4.2
21	6-19-17/09:19-21	-20.3	-1.9	3
22	6-20-17/03:16-18	-23.4	-7.9	4.5
23	7-03-17/05:53-54	-17.9	3.3	1.8
24	7-12-17/00:18-20	-22.3	3.8	4
25	7-12-17/11:11-12	-24.5	3.1	4.5
26	7-12-17/14:11-13	-24.5	2.2	5
27	7-20-17/07:46-47	-20.6	8	1.3
28	7-22-17/21:23-24	-16.8	8.5	2.2
29	8-01-17/11:40-41	-22.4	8.3	2.6
30	8-03-17/08:06-08	-18.5	12.2	-0.9
31	8-04-17/16:05-06	-19.1	5.5	4
32	8-04-17/16:11-12	-19.1	5.5	4.1

33	8-09-17/07:33-35	-20.6	13.6	-0.3
34	8-12-17/01:19-20	-19.6	14.4	2.5
35	8-15-17/17:45-47	-19.2	10.1	3.1
36	8-18-17/16:56-58	-17.4	9.1	2.7
37	8-20-17/10:25-26	-17.4	16.7	-3.6
38	8-23-17/12:50-51	-18.3	16.9	-2.8
39	8-25-17/16:08-10	-12.2	17.2	-3.1
40	8-25-17/20:14-15	-14.1	18.2	0.3
41	8-25-17/20:53-54	-14.4	18.3	0.7
42	8-26-17/17:59-01	-18	15.3	1.4
43	8-29-17/06:40-41	-17.2	18	-2
44	8-29-17/18:41-42	-16.6	13.5	2
45	8-29-17/20:09-11	-16.2	12.6	2.8
46	9-01-17/01:05-06	-16.3	18.9	1.5
47	9-01-17/01:26-27	-16.4	18.9	1.4
48	6-15-18/00:12-14	-19.7	-15.1	4.7
49	6-15-18/20:54-56	-11.7	-14.7	2.7
50	6-15-18/22:40-42	-10.5	-14.2	2.1
51	6-16-18/21:49-51	-15.8	-5.3	4.1
52	6-16-18/22:59-01	-16.5	-6	4.3
53	6-19-18/14:46-48	-13.9	-1.7	4.5
54	6-19-18/15:28-30	-14.5	-2.2	4.7
55	6-19-18/16:41-43	-15.4	-3.2	5
56	6-19-18/18:53-55	-16.8	-5	5
57	6-19-18/19:40-42	-17.3	-5.5	5
58	6-22-18/14:51-53	-17.2	-3.2	6
59	6-25-18/18:40-42	-20.9	-6.8	6.8

60	6-25-18/18:59-00	-20.9	-7	6.7
61	6-25-18/19:04-06	-21	-7.1	6.7
62	6-25-18/20:09-11	-21.2	-7.8	6.5
63	6-25-18/21:30-31	-21.5	-8.4	6.3
64	6-25-18/22:15-17	-21.6	-8.7	6.3
65	6-26-18/15:54-56	-19.9	-11	8.4
66	6-26-18/16:06-08	-19.8	-11.1	8.2
67	6-26-18/19:16-18	-18.6	-12.4	6.1
68	6-26-18/19:39-40	-18.4	-12.5	5.9
69	6-26-18/20:29-31	-18	-12.6	5.4
70	6-26-18/21:09-11	-17.7	-12.7	5.2
71	6-26-18/22:15-17	-17.1	-12.8	4.8
72	6-26-18/23:55-57	-16.2	-12.6	4.7
73	6-27-18/00:10-11	-16.1	-12.6	4.7
74	6-27-18/00:54-56	-15.6	-12.4	4.7
75	6-27-18/02:05-07	-14.9	-12.1	4.9
76	6-27-18/02:25-27	-14.7	-12	5
77	6-28-18/16:34-36	-21.7	-5.8	7.8
78	6-28-18/20:01-03	-22.2	-8.1	7
79	6-28-18/22:00-01	-22.3	-8.9	6.7
80	6-28-18/22:53-55	-22.4	-9.2	6.7
81	6-29-18/18:20-22	-17.5	-11.3	6.3
82	7-05-18/18:42-44	-11.7	-9	4.3
83	7-05-18/19:05-07	-11.4	-9	4.1
84	7-05-18/20:41-43	-9.7	-8.7	3.1
85	7-06-18/12:58-00	-14.4	2.6	4.2
86	7-06-18/13:22-24	-14.8	2.4	4.4

87	7-07-18/14:40-42	-23.1	-4.6	9.1
88	7-09-18/13:30-31	-18.3	2.1	5.7
89	7-09-18/14:32-34	-18.9	1.6	6.1
90	7-09-18/17:17-19	-20.4	0	6.8
91	7-11-18/01:55-56	-18.6	-7.9	6.3
92	7-13-18/21:19-21	-19	-7.3	6.2
93	7-13-18/21:59-01	-18.7	-7.4	6
94	7-14-18/21:56-57	-12.2	3.5	4.2
95	7-15-18/16:31-33	-23.1	0.3	7.7
96	7-19-18/18:10-11	-15.8	-5.5	5.7
97	7-20-18/16:28-30	-15.1	5.3	4.2
98	7-20-18/17:25-27	-15.9	5	4.7
99	7-23-18/12:44-46	-15.5	6.5	3.3
100	7-23-18/13:22-24	-16.1	6.5	3.6
101	7-23-18/14:07-09	-16.6	6.3	3.9
102	7-23-18/18:00-01	-19.2	5	5.9
103	7-24-18/20:09-10	-23	-1.4	7.5
104	7-26-18/11:21-22	-17.6	7.2	3.7
105	7-26-18/12:09-11	-18.2	7.1	3.9
106	7-26-18/13:01-03	-18.7	7	4.2
107	7-26-18/15:01-03	-19.9	6.5	5.1
108	8-01-18/09:51-53	-21	8.3	4.3
109	8-01-18/12:58-00	-22.2	7.9	4.9
110	8-01-18/15:39-41	-22.9	6.9	5.9
111	8-01-18/18:47-48	-23.5	5.4	7
112	8-05-18/16:28-30	-16.4	-0.5	5
113	8-05-18/17:11-13	-15.8	-0.9	4.8

114	8-05-18/18:00-02	-15.1	-1.3	4.6
115	8-06-18/15:36-37	-14.7	9.7	2.6
116	8-09-18/15:18-19	-17.2	10.7	2.9
117	8-09-18/17:20-22	-18.4	10.4	4.2
118	8-12-18/15:37-39	-19.4	11.5	3.3
119	8-13-18/10:21-23	-22.9	8.7	3.9
120	8-13-18/11:30-31	-22.8	8.4	3.9
121	8-13-18/13:20-21	-22.6	7.7	4.2
122	8-13-18/14:10-12	-22.4	7.4	4.4
123	8-15-18/06:59-00	-16.6	12.2	2
124	8-15-18/07:44-46	-17	12.3	1.8
125	8-15-18/08:30-31	-17.5	12.4	1.6
126	8-15-18/09:40-41	-18.1	12.5	1.4
127	8-15-18/10:10-12	-18.4	12.5	1.4
128	8-15-18/13:28-30	-19.9	12.4	2.2
129	8-15-18/14:29-30	-20.3	12.3	2.7
130	8-15-18/23:34-36	-22.5	9.7	6.3
131	8-16-18/12:00-01	-21.7	7.7	3.6
132	8-16-18/12:58-00	-21.4	7.3	3.7
133	8-16-18/17:47-49	-19.6	4.5	4.7
134	8-16-18/20:06-07	-18.4	3.1	4.7
135	8-17-18/19:35-36	-10.8	10.9	2.8
136	8-18-18/06:29-31	-18.2	13.1	2.3
137	8-18-18/07:01-03	-18.5	13.2	2.1
138	8-18-18/08:20-22	-19.1	13.3	1.7
139	8-18-18/09:11-13	-19.4	13.3	1.5
140	8-18-18/13:59-00	-21	12.9	2.3

141	8-18-18/16:10-11	-21.5	12.3	3.6
142	8-18-18/16:31-33	-21.6	12.2	3.8
143	8-18-18/18:48-50	-22	11.3	5.1
144	8-19-18/10:58-59	-20.4	7.3	3.1
145	8-19-18/11:39-40	-20.2	7	3.1
146	8-19-18/12:17-19	-19.9	6.7	3.2
147	8-19-18/13:09-11	-19.6	6.2	3.3
148	7-01-19/18:33-35	-13.5	-15.3	1.8
149	7-01-19/19:31-33	-12.8	-15	0.9
150	7-04-19/22:47-49	-19	-16.2	2.3
151	7-04-19/21:59-00	-19.3	-16.2	2.6
152	7-05-19/00:59-01	-17.9	-15.8	2.4
153	7-05-19/01:55-57	-17.3	-15.6	2.6
154	7-05-19/02:35-37	-17	-15.4	2.8
155	7-05-19/03:23-25	-16.5	-15.2	3.1
156	7-05-19/07:15-17	-14	-13.7	4.4
157	7-08-19/12:07-09	-19.2	-13.1	7.5
158	7-08-19/13:28-30	-18.5	-13.3	6.8
159	7-08-19/14:22-24	-18	-13.4	6.2
160	7-08-19/16:18-20	-16.8	-13.7	4.5
161	7-08-19/17:59-01	-15.7	-13.7	2.9
162	7-08-19/18:22-24	-15.5	-13.6	2.6
163	7-08-19/19:29-30	-14.7	-13.5	1.6
164	7-08-19/20:59-00	-13.5	-13.1	0.7
165	7-08-19/22:01-03	-12.7	-12.7	0.2
166	7-08-19/23:20-21	-11.5	-12.2	-0.1
167	7-09-19/00:39-40	-10.3	-11.5	-0.2

168	7-09-19/03:09-11	-7.7	-10.1	0
169	7-10-19/20:11-12	-25.5	-10.3	7.6
170	7-14-19/23:08-10	-25.4	-11.7	5.7
171	7-15-19/00:03-05	-25.2	-11.8	5.6
172	7-15-19/15:47-49	-18.8	-11.3	5.1
173	7-15-19/16:10-12	-18.5	-11.4	4.8
174	7-15-19/18:59-00	-16.6	-11.6	2.5
175	7-15-19/19:47-49	-16	-11.5	1.9
176	7-15-19/23:40-42	-12.6	-10.6	0.4
177	7-16-19/00:37-39	-11.7	-10.2	0.3
178	7-16-19/16:00-01	-10.8	3	5.1
179	7-17-19/20:00-01	-26.5	-6.9	8
180	7-19-19/14:13-15	-10.9	-8.8	2.5
181	7-21-19/21:00-02	-27	-8.1	6.4
182	7-23-19/05:35-36	-7	-7.1	0.5
183	7-25-19/17:00-01	-25.7	-6.8	6.3
184	7-25-19/17:39-41	-25.5	-7.1	6
185	7-25-19/23:39-40	-23.1	-8.5	3.7
186	7-26-19/00:29-30	-22.7	-8.5	3.7
187	7-26-19/02:18-20	-21.7	-8.4	3.7
188	7-26-19/11:48-50	-14.5	-7.6	3.5
189	7-26-19/12:21-23	-13.9	-7.6	3.3
190	7-28-19/18:20-21	-28	-3.5	7.1
191	7-28-19/19:02-04	-27.9	-3.9	7
192	7-29-19/15:22-24	-21.6	-6.4	4.6
193	7-29-19/16:51-52	-20.7	-6.9	3.9
194	7-29-19/18:49-51	-19.3	-7.3	2.8

195	8-01-19/18:29-31	-26.1	-4.3	5.2
196	8-01-19/23:39-40	-24.1	-5.6	3.8
197	8-05-19/13:25-27	-23.6	-3.3	4.5
198	8-05-19/14:22-24	-23.1	-3.6	4.2
199	8-05-19/17:29-31	-21.2	-4.7	3.1
200	8-05-19/18:17-18	-20.7	-4.9	2.7
201	8-05-19/18:44-46	-20.3	-5.1	2.5
202	8-08-19/12:29-30	-27.9	1.4	5.2
203	8-08-19/20:39-40	-25.9	-2	4.1
204	8-09-19/10:59-01	-17.2	-4.1	2.5
205	8-10-19/15:17-19	-19.3	8.5	4.9
206	8-10-19/16:46-48	-20.4	8	5.6
207	8-10-19/13:41-43	-18.1	8.8	4.2
208	8-12-19/12:36-38	-24.4	-0.4	3.4
209	8-12-19/13:39-40	-23.9	-0.7	3.2
210	8-15-19/17:22-23	-27.1	2.4	3.7
211	8-16-19/10:32-34	-18.4	-2.1	1.6
212	8-17-19/12:12-14	-15.8	10.5	2.7
213	8-17-19/13:34-36	-16.9	10.6	3.1
214	8-17-19/15:01-02	-18	10.5	3.7
215	8-31-19/13:03-05	-13.9	13.6	0.7
216	8-31-19/15:28-30	-15.7	14.1	1.7
217	9-01-19/13:34-36	-25.4	13.7	-0.1
218	9-02-19/21:44-46	-19.2	3.1	-0.3
219	9-04-19/05:35-37	-16.3	15.3	1.6
220	9-04-19/06:07-09	-16.7	15.4	1.2
221	9-04-19/07:06-07	-17.3	15.6	0.6

222	9-04-19/13:21-22	-20.6	16.1	-0.4
223	9-04-19/15:40-41	-21.6	16	0.8
224	9-04-19/16:30-31	-22	16	1.3
225	9-06-19/00:10-12	-23.6	8.5	0.6
226	9-06-19/02:54-56	-22.6	7.4	-0.3
227	9-07-19/07:09-10	-7	12	0.7
228	9-07-19/09:41-43	-9.5	13.5	-0.3
229	9-07-19/10:39-40	-10.3	14	-0.5
230	9-07-19/13:35-36	-12.7	15.2	-0.2
231	9-07-19/16:24-25	-14.7	15.9	1.3
232	9-08-19/18:05-07	-24.5	15.5	0.8
233	9-09-19/04:39-40	-24.6	12.7	-0.7
234	7-01-20/03:56-57	-16.8	-6.4	7.1
235	7-01-20/15:55-56	-21.6	-11.8	7.3
236	7-01-20/16:39-40	-21.8	-12.4	6.8
237	7-01-20/19:17-18	-22.3	-14.1	4.8
238	7-01-20/21:36-38	-22.5	-15.1	3.4
239	7-02-20/00:16-18	-22.7	-15.8	3
240	7-02-20/16:51-52	-20.7	-18	2.3
241	7-02-20/22:09-10	-18.9	-17.9	-2.1
242	7-02-20/23:47-49	-18.2	-17.7	-2.4
243	7-03-20/04:22-23	-16	-17.2	-0.8
244	7-03-20/06:56-58	-14.5	-16.7	0.4
245	7-03-20/09:50-51	-12.7	-15.9	1
246	7-05-20/17:15-16	-23.7	-15.1	4.6
247	7-05-20/18:34-35	-23.6	-15.6	3.3
248	7-05-20/19:28-30	-23.5	-15.9	2.6

249	7-05-20/21:06-07	-23.3	-16.2	1.5
250	7-05-20/23:26-27	-23	-16.5	0.8
251	7-06-20/00:35-36	-22.8	-16.6	0.8
252	7-06-20/02:02-03	-22.4	-16.7	1.1
253	7-06-20/15:08-09	-17.7	-16.4	1.5
254	7-06-20/15:52-53	-17.3	-16.3	0.8
255	7-06-20/16:48-49	-16.8	-16.2	-0.2
256	7-06-20/17:28-29	-16.4	-16.1	-0.9
257	7-06-20/18:40-42	-15.7	-15.7	-2.1
258	7-08-20/17:14-15	-23.4	-10.1	6.6
259	7-08-20/23:39-40	-24.3	-13	3.7
260	7-09-20/01:23-24	-24.4	-13.3	3.8
261	7-09-20/18:52-53	-22	-15.7	0.7
262	7-09-20/21:32-33	-21	-15.7	-1.2
263	7-09-20/21:59-00	-20.9	-15.7	-1.3
264	7-10-20/03:35-36	-18.3	-15.4	-0.8
265	7-10-20/06:07-08	-16.8	-15.1	0.3
266	7-10-20/10:58-59	-13.5	-14.1	0.9
267	7-10-20/12:54-56	-12	-13.5	0.1
268	7-10-20/13:38-39	-11.3	-13.2	-0.3
269	7-12-20/18:24-25	-25.1	-12.7	3.8
270	7-12-20/19:32-33	-25.1	-13.1	3
271	7-12-20/20:11-12	-25	-13.2	2.6
272	7-12-20/21:24-26	-24.9	-13.5	1.9
273	7-12-20/22:21-22	-24.8	-13.7	1.6
274	7-12-20/23:07-09	-24.6	-13.8	1.4
275	7-13-20/02:56-58	-23.9	-14.1	1.9

276	7-13-20/03:48-49	-23.7	-14.1	2.2
277	7-13-20/04:47-48	-23.4	-14.1	2.6
278	7-13-20/17:32-34	-17.8	-14.2	-0.7
279	7-13-20/19:08-09	-16.8	-13.8	-2
280	7-15-20/16:56-58	-24.4	-6.9	6.6
281	7-15-20/19:13-15	-25	-8.3	5.5
282	7-15-20/20:07-09	-25.1	-8.8	5.1
283	7-15-20/22:22-24	-25.5	-9.6	4.4
284	7-16-20/17:26-28	-24	-12.8	2.2
285	7-16-20/21:51-53	-22.4	-13.2	-0.7
286	7-17-20/05:33-35	-18.5	-13.1	0.2
287	7-17-20/06:55-57	-17.6	-13	0.6
288	7-17-20/09:03-05	-16.1	-12.7	0.9
289	7-17-20/10:23-25	-15.1	-12.5	0.9
290	7-17-20/11:45-47	-14	-12.2	0.6
291	7-17-20/14:15-17	-11.7	-11.5	-0.7
292	7-20-20/10:50-00	-22.7	-11.5	3.3
293	7-20-20/11:49-51	-22.3	-11.6	3.1
294	7-20-20/16:41-43	-19.7	-12	0.2
295	7-22-20/18:52-54	-25.8	-5.2	5.6
296	7-23-20/14:54-56	-25.9	-9.2	3.7
297	7-23-20/16:58-59	-25.4	-9.9	2.4
298	7-24-20/04:31-33	-20.4	-10.9	-0.2
299	7-24-20/06:03-05	-19.5	-11	0.1
300	7-24-20/07:26-28	-18.5	-10.9	0.4
301	7-24-20/08:46-48	-17.5	-10.9	0.6
302	7-24-20/09:20-21	-17.1	-10.8	0.6

303	7-24-20/12:05-06	-14.8	-10.6	0.2
304	7-25-20/15:57-59	-18.9	1.8	6.5
305	7-25-20/16:09-10	-24.6	-2.3	6
306	7-27-20/09:48-50	-24.2	-8.9	2.7
307	7-29-20/16:31-32	-25.7	-0.8	5.6
308	7-29-20/19:19-20	-26.5	-2.3	5.1
309	7-30-20/15:02-04	-26.8	-6.4	2.8
310	7-30-20/13:11-12	-27.1	-5.8	3.4
311	7-30-20/16:10-12	-26.5	-6.7	2.2
312	7-31-20/05:51-53	-20.4	-8.8	-0.3
313	7-31-20/06:48-50	-19.7	-8.8	-0.2
314	7-31-20/09:09-10	-18	-9	0.1
315	8-02-20/16:11-13	-28.1	-2.4	3.7
316	8-03-20/00:18-20	-27.7	-4.8	1.6
317	8-03-20/03:28-30	-27.1	-5.3	1.4
318	8-03-20/03:44-46	-27	-5.3	1.4
319	8-03-20/04:19-21	-26.9	-5.4	1.4
320	8-03-20/08:57-59	-25.4	-6.1	1.6
321	8-05-20/13:16-18	-24.6	3.4	4.6
322	8-05-20/16:39-40	-25.9	1.9	4.6
323	8-05-20/20:26-28	-27	0.3	4.3
324	8-06-20/12:09-10	-27.9	-2.7	2.3
325	8-08-20/13:40-41	-16.8	6.8	4.2
326	8-08-20/14:50-51	-17.8	6.5	4.5
327	8-08-20/15:48-50	-18.6	6.2	4.7
328	8-08-20/16:58-00	-19.5	5.8	5
329	8-22-20/13:08-10	-15.4	10.3	1.9

330	8-22-20/14:23-25	-16.5	10.3	2.2
331	8-23-20/06:51-53	-25.7	8.6	0.6
332	8-23-20/07:36-38	-25.9	8.5	0.3
333	8-26-20/06:55-57	-19.5	11.3	1.3
334	8-26-20/12:05-07	-22.5	10.9	-0.1
335	8-27-20/05:19-20	-27.3	7.6	-1
336	8-29-20/07:57-59	-9.6	10.5	1.6
337	8-29-20/08:37-39	-10.3	10.8	1.3
338	8-29-20/11:08-10	-12.9	11.6	0.7
339	8-29-20/12:36-38	-14.3	11.8	0.7
340	8-29-20/13:19-20	-14.9	11.9	0.8
341	8-29-20/14:46-48	-16.1	12	1.2
342	9-02-20/06:00-01	-17.8	13.1	0.7
343	9-02-20/07:30-31	-18.8	13.1	-0.3
344	9-02-20/08:40-42	-19.5	13.1	-0.9
345	9-03-20/00:40-41	-25.7	11.5	0
346	9-03-20/03:00-02	-26.1	11	-1.2
347	9-05-20/07:51-53	-8.4	11.4	0.9
348	9-05-20/09:31-33	-10.1	12.2	0.2
349	9-05-20/13:02-05	-13.4	13.3	-0.3
350	9-05-20/14:07-09	-14.2	13.5	-0.1
351	9-05-20/15:43-45	-15.5	13.8	0.5
352	9-09-20/07:25-27	-17.4	15.1	-1.6
353	9-09-20/17:59-01	-22.4	15.1	-1.2
354	9-09-20/18:40-42	-22.6	15	-0.9
355	9-09-20/19:49-51	-23	15	-0.5
356	9-09-20/22:00-02	-23.6	14.7	-0.3

357	9-09-20/22:54-56	-23.8	14.6	-0.4
358	9-12-20/08:49-51	-8.6	13	-0.3
359	9-12-20/10:26-28	-10.1	13.7	-1
360	9-12-20/11:11-13	-10.7	14	-1.2
361	9-12-20/14:09-10	-13.1	15	-1.1
362	9-12-20/16:23-25	-14.7	15.6	-0.2
363	9-12-20/19:01-02	-16.4	16	1
364	9-12-20/20:10-11	-17.1	16.1	1.4
365	9-12-20/22:05-07	-18.2	16.3	1.5
366	9-12-20/23:22-24	-18.8	16.4	1.3
367	9-13-20/00:31-33	-19.4	16.4	0.9
368	9-13-20/01:55-57	-20	16.5	0
369	9-13-20/02:50-52	-20.4	16.4	-0.7
370	9-29-21/20:13-15	-12.9	18.5	-2.8
371	9-29-21/21:20-21	-13.5	18.8	-2.7
372	9-29-21/22:23-25	-14	19.1	-2.8
373	9-29-21/23:09-10	-14.3	19.2	-3.1
374	9-26-21/00:44-46	-9.4	15.4	-0.1
375	9-26-21/18:35-37	-18.7	18.2	-6.6
376	9-23-21/20:38-40	-22.4	14.9	-8.2
377	9-22-21/07:00-01	-5.2	11.4	-0.9
378	9-19-21/00:54-55	-11.6	14.4	0.1
379	9-19-21/01:30-31	-12.1	14.6	-0.3
380	9-19-21/02:20-21	-12.7	14.8	-1
381	9-16-21/00:38-39	-19.8	15.4	-2.9
382	9-15-21/06:19-20	-6.3	10.8	-0.1
383	9-12-21/03:20-22	-15.3	13.6	-1.2

384	9-12-21/05:40-42	-16.9	13.6	-3.2
385	9-08-21/07:00-02	-8.5	10.5	-0.2
386	9-08-21/09:00-01	-10.7	11.3	-1.4
387	9-05-21/01:00-01	-15.3	11.6	1
388	9-04-21/22:20-21	-12.9	11	2
389	9-02-21/00:12-14	-23	10.6	-1.2
390	9-01-21/06:29-30	-9.5	9.6	0.7
391	9-01-21/08:24-25	-11.7	10.1	-0.4
392	8-29-21/01:13-14	-16.8	9.8	1.6
393	8-29-21/03:15-16	-18.4	9.9	0.5
394	8-28-21/17:51-52	-9.3	8.7	2.2
395	8-28-21/21:24-25	-13.3	9.4	2.6
396	8-28-21/23:18-20	-15.2	9.6	2.3
397	8-25-21/08:34-35	-13.1	8.9	0.4
398	8-25-21/10:19-20	-14.9	9	-0.2
399	8-21-21/19:35-36	-21.7	6.8	0
400	8-21-21/17:45-47	-20.6	7	0.4
401	8-18-21/09:40-41	-15.6	7.6	1.1
402	8-18-21/20:29-30	-23.4	5.8	1.1
403	8-15-21/06:49-50	-22.9	5	0.8
404	8-15-21/08:30-31	-23.8	4.6	0.3
405	8-14-21/18:22-24	-12.4	6.4	3.4
406	8-14-21/19:26-28	-13.7	6.2	3.6
407	8-01-21/10:09-10	-25	-1.1	2.6
408	7-29-21/02:51-53	-26.2	-4.7	1.5
409	7-29-21/04:40-41	-26.6	-5.1	1.5
410	7-29-21/05:58-59	-26.8	-5.5	1.6

411	7-29-21/07:11-13	-27	-5.7	1.6
412	7-28-21/17:10-11	-22.7	-1.4	3.5
413	7-28-21/19:07-09	-23.6	-2.4	3
414	7-28-21/20:20-22	-24.2	-2.9	2.7
415	7-26-21/07:05-06	-26.1	-10.4	0
416	7-26-21/08:19-20	-25.9	-10.6	0.2
417	7-26-21/09:18-20	-25.6	-10.8	0.3
418	7-26-21/10:48-50	-25.3	-11.1	0.2
419	7-26-21/11:27-29	-25.1	-11.2	0.1
420	7-25-21/14:05-06	-25.9	-5.6	3.1
421	7-25-21/15:40-41	-26.2	-6.3	2.4
422	7-25-21/16:32-34	-26.4	-6.7	2
423	7-25-21/17:25-27	-26.5	-7	1.6
424	7-22-21/02:28-0:	-25.6	-10.3	0
425	7-22-21/05:41-43	-26.1	-8.4	2.2
426	7-22-21/06:40-41	-26.2	-8.6	2.3
427	7-22-21/11:10-11	-26.3	-9.7	2.5
428	7-21-21/13:36-38	-20.6	-2	4.9
429	7-19-21/05:53-54	-24.9	-12.9	0
430	7-19-21/07:13-14	-24.6	-13.2	0.5
431	7-19-21/08:40-42	-24.3	-13.4	0.8
432	7-19-21/13:39-40	-22.8	-14.1	-0.1
433	7-19-21/15:01-03	-22.3	-14.2	-1.1
434	7-18-21/06:51-52	-22.9	-5.8	4.5
435	7-18-21/15:00-01	-25.1	-8.9	3.3
436	7-17-21/20:26-28	-16.8	-2.2	5
437	7-16-21/08:50-52	-18.8	-15.5	-1.3

438	7-16-21/11:12-14	-17.4	-15.3	-1.2
439	7-16-21/13:00-01	-16.3	-15.1	-1.9
440	7-15-21/05:07-08	-24.8	-11.3	2.2
441	7-15-21/11:46-48	-24.9	-12.8	3
442	7-15-21/12:54-56	-24.8	-13.2	2.6
443	9-16-22/14:10-20	-13.9	11.2	-6.7
444	8-26-22/03:55-56	-10.2	6.8	-0.3
445	8-19-22/01:13-14	-8.5	5.5	1.2
446	8-12-22/00:20-22	-9.8	4.3	1.7
447	8-11-22/22:55-00	-7.5	4.2	2
448	8-10-22/02:00-02	-27.5	-5.7	-6.1
449	8-10-22/09:59-00	-26	-8.9	-4.8
450	8-09-22/05:29-30	-24.6	-0.8	-2.2
451	7-24-22/07:40-41	-17.6	-15.1	-4.5
452	7-24-22/13:10-20	-13.8	-14.3	-4
453	7-23-22/06:55-00	-25.6	-12.6	-2.4
454	7-23-22/11:30-40	-25.1	-13.9	-1.8
455	7-22-22/01:00-10	-14.8	-1	1.9
456	7-22-22/03:09-10	-16.8	-2	1.5
457	7-22-22/03:39-40	-17.2	-2.2	1.4
458	7-22-22/09:30-40	-21.2	-4.9	1.2
459	7-22-22/08:00-30	-20.7	-4.5	1.2
460	7-20-22/07:40-41	-22.2	-16.2	-3.5
461	7-20-22/08:54-55	-21.8	-16.4	-3.1
462	7-20-22/09:58-00	-21.4	-16.5	-2.8
463	7-20-22/10:55-00	-21	-16.6	-2.8
464	7-20-22/12:14-15	-20.4	-16.6	-3

465	7-20-22/13:27-28	-19.9	-16.5	-3.5
466	7-20-22/14:20-22	-19.5	-16.4	-4
467	7-19-22/05:14-16	-23.8	-9.7	-0.9
468	7-16-22/10:34-36	-23.6	-16.4	-1.4
469	7-16-22/13:41-43	-23	-16.9	-2.4
470	7-15-22/05:55-57	-19.2	-6.1	1.5
471	7-15-22/06:40-42	-19.6	-6.4	1.6
472	7-15-22/08:49-51	-20.7	-7.5	1.8
473	7-13-22/09:21-23	-19.4	-18.5	-3
474	7-13-22/10:55-00	-18.7	-18.5	-2.8
475	7-13-22/11:12-14	-18.6	-18.5	-2.8
476	7-12-22/07:19-20	-23.1	-13.4	-0.2

A.2.2 Ion-Coupled Reconnection

Table A.2: List of Ion-Coupled Reconnection Events observed by MMS in Earth's magnetotail from 2017-2022.

Event #	**Date/Time**	**X (GSM)**	**Y (GSM)**	**Z (GSM)**
1	7-11-17/22:33-35	-21.6	4.1	3.8
2	8-10-17/12:18-19	-14.7	4.1	3.2
3	6-02-17/10:03-04	-17	-5.5	2
4	6-02-17/21:43-45	-20.8	-11.5	0.3
5	6-05-17/13:41-42	-20.7	-8.6	3.5
6	6-11-17/17:01-02	-22.3	-10.9	4.1
7	6-11-17/20:28-29	-21.7	-12.1	2.6
8	6-13-17/21:32-33	-21.1	-5.8	1.9
9	6-14-17/06:49-50	-22.9	-8.1	4.7

10	6-15-17/01:41-42	-18.6	-12	3.4
11	6-19-17/04:59-00	-17.6	-0.7	1.9
12	6-19-17/09:48-49	-20.5	-2	3.2
13	6-20-17/16:05-06	-19.6	-9.3	5.8
14	6-22-17/07:37-38	-21.8	-2	3.6
15	6-22-17/13:16-17	-23.4	-3.4	4.8
16	6-25-17/05:37-38	-22.8	-2.1	3.9
17	6-27-17/22:41-42	-22.1	-1.2	3.4
18	6-28-17/04:23-24	-23.7	-2.1	4.4
19	6-28-17/16:33-34	-23.7	-4.8	5.8
20	7-04-17/15:48-49	-21.3	-3.9	6.3
21	7-04-17/16:59-00	-20.8	-4.5	6
22	7-06-17/01:40-41	-18.3	3.6	2.4
23	7-06-17/06:25-26	-21.1	3.2	2.8
24	7-06-17/15:46-47	-24.2	1.3	4.5
25	7-06-17/19:37-38	-24.6	-0.4	5
26	7-06-17/22:40-41	-24.6	-1.5	5.2
27	7-09-17/10:48-49	-24.1	3	3.9
28	7-15-17/10:20-21	-24.4	3.4	4.7
29	7-17-17/07:52-53	-18.1	7.3	0.7
30	7-17-17/08:47-48	-18.7	7.3	0.6
31	7-17-17/14:43-44	-21.8	6.8	2.2
32	7-18-17/08:28-29	-23.9	3.8	4.8
33	7-18-17/13:14-15	-22.8	2.7	5.2
34	7-18-17/19:01-02	-20.4	-0.3	5.7
35	7-20-17/11:38-39	-22.2	7.7	1.6
36	7-20-17/13:07-08	-22.7	7.6	2

37	7-20-17/19:20-21	-24	5.6	4.7
38	7-21-17/14:15-16	-20.5	1.9	5.3
39	7-23-17/00:38-39	-18.9	8.4	2.8
40	7-23-17/17:21-22	-23.9	6.6	4.2
41	7-24-17/12:50-51	-18.6	2	5
42	7-26-17/02:44-45	-21.7	9	3.2
43	7-26-17/11:34-35	-23.6	8.5	2.2
44	7-26-17/13:20-21	-23.7	8.1	2.7
45	7-26-17/18:03-04	-23.5	6.2	4.7
46	7-29-17/02:52-53	-22.6	9.4	3.6
47	7-29-17/08:23-24	-23.3	9.1	2.3
48	7-29-17/09:24-25	-23.3	8.9	2.3
49	7-29-17/12:58-59	-22.8	7	3.9
50	7-29-17/15:48-49	-21.6	10.8	3.2
51	7-31-17/19:26-27	-22	10.4	3.9
52	7-31-17/20:59-00	-22.5	9.9	4.4
53	7-31-17/23:49-50	-22.8	8.9	2.5
54	8-01-17/09:01-02	-22.7	8.7	2.4
55	8-01-17/09:58-59	-22.6	8.5	2.5
56	8-01-17/11:00-01	-22.1	7.8	3
57	8-01-17/13:04-05	-21.6	11.9	1.6
58	8-03-17/16:30-31	-21.7	8.5	2.6
59	8-04-17/09:02-03	-16.2	12.5	1.8
60	8-06-17/00:11-12	-16.9	12.7	1.7
61	8-06-17/01:22-23	-22.1	11.5	3.2
62	8-06-17/18:22-23	-22.2	10.3	4.6
63	8-06-17/21:49-50	-19.9	7.6	2.7

64	8-07-17/09:12-13	-15.3	3.3	4
65	8-07-17/17:04-05	-21.7	12	2.2
66	8-09-17/16:37-38	-16.6	5.7	2.9
67	8-10-17/10:17-18	-15.1	4.5	3.1
68	8-10-17/12:22-23	-13.2	3	3.4
69	8-10-17/13:00-01	-12	2.1	3.5
70	8-10-17/14:30-31	-20.6	14.2	0.8
71	8-10-17/15:42-43	-13.4	-3	3.9
72	8-12-17/05:24-25	-14.6	-4.1	4
73	6-16-18/18:44-45	-15.9	-5.5	4.2
74	6-16-18/20:10-11	-16.4	-6	4.3
75	6-16-18/22:05-06	-16.1	-4.1	5
76	6-16-18/23:03-04	-16.7	-4.8	5
77	6-19-18/17:47-48	-17.3	-5.5	5
78	6-19-18/18:38-39	-18.1	-2.3	6.6
79	6-19-18/19:40-41	-20.7	-6.5	6.9
80	6-25-18/11:45-46	-20.9	-7	6.7
81	6-25-18/18:13-14	-21.5	-8.4	6.3
82	6-25-18/18:59-00	-19.1	-12	7
83	6-25-18/21:30-31	-18.5	-12.4	6.1
84	6-26-18/18:04-05	-17.8	-12.7	5.2
85	6-26-18/19:22-23	-17.1	-12.8	4.8
86	6-26-18/20:55-05	-16.9	-12.7	4.7
87	6-26-18/22:15-16	-11.3	0.4	3.6
88	6-26-18/22:49-50	-20.8	-3.5	7.9
89	6-27-18/22:58-59	-21.6	-5.5	7.9
90	6-28-18/13:02-03	-21.7	-5.8	7.8

91	6-28-18/16:07-08	-22	-7.1	7.4
92	6-28-18/16:35-36	-17.7	-11.2	6.6
93	6-28-18/18:21-22	-22.1	-3.9	8.6
94	6-29-18/17:59-00	-12.3	2.2	3.6
95	7-01-18/13:13-14	-12.9	1.9	3.9
96	7-03-18/15:15-16	-13.5	1.6	4.2
97	7-03-18/15:51-52	-10.6	-8.9	3.6
98	7-03-18/16:20-21	-10	-8.8	3.2
99	7-05-18/19:50-51	-12.6	3	3.4
100	7-05-18/20:22-23	-13.1	3	3.6
101	7-06-18/11:13-14	-14.1	2.7	4
102	7-06-18/11:38-39	-16.6	2.8	4.9
103	7-06-18/12:37-38	-19.6	1	6.4
104	7-09-18/11:09-10	-20	0.5	6.7
105	7-09-18/15:42-43	-19.5	-7.1	6.4
106	7-09-18/16:36-37	-19.4	-7.1	6.4
107	7-13-18/20:34-35	-19	-7.3	6.1
108	7-13-18/20:46-47	-22.2	2.1	7.1
109	7-13-18/21:24-25	-22.4	1.9	7.2
110	7-15-18/13:14-15	-23.1	0.4	7.7
111	7-15-18/13:46-47	-18.8	-5.6	6.8
112	7-15-18/16:32-33	-12.9	4.5	4
113	7-16-18/17:50-51	-13.2	4.4	4.2
114	7-17-18/18:24-25	-16.7	-5	6.3
115	7-17-18/18:43-44	-16.4	-5.1	6.1
116	7-19-18/17:01-02	-16.1	-5.3	5.9
117	7-19-18/17:23-24	-14.2	6.6	2.7

118	7-19-18/17:50-51	-14.5	6.6	2.9
119	7-23-18/11:15-16	-15.2	6.6	3.1
120	7-23-18/11:37-38	-15.4	6.5	3.2
121	7-23-18/12:20-21	-20.1	4.4	6.5
122	7-23-18/12:37-38	-23.5	-0.1	7.7
123	7-23-18/19:35-36	-23	-1.4	7.5
124	7-24-18/17:46-47	-17.5	7.2	3.6
125	7-24-18/20:09-10	-18.6	7	4.1
126	7-26-18/11:12-13	-19.9	6.5	5.1
127	7-26-18/12:54-55	-20.1	7.7	4.3
128	7-26-18/15:02-03	-20.1	7.7	4.3
129	7-29-18/11:40-41	-23.1	8.2	4.9
130	8-04-18/12:59-00	-19.7	2.1	5.5
131	8-05-18/11:35-36	-18.1	0.8	5.3
132	8-05-18/14:11-12	-16.4	-0.5	5
133	8-05-18/16:28-29	-16.1	0.7	4.6
134	8-08-18/12:38-39	-18.3	10.5	4
135	8-09-18/17:05-06	-19.4	11.5	3.3
136	8-12-18/15:37-38	-20.8	10.5	5.5
137	8-12-18/19:07-08	-22.9	8.7	3.9
138	8-13-18/10:22-23	-22.8	8.4	3.9
139	8-13-18/11:29-30	-16.4	12.2	2.1
140	8-15-18/06:44-45	-22.5	9.7	6.3
141	8-15-18/23:35-36	-21.7	7.8	3.6
142	8-16-18/11:50-51	-21.6	7.5	3.6
143	8-16-18/12:22-23	-19.8	4.8	4.6
144	8-16-18/17:25-26	-10.8	10.9	2.8

145	8-17-18/19:37-38	-18.6	13.2	2
146	8-18-18/07:17-18	-21.2	12.7	2.8
147	8-18-18/14:49-50	-21.4	12.5	3
148	8-18-18/15:17-18	-21.5	12.3	3.6
149	8-18-18/16:10-11	-21.8	11.8	4.4
150	8-18-18/17:30-31	-22	11.3	5.1
151	8-18-18/18:48-49	-21.9	8.8	4.2
152	8-19-18/05:29-30	-21.4	8.3	3.4
153	8-19-18/07:49-50	-20.4	7.2	3.1
154	8-19-18/11:00-01	-20.2	7	3.1
155	8-19-18/11:37-38	-20.2	7	3.1
156	7-01-19/21:06-08	-11.6	-14.3	-0.1
157	7-04-19/21:17-19	-19.6	-16.3	2.8
158	7-04-19/21:59-00	-19.3	-16.2	2.6
159	7-04-19/22:48-50	-19	-16.2	2.3
160	7-05-19/01:20-21	-17.7	-15.7	2.4
161	7-05-19/14:29-31	-7.7	-10.7	2
162	7-06-19/16:48-50	-20.8	-5.4	8.6
163	7-06-19/17:09-11	-21	-5.7	8.6
164	7-08-19/00:09-10	-23.6	-14.9	5
165	7-08-19/17:04-06	-16.3	-13.7	3.8
166	7-09-19/02:40-41	-8.2	-10.4	-0.1
167	7-10-19/20:10-12	-25.5	-10.3	7.6
168	7-12-19/08:59-01	-14.2	-11.4	4.6
169	7-13-19/17:29-30	-21.7	-3.1	8.4
170	7-15-19/15:15-17	-19.1	-11.2	5.5
171	7-16-19/14:21-22	-8.5	3.7	4

172	7-17-19/18:02-03	-26.2	-5.7	8.6
173	7-22-19/17:09-11	-19.4	-9.4	3.9
174	7-22-19/19:48-50	-17.4	-9.7	2.1
175	7-24-19/15:41-43	-26.1	-0.8	8.4
176	7-24-19/17:04-06	-26.4	-1.7	8.4
177	7-25-19/20:19-21	-24.5	-8	4.7
178	7-25-19/21:40-42	-24	-8.3	4.2
179	7-26-19/13:50-52	-12.3	-7.5	2.6
180	7-29-19/15:55-57	-21.3	-6.6	4.4
181	7-29-19/16:05-07	-21.2	-6.7	4.3
182	8-01-19/16:27-29	-26.7	-3.4	5.9
183	8-01-19/19:39-41	-25.7	-4.7	4.8
184	8-01-19/20:59-01	-25.2	-5.1	4.4
185	8-01-19/22:29-30	-24.6	-5.4	4
186	8-02-19/10:19-20	-17.1	-5.8	3.4
187	8-03-19/18:57-59	-22.3	4.5	7.2
188	8-05-19/12:29-30	-24	-3	4.7
189	8-05-19/15:52-54	-22.2	-4.2	3.7
190	8-05-19/16:19-21	-21.9	-4.3	3.6
191	8-05-19/21:27-29	-18.2	-5.5	1.5
192	8-06-19/03:41-43	-11.7	-5.7	0.5
193	8-07-19/13:27-29	-25.2	6.3	5.7
194	8-07-19/15:00-02	-25.8	5.7	6.1
195	8-08-19/12:49-51	-27.9	1.3	5.2
196	8-08-19/13:54-56	-27.7	0.9	5.2
197	8-08-19/17:14-16	-26.9	-0.7	4.8
198	8-08-19/19:03-05	-26.4	-1.5	4.5

199	8-08-19/22:09-10	-25.3	-2.4	3.8
200	8-09-19/12:13-15	-16	-4.3	2.2
201	8-10-19/13:24-26	-17.9	8.8	4.1
202	8-10-19/14:43-45	-18.9	8.6	4.6
203	8-10-19/15:04-06	-19.2	8.5	4.8
204	8-11-19/12:39-40	-27.9	5.7	4.9
205	8-11-19/13:51-53	-28.1	5.3	5.1
206	8-11-19/18:37-39	-28.4	3.2	5.6
207	8-12-19/10:54-56	-25.2	0.2	3.6
208	8-12-19/11:24-26	-25	0	3.5
209	8-12-19/14:19-20	-23.6	-1	3.1
210	8-12-19/14:48-50	-23.3	-1.2	3.1
211	8-12-19/17:31-33	-16.3	-3.8	0.6
212	8-13-19/00:17-19	-12.3	-4.3	0.3
213	8-13-19/03:50-52	-23.9	9.3	3.9
214	8-14-19/11:41-43	-24.8	8.9	4.4
215	8-14-19/13:50-52	-25.1	8.6	4.6
216	8-14-19/14:41-43	-25.5	8.3	5
217	8-14-19/15:39-41	-25.6	8.2	5.1
218	8-14-19/16:00-02	-27.8	4	3.6
219	8-15-19/13:21-23	-27.6	3.5	3.7
220	8-15-19/14:40-41	-26.1	1	3.5
221	8-15-19/20:44-46	-25.9	0.8	3.4
222	8-15-19/21:22-23	-24.5	0	2.7
223	8-16-19/01:01-03	-20.6	-1.3	1.8
224	8-16-19/07:39-41	-20.1	-1.5	1.8
225	8-16-19/08:24-26	-19.3	-1.8	1.7

226	8-16-19/09:29-31	-12.6	9.9	2.5
227	8-17-19/08:51-53	-15.3	10.5	2.6
228	8-17-19/11:40-42	-11.5	12.8	0.4
229	8-31-19/10:19-21	-12.5	13.2	0.4
230	8-31-19/11:29-31	-12.7	13.2	0.4
231	8-31-19/11:42-44	-12.9	13.3	0.4
232	8-31-19/11:56-58	-23.5	14.7	1.1
233	9-01-19/06:30-32	-23.8	14.6	0.6
234	9-01-19/07:25-27	-24.1	14.5	0.2
235	9-01-19/08:09-11	-24.2	14.5	0
236	9-01-19/08:44-46	-25.6	13.5	0.5
237	9-01-19/14:57-59	-26	12.9	1.7
238	9-01-19/17:24-26	-26	12.7	2
239	9-01-19/17:54-56	-19.7	3.4	-0.3
240	9-02-19/21:04-06	-16.4	1.4	-0.9
241	9-03-19/01:14-16	-18.2	15.8	-0.2
242	9-04-19/08:41-43	-18.7	15.9	-0.5
243	9-04-19/09:34-36	-19.1	15.9	-0.7
244	9-04-19/10:18-19	-25.2	11.2	-0.1
245	9-05-19/17:03-05	-25.1	10.9	0.2
246	9-05-19/17:48-50	-24.8	10.3	0.8
247	9-05-19/19:28-30	-24.5	9.8	1
248	9-05-19/20:49-51	-24.4	9.6	1
249	9-05-19/21:09-10	-24.1	9.1	0.9
250	9-05-19/22:32-33	-23.9	8.8	0.8
251	9-05-19/23:15-16	-23.7	8.5	0.7
252	9-06-19/00:02-04	-23	7.8	0.1

253	9-06-19/01:55-57	-22.5	7.2	-0.4
254	9-06-19/03:15-17	-22	6.7	-0.8
255	9-06-19/04:24-26	-21.5	6.1	-1.2
256	9-06-19/05:29-31	-21.1	5.7	-1.4
257	9-06-19/06:10-12	-10.7	14.2	-0.5
258	9-07-19/11:09-11	-11.6	14.6	-0.5
259	9-07-19/12:10-12	-13.8	15.6	0.5
260	9-07-19/15:01-02	-15.5	16.1	2.1
261	9-07-19/17:31-33	-15.7	16.1	2.4
262	9-07-19/17:55-57	-24.4	15.7	0.3
263	9-08-19/17:15-17	-24.7	15.1	1.6
264	9-08-19/19:44-46	-24.7	14.9	1.8
265	9-08-19/20:27-29	-24.8	14.7	2
266	9-08-19/21:10-12	-24.9	14.1	1.8
267	9-08-19/23:35-37	-24.8	13.9	1.6
268	9-09-19/00:27-29	-24.8	13.7	1.2
269	9-09-19/01:18-19	-24.8	13.5	0.8
270	9-09-19/02:04-06	-24.7	13.1	0.1
271	9-09-19/03:19-21	-24.7	12.9	-0.4
272	9-09-19/04:04-06	-21.7	-2.2	2.4
273	7-01-20/20:48-50	-22.5	-14.8	3.8
274	7-01-20/22:29-31	-22.6	-15.3	3.1
275	7-02-20/18:28-30	-20.2	-18.1	0.5
276	7-11-20/20:42-44	-20.8	-6.2	6.5
277	7-13-20/05:41-42	-23.1	-14.1	2.9
278	7-13-20/06:30-31	-22.9	-14.1	3.2
279	7-13-20/10:50-51	-21.3	-14	3.8

280	7-15-20/23:19-20	-25.6	-9.9	4.2
281	7-16-20/14:50-51	-24.7	-12.1	4.3
282	7-16-20/18:10-11	-23.7	-13	1.6
283	7-16-20/19:47-49	-23.2	-13.1	0.4
284	7-17-20/03:25-26	-19.8	-13.2	-0.6
285	7-18-20/15:18-20	-18.1	0	7
286	7-19-20/16:07-09	-26.5	-8.6	5.3
287	7-20-20/01:01-03	-25.7	-11	1.8
288	7-20-20/05:34-35	-24.6	-11.3	2.7
289	7-22-20/11:35-37	-23.3	-1.1	7
290	7-27-20/01:33-35	-26.7	-8.1	1.8
291	7-27-20/02:33-35	-26.5	-8.2	1.8
292	7-27-20/03:45-46	-26.2	-8.4	2
293	7-27-20/04:01-03	-26.1	-8.4	2
294	7-27-20/11:03-05	-23.7	-9.1	2.5
295	7-27-20/11:44-46	-23.4	-9.2	2.4
296	7-29-20/14:59-00	-25.1	0	5.8
297	7-30-20/15:55-57	-26.5	-6.7	2.4
298	7-31-20/01:54-56	-22.7	-8.3	-0.9
299	7-31-20/02:58-00	-22.1	-8.5	-0.8
300	7-31-20/10:23-25	-17	-9	0
301	8-02-20/14:45-50	-28	-1.8	4
302	8-02-20/16:59-01	-28.1	-2.7	3.5
303	8-02-20/22:30-32	-27.9	-4.4	1.9
304	8-02-20/23:05-06	-27.8	-4.6	1.7
305	8-03-20/01:21-23	-27.5	-5	1.5
306	8-03-20/02:33-35	-27.3	-5.1	1.4

307	8-03-20/05:48-50	-26.5	-5.6	1.5
308	8-03-20/07:46-48	-25.9	-5.9	1.6
309	8-03-20/08:05-07	-25.7	-6	1.6
310	8-03-20/12:15-17	-24	-6.7	1.2
311	8-05-20/11:53-55	-23.9	3.8	4.5
312	8-05-20/14:20-21	-25	3	4.6
313	8-05-20/15:08-10	-25.4	2.6	4.6
314	8-05-20/19:47-49	-26.9	0.6	4.4
315	8-05-20/18:32-33	-26.5	1.1	4.5
316	8-05-20/20:12-13	-27	0.4	4.3
317	8-05-20/20:40-41	-27.1	0.2	4.3
318	8-05-20/21:00-01	-27.2	0.1	4.2
319	8-06-20/11:07-09	-28	-2.4	2.4
320	8-06-20/11:49-50	-27.9	-2.6	2.3
321	8-24-20/00:49-50	-27.5	4.3	-0.7
322	8-24-20/01:39-40	-27.4	4	-0.9
323	8-24-20/02:57-59	-27.2	3.6	-1.3
324	8-24-20/03:48-50	-27.1	3.3	-1.5
325	8-26-20/03:23-25	-16.9	10.9	3.3
326	8-26-20/06:09-10	-19	11.2	1.8
327	8-26-20/09:58-00	-21.4	11.2	0.1
328	8-26-20/10:15-17	-21.5	11.1	0
329	8-26-20/17:54-55	-24.9	10	1.2
330	8-26-20/20:24-26	-25.7	9.5	1.7
331	8-26-20/21:55-56	-26.1	9.2	1.7
332	8-26-20/22:59-00	-26.4	9	1.5
333	8-26-20/23:35-37	-26.5	8.9	1.4

334	8-27-20/00:10-11	-26.6	8.8	1.2
335	8-27-20/01:21-23	-26.8	8.6	0.8
336	8-27-20/03:00-01	-27.1	8.2	0.1
337	8-29-20/09:31-33	-11.3	11.1	1
338	8-29-20/16:24-26	-17.4	12.1	1.8
339	8-29-20/17:30-31	-18.1	12.1	2.2
340	8-29-20/19:17-19	-19.3	11.9	2.8
341	8-29-20/19:40-41	-19.6	11.9	2.9
342	8-29-20/21:29-30	-20.7	11.8	3.2
343	8-29-20/22:29-30	-21.2	11.7	3.2
344	8-29-20/23:24-26	-21.7	11.7	3
345	8-30-20/00:49-51	-22.4	11.7	2.5
346	8-30-20/02:28-30	-23.2	11.7	1.7
347	8-30-20/04:49-50	-24.1	11.5	0.3
348	8-30-20/05:50-51	-24.5	11.4	-0.4
349	9-02-20/06:40-41	-18.3	13.1	0.2
350	9-02-20/17:45-46	-23.8	12.6	-0.1
351	9-02-20/18:56-58	-24.2	12.4	0.3
352	9-02-20/21:00-01	-24.8	12.1	0.7
353	9-05-20/10:20-21	-10.9	12.5	-0.1
354	9-05-20/11:50-52	-12.3	13	-0.3
355	9-05-20/12:37-39	-13	13.2	-0.3
356	9-05-20/19:04-05	-17.8	14	1.9
357	9-06-20/02:35-36	-21.8	14.1	0.6
358	9-12-20/07:44-46	-7.5	12.4	0.3
359	9-12-20/08:11-13	-8	12.7	0
360	9-13-20/03:26-28	-20.6	16.4	-1.2

361	9-22-21/07:57-59	-6.2	12.1	-1.7
362	9-22-21/08:30-32	-6.7	12.4	-2.1
363	9-08-21/09:31-33	-11.2	11.4	-1.7
364	9-05-21/02:23-24	-16.4	11.8	0.2
365	8-28-21/17:01-03	-8.2	8.5	2
366	8-26-21/03:40-41	-25.5	7.1	-1.9
367	8-22-21/06:28-30	-21.9	7.3	-0.3
368	8-22-21/07:20-21	-22.4	7.2	-0.7
369	8-18-21/10:34-36	-23.7	5.2	-0.1
370	8-15-21/01:41-43	-19.5	5.6	2.8
371	8-15-21/03:38-40	-20.9	5.4	2
372	8-15-21/05:02-03	-21.8	5.3	1.5
373	8-15-21/05:52-54	-22.3	5.1	1.1
374	8-15-21/07:41-42	-23.3	4.8	0.5
375	8-15-21/08:07-08	-23.6	4.7	0.4
376	8-14-21/16:03-05	-9.4	6.6	2.9
377	8-01-21/11:06-07	-25.4	-1.4	2.5
378	7-29-21/00:18-19	-25.6	-4.1	1.8
379	7-29-21/04:17-19	-26.5	-5.1	1.5
380	7-29-21/05:18-19	-26.7	-5.3	1.5
381	7-29-21/08:19-20	-27.1	-6	1.7
382	7-26-21/05:12-13	-26.4	-9.9	-0.5
383	7-26-21/06:10-11	-26.3	-10.2	-0.2
384	7-26-21/06:39-40	-26.2	-10.3	-0.1
385	7-22-21/02:12-13	-25.5	-7.6	1.7
386	7-22-21/04:25-26	-25.9	-8.1	2
387	7-22-21/05:20-21	-26	-8.3	2.1

388	7-22-21/06:05-06	-26.1	-8.5	2.2
389	7-22-21/10:56-57	-26.3	-9.6	2.6
390	7-21-21/12:49-50	-20.1	-1.5	5
391	7-18-21/14:35-36	-25.1	-8.7	3.6
392	7-17-21/17:25-26	-13.9	-0.1	5.3
393	7-17-21/19:47-48	-16.2	-1.8	5.1
394	7-15-21/14:28-29	-24.7	-13.6	1.7
395	7-15-21/14:59-01	-24.6	-13.8	1.3
396	8-23-22/02:49-50	-21.3	5.5	-2.9
397	8-20-22/01:03-05	-26.4	2.2	-4.8
398	8-19-22/03:51-52	-12.2	5.7	0
399	8-19-22/04:19-20	-12.8	5.7	-0.2
400	7-22-22/05:57-59	-18.9	-3.2	1.3
401	7-21-22/20:35-36	-9	1.2	2.7
402	7-21-22/23:40-42	-13.3	-0.4	2.2
403	7-19-22/06:10-11	-24	-10.1	-0.7
404	7-19-22/10:58-00	-24.8	-11.9	-0.1
405	7-12-22/02:12-15	-22.2	-11.2	-1.7
406	7-12-22/03:29-30	-22.5	-11.8	-1.4
407	7-12-22/06:16-19	-23	-13	-0.6
408	7-11-22/11:45-50	-14.7	-3	3
409	7-11-22/12:15-20	-15.1	-3.4	3
410	7-11-22/14:41-43	-17	-5.2	2.5

A.2.3 Ion Diffusion Regions

Table A.3: List of Ion Diffusion Region Events observed by MMS in Earth's magnetotail from 2017-2022. Several events were also identified in *Rogers et al.*, 2023

Event #	**Date/Time**	**X (GSM)**	**Y (GSM)**	**Z (GSM)**
1	5-28-17/03:57-00	-19.3	-11.8	0.8
2	7-03-17/05:26-29	-17.6	3.3	1.7
3	7-06-17/15:34-37	-24.1	1.4	4.4
4	7-06-17/15:40-50	-24.2	1.3	4.5
5	7-11-17/22:33-36	-21.6	4.1	3.8
6	7-17-17/07:45-55	-18.1	7.3	0.7
7	7-17-17/14:35-50	-21.8	6.8	2.1
8	7-26-17/00:02-05	-20.7	9.1	3.5
9	7-26-17/02:40-55	-21.7	9	3.2
10	7-26-17/07:00-03	-22.9	9	2.3
11	7-26-17/07:27-30	-23	8.9	2.2
12	8-06-17/05:13-16	-18.9	13	0.4
13	8-07-17/15:37-40	-16.4	4.4	3.8
14	8-10-17/12:15-30	-15.2	4.5	3.1
15	8-23-17/17:53-56	-18.8	16.1	1.1
16	6-28-18/18:20-30	-22	-7.1	7.4
17	7-06-18/11:00-15	-12.7	3	3.4
18	8-08-18/12:35-45	-16.1	0.8	4.6
19	8-15-18/11:57-00	-19.2	12.5	1.6
20	8-26-18/06:38-41	-9.5	12.6	-0.1
21	8-27-18/11:39-42	-21.1	13.3	0.8
22	8-27-18/12:14-17	-21.1	13.1	1
23	9-10-18/17:14-17	-18.2	15.9	1.3

24	9-10-18/23:57-59	-17.5	12.7	3.1
25	7-05-19/14:25-35	-7.7	-10.7	2
26	7-06-19/16:45-55	-20.8	-5.4	8.7
27	7-25-19/21:40-43	-24	-8.3	4.2
28	8-08-19/22:00-15	-25.3	-2.4	3.8
29	8-12-19/14:15-25	-23.6	-1	3.1
30	8-12-19/17:35-45	-21.6	-2.2	2.4
31	8-15-19/20:40-55	-26.1	1	3.5
32	8-31-19/11:55-10	-13	13.3	0.4
33	9-02-19/21:00-10	-19.7	3.4	-0.3
34	9-04-19/08:35-45	-18.3	15.8	-0.2
35	9-06-19/04:25-35	-21.9	6.6	-0.9
36	7-13-20/05:45-00	-23.1	-14.1	3
37	7-18-20/15:15-25	-18.1	0.1	7
38	8-02-20/14:45-55	-28	-1.8	4
39	8-02-20/16:55-05	-28.1	-2.7	3.5
40	8-03-20/01:05-15	-27.5	-4.9	1.5
41	8-05-20/14:15-25	-25.1	2.9	4.6
42	8-26-20/10:10-20	-21.5	11.1	0
43	8-29-20/09:55-05	-11.7	11.2	0.9
44	8-30-20/04:50-00	-24.1	11.5	0.3
45	9-02-20/18:40-00	-24.2	12.4	0.3
46	8-01-21/11:05-15	-25.4	-1.5	2.5
47	8-19-22/03:15-25	-11.5	5.7	0.3
48	7-12-22/06:10-25	-23	-13	-0.6
49	7-11-22/12:10-20	-15.1	-3.4	3

A.2.4 Electron-Only Reconnection Candidates

Table A.4: List of Electron-Only Reconnection Candidates observed by MMS in Earth's magnetotail from 2017-2022.

Event #	**Date/Time**	**X (GSM)**	**Y (GSM)**	**Z (GSM)**
1	7-20-17/09:59-10	-21.6	7.9	1.3
2	6-17-17/20:24-25	-19.3	-11.1	3.5
3	7-26-17/17:39-40	-23.5	6.4	4.6
4	8-14-17/18:56-57	-18.5	15.5	1.3
5	8-23-17/11:19-20	-18.1	17.1	-3.4
6	7-26-18/13:05-06	-18.7	7.0	4.2
7	7-05-19/01:55-56	-17.4	-15.6	2.6
8	8-31-19/11:30-31	-12.5	13.2	0.4
9	8-03-20/00:35-36	-28	-5	1
10	8-05-20/19:42-43	-27	0	4
11	9-09-20/20:06-07	-23	15	4
12	9-13-20/02:43-44	-20	15	5

A.3 Lu et al. Simulations

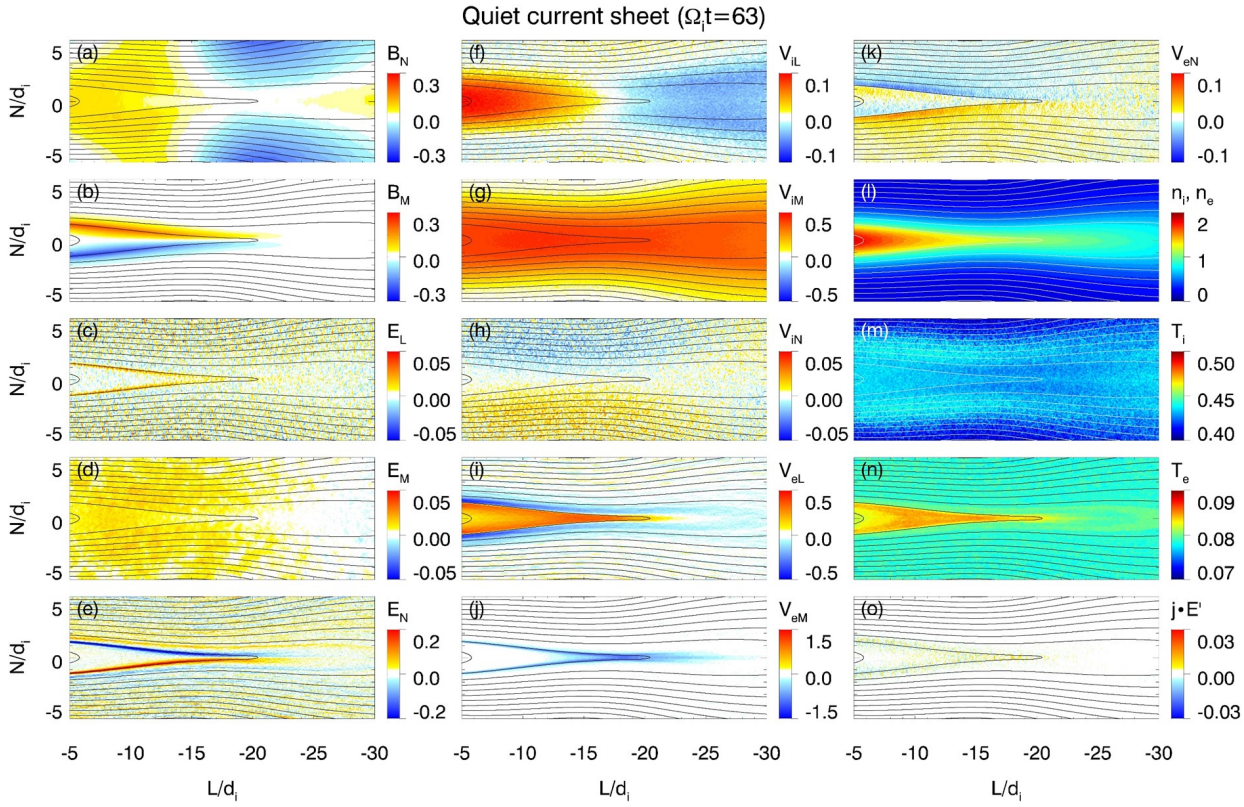

Figure A.2: Colored 2-D contours of (a, b) normal magnetic field B_N and out-of-plane magnetic field B_M (in unit of B_0) (c-e) electric field E_L, E_M, E_N (in unit of $V_A B_0$), (f-h) ion flow velocity V_{iL}, V_{iM}, V_{iN} (in unit of V_A), (i-k) electron flow velocity V_{eL}, V_{eM}, V_{eN} (in unit of V_A), (l) plasma density n_i, n_e (in unit of n_0), (m) ion temperature T_i (in unit of $m_i V_A^2$), (n) electron temperature T_e (in unit of $m_i V_A^2$), and (o) energy conversion $j \cdot E'$ (in unit of $e n_0 V_A^2 B_0$) in quiet current sheet at $\Omega_i t = 63$ in Case 1. The black curves represent the magnetic field lines in the L-N plane. (*Lu et al.*, 2022)

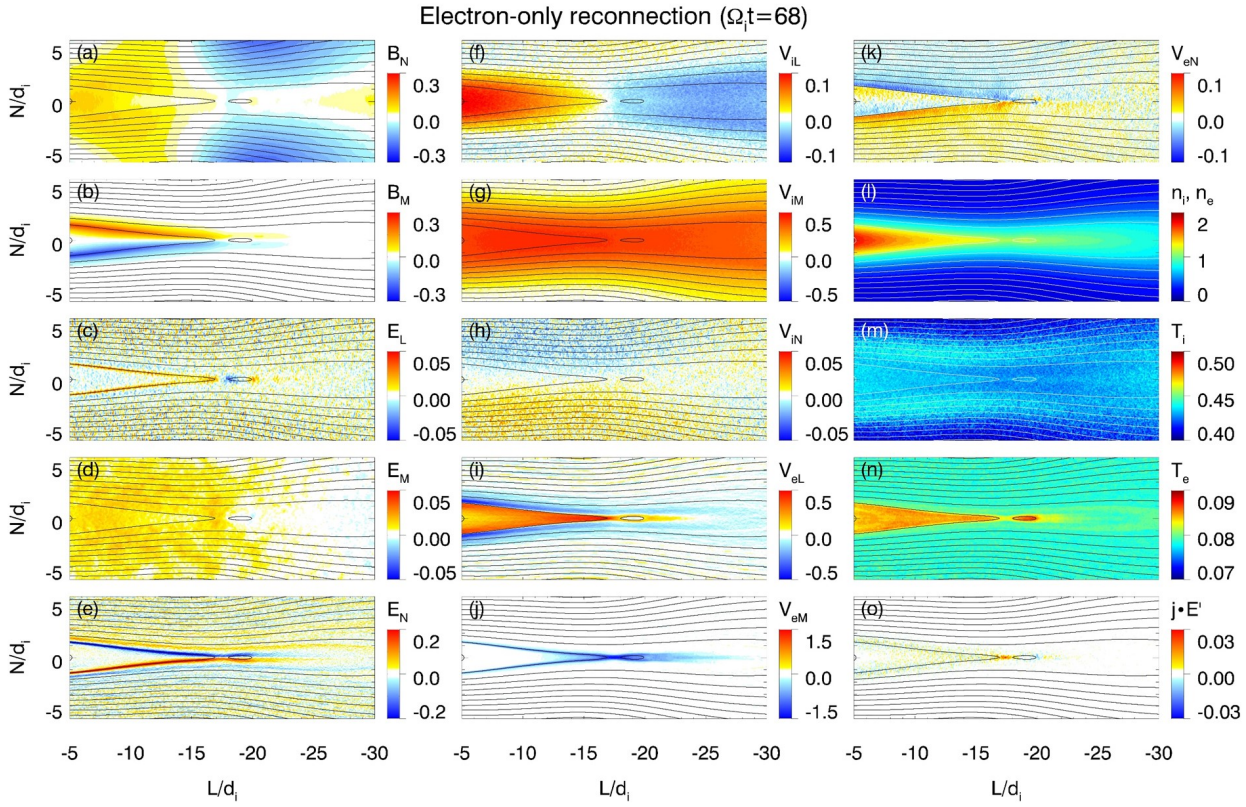

Figure A.3: Same format as Figure A.2, but in electron-only reconnection at $\Omega_i t = 68$. (*Lu et al.*, 2022)

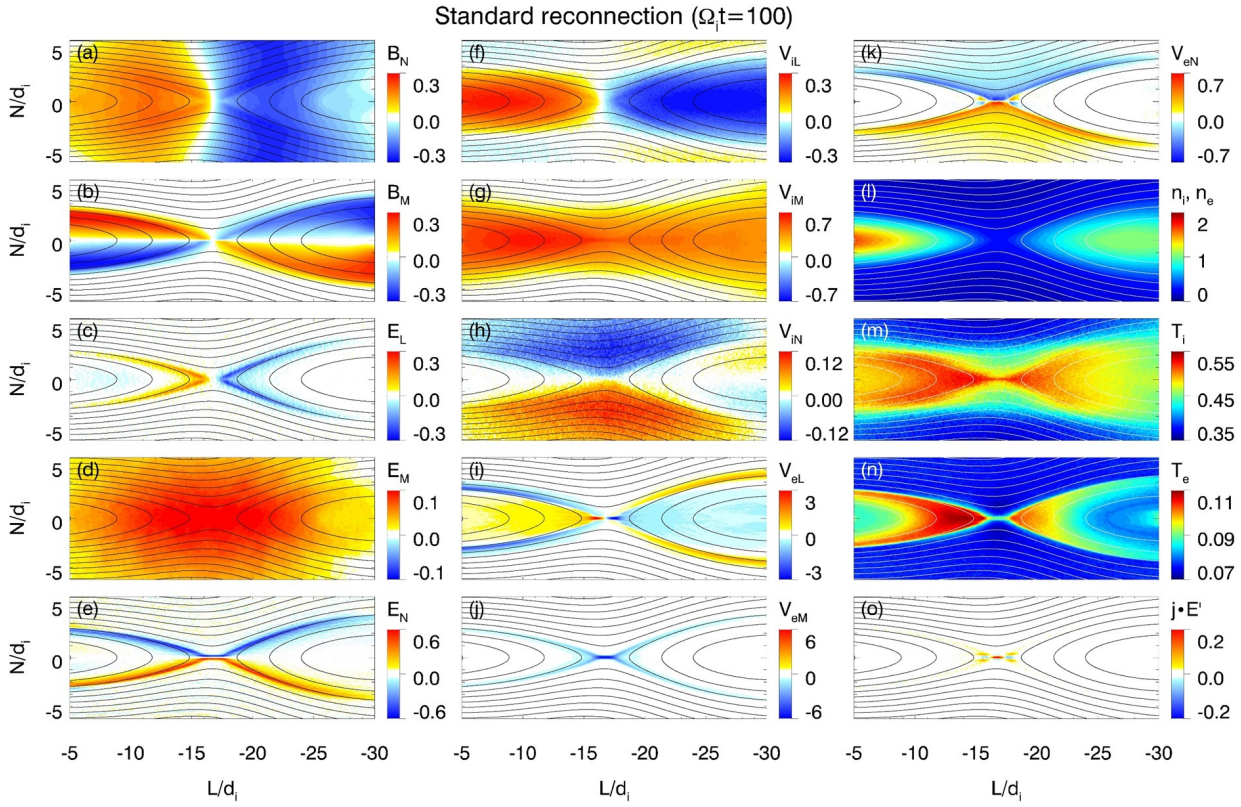

Figure A.4: Same format as Figure A.2, but in standard reconnection at $\Omega_i t = 100$.(*Lu et al.*, 2022)

Bibliography

Angelopoulos, V., W. Baumjohann, C. F. Kennel, F. V. Coroniti, M. G. Kivelson, R. Pellat, R. J. Walker, H. Lühr, and G. Paschmann (1992). Bursty bulk flows in the inner central plasma sheet. *Journal of Geophysical Research: Space Physics*, *97*(A4), 4027–4039, doi: https://doi.org/10.1029/91JA02701, _eprint: https://agupubs.onlinelibrary.wiley.com/doi/pdf/10.1029/91JA02701.

Argall, M. R., et al. (2018). Electron Dynamics Within the Electron Diffusion Region of Asymmetric Reconnection. *Journal of Geophysical Research: Space Physics*, *123*(1), 146–162, doi: 10.1002/2017JA024524, _eprint: https://onlinelibrary.wiley.com/doi/pdf/10.1002/2017JA024524.

Artemyev, A. V., V. Angelopoulos, I. Y. Vasko, A. A. Petrukovich, A. Runov, Y. Saito, L. A. Avanov, B. L. Giles, C. T. Russell, and R. J. Strangeway (2020). Contribution of Anisotropic Electron Current to the Magnetotail Current Sheet as a Function of Location and Plasma Conditions. *Journal of Geophysical Research: Space Physics*, *125*(1), e2019JA027,251, doi: 10.1029/2019JA027251, _eprint: https://onlinelibrary.wiley.com/doi/pdf/10.1029/2019JA027251.

Blasl, K. A., T. K. M. Nakamura, R. Nakamura, A. Settino, H. Hasegawa, Z. Vörös, M. Hosner, D. Schmid, M. Volwerk, Owen W. Roberts, E. Panov, Yi-Hsin Liu, F. Plaschke, J. E. Stawarz, and J. C. Holmes (2023). Electron-Scale Reconnecting Current Sheet Formed Within the Lower-Hybrid Wave-Active Region of Kelvin-Helmholtz Waves. *Geo-*

physical Research Letters, *50*(19), e2023GL104,309, doi: 10.1029/2023GL104309, _eprint: https://onlinelibrary.wiley.com/doi/pdf/10.1029/2023GL104309.

Burch, J. L., T. E. Moore, R. B. Torbert, and B. L. Giles (2016a). Magnetospheric Multiscale Overview and Science Objectives. *Space Science Reviews*, *199*(1), 5–21, doi: 10.1007/s11214-015-0164-9.

Burch, J. L., et al. (2016b). Electron-scale measurements of magnetic reconnection in space. *Science*, *352*(6290), aaf2939, doi: 10.1126/science.aaf2939, publisher: American Association for the Advancement of Science.

Chanteur, Gérard and Christopher C. Harvey (1998). Spatial Interpolation for Four Spacecraft: Application to Magnetic Gradients. *ISSI Scientific Reports Series*, *1*, 371–394, aDS Bibcode: 1998ISSIR...1..371C.

Chen, L.-J., S. Wang, M. Hesse, R. E. Ergun, T. Moore, B. Giles, N. Bessho, C. Russell, J. Burch, R. B. Torbert, K. J. Genestreti, W. Paterson, C. Pollock, B. Lavraud, O. Le Contel, R. Strangeway, Yu V. Khotyaintsev, and P.-A. Lindqvist (2019). Electron Diffusion Regions in Magnetotail Reconnection Under Varying Guide Fields. *Geophysical Research Letters*, *46*(12), 6230–6238, doi: 10.1029/2019GL082393, _eprint: https://agupubs.onlinelibrary.wiley.com/doi/pdf/10.1029/2019GL082393.

Coppi, B., G. Laval, and R. Pellat (1966). Dynamics of the Geomagnetic Tail. *Physical Review Letters*, *16*(26), 1207–1210, doi: 10.1103/PhysRevLett.16.1207, publisher: American Physical Society.

Dai, Lei and Chi Wang (2022). Kinetic Alfven wave (KAW) eigenmode in magnetosphere magnetic reconnection. *Reviews of Modern Plasma Physics*, *7*(1), 3, doi: 10.1007/s41614-022-00107-y.

Davis, T. Neil and Masahisa Sugiura (1966). Auroral electrojet activity index AE and its

universal time variations. *Journal of Geophysical Research (1896-1977)*, *71*(3), 785–801, doi: 10.1029/JZ071i003p00785.

Dungey, J. W. (1961). Interplanetary Magnetic Field and the Auroral Zones. *Physical Review Letters*, *6*(2), 47–48, doi: 10.1103/PhysRevLett.6.47.

Dunlop, Malcolm W., TieYan Wang, XiangCheng Dong, Stein Haarland, QuanQi Shi, HuiShan Fu, Johan De Keyser, Chao Shen, ZhaoJin Rong, Christophe Phillippe Escoubet, ZuYin Pu, and Jonathan Eastwood (2021). Multispacecraft Measurements in the Magnetosphere, in *Magnetospheres in the Solar System*, pp. 637–656, American Geophysical Union (AGU), doi: 10.1002/9781119815624.ch40, section: 40 _eprint: https://onlinelibrary.wiley.com/doi/pdf/10.1002/9781119815624.ch40.

Eastwood, J. P., T. D. Phan, M. Øieroset, and M. A. Shay (2010). Average properties of the magnetic reconnection ion diffusion region in the Earth's magnetotail: The 2001–2005 Cluster observations and comparison with simulations. *Journal of Geophysical Research: Space Physics*, *115*(A8), doi: 10.1029/2009JA014962.

Egedal, J., W. Daughton, and A. Le (2012). Large-scale electron acceleration by parallel electric fields during magnetic reconnection. *Nature Physics*, *8*(4), 321–324, doi: 10.1038/nphys2249, number: 4 Publisher: Nature Publishing Group.

Eriksson, Elin, Andris Vaivads, Daniel B. Graham, Andrey Divin, Yuri V. Khotyaintsev, Emiliya Yordanova, Mats André, Barbara L. Giles, Craig J. Pollock, Christopher T. Russell, Olivier Le Contel, Roy B. Torbert, Robert E. Ergun, Per-Arne Lindqvist, and James L. Burch (2018). Electron Energization at a Reconnecting Magnetosheath Current Sheet. *Geophysical Research Letters*, *45*, 8081–8090, doi: 10.1029/2018GL078660, aDS Bibcode: 2018GeoRL..45.8081E.

Farrugia, C. J., et al. (2021). An Encounter With the Ion and Electron Diffusion Regions at a Flapping and Twisted Tail Current Sheet. *Journal of Geophysical Research: Space*

Physics, *126*(3), e2020JA028,903, doi: https://doi.org/10.1029/2020JA028903, _eprint: https://agupubs.onlinelibrary.wiley.com/doi/pdf/10.1029/2020JA028903.

Forbes, T. G., E. W. Hones, S. J. Bame, J. R. Asbridge, G. Paschmann, N. Sckopke, and C. T. Russell (1981). Evidence for the tailward retreat of a magnetic neutral line in the magnetotail during substorm recovery. *Geophysical Research Letters*, *8*(3), 261–264, doi: 10.1029/GL008i003p00261, _eprint: https://agupubs.onlinelibrary.wiley.com/doi/pdf/10.1029/GL008i003p00261.

Fu, X. R., Q. M. Lu, and S. Wang (2006). The process of electron acceleration during collisionless magnetic reconnection. *Physics of Plasmas*, *13*(1), 012,309, doi: 10.1063/1.2164808, publisher: American Institute of Physics.

Gao, J. W., Z. J. Rong, Y. H. Cai, A. T. Y. Lui, A. A. Petrukovich, C. Shen, M. W. Dunlop, Y. Wei, and W. X. Wan (2018). The Distribution of Two Flapping Types of Magnetotail Current Sheet: Implication for the Flapping Mechanism. *Journal of Geophysical Research: Space Physics*, *123*(9), 7413–7423, doi: https://doi.org/10.1029/2018JA025695, _eprint: https://agupubs.onlinelibrary.wiley.com/doi/pdf/10.1029/2018JA025695.

Genestreti, K. J., J. L. Burch, P. A. Cassak, R. B. Torbert, R. E. Ergun, A. Varsani, T. D. Phan, B. L. Giles, C. T. Russell, S. Wang, M. Akhavan-Tafti, and R. C. Allen (2017). The Effect of a Guide Field on Local Energy Conversion During Asymmetric Magnetic Reconnection: MMS Observations. *Journal of Geophysical Research: Space Physics*, *122*(11), 11,342–11,353, doi: 10.1002/2017JA024247, _eprint: https://onlinelibrary.wiley.com/doi/pdf/10.1002/2017JA024247.

Horiuchi, Ritoku, Shunsuke Usami, and Hiroaki Ohtani (2014). Influence of a Guide Field on Collisionless Driven Reconnection. *Plasma and Fusion Research*, *9*, 1401,092–1401,092, doi: 10.1585/pfr.9.1401092.

Huang, C. Y., L. A. Frank, W. K. Peterson, D. J. Williams, W. Lennartsson, D. G.

Mitchell, R. C. Elphic, and C. T. Russell (1987). Filamentary structures in the magnetotail lobes. *Journal of Geophysical Research: Space Physics*, *92*(A3), 2349–2363, doi: 10.1029/JA092iA03p02349.

Huang, S. Y., Q. Y. Xiong, L. F. Song, J. Nan, Z. G. Yuan, K. Jiang, X. H. Deng, and L. Yu (2021). Electron-only Reconnection in an Ion-scale Current Sheet at the Magnetopause. *The Astrophysical Journal*, *922*(1), 54, doi: 10.3847/1538-4357/ac2668, publisher: The American Astronomical Society.

Huang, S. Y., K. Jiang, Z. G. Yuan, F. Sahraoui, L. H. He, M. Zhou, H. S. Fu, X. H. Deng, J. S. He, D. Cao, X. D. Yu, D. D. Wang, J. L. Burch, C. J. Pollock, and R. B. Torbert (2018). Observations of the Electron Jet Generated by Secondary Reconnection in the Terrestrial Magnetotail. *The Astrophysical Journal*, *862*(2), 144, doi: 10.3847/1538-4357/aacd4c, publisher: American Astronomical Society.

Hubbert, M., Y. Qi, C. T. Russell, J. L. Burch, B. L. Giles, and T. E. Moore (2021a). Electron-Only Tail Current Sheets and Their Temporal Evolution. *Geophysical Research Letters*, *48*(5), e2020GL091,364, doi: 10.1029/2020GL091364, _eprint: https://agupubs.onlinelibrary.wiley.com/doi/pdf/10.1029/2020GL091364.

Hubbert, M., Y. Qi, C. T. Russell, J. L. Burch, B. L. Giles, and T. E. Moore (2021b). Electron-Only Tail Current Sheets and Their Temporal Evolution. *Geophysical Research Letters*, *48*(5), e2020GL091,364, doi: 10.1029/2020GL091364.

Hubbert, M., C. T. Russell, Yi Qi, S. Lu, J. L. Burch, B. L. Giles, and T. E. Moore (2022). Electron-Only Reconnection as a Transition Phase From Quiet Magnetotail Current Sheets to Traditional Magnetotail Reconnection. *Journal of Geophysical Research: Space Physics*, *127*(3), e2021JA029,584, doi: 10.1029/2021JA029584.

Jiang, K., S. Y. Huang, Z. G. Yuan, X. H. Deng, Y. Y. Wei, Q. Y. Xiong, S. B. Xu, J. Zhang, Z. H. Zhang, R. T. Lin, and L. Yu (2022). Sub-

Structures of the Separatrix Region During Magnetic Reconnection. *Geophysical Research Letters*, *49*(6), e2022GL097,909, doi: 10.1029/2022GL097909, _eprint: https://onlinelibrary.wiley.com/doi/pdf/10.1029/2022GL097909.

Johnson, Francis S. (1960). The gross character of the geomagnetic field in the solar wind. *Journal of Geophysical Research (1896-1977)*, *65*(10), 3049–3052, doi: 10.1029/JZ065i010p03049.

Karimabadi, H., W. Daughton, P. L. Pritchett, and D. Krauss-Varban (2003a). Ion-ion kink instability in the magnetotail: 1. Linear theory. *Journal of Geophysical Research: Space Physics*, *108*(A11), doi: 10.1029/2003JA010026, _eprint: https://onlinelibrary.wiley.com/doi/pdf/10.1029/2003JA010026.

Karimabadi, H., P. L. Pritchett, W. Daughton, and D. Krauss-Varban (2003b). Ion-ion kink instability in the magnetotail: 2. Three-dimensional full particle and hybrid simulations and comparison with observations. *Journal of Geophysical Research: Space Physics*, *108*(A11), doi: 10.1029/2003JA010109, _eprint: https://onlinelibrary.wiley.com/doi/pdf/10.1029/2003JA010109.

King, J. H. and N. E. Papitashvili (2005). Solar wind spatial scales in and comparisons of hourly Wind and ACE plasma and magnetic field data. *Journal of Geophysical Research: Space Physics*, *110*(A2), doi: 10.1029/2004JA010649.

Lapenta, Giovanni, Stefano Markidis, Martin V. Goldman, and David L. Newman (2015). Secondary reconnection sites in reconnection-generated flux ropes and reconnection fronts. *Nature Physics*, *11*(8), 690–695, doi: 10.1038/nphys3406, number: 8 Publisher: Nature Publishing Group.

Lapenta, Giovanni, Francesco Pucci, Vyacheslav Olshevsky, Sergio Servidio, Luca Sorriso-Valvo, David L. Newman, and Martin V. Goldman (2018). Nonlinear waves and insta-

bilities leading to secondary reconnection in reconnection outflows. *Journal of Plasma Physics*, *84*(1), 715840,103, doi: 10.1017/S002237781800003X.

Lee, L. C. and K. H. Lee (2020). Fluid and kinetic aspects of magnetic reconnection and some related magnetospheric phenomena. *Reviews of Modern Plasma Physics*, *4*(1), 9, doi: 10.1007/s41614-020-00045-7.

Lembège, B. and R. Pellat (1982). Stability of a thick two-dimensional quasineutral sheet. *The Physics of Fluids*, *25*(11), 1995–2004, doi: 10.1063/1.863677.

Lepping, R. P., M. H. Acũna, L. F. Burlaga, W. M. Farrell, J. A. Slavin, K. H. Schatten, F. Mariani, N. F. Ness, F. M. Neubauer, Y. C. Whang, J. B. Byrnes, R. S. Kennon, P. V. Panetta, J. Scheifele, and E. M. Worley (1995). The WIND magnetic field investigation. *Space Science Reviews*, *71*(1), 207–229, doi: 10.1007/BF00751330, company: Springer Distributor: Springer Institution: Springer Label: Springer Number: 1 Publisher: Kluwer Academic Publishers.

Li, Xinmin, Rongsheng Wang, Quanming Lu, Kyoung-Joo Hwang, Qiugang Zong, Christopher T. Russell, and Shui Wang (2019). Observation of Nongyrotropic Electron Distribution Across the Electron Diffusion Region in the Magnetotail Reconnection. *Geophysical Research Letters*, *46*(24), 14,263–14,273, doi: 10.1029/2019GL085014, _eprint: https://agupubs.onlinelibrary.wiley.com/doi/pdf/10.1029/2019GL085014.

Lin, R. P., K. A. Anderson, S. Ashford, C. Carlson, D. Curtis, R. Ergun, D. Larson, J. McFadden, M. McCarthy, G. K. Parks, H. Rème, J. M. Bosqued, J. Coutelier, F. Cotin, C. D'Uston, K. P. Wenzel, T. R. Sanderson, J. Henrion, J. C. Ronnet, and G. Paschmann (1995). A three-dimensional plasma and energetic particle investigation for the wind spacecraft. *Space Science Reviews*, *71*(1), 125–153, doi: 10.1007/BF00751328.

Liu, Jing, Libo Liu, Takuji Nakamura, Biqiang Zhao, Baiqi Ning, and A. Yoshikawa (2014). A case study of ionospheric storm effects during long-lasting southward IMF Bz-driven

geomagnetic storm. *Journal of Geophysical Research: Space Physics*, *119*(9), 7716–7731, doi: 10.1002/2014JA020273.

Liu, Yi-Hsin, M. Hesse, F. Guo, W. Daughton, H. Li, P.A. Cassak, and M.A. Shay (2017). Why does Steady-State Magnetic Reconnection have a Maximum Local Rate of Order 0.1? *Physical Review Letters*, *118*(8), 085,101, doi: 10.1103/PhysRevLett.118.085101, publisher: American Physical Society.

Liu, Yi-Hsin, T. C. Li, M. Hesse, W. J. Sun, J. Liu, J. Burch, J. A. Slavin, and K. Huang (2019). Three-Dimensional Magnetic Reconnection With a Spatially Confined X-Line Extent: Implications for Dipolarizing Flux Bundles and the Dawn-Dusk Asymmetry. *Journal of Geophysical Research: Space Physics*, *124*(4), 2819–2830, doi: 10.1029/2019JA026539, _eprint: https://onlinelibrary.wiley.com/doi/pdf/10.1029/2019JA026539.

Lu, San, A. V. Artemyev, V. Angelopoulos, P. L. Pritchett, and A. Runov (2019). Effects of Cross-Sheet Density and Temperature Inhomogeneities on Magnetotail Reconnection. *Geophysical Research Letters*, *46*(1), 28–36, doi: 10.1029/2018GL081420, _eprint: https://onlinelibrary.wiley.com/doi/pdf/10.1029/2018GL081420.

Lu, San, Quanming Lu, Rongsheng Wang, Philip L. Pritchett, Mark Hubbert, Yi Qi, Kai Huang, Xinmin Li, and C. T. Russell (2022). Electron-Only Reconnection as a Transition From Quiet Current Sheet to Standard Reconnection in Earth's Magnetotail: Particle-In-Cell Simulation and Application to MMS Data. *Geophysical Research Letters*, *49*(11), e2022GL098,547, doi: 10.1029/2022GL098547.

Lu, San, et al. (2020). Magnetotail reconnection onset caused by electron kinetics with a strong external driver. *Nature Communications*, *11*(1), 5049, doi: 10.1038/s41467-020-18787-w.

Lui, A. T. Y. (1984). Characteristics of the Cross-Tail Current in the Earth's Magneto-

tail, in *Magnetospheric Currents*, pp. 158–170, American Geophysical Union (AGU), doi: 10.1029/GM028p0158.

Mallet, Alfred (2020). The onset of electron-only reconnection. *Journal of Plasma Physics*, *86*(3), 905860,301, doi: 10.1017/S0022377819000941, arXiv: 1912.02286.

Man, H. Y., M. Zhou, Y. Y. Yi, Z. H. Zhong, A. M. Tian, X. H. Deng, Y. Khotyaintsev, C. T. Russell, and B. L. Giles (2020a). Observations of Electron-Only Magnetic Reconnection Associated With Macroscopic Magnetic Flux Ropes. *Geophysical Research Letters*, *47*(19), e2020GL089,659, doi: 10.1029/2020GL089659, _eprint: https://agupubs.onlinelibrary.wiley.com/doi/pdf/10.1029/2020GL089659.

Man, H. Y., M. Zhou, Y. Y. Yi, Z. H. Zhong, A. M. Tian, X. H. Deng, Y. Khotyaintsev, C. T. Russell, and B. L. Giles (2020b). Observations of Electron-Only Magnetic Reconnection Associated With Macroscopic Magnetic Flux Ropes. *Geophysical Research Letters*, *47*(19), e2020GL089,659, doi: 10.1029/2020GL089659.

Man, H. Y., M. Zhou, X. H. Deng, H. S. Fu, Z. H. Zhong, Z. Z. Chen, C. T. Russell, R. J. Strangeway, W. R. Paterson, B. L. Giles, P.-A. Lindqvist, R. E. Ergun, and J. L. Burch (2018). In Situ Observation of Magnetic Reconnection Between an Earthward Propagating Flux Rope and the Geomagnetic Field. *Geophysical Research Letters*, *45*(17), 8729–8737, doi: 10.1029/2018GL079778.

Mandt, M. E., R. E. Denton, and J. F. Drake (1994). Transition to whistler mediated magnetic reconnection. *Geophysical Research Letters*, *21*(1), 73–76, doi: 10.1029/93GL03382, _eprint: https://onlinelibrary.wiley.com/doi/pdf/10.1029/93GL03382.

Masahito, Nose, Sugiura Masahisa, Kamei Toyohisa, and Iyemori Toshihiko (2017). AE Index. *(No Title)*, doi: 10.17593/15031-54800.

Matthaeus, W. H. and S. L. Lamkin (1986). Turbulent magnetic reconnection. *The Physics of Fluids*, *29*(8), 2513–2534, doi: 10.1063/1.866004.

Meyer, John C., Structure of the diffusion region in three dimensional magnetic reconnection, Ph.D. thesis, University of Delaware, (2015).

Moldwin, Mark B. and W. Jeffrey Hughes (1994). Observations of earthward and tailward propagating flux rope plasmoids: Expanding the plasmoid model of geomagnetic substorms. *Journal of Geophysical Research: Space Physics*, *99*(A1), 183–198, doi: https://doi.org/10.1029/93JA02102, _eprint: https://agupubs.onlinelibrary.wiley.com/doi/pdf/10.1029/93JA02102.

Nagai, T., M. Fujimoto, R. Nakamura, W. Baumjohann, A. Ieda, I. Shinohara, S. Machida, Y. Saito, and T. Mukai (2005). Solar wind control of the radial distance of the magnetic reconnection site in the magnetotail. *Journal of Geophysical Research: Space Physics*, *110*(A9), doi: 10.1029/2005JA011207, _eprint: https://onlinelibrary.wiley.com/doi/pdf/10.1029/2005JA011207.

Nagai, T., M. Fujimoto, Y. Saito, S. Machida, T. Terasawa, R. Nakamura, T. Yamamoto, T. Mukai, A. Nishida, and S. Kokubun (1998). Structure and dynamics of magnetic reconnection for substorm onsets with Geotail observations. *Journal of Geophysical Research: Space Physics*, *103*(A3), 4419–4440, doi: 10.1029/97JA02190.

Nakamura, R., W. Baumjohann, A. Runov, M. Volwerk, T. L. Zhang, B. Klecker, Y. Bogdanova, A. Roux, A. Balogh, H. Rème, J. A. Sauvaud, and H. U. Frey (2002). Fast flow during current sheet thinning. *Geophysical Research Letters*, *29*(23), 55–1–55–4, doi: 10.1029/2002GL016200, _eprint: https://onlinelibrary.wiley.com/doi/pdf/10.1029/2002GL016200.

Newell, Patrick T. and Kan Liou (2011). Solar wind driving and substorm triggering. *Journal of Geophysical Research: Space Physics*, *116*(A3), doi: 10.1029/2010JA016139.

Nishida, A. and S. W. H. Cowley (1998). *New Perspectives on the Earth's Magnetotail*, American Geophysical Union, google-Books-ID: wgKZGDA6H5UC.

NOAA, Solar Wind NOAA / NWS Space Weather Prediction Center, https://www.swpc.noaa.gov/phenomena/solar-wind, (2023).

Oka, M., T.-D. Phan, M. Øieroset, and V. Angelopoulos (2016). In situ evidence of electron energization in the electron diffusion region of magnetotail reconnection. *Journal of Geophysical Research: Space Physics*, *121*(3), 1955–1968, doi: 10.1002/2015JA022040, _eprint: https://agupubs.onlinelibrary.wiley.com/doi/pdf/10.1002/2015JA022040.

Phan, T. D., et al. (2018). Electron magnetic reconnection without ion coupling in Earth's turbulent magnetosheath. *Nature*, *557*(7704), 202–206, doi: 10.1038/s41586-018-0091-5, number: 7704 Publisher: Nature Publishing Group.

Pollock, C., et al. (2016). Fast Plasma Investigation for Magnetospheric Multiscale. *Space Science Reviews*, *199*(1), 331–406, doi: 10.1007/s11214-016-0245-4.

Pritchett, P. L. (2001). Collisionless magnetic reconnection in a three-dimensional open system. *Journal of Geophysical Research: Space Physics*, *106*(A11), 25,961–25,977, doi: 10.1029/2001JA000016, _eprint: https://agupubs.onlinelibrary.wiley.com/doi/pdf/10.1029/2001JA000016.

Pucci, F., S. Usami, H. Ji, X. Guo, R. Horiuchi, S. Okamura, W. Fox, J. Jara-Almonte, M. Yamada, and J. Yoo (2018). Energy transfer and electron energization in collisionless magnetic reconnection for different guide-field intensities. *Physics of Plasmas*, *25*(12), 122,111, doi: 10.1063/1.5050992.

Pyakurel, P. S., T. D. Phan, J. F. Drake, M. A. Shay, M. Øieroset, C. C. Haggerty, J. Stawarz, J. L. Burch, R. E. Ergun, D. J. Gershman, B. L. Giles, R. B. Torbert, R. J. Strangeway, and C. T. Russell (2023). On the Short-scale Spatial Variability of Electron Inflows in Electron-only Magnetic Reconnection in the Turbulent Magnetosheath Observed by MMS. *The Astrophysical Journal*, *948*(1), 20, doi: 10.3847/1538-4357/acb6f1, publisher: The American Astronomical Society.

Qi, Y., C. T. Russell, Ying-Dong Jia, and M. Hubbert (2020). Temporal Evolution of Flux Tube Entanglement at the Magnetopause as Observed by the MMS Satellites. *Geophysical Research Letters*, *47*(23), e2020GL090,314, doi: 10.1029/2020GL090314.

Qi, Yi, Tak Chu Li, Christopher T. Russell, Robert E. Ergun, Ying-Dong Jia, and Mark Hubbert (2022). Magnetic Flux Transport Identification of Active Reconnection: MMS Observations in Earth's Magnetosphere. *The Astrophysical Journal Letters*, *926*(2), L34, doi: 10.3847/2041-8213/ac5181.

Retinò, A., D. Sundkvist, A. Vaivads, F. Mozer, M. André, and C. J. Owen (2007). In situ evidence of magnetic reconnection in turbulent plasma. *Nature Physics*, *3*(4), 235–238, doi: 10.1038/nphys574, number: 4 Publisher: Nature Publishing Group.

Retinò, A., A. Vaivads, M. André, F. Sahraoui, Y. Khotyaintsev, J. S. Pickett, M. B. Bavassano Cattaneo, M. F. Marcucci, M. Morooka, C. J. Owen, S. C. Buchert, and N. Cornilleau-Wehrlin (2006). Structure of the separatrix region close to a magnetic reconnection X-line: Cluster observations. *Geophysical Research Letters*, *33*(6), doi: 10.1029/2005GL024650, _eprint: https://onlinelibrary.wiley.com/doi/pdf/10.1029/2005GL024650.

Richard, Robert L., Raymond J. Walker, Richard D. Sydora, and Maha Ashour-Abdalla (1989). The coalescence of magnetic flux ropes and reconnection in the magnetotail. *Journal of Geophysical Research: Space Physics*, *94*(A3), 2471–2483, doi: 10.1029/JA094iA03p02471, _eprint: https://onlinelibrary.wiley.com/doi/pdf/10.1029/JA094iA03p02471.

Rogers, A. J., C. J. Farrugia, and R. B. Torbert (2019). Numerical Algorithm for Detecting Ion Diffusion Regions in the Geomagnetic Tail With Applications to MMS Tail Season 1 May to 30 September 2017. *Journal of Geophysical Research: Space Physics*, *124*(8), 6487–6503, doi: 10.1029/2018JA026429.

Rogers, A. J., C. J. Farrugia, R. B. Torbert, and T. J. Rogers (2023). Applying Magnetic Curvature to MMS Data to Identify Thin Current Sheets Relative to Tail Reconnection. *Journal of Geophysical Research: Space Physics*, *128*(1), e2022JA030,577, doi: 10.1029/2022JA030577, _eprint: https://onlinelibrary.wiley.com/doi/pdf/10.1029/2022JA030577.

Runov, A., V. Angelopoulos, M. I. Sitnov, V. A. Sergeev, J. Bonnell, J. P. McFadden, D. Larson, K.-H. Glassmeier, and U. Auster (2009). THEMIS observations of an earthward-propagating dipolarization front. *Geophysical Research Letters*, *36*(14), doi: 10.1029/2009GL038980, _eprint: https://onlinelibrary.wiley.com/doi/pdf/10.1029/2009GL038980.

Russell, C. T. and R. L. McPherron (1973). The magnetotail and substorms. *Space Science Reviews*, *15*(2), 205–266, doi: 10.1007/BF00169321.

Russell, C. T., M. M. Mellott, E. J. Smith, and J. H. King (1983). Multiple spacecraft observations of interplanetary shocks: Four spacecraft determination of shock normals. *Journal of Geophysical Research: Space Physics*, *88*(A6), 4739–4748, doi: 10.1029/JA088iA06p04739, _eprint: https://onlinelibrary.wiley.com/doi/pdf/10.1029/JA088iA06p04739.

Russell, C. T., M. R. Arghavani, and J. G. Luhmann (1984). Interplanetary field enhancements in the solar wind: Statistical properties at 0.72 AU. *Icarus*, *60*(2), 332–350, doi: 10.1016/0019-1035(84)90194-5.

Russell, C. T., et al. (2016). The Magnetospheric Multiscale Magnetometers. *Space Science Reviews*, *199*(1), 189–256, doi: 10.1007/s11214-014-0057-3.

Sergeev, V., A. Runov, W. Baumjohann, R. Nakamura, T. L. Zhang, A. Balogh, P. Louarnd, J.-A. Sauvaud, and H. Reme (2004). Orientation and propagation of current sheet os-

cillations. *Geophysical Research Letters*, *31*(5), doi: 10.1029/2003GL019346, _eprint: https://onlinelibrary.wiley.com/doi/pdf/10.1029/2003GL019346.

Servidio, S., W. H. Matthaeus, M. A. Shay, P. A. Cassak, and P. Dmitruk (2009). Magnetic Reconnection in Two-Dimensional Magnetohydrodynamic Turbulence. *Physical Review Letters*, *102*(11), 115,003, doi: 10.1103/PhysRevLett.102.115003, publisher: American Physical Society.

Sharma Pyakurel, P., M. A. Shay, T. D. Phan, W. H. Matthaeus, J. F. Drake, J. M. TenBarge, C. C. Haggerty, K. G. Klein, P. A. Cassak, T. N. Parashar, M. Swisdak, and A. Chasapis (2019). Transition from ion-coupled to electron-only reconnection: Basic physics and implications for plasma turbulence. *Physics of Plasmas*, *26*(8), 082,307, doi: 10.1063/1.5090403, publisher: American Institute of Physics.

Shay, M. A., J. F. Drake, B. N. Rogers, and R. E. Denton (1999). The scaling of collisionless, magnetic reconnection for large systems. *Geophysical Research Letters*, *26*(14), 2163–2166, doi: 10.1029/1999GL900481, _eprint: https://onlinelibrary.wiley.com/doi/pdf/10.1029/1999GL900481.

Shen, C. and M. Dunlop (2023). Field Gradient Analysis Based on a Geometrical Approach. *Journal of Geophysical Research: Space Physics*, *128*(6), e2023JA031,313, doi: 10.1029/2023JA031313, _eprint: https://onlinelibrary.wiley.com/doi/pdf/10.1029/2023JA031313.

Sitnov, Mikhail, Joachim Birn, Banafsheh Ferdousi, Evgeny Gordeev, Yuri Khotyaintsev, Viacheslav Merkin, Tetsuo Motoba, Antonius Otto, Evgeny Panov, Philip Pritchett, Fulvia Pucci, Joachim Raeder, Andrei Runov, Victor Sergeev, Marco Velli, and Xuzhi Zhou (2019). Explosive Magnetotail Activity. *Space Science Reviews*, *215*(4), 31, doi: 10.1007/s11214-019-0599-5.

Snekvik, K., E. Tanskanen, N. Østgaard, K. Laundal, E. I. Gordeev, and A. L. Borg

(2012). Changes in the magnetotail configuration before near-Earth reconnection. *Journal of Geophysical Research: Space Physics*, *117*(A2), doi: 10.1029/2011JA017040, _eprint: https://onlinelibrary.wiley.com/doi/pdf/10.1029/2011JA017040.

Sonnerup, B. U. Ö. (1979). *Magnetic field reconnection*, vol. 3.

Sonnerup, Bengt U. Ö. and Maureen Scheible (1998). Minimum and Maximum Variance Analysis. *ISSI Scientific Reports Series*, *1*, 185–220.

Stawarz, J. E., J. P. Eastwood, T. D. Phan, I. L. Gingell, M. A. Shay, J. L. Burch, R. E. Ergun, B. L. Giles, D. J. Gershman, O. Le Contel, P.-A. Lindqvist, C. T. Russell, R. J. Strangeway, R. B. Torbert, M. R. Argall, D. Fischer, W. Magnes, and L. Franci (2019). Properties of the Turbulence Associated with Electron-only Magnetic Reconnection in Earth's Magnetosheath. *The Astrophysical Journal Letters*, *877*(2), L37, doi: 10.3847/2041-8213/ab21c8.

Swisdak, M. (2016). Quantifying gyrotropy in magnetic reconnection. *Geophysical Research Letters*, *43*(1), 43–49, doi: 10.1002/2015GL066980, _eprint: https://onlinelibrary.wiley.com/doi/pdf/10.1002/2015GL066980.

Torbert, R. B., et al. (2018). Electron-scale dynamics of the diffusion region during symmetric magnetic reconnection in space. *Science*, *362*(6421), 1391–1395, doi: 10.1126/science.aat2998, publisher: American Association for the Advancement of Science Section: Report.

Tsyganenko, N. A. (1995). Modeling the Earth's magnetospheric magnetic field confined within a realistic magnetopause. *Journal of Geophysical Research: Space Physics*, *100*(A4), 5599–5612, doi: 10.1029/94JA03193, _eprint: https://onlinelibrary.wiley.com/doi/pdf/10.1029/94JA03193.

Tóth, Gábor, Yuxi Chen, Tamas I. Gombosi, Paul Cassak, Stefano Markidis, and Ivy Bo Peng (2017). Scaling the Ion Inertial Length and Its Implications for Modeling Recon-

nection in Global Simulations. *Journal of Geophysical Research: Space Physics*, *122*(10), 10,336–10,355, doi: 10.1002/2017JA024189.

Ueno, G., S. Machida, T. Mukai, Y. Saito, and A. Nishida (1999). Distribution of X-type magnetic neutral lines in the magnetotail with Geotail observations. *Geophysical Research Letters*, *26*(22), 3341–3344, doi: 10.1029/1999GL010714, _eprint: https://onlinelibrary.wiley.com/doi/pdf/10.1029/1999GL010714.

Ukhorskiy, A. Y., M. I. Sitnov, V. G. Merkin, M. Gkioulidou, and D. G. Mitchell (2017). Ion acceleration at dipolarization fronts in the inner magnetosphere. *Journal of Geophysical Research: Space Physics*, *122*(3), 3040–3054, doi: 10.1002/2016JA023304, _eprint: https://onlinelibrary.wiley.com/doi/pdf/10.1002/2016JA023304.

Vaivads, A., Y. Khotyaintsev, M. André, A. Retinò, S. C. Buchert, B. N. Rogers, P. Décréau, G. Paschmann, and T. D. Phan (2004). Structure of the Magnetic Reconnection Diffusion Region from Four-Spacecraft Observations. *Physical Review Letters*, *93*(10), 105,001, doi: 10.1103/PhysRevLett.93.105001, publisher: American Physical Society.

Vega, Cristian, Vadim Roytershteyn, Gian Luca Delzanno, and Stanislav Boldyrev (2020). Electron-only Reconnection in Kinetic-Alfvén Turbulence. *The Astrophysical Journal*, *893*(1), L10, doi: 10.3847/2041-8213/ab7eba, publisher: American Astronomical Society.

Vogiatzis, I. I., O. E. Malandraki, Q.-G. Zong, X.-Z. Zhou, T. E. Sarris, E. T. Sarris, H. Zhang, and T. A. Fritz (2011). THEMIS observations of earthward convected flux ropes triggering field dipolarization/substorm expansion and associated particle energization. *Annales Geophysicae*, *29*(11), 2117–2130, doi: 10.5194/angeo-29-2117-2011.

Voigt, Gerd-Hannes (1984). The shape and position of the plasma sheet in Earth's magnetotail. *Journal of Geophysical Research: Space Physics*, *89*(A4), 2169–2179, doi: 10.1029/JA089iA04p02169, _eprint: https://onlinelibrary.wiley.com/doi/pdf/10.1029/JA089iA04p02169.

Walker, R. J., R. L. Richard, T. Ogino, and M. Ashour-Abdalla (1999). The response of the magnetotail to changes in the IMF orientation: The magnetotail's long memory. *Physics and Chemistry of the Earth, Part C: Solar, Terrestrial & Planetary Science*, *24*(1), 221–227, doi: 10.1016/S1464-1917(98)00032-4.

Walker, Raymond J., Giovanni Lapenta, Haoming Liang, Jean Berchem, Mostafa El-Alaoui, and Melvyn L. Goldstein (2018). Structure and Dynamics of Three-Dimensional Magnetotail Reconnection. *Journal of Geophysical Research: Space Physics*, *123*(10), 8241–8260, doi: 10.1029/2018JA025509, _eprint: https://onlinelibrary.wiley.com/doi/pdf/10.1029/2018JA025509.

Wang, Rongsheng, Quanming Lu, San Lu, Christopher T. Russell, J. L. Burch, Daniel J. Gershman, W. Gonzalez, and Shui Wang (2020a). Physical Implication of Two Types of Reconnection Electron Diffusion Regions With and Without Ion-Coupling in the Magnetotail Current Sheet. *Geophysical Research Letters*, *47*(21), e2020GL088,761, doi: 10.1029/2020GL088761.

Wang, Rongsheng, Quanming Lu, Rumi Nakamura, Wolfgang Baumjohann, Can Huang, Christopher T. Russell, J. L. Burch, Craig J. Pollock, Dan Gershman, R. E. Ergun, Shui Wang, P. A. Lindqvist, and Barbara Giles (2018). An Electron-Scale Current Sheet Without Bursty Reconnection Signatures Observed in the Near-Earth Tail. *Geophysical Research Letters*, *45*(10), 4542–4549, doi: 10.1002/2017GL076330, _eprint: https://agupubs.onlinelibrary.wiley.com/doi/pdf/10.1002/2017GL076330.

Wang, Shimou, Rongsheng Wang, Quanming Lu, Huishan Fu, and Shui Wang (2020b). Direct evidence of secondary reconnection inside filamentary currents of magnetic flux ropes during magnetic reconnection. *Nature Communications*, *11*(1), 3964, doi: 10.1038/s41467-020-17803-3, bandiera_abtest: a Cc_license_type: cc_by Cg_type: Nature Research Journals Number: 1 Primary_atype: Research Publisher: Nature Publishing Group Sub-

ject_term: Magnetospheric physics;Planetary science Subject_term_id: magnetospheric-physics;planetary-science.

Xiao, Sudong, Tielong Zhang, Yasong Ge, Guoqiang Wang, Wolfgang Baumjohann, and Rumi Nakamura (2016). A statistical study on the shape and position of the magnetotail neutral sheet. *Annales Geophysicae*, *34*(2), 303–311, doi: 10.5194/angeo-34-303-2016, publisher: Copernicus GmbH.

Yamada, Masaaki, Russell Kulsrud, and Hantao Ji (2010). Magnetic reconnection. *Reviews of Modern Physics*, *82*(1), 603–664, doi: 10.1103/RevModPhys.82.603, publisher: American Physical Society.

Yu, Xiancai, Rongsheng Wang, Quanming Lu, Christopher T. Russell, and Shui Wang (2019). Nonideal Electric Field Observed in the Separatrix Region of a Magnetotail Reconnection Event. *Geophysical Research Letters*, *46*(19), 10,744–10,753, doi: 10.1029/2019GL082538, _eprint: https://agupubs.onlinelibrary.wiley.com/doi/pdf/10.1029/2019GL082538.

Zeiler, A., D. Biskamp, J. F. Drake, B. N. Rogers, M. A. Shay, and M. Scholer (2002). Three-dimensional particle simulations of collisionless magnetic reconnection. *Journal of Geophysical Research: Space Physics*, *107*(A9), SMP 6–1–SMP 6–9, doi: 10.1029/2001JA000287, _eprint: https://onlinelibrary.wiley.com/doi/pdf/10.1029/2001JA000287.

Zelenyi, Lev and Anton Artemyev (2013). Mechanisms of Spontaneous Reconnection: From Magnetospheric to Fusion Plasma. *Space Science Reviews*, *178*(2), 441–457, doi: 10.1007/s11214-013-9959-8.

Zhang, Mao, Rongsheng Wang, Quanming Lu, and Shui Wang (2020). Observation of the Tailward Electron Flows Commonly Detected at the Flow Boundary of the Earthward

Ion Bursty Bulk Flows in the Magnetotail. *The Astrophysical Journal*, *891*(2), 175, doi: 10.3847/1538-4357/ab72a8, publisher: The American Astronomical Society.

Zhao, Cong, Statistical Study on Two Types Of Flux Transfer Events Observed By MMS Spacecraft, Ph.D. thesis, UCLA, (2019).

Zhou, M., H. Y. Man, X. H. Deng, Y. Pang, Y. Khotyaintsev, G. Lapenta, Y. Y. Yi, Z. H. Zhong, and W. Q. Ma (2021). Observations of Secondary Magnetic Reconnection in the Turbulent Reconnection Outflow. *Geophysical Research Letters*, *48*(4), e2020GL091,215, doi: 10.1029/2020GL091215.

Zhou, M., et al. (2017). Coalescence of Macroscopic Flux Ropes at the Subsolar Magnetopause: Magnetospheric Multiscale Observations. *Physical Review Letters*, *119*(5), 055,101, doi: 10.1103/PhysRevLett.119.055101, publisher: American Physical Society.

Zhou, M., X. H. Deng, Z. H. Zhong, Y. Pang, R. X. Tang, M. El-Alaoui, R. J. Walker, C. T. Russell, G. Lapenta, R. J. Strangeway, R. B. Torbert, J. L. Burch, W. R. Paterson, B. L. Giles, Y. V. Khotyaintsev, R. E. Ergun, and P.-A. Lindqvist (2019). Observations of an Electron Diffusion Region in Symmetric Reconnection with Weak Guide Field. *The Astrophysical Journal*, *870*(1), 34, doi: 10.3847/1538-4357/aaf16f, publisher: American Astronomical Society.

Zhou, X.-Z., V. Angelopoulos, V. A. Sergeev, and A. Runov (2010). Accelerated ions ahead of earthward propagating dipolarization fronts. *Journal of Geophysical Research: Space Physics*, *115*(A5), doi: 10.1029/2010JA015481.

Zhu, Zhongwei and R. M. Winglee (1996). Tearing instability, flux ropes, and the kinetic current sheet kink instability in the Earth's magnetotail: A three-dimensional perspective from particle simulations. *Journal of Geophysical Research: Space Physics*, *101*(A3), 4885–4897, doi: 10.1029/95JA03144, _eprint: https://onlinelibrary.wiley.com/doi/pdf/10.1029/95JA03144.

Øieroset, M., et al. (2021). Spatial evolution of magnetic reconnection diffusion region structures with distance from the X-line. *Physics of Plasmas*, *28*(12), 122,901, doi: 10.1063/5.0072182, publisher: American Institute of Physics.